ABSTRACT

Title of dissertation: FLIGHT DYNAMICS SIMULATION MODELING
                          AND CONTROL OF A LARGE
                          FLEXIBLE TILTROTOR AIRCRAFT

                          Ondrej Juhasz, Doctor of Philosophy, 2014

Dissertation directed by: Professor Roberto Celi
                           Department of Aerospace Engineering

A high order rotorcraft mathematical model is developed and validated against the XV-15 and a Large Civil Tiltrotor (LCTR) concept. The mathematical model is generic and allows for any rotorcraft configuration, from single main rotor helicopters to coaxial and tiltrotor aircraft. Rigid-body and inflow states, as well as flexible wing and blade states are used in the analysis. The separate modeling of each rotorcraft component allows for structural flexibility to be included, which is important when modeling large aircraft where structural modes affect the flight dynamics frequency ranges of interest, generally 1 to 20 rad/sec. Details of the formulation of the mathematical model are given, including derivations of structural, aerodynamic, and inertial loads. The linking of the components of the aircraft is developed using an approach similar to multibody analyses by exploiting a tree topology, but without equations of constraints. Assessments of the effects of wing flexibility are given. Flexibility effects are evaluated by looking at the nature of the couplings between rigid-body modes and wing structural modes and vice versa. The

effects of various different forms of structural feedback on aircraft dynamics are analyzed. A proportional-integral feedback on the structural acceleration is deemed to be most effective at both improving the damping and reducing the overall excitation of a structural mode. A model following control architecture is then implemented on full order flexible LCTR models. For this aircraft, the four lowest frequency structural modes are below 20 rad/sec, and are thus needed for control law development and analysis. The impact of structural feedback on both Attitude-Command, Attitude-Hold (ACAH) and Translational Rate Command (TRC) response types are investigated. A rigid aircraft model has optimistic performance characteristics, and a control system designed for a rigid aircraft could potentially destabilize a flexible one. The various control systems are flown in a fixed-base simulator. Pilot inputs and aircraft performance are recorded and analyzed.

FLIGHT DYNAMICS SIMULATION MODELING AND CONTROL OF A LARGE FLEXIBLE TILTROTOR AIRCRAFT

by

Ondrej Juhasz

Dissertation submitted to the Faculty of the Graduate School of the
University of Maryland, College Park in partial fulfillment
of the requirements for the degree of
Doctor of Philosophy
2014

Advisory Committee:
Professor Roberto Celi, Chair/Advisor
Professor Sung Lee
Professor Inderjit Chopra
Professor James Baeder
Professor Balakumar Balachandran

Acknowledgments

There are many people that have contributed to making my graduate experience successful and without whom I would not have finished. They have provided encouragement and support, and often times just made themselves available to listen.

I would like to thank Professor Roberto Celi for taking me on as a graduate student and having faith in my ability to succeed. He has spent much time explaining, and re-explaining, various aspects of flight dynamics to me, and for that I am very grateful.

Dr. Mark Tischler has also provided great guidance to me in terms of flight controls. He gave me an opportunity to directly engage with and learn from him in California, giving me a much more well-rounded graduate experience. My dissertation and I thank you for always asking for more and never settling for the inadequate.

I would like to thank Professors James Baeder, Balakumar Balachandran, Inderjit Chopra and Sung Lee for agreeing to be on my committee and taking the time to review this dissertation.

Other graduate students often provided help and distraction in lab, both of which were always needed. Thanks go to Cal and John for being good friends in and out of school. Hopefully we remain close friends now that we live in different parts of the country. I would also like to thank Monica, Barath, Kumar, Jillian, and Ananth for their support and friendship.

Table of Contents

List of Tables

List of Figures

List of Symbols and Abbreviations

$\mathbf{a}_B$	acceleration vector of point on elastic beam
A, B, C, D	linear system matrices
D	derivative gain
e	elastic axis offset
EI	elastic beam stiffness per unit span
$f_{v,w}$	chord and beam forcing per unit span within finite element
$\mathbf{F}v, w$	chord and beam integrated forcing at finite element node j
$\mathbf{F}_{I,A,S,D,E}$	modal force vectors
g	gravitational acceleration
GJ	torsional stiffness per unit span
$\mathbf{H}$	finite element shape function vector
I	integral gain
K	control system gain
$\mathbf{K}$	stiffness matrix
m	elastic beam mass distribution per unit span
m_ϕ	torsional moment per unit span within finite element
$\mathbf{M}$	mass matrix
$\mathbf{M}_\phi$	Integrated moment at finite element node j
$\mathbf{n}$	nodal displacement vector
n^j	unit vector in coordinate system j
$\mathbf{N}$	blade structural eigenvector matrix
N_B	number of flexible beams
N_E	number of finite elements
N_h	number of beam harmonics used in trim
N_M	number of beam modes retained
N_R	number of rotors
N_W	number of wings
p	elastic beam external forcing per unit span
$\mathbf{p}_I$	inertial forcing vector along beam span
P	proportional gain
$\mathbf{P}$	displacement vector of any point in multibody system
$\mathbf{q}$	displacement vector
$\bar{\mathbf{q}}$	displacement vector including structural effects
$\mathbf{q}_I$	inertial moment vector along beam span
$\mathbf{r}$	displacement vector to arbitrary point within a body
$\mathbf{r}_B$	position vector of point on elastic beam
S^{jk}	transformation matrix from body k to body j
S^{RF}	transformation matrix from fixed to rotating coordinate systems
u	longitudinal aircraft velocity, state-space control vector
v	elastic beam chordwise displacement/lateral aircraft velocity
$v_{,x}$ and $v_{,xx}$	spatial derivatives of beam chordwise displacement

v	eigenvector
V	matrix of mode shapes used for modal coordinate transformation
w	elastic beam beamwise displacement/vertical aircraft velocity
w_i	gaussian quadrature weight
$w_{,x}$ and $w_{,xx}$	spatial derivatives of beam beamwise displacement
x	linear system state, beam displacement variable
x	state vector
x_0	beam displacement variable
y_0	chordwise displacement from beam elastic axis
y,**ẏ**, **ÿ**	vector of finite element nodal displacements, velocities and accelerations
z_0	beamwise displacement from beam elastic axis

α	aircraft angle of attack
β	aircraft sideslip angle
β_N	nacelle angle
β_P	blade precone angle
δ	pilot control input
ϵ	strain component
η	local coordinate within finite element, modal structural displacement within flexible state-space model
ζ	displacement to first body from reference point in multibody system, damping ratio
θ	aircraft pitch attitude
θ_G	non-elastic pitch (torsion) deflection at beam element
τ	time delay
ϕ	elastic beam torsion displacement, aircraft roll attitude
Φ	influence coefficient
ψ	azimuth angle
ω	natural frequency
Ω	rotor speed
Ω^{kj}	skew-symmetric matrix comparing angular velocities between multiple bodies

ACAH	Attitude Command, Attitude Hold
DAE	Differential Algebraic Equation
HQ(R)	Handling Quality (Rating)
ODE	Ordinary Differential Equation
MCT	Multi-Blade Coordinate Transformation
PID	Proportional-Integral-Derivative
PIO	Pilot Induced Oscillation
RC	Rate Command
TRC	Translational Rate Command

Chapter 1: Introduction

This chapter provides motivation for the dissertation and discusses prior work on tiltrotor flight dynamics modeling and control. Flexible aircraft modeling in general and tiltrotor simulation tools are also discussed

1.1 Motivation

Tiltrotor configurations have been proposed for both civil and military heavy-lift vertical take-off and landing (VTOL) missions. An in-depth NASA investigation examined several types of rotorcraft for large civil transport applications, and concluded that the tiltrotor had the best potential to meet the desired technology goals [1]. Goals were included for hover and cruise efficiency, empty weight fraction, and noise. The tiltrotor also presented the lowest developmental risk of the configurations analyzed. One of the four highest risk areas identified by the investigation was the need for broad spectrum active control, including flight control systems, rotor load limiting, and vibration and noisetiltion [1].

The development of a high-order model is paramount for accurately predicting a wide range of stability phenomena that tiltrotors are susceptible to, and it is one of the main subjects of this dissertation. The best known aeromechanic stability

problem for tiltrotor aircraft is whirl-flutter, which occurs at high advance ratios, and usually limits forward flight speed. At hover and low speeds, pilot inputs can excite low frequency wing structural modes for large tiltrotor configurations like the Large Civil Tiltrotor 2 (LCTR2, herein referred to as LCTR), Fig. 1.1. Lateral stick inputs, for example, result in antisymmetric wing bending motion. This wing structural response can cause low stability margins if the dynamics are not accounted for in flight control design. The structural modes for future large tiltrotors are likely to be in the range of interest for control system design, around 1/3 to 3 times the response crossover frequency, generally 1 to 20 rad/sec.

Most rotorcraft also tend to have increased levels of augmentation compared to fixed-wing aircraft, especially in hover and low speed where precision flying is necessary. The effect of fuselage feedback on the structural modes is not well understood, and the effects of structural feedback on the overall aircraft motion also need to be investigated. Structural sensors at the wing root and wing tip provide wing bending information, and combinations of these sensors may be used to improve structural damping and reduce overall structural excitation. Clearly, the success of future aircraft configurations will require an improved fundamental understanding of the interactions between handling qualities, high-gain flight control systems, and aircraft structural dynamics.
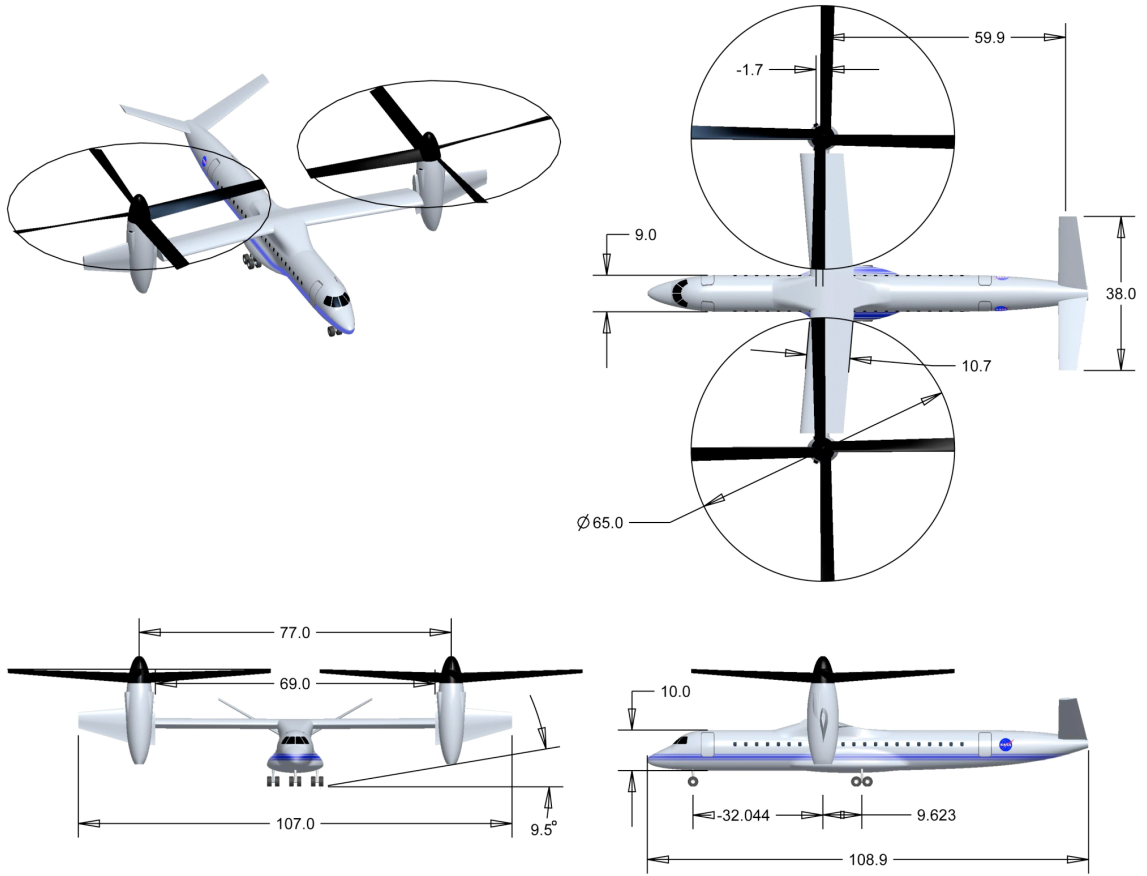
Figure 1.1: Configuration and dimensions of the NASA Large Civil Tiltrotor (LCTR) (from Ref. 2).

1.2 Background

In order to evaluate aircraft performance and enable the design of a control system that gives good handling qualities, accurate, real-time models are needed. These models can be used for pilot simulations and control system design. Details on tiltrotor modeling and controls work are presented first. Detail is also given on various comprehensive models used for rotorcraft and tiltrotor analysis. Because this dissertation is focused on a flexible aircraft, background information on flexible

3

aircraft control is also given.

1.2.1   Flight Dynamics Modeling and Handling Qualities of Tiltrotors

Several aircraft with tilting thrust components were developed in the 1950's and 1960's. With a fixed wing and tilting rotor systems the Bell XV-3 was the original tiltrotor. Teetering rotors were mounted on long rotating shafts and were powered by an engine in the fuselage. The Vertol VZ-2 was a tilt-wing aircraft. The entire wing system including the rotors were vertical in hover and tilted forward for cruise. The Doak VZ-4 had fixed wings and tilting ducts mounted at the end of the wings. Finally, the Curtiss-Wright X-100 had small tilting rotors connected to a small wing. Each of these aircraft were powered by a single engine located in the fuselage. Handling quality and dynamic characteristics for these aircraft are summarized in Ref. 3. All of the aircraft exhibited generally poor handling qualities in hover. The VZ-4 had inadequate roll control due to the use of guide vanes during hover. The VZ-2 exhibited very low longitudinal damping characteristics, making hovering very difficult. All of the aircraft had deficient yaw characteristics due to nearly no damping in the yaw axis. This led to buffeting in yaw, or difficulty in controlling heading. Many of these deficiencies were due to rotor inflow recirculation in ground effect. Overall, the XV-3 exhibited the fewest problems in terms of stability and control, as well as handling qualities.

Even though the XV-3 was generally the best behaved, it had several notable issues. During low speed flight, weak lateral-directional dynamic stability

and longitudinal and directional controllability were experienced [4]. These issues were attributed to rotor wash at low altitudes. During cruise, lateral-directional (dutch-roll) and longitudinal (short-period) damping was reduced as speed was increased [5]. This was found to be due to large inplane rotor forces created from large flapping as a result of aircraft angular rates. In spite of these issues, the tiltrotor configuration proved to be effective and transition between helicopter and airplane mode was shown to be safe, paving the way for additional research efforts for this configuration.

1.2.1.1   XV-15

During the 1970's work began on the XV-15 (Bell Model 301), shown in Fig. 1.2 and described in Ref. 6. The XV-15 is a 13,000 lb tiltrotor. Each rotor has three 12.5 foot radius blades mounted on a gimbaled hub. A large modeling effort was undertaken to accompany development and flight test of the aircraft. This modeling effort included development of a real-time flight simulation model for the Bell Model 301 [7]. The simulation model consisted of aerodynamic tuning based on semispan and 1/5 model scale wind-tunnel data [8, 9]. Model scale data helped determine rotor loading on the wing and other non-linearities, such as wake impingement on the horizontal tails in yaw. The model scale data was also used to ensure adequate dutch-roll and short-period damping, and it also ensured that the aircraft would remain flutter free in its flight envelope. Through this simulation model, initial handling qualities predictions were made based on specifications found in

MIL-SPEC-83300 [10]. Level 1 handling qualities were predicted based on longitudinal and lateral/directional mode frequency and damping characteristics [7]. This simulation model was later transformed to the GTRSIM model [11], described later. Reference 12 provides comparisons between the models developed for the XV-15 and flight data. Overall, the models show excellent correlation with flight data.

Figure 1.2: XV-15 in hover (NASA file photo)

A comprehensive analytical model of the tiltrotor wing/nacelle/rotor system model was derived in Ref. 13. This model was used in Ref. 14 to compare the dynamics of various tiltrotor rotor types. The model lacked rigid-body degrees of freedom and focused more on aeroelasticity of the wing/nacelle/rotor system. Using a similar model, stability and trim characteristics of the XV-15 were also investigated for a variety of nacelle angles [15]. With the nacelles in the cruise configuration, instability was predicted to occur near 300 knots at sea level. Comparisons of frequency and damping of flight dynamics modes in cruise and hover for varying quasi-steady models were also given.

The simulation model was used extensively in various simulators to help support handling qualities investigations, flight control design, failure mode reconfiguration, cockpit layout, and various other operational considerations [16]. This model helped to identify several limitations of the simulators. Pilots encountered vertical PIOs (pilot induced oscillations) near hover and the cause was identified as being due to visual system and engine model time-constant problems. Low roll damping caused the pilots to encounter PIOs in the lateral axis. This was encountered in the real aircraft, but it was not as prevalent as in the simulator. Simulator limitations also included a poor field of view so many missions were not able to be evaluated.

Initial flight control development and tuning of the XV-15 is presented in Ref. 17. The goal was to develop an aircraft with Level 1 handling qualities with the stability and control augmentation system (SCAS) off and the force feel system (FFS) on. The FFS aids the pilot in overcoming control system inertia and frictional forces during hover. It also allows for the tuning of the stick characteristics (natural frequency and damping) as well as static force characteristics. Reference 17 gives the improvements in the dutch-roll, short-period, and phugoid modes' damping due to the SCAS. Using the aforementioned model in piloted simulations resulted in SCAS gain changes that improved turn coordination, attitude retention disengagement alterations, and changes in stick force characteristics. Pilots gave Level 1 handling qualities ratings (HQR) with the SCAS and FFS active. These ratings did not change greatly due to a single channel failure in any mode. However, in hover with the SCAS and FFS off, pilots gave Level 3 HQRs due to the large increase in workload.

Flight dynamics models of the XV-15 were also obtained from flight test. Frequency domain identification of the XV-15 was performed in hover and cruise [18,19]. The pilots were instructed to fly frequency sweeps and time history data of the pilot input and aircraft responses were collected and converted to the frequency domain. Depending on the frequency range of interest, models obtained from flight test have the advantage that they can reduce highly-complex non-linear coupled systems into simple input-output frequency response relationships. Transfer function or linear models can then be fit to these input-output frequency responses to form a complete model of the aircraft. References 18 and 19 also present time history validation of identified models. Reference 20 also shows the identification of XV-15 structural modes using the same techniques.

1.2.1.2 V-22

After the XV-15 program showed excellent potential for the tiltrotor configuration, the JVX (V-22) program aimed to deliver tiltrotor technology to military customers in a production aircraft [21]. The V-22, shown in Fig. 1.3, is currently being fielded by the US Marines and Air Force. V-22 flight dynamics modeling capabilities descended directly from the XV-15 program as both aircraft were developed by Bell. Reference 12 showed excellent correlation of a "GTR" model to flight data. This model was scaled to the V-22 and was used for control law development [22].

An explicit model following type control algorithm was developed for the V-22 [23]. The control scheme contains a Primary Flight Control System (PFCS) that

Figure 1.3: V-22 in hover (NASA file photo)

improves basic aircraft stability. An Automatic Flight Control System (AFCS) helps provide Level 1 handling qualities through the model following architecture. Level 1 handling qualities ratings were obtained for all but one task throughout the test envelope [23]. The in-ground-effect precision hover task gave Level 2 ratings.

It is noted in Refs. 22 and 24 that certain structural loads exceeded their design limit during these tasks, and load limiting control laws were developed. In hover and conversion mode, rotor flapping was limited to prevent the rotor hub from potentially striking the mast. In cruise, load limiting control laws aimed to reduce the inplane forcing created by rotor precession during high speed aircraft pitching. The control laws also aimed to remove the rotor components from the short-period mode by an eigenstructure assignment method [24]. Control law development for the V-22 was seen as a compromise between handling qualities, structural, and aeroservoelastic stability requirements. Specifications mandated a 4g maneuver envelope at 345 knots. The aircraft was also required to hover at 47,500 lb gross weight with Level 1

handling qualities. The model following control system was found to be well suited

for such a large variety of loading and mission requirements [25].

Structural characteristics for the V-22 fuselage and rotors are given in Ref. 26.

The structural design of the V-22 used lessons learned from the XV-15 program to

improve the structural dynamics of the aircraft. Changes made include increasing

separation of the rotor inplane cyclic frequency from 1/rev, and improving airframe

natural frequency placements. Using analytical tools during the entire design process

as well as extensive validation efforts led to accurate modeling capabilities.

1.2.1.3 LCTR Control in Hover

Tiltrotors offer more control effectors than single main rotor helicopters. Each

rotor can be controlled independently and the nacelles are allowed to move as well.

Lateral control can come from differential collective on the rotors to roll the aircraft,

or symmetric lateral cyclic commands to produce lateral forcing by directly tilting

the rotor thrust vectors. Similarly, longitudinal control can come from moving

the nacelles fore and aft, or symmetric longitudinal cyclic can be used to produce

pitching moments. Given the possibility of having multiple controls in each axis,

studies have been done on tiltrotors to determine the piloted preferred response

types.

Bare-airframe single main rotor helicopters exhibit a rate command (RC) re-

sponse type in which pilot inputs result in angular or vertical rates, depending on the

control input. Control augmentation systems are used to improve handling qualities

by using an attitude-command attitude-hold (ACAH) system for cyclic commands. Here a unit cyclic stick deflection corresponds to an angular deflection from trim. That deflection is held until the pilot moves the cyclic stick to a different value. The collective stick commands a vertical velocity in the heave axis, and the pedals command yaw rates. With these response types, the nacelles may be held in a vertical position. A pure translational rate command (TRC) response type commands no angular deflection from the trim state. A translational rate can also be achieved by pitching the rotorcraft, but for tiltrotors it is achieved by tilting the thrust vector. The attitude of the aircraft can be controlled separately and may or may not be altered in a TRC control scheme. In the lateral axis, the symmetric lateral cyclic moves the thrust vector to create lateral motion. In the longitudinal axis, the nacelles are moved forward and back to create longitudinal motion. The heave and pedal axes remain unchanged from the ACAH system. Given the possibility of having either an ACAH or TRC response type to cyclic inputs, or a combination of the two, piloted simulations are needed to determine the configuration most preferred by pilots.

Piloted studies have recently been conducted in NASA's Vertical Motion Simulator [27–31]. These studies were designed to test hover and low speed handling qualities and control system architectures of the LCTR. Although CAMRAD (described in Sec. 1.2.2) is not a real-time tool, linear models derived from CAMRAD were used in many of these studies. The models were based on a combination of reduced-order stability derivative models and more detailed rigid-body models that included rotor flapping dynamics but lacked structural flexibility. Despite these limi-

tations, the linear rigid-body model was sufficient for determining handling qualities characteristics of large tiltrotors.

Reference 28 investigated effects of pilot station offset and command model delay on piloted handling qualities for an ACAH control system. The results show that a large pilot to CG offset resulted in a tradeoff between undesirable accelerations at the pilot station in the longitudinal and directional axes for quick aircraft command models and sluggish aircraft performance for slower command models. New boundaries were suggested for the ADS-33E [32] bandwidth criteria. Many of the proposed boundaries differ significantly from the classical ones.

Reference 29 investigates varying commanded response types in hover. Comparisons are drawn between ACAH and TRC modes with varying TRC inceptor types and nacelle motion limits. The results showed that there was a preference of TRC mode over ACAH, primarily so that sight lines to the runway were maintained. Pilots also preferred a decoupled TRC system and gave Level 1 handling qualities when objectionable pitch/heave couplings were removed in the longitudinal axis. Manual control of the nacelle angle was rated poorly due to difficulty in reconfiguring the aircraft back to a hover state after a maneuver was performed. A final NASA piloted simulation study [31] focused on TRC mode. The results show that nacelle bandwidths above 4 rad/sec gave Level 1 handing qualities ratings, and TRC control sensitivities of 10 ft/sec per inch of control was preferred in both axes.

1.2.1.4 Other Tiltrotor Handling Qualities Research

There are relatively few handling qualities criteria for tiltrotor aircraft. Based on LCTR work, new boundaries were established for ADS-33E bandwidth criteria for large tiltrotors. In hover, tiltrotors are expected to have the same dynamic behavior as traditional helicopters and follow ADS-33E. In cruise, they are expected to behave as fixed wing aircraft and follow specifications such as MIL-STD-1797B [33]. The transition zone between hover and cruise has not been well investigated and only general guidelines exist, as in MIL-83300 [10].

Initial steps in developing tiltrotor specific requirements are given in Ref. 34. This reference suggests new mission task elements (MTEs) that evaluate aircraft performance in mid-speed ranges and are representative of search-and-rescue or terrain following maneuvers. Also noted is the need for comprehensive simulations and flight tests for definition of specification boundaries. A new "Roll-Step" mission task element was flown and evaluated by test pilots on an XV-15 model. The model was developed using FLIGHTLAB (discussed in a later section). The ADS-33E bandwidth criteria was also evaluated within the aircraft's conversion corridor. The handling quality ratings were generally consistent with the boundaries. Another study used the same model to evaluate the XV-15 in low speed, transition, and high speed flight [35]. A model following control system was designed to give an ACAH response in hover and RCAH response in forward flight. The control system was evaluated in a motion based simulator and generally gave Level 1 handling qualities.

Load alleviating control laws were developed for a EUROTILT tiltrotor in

Ref. 36. These control laws aimed to reduce inplane forcing generated by the rotors due to maneuvering in cruise and to some extent hover. Similar load alleviating control laws were developed during the V-22 program [22] [24]. Rotor longitudinal cyclic and elevators were used to reduce loads in cruise. It was noted that in piloted simulations, load amplification was observed in maneuvers not accounted for during the control design. This highlights the complex nature of control law design, particularly structural load control design. Generally, there are tradeoffs in structural control for performance or actuator usage. The simulation used was FLIGHTLAB model that had rigid-blades and dynamic inflow [36]. Modeling simplifications were needed tin order to run the software in real time. This level of modeling was adequate to retain key flight dynamics characteristics of the aircraft for piloted simulations.

The BA-609 represents the first civil tiltrotor, and it is currently undergoing certification trials. A highly reliable flight control system is key to minimizing pilot workload and satisfying stringent handling qualities over the large flight envelope. The flight envelope for this aircraft range from a 35 knot tailwind hover to a 3g pull-up at Mach 0.55 [37]. The BA-609 lacks lateral cyclic rotor control and uses differential collective for lateral commands in hover. In cruise, differential collective to the rotors provides yaw control. Control laws provide rate-command responses to cyclic inputs. In yaw, a rate-command response and turn-coordination are implemented. There is gain-scheduling based on nacelle angle. The BA-609 has nacelle angle dependent notch filters on structural modes excited by longitudinal, lateral, and collective inputs. The aircraft also has a flapping controller in cruise to reduce

blade loads. In addition, Reference 37 also includes mission tasks flown to evaluate the aircraft. Even though formal pilot evaluations were not always obtained, pilot comments were used to update the control laws.

1.2.2 Comprehensive Tiltrotor Modeling Tools

As previously described, the XV-15 was developed in the 1970's and 1980's. To support analysis of flight dynamics, pilot-in-the-loop simulation, and flight control, the Generic Tilt-Rotor Simulation (GTRSIM) was developed [11]. GTRSIM is based heavily on wind tunnel data from the XV-15 in the form of look-up tables to augment the rigid-body dynamics [8] [9]. The detailed look-up tables include effects of nacelle angle, sideslip, flaperon deflections, Mach number, etc., on aerodynamic coefficients, and they also contain correction factors to the dynamic response of the aircraft. While accurate and capable of real-time execution, GTRSIM is highly dependent upon empirical data. The software may suffer problems due to scaling or for configurations that are slightly different than the XV-15. This software is also not suitable for rotor dynamics analyses as it retains a momentum theory type rotor system.

Later, CAMRAD, a comprehensive aeromechanics and dynamics model capable of multi-rotor and flexible airframe modeling, was developed [38]. CAMRAD originated in the extensive analytical analysis of tiltrotor dynamics across a very broad flight envelope [13–15].

CAMRAD was updated to CAMRAD2 [39, 40]. The update offers a larger

suite of analysis tools, and it has been used extensively for tiltrotor development and analysis, including the heavy lift helicopters that are of interest herein. Much of the work looked at high speed whirl-flutter and methods to improve aircraft performance while maintaing stability [41–43]. Analyses using this tool have also focused on optimization of the large civil tiltrotor for performance and whirl-flutter [2]. Performance optimization included rotor sizing and geometry as well as cruise tip speeds. Whirl-flutter optimization included cruise tip speeds, precone and other rotor metrics.

MBDyn [44], a multi-body dynamics code developed at Politecnico di Milano has often been used to model flexible tiltrotors. MBDyn has various elastic blade and wake models. Much work has been constrained to modeling a single wing-pylon-rotor system, and in examining ways to stabilize the wing-pylon-rotor system [45]. Generalized predictive control systems have also been created for reduced-order tiltrotor models where a revolute joint is used to hold the aircraft at the center of mass and only allow for pitch motion to be studied [46]. Created in a full multi-body architecture using constraint equations, linearized equations of motion cannot be extracted directly from this form of model. A linear model can be extracted from a time history of aircraft motion or by condensing out equations of constraint from the system.

FLIGHTLAB [47] is widely used in industry for single main rotor helicopter modeling and simulation as it allows for rapid prototyping of aircraft configurations. It has also been used for tiltrotor modeling [34, 36, 48] . FLIGHTLAB is of multi-body form and can be executed in real-time. Parallelization enables real-time

execution of the program even when flexible blades are included [49]. In addition to flexible blades, vortex wakes can also be modeled.

The University of Maryland has done extensive work on tiltrotor aeroelastic modeling using the code UMARC. The basic tiltrotor model was developed in Ref. 50. The results show excellent predictions of flutter velocities, trim conditions and rotor loads. The work has generally dealt with aeroelastic stability and whirl-flutter modeling of various rotor systems [51–53]. Aeroelastic tailoring of rotor blades to improve flutter boundaries was also performed [54]. A thorough description of UMARC and other comprehensive rotorcraft analyses and their histories can be found in Ref. [55].

The model used in this work, referred to as HeliUM 2, has been in development at the University of Maryland for many years and is a successor to the model first mentioned in Ref. 56. It originated from the NASA version of GenHel, built from a mathematical model by Howlett [57], and over time has evolved to include flexible rotors [58] and free-vortex wake models [59]. More recently, the code has been augmented to include multi-rotor capabilities. The current research effort has expanded this to include flexible wings and an overall multi-body-like formulation. The formulation of the flexibility does not include algebraic constraints and leaves the equations of motion as ordinary differential equations (ODE), allowing for more straightforward time integration and linearization. The model is generic and allows for any rotorcraft configuration, from single main rotor helicopters to coaxial and tiltrotor aircraft. Fuselage and wing aerodynamics portions of GTRSIM were added to this model. Therefore, the model was validated against the XV-15 before being

17

scaled to the LCTR configuration.

1.2.3 Control and Modeling of Flexible Aircraft

Flexible aircraft models have long been used to model fixed-wing aircraft. Flexible fuselage modeling of rotary-wing aircraft has been slow to follow, most likely because fixed-wing aircraft generally have much larger and thinner fuselages than rotary-wing aircraft, which are generally as compact as possible to reduce rotor interference effects. Fixed-wing aircraft also tend to be much larger than rotorcraft, having structural modes which are at low frequencies. Modeling structural modes becomes important for flutter analysis or for flight dynamics research if the modes are of low enough frequency.

While a wide range of flexible aircraft models exist, this discussion will be limited to flexible models created for flight control research. Historically, the flexible models have been derived from fitting flight data to some assumed structural deflections taken to be comprised of a few modes. The mode shapes came from ground shake tests, flight data, or intuition. In rare cases, finite element models were used to obtain the mode shapes. More recently, analytical models have also been used. In these models, interaction coefficients of the structural and rigid-body modes are determined based on lifting-line theory. Full multi-body dynamic type models, such as the one created for this dissertation, have also begun to gain prominence.

Flexible aircraft control tends to fall into two categories: reduction of structural loads for improvements in fatigue life, or vibration (acceleration) reduction

to improve ride quality. For military aircraft, the acceleration at the pilot station is minimized, while for commercial aircraft acceleration at some location in the fuselage is minimized (to improve passenger comfort). The overall goal of both categories is the same; the reduction of structural oscillation. In either case, wing tip acceleration is generally used as the feedback parameter.

Flexible aircraft models were first used to improve the flutter response of fixed-wing aircraft. The B-52 CCV (Controls Configured Vehicle) was one of the first aircraft to demonstrate benefits of active controls [60, 61]. The flutter speed of this aircraft was increased by 30% by using the outboard aileron and flaperons to suppress vertical acceleration of the wing. The power spectral density (PSD) of the vertical acceleration at the structural mode frequencies was significantly reduced. The model for this aircraft came from fitting aerodynamic model parameters to flight data and included 30 states, at least seven of which were vibratory modes.

Investigations into a Load Alleviation and Mode Control System (LAMS) were done on a YF-12 aircraft, the predecessor to the SR-71. Various different actuator systems were compared in theory to remove motion at the pilot station due to structural oscillation [62]. The damping of the structural modes and the RMS acceleration were shown to be much improved with the LAMS system operational. The elastic model from the aircraft came from a two dimensional finite element representation and included effects of structural deformation on aerodynamic terms. Powers [63] developed a flexible model of the SR-71 for use in handling qualities research. The flexible mode was identified by fitting an elastic beam mode shape to ground vibration test data. The unknowns in the mode shape were then calibrated

using flight data. The resulting flexible mode was added to rigid-body dynamics to form the complete aircraft model.

More recently, NASA has used a modified F-111 to test a Maneuver Loads Control (MLC) system [64]. This system aimed to minimize root bending moments during maneuvers by driving the lift vector of the wing inboard, reducing the moment arm. This was accomplished by using the wing flaps to change the camber of the wing. Some of the most recent flexible aircraft flight testing occurred during NASA's F/A-18 Active Aeroelastic Wing (AAW) program [65]. The control laws for this aicraft [66] were designed to not exceed certain wing load criteria during roll maneuvers. The loads model used was derived by fitting structural coefficients to flight data [67]. A flexible model for this system was created and used in the NASA Dryden flight simulator by summing rigid-body and structural dynamics at the outputs [68].

A CH-53K helicopter was modeled with flexibility for stability studies with a slung load [69]. Here, linear rigid-body dynamics and structural dynamics are modeled separately. The rigid-body dynamics provide forcing to the structural modes. This model type was validated against flight data from previous CH-53 configurations.

Structural control has also been implemented on production vehicles, not just for research purposes. The B-1 has structural control vanes located near the pilot station. The B-1 was designed to be a low-level penetration bomber, with the potential of flying through heavy turbulence. Vibration at the pilot station could cause fatigue, and the control vanes were added early on in the design process to

reduce structural vibration as much as possible [70, 71]. Use of the control vanes provided great reduction of the crew sensitivity index, a measure of discomfort at given frequencies. It is a function of turbulence levels, human perception of vibration, and acceleration of the aircraft.

Commercial aircraft manufacturers also use structural feedback to improve passenger ride quality in turbulence. Airbus [72] cites an ability to reduce structural vibration by a factor of two using advanced control laws. Their flexible models for control law design come from flight test [73, 74]. Reference 74 shows the PSD of lateral acceleration is significantly reduced at the structural frequencies when flying in turbulence. Boeing [75] also derives models from flight data; These models contain rigid-body modes and 15 structural modes. No coupling is present between the rigid-body and structural modes to simplify the identification. Large reductions in accelerations at varying fuselages stations can be obtained. The Boeing 787 contains both gust load alleviation and maneuver load control laws [76]. In additional to reduction in acceleration, an additional benefit of these control laws is a reduction in aircraft structural weight due to decreased loads.

High fidelity modeling tools are required for accurate flexible aircraft modeling and simulation. The models presented thus far are generally obtained from or tuned with flight test data. Modeling requires accurate representations of aircraft structural parameters. The development of an analytical formulation for the linear equations of motion for a flexible aircraft are described in Ref. 77. The starting point is a rigid-body model. Changes in aerodynamics due to flexibility add forcing to the rigid-body equations. In addition, changes in rigid-body dynamics add forcing

21

to the structural beam equations, giving a fully coupled flexible system. A mean axis assumption is used, where the aircraft motion corresponds not to a physical quantity in the aircraft, but instead a location where mass moments of inertia remain constant. The multi-body formulation used in this dissertation is derived from Reference 78. The multi-body formulation simplifies the addition of elasticity effects by augmenting displacement and rotation vectors, along with their time derivatives.

A formulation similar to that of Ref. 77 is used to derive the flexible equations of motion for a generic transport model (GTM) [79]. Here, a one-dimensional analytical beam model with coupled bending-torsion dynamics models the aircrafts flexible wings. The Galerkin method is used to develop the equations of motion for the orthogonal modes. Fully coupled mass, stiffness, and damping matrices are created. The longitudinal dynamics and first bending and torsion modes are analyzed and an adaptive control system is created. In this formulation, the rigid-body dynamics are augmented with contributions due to flexibility.

References 80, 81, and 82 describe the derivation of flexible aircraft equations of motion in similar fashions. Lagrange's Equations are used, where potential and kinetic energies are obtained for components of the flexible aircraft. In these analyses, the energies include contributions from the fuselage, wings, and empennage as separate quantities. Orthogonal mode shapes are also assumed to be known a priori and available during the solution process.

1.2.4 Comments on Literature

There is a general gap in modeling used for flight controls development versus that used for rotor dynamics and loads prediction. Flight control designers generally do not have access to high-order comprehensive analyses, and therefore use much simpler models. Models such as GTRSIM are based on theory, but are empirically corrected to match flight test data. Using these types of models to predict new aircraft behavior is problematic. As such, linearized models from comprehensive analyses such as FLIGHTLAB, CAMRAD2, and the model developed here are beginning to play a large role in control system design.

The fixed-wing community has much more experience in control design for flexible aircraft. Experiences from these programs provide insight into the starting point for flexible aircraft control. Accelerations at the wing tips or the nose and tail provide adequate feedback signals for structural motion. In terms of modeling, a few low frequency modes are generally adequate for stability and aircraft flutter calculations. For rotorcraft, where rotor modes are also important, many more modes are required to model the entire aircraft. Analytical equations become increasingly less tractable as the number of modes increases. Numerical formulations are required for rotorcraft which generally contain several rotor modes as well as flexible structural modes.

1.3   Contributions of Dissertation

There are many comprehensive code bases that can be used to model flexible rotorcraft. This dissertation introduces and applies a comprehensive model with a new structural formulation to study the flight dynamics and control of a large flexible tiltrotor aircraft. The benefits of this model architecture are in maintaining the equations of motion in simple ODE (ordinary differential equation) form, which decreases computational costs and makes real-time implementation possible. In addition, it is simple to obtain linear models from this system architecture.

A comparison between different flexible linear model architectures is presented. Linear flexible models can be obtained from a variety of sources and different model types are compared in an effort to link the models and provide a methodology in converting from one structure to another.

This dissertation also includes a comprehensive control synthesis for the flexible tiltrotor. In past literature, control synthesis was performed on rigid tiltrotors. Here, a solution is obtained that ensures that stability, model following, disturbance rejection, and bandwidth requirements are all fulfilled while minimizing structural oscillations through active control of structural modes. The contributions are described in greater detail below.

- **Muti-body like rotorcraft modeling:**

  Multi-body solvers generally contain numerical kinematics for the motion of bodies held together by constraint equations. The formulation presented in this dissertation retains the numerical kinematics but does not include alge-

braic constraint equations. This formulation leaves the equations of motion as ODEs. The bodies are assumed to be rigidly connected to each other with motion between the bodies allowed only through flexibility.

- **Comprehensive comparisons between different flexible aircraft models:**

  Comparisons are given between different linear model structures. Flexible models can come from multi-body simulations (like the one developed in this disseration), rigid-body aircraft models augmented to include structural flexibility, or flight data. The models are shown to be coupled by the off-diagonal terms. Conversions are given between the complicated multi-body model structures to decoupled flexible model structures. A decoupled model is the simplest model type, where all interaction between the flexible mode and fuselage dynamics is obtained through an influence coefficient in the output equation.

- **Development of advanced control laws for flexible aircraft:**

  Attitude-Command, Attitude-Hold (ACAH) and Translational Rate Command (TRC) control modes are developed for the flexible LCTR aircraft. Comparisons are given between control systems that only ensure stability at structural frequencies, passively control structural oscillation through the use of notch filters, and actively control structural oscillation using structural feedback. It is shown that control systems that do not account for structural flexibility have degraded, potentially unstable performance, and structural control

techniques can be used to give large reductions in structural motion.

1.4 Organization of Dissertation

Chapter 2 presents the theoretical development of the model. Kinematics and coordinate system transformations are discussed. The finite element beam model used for the rotor, nacelle, and wing is also presented. The system state vector is developed in this chapter, including rigid-body, inflow, and flexible beam degrees of freedom. Governing equations for each degree of freedom are also discussed.

Chapter 3 discusses the development of the aircraft model from its components described in Chapter 2. The connection of various bodies into a tree structure is explained. The use of the modal coordinate transformation to reduce the system degrees of freedom is also discussed. In addition, linearization and time integration of the aircraft model are also presented.

Chapter 4 presents validation of the model. The initial validation is against a rigid XV-15. The XV-15 validation data consists of identified models from flight data, as well as simulation models. The LCTR model is then validated against another comprehensive model. Nacelle dynamics are also validated against the existing literature.

Chapter 5 examines different flexible linear model architectures. Descriptions for each model are given with examples from the literature. A flexible LCTR model is converted to each model structure type.

Chapter 6 builds the control system for the flexible LCTR aircraft and pro-

vides comparisons between different control strategies. This chapter also looks at the robustness of the system, costs of structural feedback and sensitivities of the specifications to changes in structural gains.

Chapter 7 compares the performance of the aircraft with and without structural feedback in a fixed-base piloted simulation and provides pilot comments.

Chapter 8 provides key conclusions from this dissertation and suggests future work.

The appendices show the derivation of the kinematic relations, include additional details regarding flexible model architectures, and detail various structural feedback concepts.

Chapter 2:   Theoretical Development

A description of the formulation of the equations of motion is given in this chapter. The model is entirely composed of a coupled set of nonlinear ODEs, and key coordinate systems used during the analysis are discussed. Rigid-body equations of motion along with elastic beam equations used to model rotor blade and wing flexibility are also discussed. A finite-state inflow model is used for each rotor to retain the system in ODE form. The full system state vector is developed from its components.

2.1   Coordinate Systems

2.1.1   Inertial Reference Coordinate System

The inertial coordinate system serves as the reference coordinate system for the development of the equations of motion. The origin of the system is the aircraft's center of mass. The z-axis ($\mathbf{n}_3^I$) of the inertial coordinate system points downwards, but the direction of the x and y axes are somewhat arbitrary. The x-axis ($\mathbf{n}_1^I$) could point north and the y-axis ($\mathbf{n}_2^I$) could point east if the trajectory of the aircraft was needed or if the aircraft had to navigate during code execution.
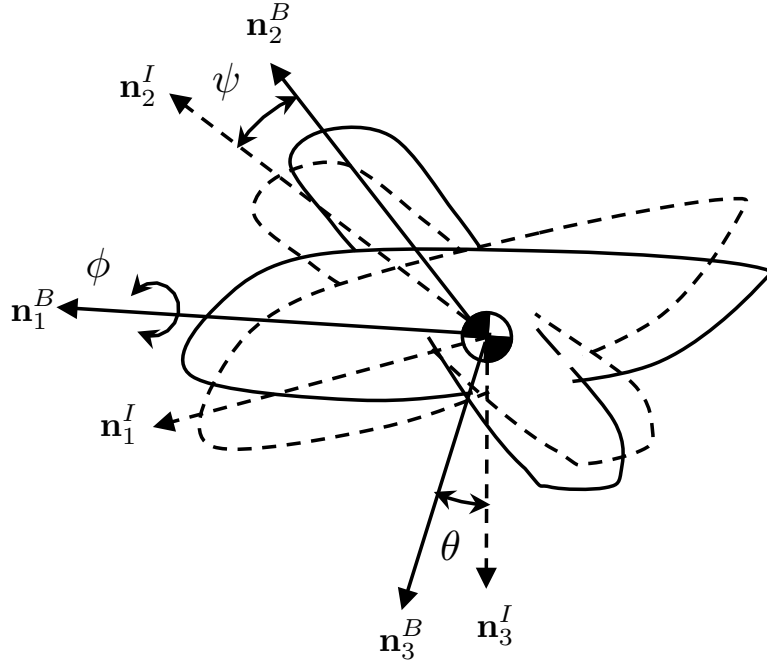
Figure 2.1: Body and inertial coordinate systems

2.1.2 Body-Fixed Coordinate System

The body coordinate system originates at the aircraft center of mass and points forward along the x-axis $(\mathbf{n}_1^B)$, out the right wing for the y-axis $(\mathbf{n}_2^B)$, and downwards for the z-axis $(\mathbf{n}_3^B)$. This coordinate system is used to define the aircraft linear and angular motion as well as the aircraft mass moments of inertia. The inertial and body coordinate system are related by the Euler angles, which define the aircraft's orientation with respect to the inertial coordinate system. The transformation from inertial to body coordinate system is shown in Figure 2.1. The aircraft is first rotated around the z-axis to form an intermediate coordinate system. This coordinate system is then rotated about the y-axis to form a second intermediate coordinate system. A final rotation of this coordinate system about the x-axis gives the body axes. The transformation matrix is given by Eqn. (2.1).

29

$$\left\{\mathbf{n}^B\right\} = \left[S^{BI}\right]\left\{\mathbf{n}^I\right\} \tag{2.1}$$

The components of $\left[S^{BI}\right]$ are:

$$S^{BI} = \begin{bmatrix} S_{11} & S_{12} & S_{13} \\ S_{21} & S_{22} & S_{23} \\ S_{31} & S_{32} & S_{33} \end{bmatrix} \tag{2.2}$$

where

$$S_{11} = \cos\theta\cos\psi$$

$$S_{12} = \cos\theta\sin\psi$$

$$S_{13} = -\sin\theta$$

$$S_{21} = \sin\phi\sin\theta\cos\psi - \cos\phi\sin\psi$$

$$S_{22} = \sin\phi\sin\theta\sin\psi + \cos\phi\cos\psi$$

$$S_{23} = \sin\phi\cos\theta$$

$$S_{31} = \cos\phi\sin\theta\cos\psi + \sin\phi\sin\psi$$

$$S_{32} = \cos\phi\sin\theta\sin\psi - \sin\phi\cos\psi$$

$$S_{33} = \cos\phi\cos\theta$$

2.1.3 Flexible Beam Coordinate Systems

The flexible beam coordinate system is used for flexible rotor blades as well as wings, moving nacelles, flexible empennages, etc. All transformations needed for the x-axis to point outwards along the elastic axis have already been performed in the process of getting to the flexible beam coordinate system. For wings, any wing sweep or dihedral/anhedral angle is accounted for in the transformation matrix from the previous body in the multi-body system to the beam.

2.1.3.1 Undeformed Beam Coordinate System

This coordinate system originates at the root of the flexible beam and points outboard along the elastic axis of the undeformed flexible beam for the x-axis ($\mathbf{n}_1^b$). The y-axis ($\mathbf{n}_2^b$) is in the chordwise direction and points forward towards the direction of travel. This axis defines the lead/lag direction of motion for rotor blades. Displacements from the elastic axis to the aerodynamic center or center of mass of the beam section are given along this direction as well. The z-axis ($\mathbf{n}_3^b$) follows the right hand rule and its direction is thus set by the x and y axes. For the standard counterclockwise rotating rotor systems, the undeformed z-axis points upward and defines the flapping or beamwise bending degree of freedom (see Fig. 2.2). In the present work, a wing will be defined as "right" or "left" depending on whether its elastic axis is to the right or left of the $x^B - z^B$ body-axis plane. The right wing has the same undeformed coordinate system as these blades. These coordinate systems described the standard form of the flexible beam. Displacements due to structural

flexibility are given in this coordinate system.

(a) Counterclockwise rotor blade

(b) "Right" wing
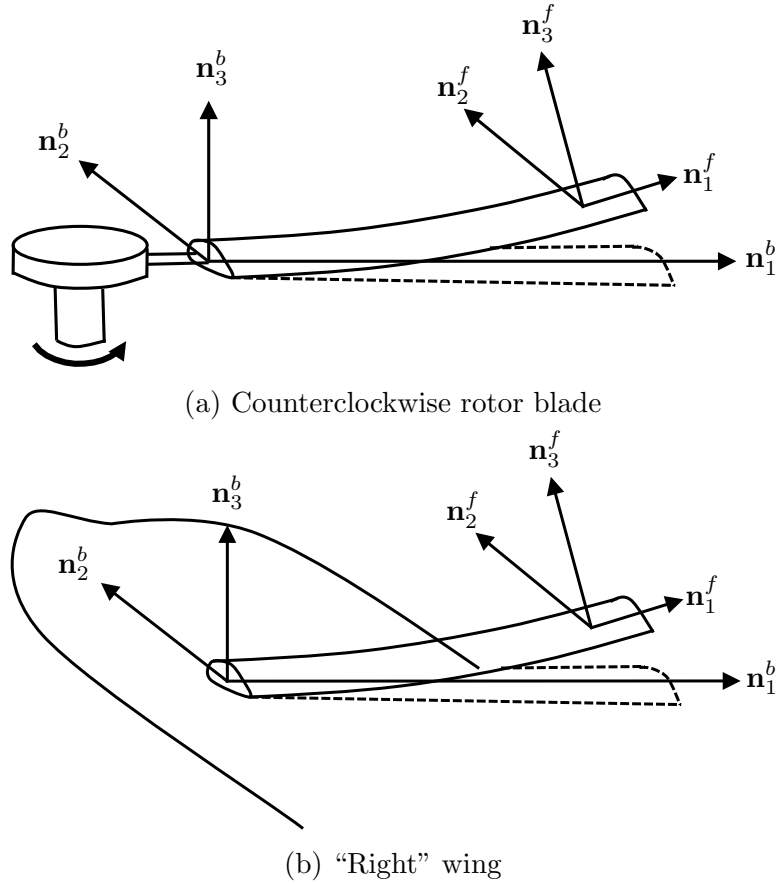
Figure 2.2: Standard undeformed (dashed) and deformed (solid) coordinate systems

The beam coordinate systems can also be oriented in a nonstandard form. Here the x-axis remains pointing outward, the y-axis remains pointing forward along the chord, but the z-axis points downward, in the opposite direction as the standard form. Figure 2.3 shows the coordinate system used for these beams. These coordinate systems are used for clockwise rotating rotor systems as well as the "left" wings This allows for rotor speed to be treated as a positive constant for both rotors. Changing the direction of the y-axis and having the z-axis point downwards also allows for the same blade section properties to be used. Since positive displace-

ments are defined in the lead direction (forward chord bending), the same CG and aerodynamic center offsets from the elastic axis may be used. This same coordinate system is also used for the "left" wing.

(a) Clockwise rotor blade

(b) "Left" wing
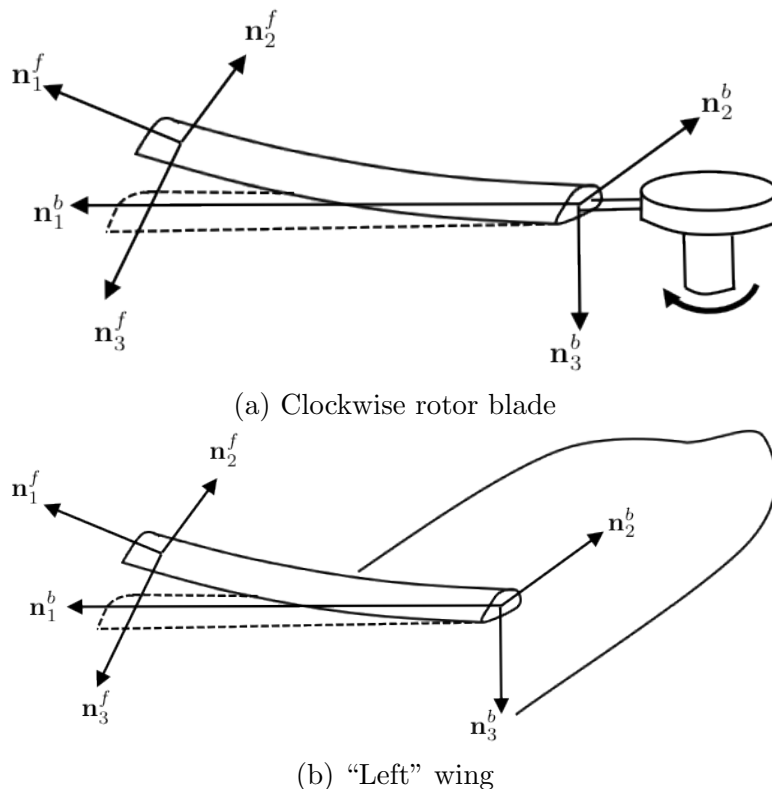
Figure 2.3: Nonstandard undeformed (dashed) and deformed (solid) coordinate systems

Wing sweep and dihedral are accounted for in transformations from the previous body to the beam undeformed coordinate system. In the tiltrotor example, sweep and dihedral are included in the transformation from the fuselage coordinate system to the wing undeformed coordinate system. Rotor blade precone is included as a separate transformation matrix, and is described in Sec. 2.1.4.3.

The nacelles retain a single rigid-body rotation mode. The nacelles contain a "pinned" boundary condition at the center node and rotate around the y-axis

($\mathbf{n}_2^b$), giving displacements in the z-axis ($\mathbf{n}_3^b$) only. The x-axis ($\mathbf{n}_1^b$) points out along the elastic axis as shown in Fig. 2.4. The deformed y-axis ($\mathbf{n}_2^f$) remains identical to the undeformed one. The "left" and "right" nacelle's coordinate systems are identical. Since the "left" and "right" wings have different coordinate systems, the transformation matrices from the wing to the nacelles are different.
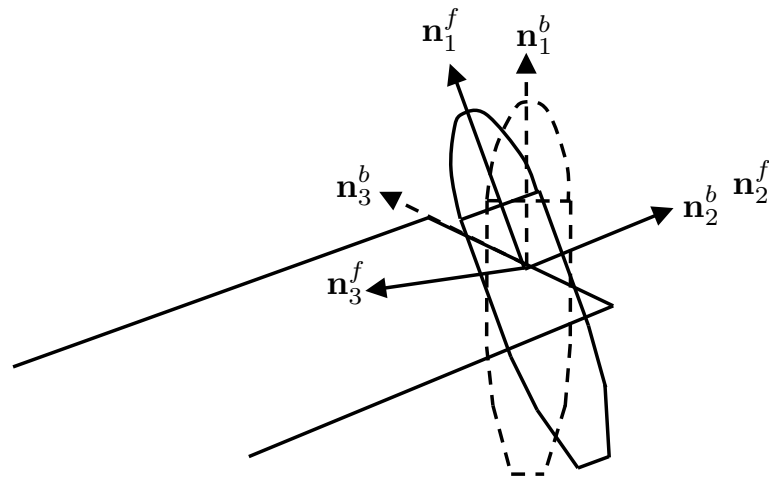
(a) "Right" nacelle coordinate systems
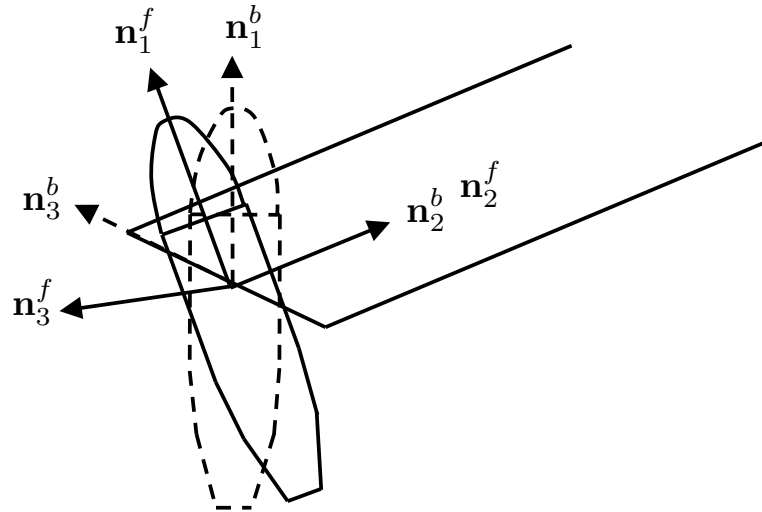
(b) "Left" nacelle coordinate systems

Figure 2.4: Rotating nacelle undeformed (dashed) and deformed (solid) coordinate systems

2.1.3.2   Deformed Beam Coordinate System

Elastic deformations add displacements and rotations to the undeformed co-ordinate system and are shown alongside the undeformed coordinate systems in Figs. 2.2-2.4. Once elastic deflections are added, the coordinate system becomes the beam deformed coordinate system. This coordinate system is dependent on the displacement along the elastic axis since elastic deformation varies along the elastic axis of the beam. Since the coordinate system varies along the beam span, its origin is located at the current spanwise location along the beam.

The transformation matrix $\left[S^{fb}\right]$ transforms the elastic axis offsets from the deformed to the undeformed coordinate system. Its components are given by Eqn. (2.1). For the elastic beam, the individual rotation angles are given in Ref. 83. They are given in the beam undeformed coordinate system and are based on elastic displacements including w in the $\mathbf{n}_3^b$ direction, v in the $\mathbf{n}_2^b$ direction, and u in the $\mathbf{n}_1^b$ direction. Elastic rotations about the $\mathbf{n}_1^b$ axis are labeled as ϕ. Spanwise derivatives of the displacement quantities are labeled $()_x$, and are used to define the rotation angles:

$$\phi = \phi \tag{2.3}$$

$$\sin\theta = -\frac{w_x}{\sqrt{1 + 2u_x + u_x^2 + v_x^2 + w_x^2}} \tag{2.4}$$

$$\cos\theta = -\frac{\sqrt{1 + 2u_x + u_x^2 + v_x^2}}{\sqrt{1 + 2u_x + u_x^2 + v_x^2 + w_x^2}} \tag{2.5}$$

$$\sin\psi = -\frac{v_x}{\sqrt{1 + 2u_x + u_x^2 + v_x^2 + w_x^2}} \tag{2.6}$$

$$\cos\psi = -\frac{1 + u_x}{\sqrt{1 + 2u_x + u_x^2 + v_x^2 + w_x^2}} \tag{2.7}$$

Local forcing along the elastic beam is determined in the deformed coordinate system since forcing takes place along the deformed beam. Bodies are connected to each other in this coordinate system as well.

During execution, all components of the system can be flexible. If a component is rigid, the flexible components are set to zero and the deformed coordinate system is identical to the undeformed one.

2.1.4 Rotor Coordinate Systems

Several coordinate systems are used for modeling the rotor system.

2.1.4.1 Non-Rotating Shaft Coordinate System

The non-rotating shaft coordinate system is centered at the hub. This coordinate system is oriented so that the positive z-axis ($\mathbf{n}_3^{NR}$) points downward along the axis of rotation of the rotor, the x-axis ($\mathbf{n}_1^{NR}$) points forward and the y-axis points

starboard. The transformation matrix between the body axes and the non-rotating shaft axes is a product of all the intermediate coordinate systems in the multi-body system and are highly dependent on the aircraft configuration (see Fig. 2.5). These transformations may include wings, nacelles, and any other components. Determination of the non-rotating shaft coordinate system is the first step towards determining blade kinematics.
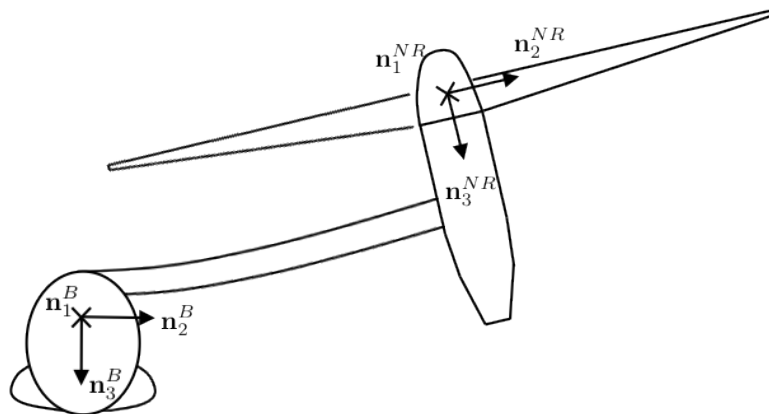
Figure 2.5: Body and non-rotating shaft coordinate systems

For a rigid aircraft, this transformation matrix is constant. For a flexible aircraft, the transformation matrix may vary with time.

2.1.4.2   Rotating Shaft Coordinate System

The rotating shaft coordinate system originates at the hub and rotates around the hub at the main rotor speed. The z-axis $(\mathbf{n}_3^R)$ points upward along the axis of rotation, the opposite of the non-rotating shaft coordinate system. Each blade has its own hub rotating coordinate system based on its current azimuth angle, ψ. The x-axis $(\mathbf{n}_1^R)$ points outward and is in the same plane as the beam elastic axis (see

Fig. 2.6). The transformation in matrix between these two coordinate systems is:

$$\mathbf{n}^R = \left[S^{R,NR} \right] \mathbf{n}_N R \tag{2.8}$$

$$\begin{Bmatrix} \mathbf{n}_1^R \\ \mathbf{n}_2^R \\ \mathbf{n}_3^R \end{Bmatrix} = \begin{bmatrix} -\cos\psi & \sin\psi & 0 \\ \sin\psi & \cos\psi & 0 \\ 0 & 0 & -1 \end{bmatrix} \begin{Bmatrix} \mathbf{n}_1^{NR} \\ \mathbf{n}_2^{NR} \\ \mathbf{n}_3^{NR} \end{Bmatrix} \tag{2.9}$$
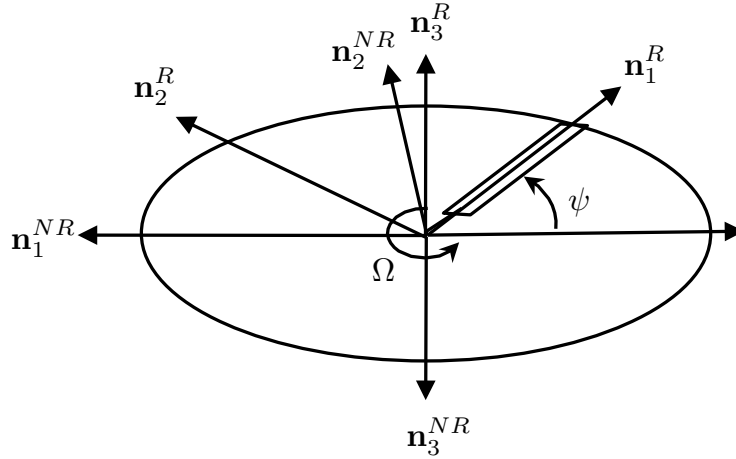
Figure 2.6: Non-rotating and rotating shaft coordinate systems

2.1.4.3 Preconed Rotating Coordinate System

The preconed coordinate system rotates the blade from the rotating shaft axes to the undeformed blade axes using the precone angle. The transformation is shown in Fig. 2.7 and is as follows:

$$\mathbf{n}^b = \left[S^{bR} \right] \mathbf{n}_R \tag{2.10}$$

$$\begin{Bmatrix} \mathbf{n}_1^b \\ \mathbf{n}_2^b \\ \mathbf{n}_3^b \end{Bmatrix} = \begin{bmatrix} \cos\beta_p & 0 & \sin\beta_p \\ 0 & 1 & 0 \\ -\sin\beta_p & 0 & \cos\beta_p \end{bmatrix} \begin{Bmatrix} \mathbf{n}_1^R \\ \mathbf{n}_2^R \\ \mathbf{n}_3^R \end{Bmatrix} \tag{2.11}$$
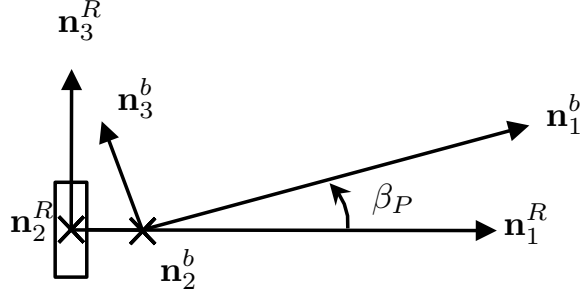
Figure 2.7: Conversion from rotating coordinate system to beam coordinate system through the precone angle

The blade undeformed coordinate system is identical to the one described in Sec. 2.1.3.1.

2.1.5 Fuselage Wind Coordinate System

The fuselage wind coordinate system is centered at the aircraft center of mass and is defined with respect to the freestream flow due to aircraft linear velocity. The wind and body coordinate systems are related by the angle of attack and sideslip. This coordinate system is used to determine aerodynamic contributions of the fuselage onto the equations of motion. The transformation from the body to the wind coordinate system is:

$$\mathbf{n}^W = \begin{bmatrix} S^{WB} \end{bmatrix} \mathbf{n}^B \tag{2.12}$$

$$
\left\{ \begin{array}{c} \mathbf{n}_1^W \\[2mm] \mathbf{n}_2^W \\[2mm] \mathbf{n}_3^W \end{array} \right\} = \left[\begin{array}{ccc} \cos\alpha_F \cos\beta_F & -\cos\alpha_F \sin\beta_F & -\sin\alpha_F \\[2mm] \sin\beta_F & \cos\beta_F & 0 \\[2mm] \sin\alpha_F \cos\beta_F & -\sin\alpha_F \sin\beta_F & \cos\alpha_F \end{array} \right] \left\{ \begin{array}{c} \mathbf{n}_1^B \\[2mm] \mathbf{n}_2^B \\[2mm] \mathbf{n}_3^B \end{array} \right\} \tag{2.13}
$$

This coordinate system is undefined in hover with zero wind speed. Generally, hover is approximated by adding a small longitudinal trim speed.

2.1.6   Beam Sectional Aerodynamics Coordinate System

In order to determine air loads, the local velocities at the beam (wing, blade, nacelle, etc.) elastic axis are needed. The elastic axis has beam (flap) and chord (lag) deflections when compared to the undeformed axes. The local angular deflection is used to determine the local velocity from the overall freestream velocity. The following transformation takes beam velocities and converts them to air velocities at a location on the deflected beam.

$$
\mathbf{V}_A = U_T \mathbf{n}_1^a + U_P \mathbf{n}_2^a + U_R \mathbf{n}_3^a \tag{2.14}
$$

The coordinate transformations is from the undeformed beam coordinate system $\mathbf{n}^b$, (Sec. 2.1.3.1):

$$
\mathbf{n}^a = \left[S^{ab} \right] \mathbf{n}^b \tag{2.15}
$$

$$
\left\{ \begin{array}{c} \mathbf{n}_1^a \\ \\ \mathbf{n}_2^a \\ \\ \mathbf{n}_3^a \end{array} \right\} = \left[\begin{array}{ccc} -\sin\zeta & \cos\zeta & 0 \\ \\ \sin\beta\cos\zeta & \sin\beta\sin\zeta & -\cos\beta \\ \\ -\cos\beta\cos\zeta & -\cos\beta\sin\zeta & -\sin\beta \end{array} \right] \left\{ \begin{array}{c} \mathbf{n}_1^b \\ \\ \mathbf{n}_2^b \\ \\ \mathbf{n}_3^b \end{array} \right\} \tag{2.16}
$$

The local beam and chord bending slopes are (flap and lag slopes for a blade):

$$
\beta = w_x \tag{2.17}
$$

$$
\zeta = v_x \tag{2.18}
$$

For beams that rotate clockwise and "left" wings (see Sec. 2.1.3.1), additional manipulations ensure that the correct aerodynamic forcing is determined when inflow and freestream airflows are included. The n_3^a vector is negated so it points upwards, as it does for the counterclockwise and "right" wings. The positive pitch angle is also negated, so positive pitch (and elastic torsion) deflections increases the angle of attack. These transformations are later removed from the aerodynamic forcing vectors to ensure loads are calculated in the appropriate coordinate systems.

2.1.7 Dynamic Inflow Coordinate System

The dynamic inflow equations are written in the tip path plane coordinate system. The tip path plane is defined by a rotation from the non-rotating shaft coordinate system by the first harmonic deflection of the flapped rotor blades. The

z-axis remains pointing down.

$$\beta_{1c} = \frac{2}{N_B} \sum_{j=1}^{N_B} \frac{w_{\text{tip}j}}{R-e} \cos \psi_j \tag{2.19}$$

$$\beta_{1s} = \frac{2}{N_B} \sum_{j=1}^{N_B} \frac{w_{\text{tip}j}}{R-e} \sin \psi_j \tag{2.20}$$

The transformation to the non-rotating shaft coordinate system is:

$$\begin{Bmatrix} \mathbf{n}_1^{NR} \\ \mathbf{n}_2^{NR} \\ \mathbf{n}_3^{NR} \end{Bmatrix} = \begin{bmatrix} \cos\beta_{1c} & \sin\beta_{1c}\sin\beta_{1s} & \sin\beta_{1c}\cos\beta_{1s} \\ 0 & \cos\beta_{1c} & -\sin\beta_{1s} \\ -\sin\beta_{1c} & \cos\beta_{1c}\sin\beta_{1s} & \cos\beta_{1c}\cos\beta_{1s} \end{bmatrix} \begin{Bmatrix} \mathbf{n}_1^{TPP} \\ \mathbf{n}_2^{TPP} \\ \mathbf{n}_3^{TPP} \end{Bmatrix} \tag{2.21}$$

2.2 Main Assumptions

1. The rigid-body equations are based on a rigid airframe and do not account for effects of structural flexibility.

2. Wind velocity is zero.

3. A three state dynamic inflow model is an accurate representation of each rotors inflow. Influences of the wings and other aircraft features on inflow are negligible.

4. Fuselage aerodynamic properties can be lumped into lift, drag, and moment coefficients.

5. The blade cross section is symmetric with respect to the major principle axis.

6. Blade chord, twist, stiffness, mass properties, and all offsets are given at discrete spanwise locations and vary linearly in between.

7. All elastic beams are composed of an isotropic, linearly elastic material.

8. All blades are identical.

9. Euler-Bernoulli beam theory is used, implying plane cross sections remain plane and perpendicular to the elastic axis during deformation. Shear is negligible. This beam theory applies to all blades, wings, and any other flexible aircraft component.

10. The rotor blades rotate at constant angular velocity.

11. The blade pitch control system and actuators are infinitely stiff and there is no freeplay in the linkages.

2.3 Kinematics and Coordinate System Transformations

The rotorcraft model consists of multiple flexible bodies arranged in a generic tree-like topology. For an example tiltrotor aircraft, shown in Fig. 2.8, the tree starts from the aircraft center of mass and branches out to the wings, nacelles, and ultimately rotors and blades. Each component within this tree is given its own coordinate system. The coordinate system serves as the basis for the formulation of flexibility contributions of that body to the overall system. Coordinate systems used in the formulation have been described in the Section 2.1.
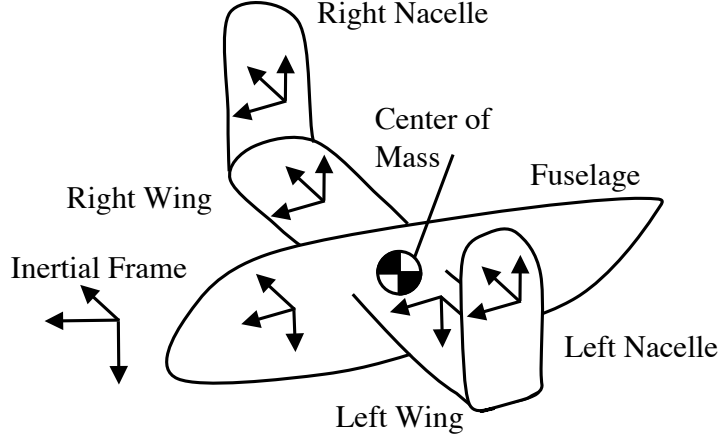
Figure 2.8: Generic tilt-rotor multi body formulation

The development of the kinematic relations between a generic set of bodies is given in Appendix A and covers derivations of the positions, velocities, and accelerations of arbitrary points within the flexible tree-like configuration.

2.4   Rigid-Body Equations of Motion

Equations of motion for the fuselage are formulated in the body axes and assume a rigid aircraft. The force and moment equations are as follows:

$$X = m\left(\dot{u} + qw - rv\right) + mg\sin\theta \tag{2.22}$$

$$Y = m\left(\dot{v} + ru - pw\right) - mg\sin\phi\cos\theta \tag{2.23}$$

$$Z = m\left(\dot{w} + pv - qu\right) - mg\cos\phi\cos\theta \tag{2.24}$$

$$L = I_{xx}\dot{p} - (I_{yy} - I_{zz})\,qr - I_{xz}\left(pq + \dot{r}\right) + I_{xy}\left(pr - \dot{q}\right) - I_{yz}\left(q^2 - r^2\right) \tag{2.25}$$

$$M = I_{yy}\dot{p} - (I_{zz} - I_{xx})\,pr + I_{xz}\left(p^2 - r^2\right) - I_{xy}\left(qr + \dot{p}\right) + I_{yz}\left(pq - \dot{r}\right) \tag{2.26}$$

$$N = I_{zz}\dot{r} - (I_{xx} - I_{yy})\,pq + I_{xz}\left(qr - \dot{p}\right) - I_{xy}\left(p^2 - q^2\right) - I_{yz}\left(pr - \dot{q}\right) \tag{2.27}$$

The kinematic equations relating the aircraft roll, pitch, and yaw rates to inertial rates are:

$$\dot{\phi} = p + q \tan\theta \sin\phi + r \tan\theta \cos\psi \tag{2.28}$$

$$\dot{\theta} = q \cos\phi - r \sin\phi \tag{2.29}$$

$$\dot{\psi} = r \frac{\cos\psi}{\cos\theta} + q \frac{\sin\phi}{\cos\theta} \tag{2.30}$$

The left hand side of the six force and moment equations contain all external forcing acting on the center of mass. This includes all forcing coming from the rotors, wings, nacelles, and any other flexible aircraft component. It also includes all aerodynamic forcing acting on the fuselage. The fuselage is only connected to a subset of bodies from the multi-body system (i.e. the wings for a tiltrotor). Rotor forcing is passed through the wings to the fuselage, and so does add directly to the fuselage equations. Since all external forcing comes integrated in the left hand side, the masses and inertias on the right hand side of the equations are for the rigid component of the fuselage only. The applied forces and moments at the center of mass are (only X-Force shown):

$$X = \sum_{k=1}^{N_R} X_{R_k}^* + \sum_{k=1}^{N_{nac}} X_{nac_k}^* + X_{TR}^{**} + X_F + \sum_{k=1}^{N_W} X_{W_k} \tag{2.31}$$

$()^*$: Forcing passed through wings $()^{**}$: Tail rotor forcing, if present

Here X_R are rotor loads from N_R rotors, X_{nac} are loads from N_{nac} nacelles, X_{TR} are tail rotor loads, X_F are fuselage/empennage loads, and X_W are wing loads from

N_W wings

The portions of the aircraft state vector associated with the rigid-body equations of motion are:

$$\mathbf{x}_{rb} = \{u \quad v \quad w \quad p \quad q \quad r \quad \phi \quad \theta \quad \psi\}^T \tag{2.32}$$

2.5 Flexible Beam Equations of Motion

In order to determine spanwise loads for any beam, local positions, velocities, and accelerations must be known. These vectors will be derived for a rotor blade and then simplifications will be given for wings, nacelles, etc. Rotor blade vectors are most complex because they contain effects due to rotor speed, elastic offsets, and precone angles.. These vectors are based of of those derived in Ref. [58].

2.5.1 Blade Position Vector

The position vector for a point on a blade is:

$$\mathbf{R}_P = \mathbf{R}_{CG} + \mathbf{R}_H + \mathbf{R}_B \tag{2.33}$$

$\mathbf{R}_{CG}$ is the position vector of the center of gravity with respect to a fixed point. $\mathbf{R}_H$ is the position vector of the hub from the CG, and $\mathbf{R}_B$ is the position vector of a point on a flexible blade with resect to the hub.

Components $\mathbf{R}_{CG} + \mathbf{R}_H$ are determined using multi-body kinematics. These values are derived in Appendix A in Eqn. (A.14). As written, these vectors in-

clude flexibility of any component up to the rotor hub. Written in the multi-body formulation:

$$\mathbf{R}_{MB} = \mathbf{R}_{CG} + \mathbf{R}_H \tag{2.34}$$

$$\mathbf{R}_{CG} = \zeta \left\{ \mathbf{n}^0 \right\} \tag{2.35}$$

$$\mathbf{R}_H = \left(\sum_{i=1}^{n-1} \{\bar{\mathbf{q}}^i\}^T \left[S^{i0} \right] + \{\bar{\mathbf{r}}^n\}^T \left[S^{\mathbf{n}0} \right] \right) \left\{ \mathbf{n}^0 \right\} \tag{2.36}$$

Where body n represents the hub. The generic displacement from the beam root for a point on the beam in the undeformed blade coordinate system is:

$$
\begin{aligned}
\mathbf{R}_B = & \left[e \cos \beta_p + x_0 + S_{21}^{fb} y_0 + S_{31}^{fb} z_0 \right] \mathbf{n}_1^b + \\
& \left[v + S_{22}^{fb} y_0 + S_{32}^{fb} z_0 \right] \mathbf{n}_2^b + \\
& \left[w - \sin \beta_p + S_{23}^{fb} y_0 + S_{33}^{fb} z_0 \right] \mathbf{n}_3^b
\end{aligned}
\tag{2.37}
$$

v and w are elastic contributions to the displacement of the elastic axis. e is the offset from the beam connection point to the start of the elastic portion of the beam. β_p is the precone angle.

In order to sum the vector above with the $\mathbf{R}_{CG}$ and $\mathbf{R}_H$ components, it must be converted to the same coordinate system. The transformation components from the blade undeformed coordinate system through the preconed, rotating shaft, non-rotating shaft, and hub coordinate system are given in the previous section. In

47

matrix form they are:

$$\{\mathbf{n}^b\} = \left[S^{b,R}\right]\left[S^{R,NR}\right]\left[S^{NR,n}\right]\left[S^{n,0}\right]\{\mathbf{n}^0\} \tag{2.38}$$

2.5.2 Blade Velocity Vector

The absolute velocity of a point on the blade is:

$$\mathbf{V}_P = \frac{d\mathbf{R}_{CG}}{dt} + \frac{d\mathbf{R}_H}{dt} + \frac{d\mathbf{R}_B}{dt} \tag{2.39}$$

As with the position vector, the first two components of the velocity vector are obtained from the multi-body solution, and are given by Eqn. (A.15). This velocity vector contains both rigid-body aircraft velocities as well as all velocity contributions due to flexibility from the CG to the hub and is written in the inertial frame.

$$\mathbf{V}_{MB} = \mathbf{V}_{CG} + \mathbf{V}_H \tag{2.40}$$

$$\mathbf{V}_{CG} = \left\{\dot{\boldsymbol{\zeta}}\right\}^T \{\mathbf{n}^0\} \tag{2.41}$$

$$\mathbf{V}_H = \left(\sum_{i=1}^{n-1}\left(\{\dot{\bar{\mathbf{q}}}^i\}^T\left[S^{i0}\right] + \{\bar{\mathbf{q}}^i\}^T\left[\dot{S}^{i0}\right]\right) + \tag{2.42}$$

$$\{\dot{\bar{\mathbf{r}}}^n\}^T\left[S^{n0}\right] + \{\bar{\mathbf{r}}^n\}^T\left[\dot{S}^{n0}\right]\right)\{\mathbf{n}^0\}$$

Where $\dot{\boldsymbol{\zeta}}$ is the aircraft velocity. The velocity of a point on the flexible blade with

respect to the hub is:

$$\frac{d\mathbf{R}_B}{dt} = \frac{\partial \mathbf{R}_B}{\partial t} + \omega \times \mathbf{R}_B \tag{2.43}$$

where ω is the total angular rate of the hub, given by the components of the skew symmetric matrix in Eqn. (A.28). This angular rate includes rigid-body rates as well as all angular rates due to structural flexibility up to the hub, and has been converted to the blade undeformed coordinate system. The partial derivative in the equation is the velocity of a point due to blade flexibility and rotor speed:

$$\frac{\partial \mathbf{R}_B}{\partial t} = \left(\frac{\partial \mathbf{R}_B}{\partial t}\right)_B + \mathbf{\Omega} \times \mathbf{R}_B \tag{2.44}$$

Where $(\dots)_B$ is the velocity of the point P as seen by an observer rotating with the blade in the rotating shaft coordinate system and $\mathbf{\Omega}$ is the main rotor speed.

$$\mathbf{\Omega} = \Omega \, \mathbf{n}_3^{NR} \tag{2.45}$$

Since the local velocity of the blade is needed for airloads calculations, all velocities are brought to the undeformed coordinate system, $\{\mathbf{n}^b\}$.

$$\mathbf{V}_P = \left(\mathbf{V}_{MB}\left[S^{0b}\right] + \left(\frac{\partial \mathbf{R}_B}{\partial t}\right)_B + \mathbf{\Omega} \times \mathbf{R}_B + \omega \times \mathbf{R}_B\right]\{\mathbf{n}^b\} \tag{2.46}$$

2.5.3 Blade Acceleration Vector

The blade acceleration vector is built the same way as the position and velocity vectors.

$$\mathbf{a}_P = \frac{d^2\mathbf{R}_{CG}}{dt^2} + \frac{d^2\mathbf{R}_H}{dt^2} + \frac{d^2\mathbf{R}_B}{dt^2} \tag{2.47}$$

$$\tag{2.48}$$

The first two components of the acceleration vector are given by the multi-body solution and give the total acceleration of the hub. These components are given by Eqn. (A.29).

$$\mathbf{a}_{MB} = \mathbf{a}_{CG} + \mathbf{a}_H \tag{2.49}$$

$$\mathbf{a}_{CG} = \left\{\ddot{\zeta}\right\}^T \left\{\mathbf{n}^0\right\} \tag{2.50}$$

$$\mathbf{a}_H = \left(\sum_{i=1}^{n-1} \left(\left\{\ddot{\bar{q}}^i\right\}^T \left[S^{i0}\right] + 2\left\{\dot{\bar{q}}^i\right\}^T \left[\dot{S}^{i0}\right] + \right. \right.$$
$$\left. \left\{\bar{q}^i\right\}^T \left[\ddot{S}^{i0}\right] \right) + \left\{\ddot{\bar{r}}^n\right\}^T \left[S^{n0}\right] + 2\left\{\dot{\bar{r}}^n\right\}^T \left[\dot{S}^{n0}\right] + \tag{2.51}$$
$$\left. \left\{\bar{r}^n\right\}^T \left[\ddot{S}^{n0}\right] \right) \left\{n^0\right\}$$

The acceleration of a point on the flexible blade with respect to the rotating hub is:

$$\frac{d^2\mathbf{R}_B}{dt^2} = \frac{\partial^2\mathbf{R}_B}{\partial t^2} + \dot{\omega} \times \mathbf{R}_B + 2\omega \times \frac{\partial \mathbf{R}_B}{\partial t} + \omega \times (\omega \times \mathbf{R}_B) \tag{2.52}$$

50

where ω and $\dot{\omega}$ are the angular velocity and acceleration vectors of the hub, including all rigid-body and flexibility effects. These vectors are converted to the blade undeformed coordinating system. The second partial derivative is the acceleration of a point on a flexible blade including rotor rotation contributions.

$$\frac{d^2\mathbf{R}_B}{dt^2} = \left(\frac{\partial^2 \mathbf{R}_B}{\partial t^2}\right)_B + \dot{\Omega} \times \mathbf{R}_B + 2\Omega \times \left(\frac{\partial \mathbf{R}_B}{\partial t}\right)_B + \Omega \times (\Omega \times \mathbf{R}_B) \qquad (2.53)$$

The full acceleration vector, converted to the beam undeformed coordinate system is;

$$\mathbf{a}_p = \left(\mathbf{a}_{MB}\left[S^{0b}\right] + \left(\frac{\partial^2 \mathbf{R}_B}{\partial t^2}\right)_B + \dot{\Omega} \times \mathbf{R}_B + 2\Omega \times \left(\frac{\partial \mathbf{R}_B}{\partial t}\right)_B \right.$$
$$\left. + \Omega \times (\Omega \times \mathbf{R}_B) + \dot{\omega} \times \mathbf{R}_B + 2\omega \times \frac{\partial \mathbf{R}_B}{\partial t} + \omega \times (\omega \times \mathbf{R}_B)\right)\left\{\mathbf{n}^b\right\} \qquad (2.54)$$

2.5.4 Simplifications for Other Beams

Other aircraft components may be flexible as well. These components are all connected to their root body, which serves the same purpose as the hub in the derivations above. From this root body, position, velocity, and acceleration vectors may be created for any point on the flexible beam and loads may be determined. For non blade components, the changes are as follows:

2.5.4.1 Position Vector

The multi-body component of the position vector, $\mathbf{R}_{MB}$, is terminated at the body just before the flexible body. The flexible components are treated as the rotor blades were in the derivations above.

The position vector of a point on the blade does not include elastic offset and blade precone.

$$e = 0 \tag{2.55}$$

$$\beta_P = 0 \tag{2.56}$$

The transformation matrix $\left[S^{fb}\right]$ now transforms the current bodies vector from the deformed to undeformed frames.

2.5.4.2 Velocity Vector

As the the position vector, the multi-body component of the velocity vector, Eqn. (2.40), is terminated at the body just prior to the flexible body. The rotor speed in Eqn. (2.44) is set to zero as well.

$$\boldsymbol{\Omega} = 0 \tag{2.57}$$

2.5.4.3   Acceleration Vector

The multi-body acceleration components are stopped at the body just prior to the current one. As in the velocity vector, rotor speed is set to zero. Here rotor angular acceleration is also set to zero.

$$\mathbf{\Omega} = 0 \tag{2.58}$$

$$\dot{\mathbf{\Omega}} = 0 \tag{2.59}$$

2.5.5   Beam Element Description

The elastic beam formulation contains coupled torsion and beamwise-chordwise (flap-lag) bending degrees of freedom, and small elastic deflections. All loads are formed in the undeformed beam coordinate system. This makes force and moment contributions to the body downstream of the elastic body easier to calculate.

Inertia and structural couplings are rigorously modeled for any combination of rotors and wings. The aerodynamic couplings need to be tailored for every specific configuration.

A thorough discussion of the elastic blade formulation can be found in Ref. 84. The following discussion summarizes the formulation and highlights the contributions from tip masses and large external objects, like the nacelle, on the beam equations. The discussion also highlights how forcing from upstream bodies impacts the beam equations of the current body in the multi-body system.

The beam equation of motion for a simplified beam bending example is:

$$\int_0^l (EI(x)w_{,xx})_{,xx} + m(x)\ddot{w} - p(x,t)dx = 0 \qquad (2.60)$$

The terms on the left hand side represent beam stiffness, mass, and external forcing. Beam deflection is assumed to be separable in space and time and to be composed of shape functions dependent on the spatial displacement, and temporal components which give amplitude variation with time.

$$w(x,t) = \mathbf{H}_w(x)\mathbf{y}_w(t) \qquad (2.61)$$

$$\qquad (2.62)$$

The left hand side of the beam equation is generally not equal to zero as the solution obtained is always an approximate solution, and is equal to a residual value.

$$\int_0^l (EI(x)w_{,xx})_{,xx} + m(x)\ddot{w} - p(x,t)dx = res_w(x,t) \qquad (2.63)$$

The Galerkin method of weighted residuals is used for approximating the solution to the beam equation of motion. Using the Galerkin method, a set of trial functions multiply the residual of the equation of motion. The coefficients for each trial function are determined so that the residual of the equation of motion is minimized. The trial functions used over each element are the Hermite interpolation polynomials

which are orthogonal and limit the displacements within the beam within each element. Therefore, the solver tries to solve the following equation.

$$\int_0^l res_w(x,t)\mathbf{H}_w^T(x)dx = 0 \qquad (2.64)$$

Since the residual itself is written out in Eqn. (2.63), the Galerkin method produces the following solution to the equation of motion:

$$\left[\int_0^{l_e} \left(EI(x)\mathbf{H}_{w,xx}(x)\mathbf{y}_w(t)\right)_{,xx} + m(x)\mathbf{H}_w(x)\ddot{\mathbf{y}}(t)_w - p(x,t)dx\right]\mathbf{H}_w^T(x) = 0 \quad (2.65)$$

Once the appropriate integrations by parts are carried out, the solution becomes:

$$\int_0^{l_e} \underbrace{\left(EI(x)\mathbf{H}_{w,xx}(x)\mathbf{H}_{w,xx}^T(x)\right)}_{[K]}\mathbf{y}_w(t)$$

$$+ \underbrace{\left(m(x)\mathbf{H}_w(x)\mathbf{H}_w^T(x)\right)}_{[M]}\ddot{\mathbf{y}}(t)_w - \underbrace{\left(p(x,t)\mathbf{H}_w^T(x)\right)}_{\mathbf{Q}(t)} dx = 0 \qquad (2.66)$$

The first terms form the stiffness matrix, the second terms form the mass matrix , and the final term consists of the external forcing vector.

2.5.5.1 Finite Element Descritization

Finite elements are used to model the flexible beams. Any number of elements may be used to model each wing, blade, nacelle, or any other flexible element. Aerodynamic, structural, and inertial forces and moments are calculated at specified internal points in each finite element, integrated to form loads at each node of the finite element. These nodal loads are transformed into modal loads using the modal coordinate transformation (discussed in later chapter), greatly reducing the total

number of degrees of freedom.

There are a total of $6N_E + 5$ nodal degrees of freedom, where N_E is the total number of finite elements used in the formulation. The nodal degrees of freedom for each finite element are displacement and slope for beamwise/flap (w) and chordwise/lag (v) motions at the inboard and outboard end of each element. Torsion (ϕ) has degrees of freedom at the inboard and outboard end, as well as at the center of each element, as shown in Fig. 2.9 for a four element beam model. For the beam model shown, there are a total of 29 degrees of freedom.
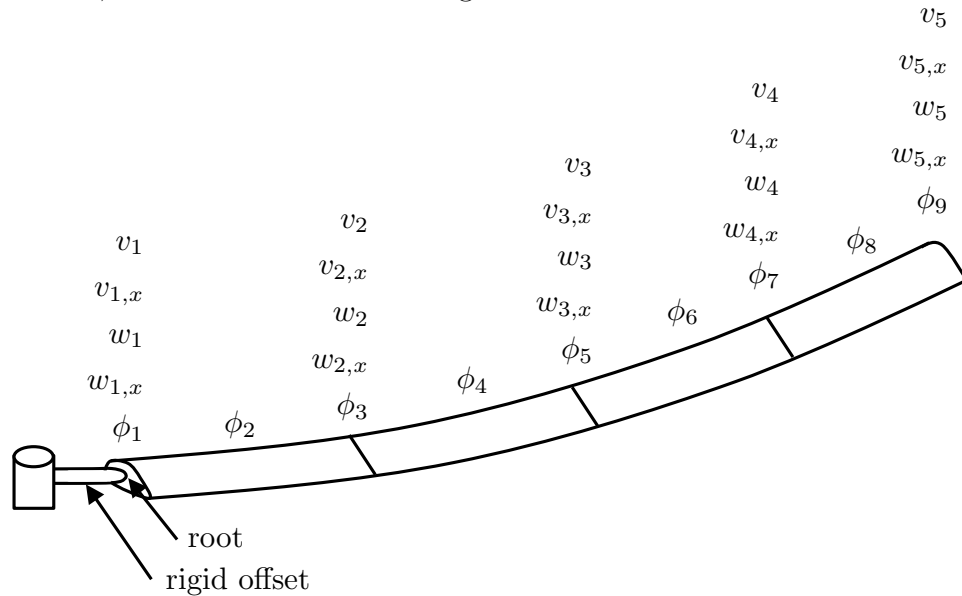
Figure 2.9: Four element finite element model of a blade with nodal degrees of freedom

Since forces and moments are integrated quantities, positions, velocities and accelerations along the entire elastic beam must be know. The mapping of the displacement between the nodes is accomplished through the use shape functions, which are Hermite polynomials. The shape functions for beam and chord bending, which contain both displacement and slope degrees of freedom at each element end

point given below in Eqn. (2.67). The variable η is a mapping variable within each element, and has a value of 0 at the inboard end of the element and 1 at the outer end. The variable x is the spanwise displacement along the beam element and is also a function of η, and l is the element length.

$$\mathbf{H}_v \left(x \right) = \mathbf{H}_w \left(x \right) = \left\{ \begin{array}{c} 1 - 3\eta^2 + 2\eta^3 \\ \eta \left(1 - 2\eta + \eta^2 \right) l \\ 3\eta^2 - 2\eta^2 \\ \eta \left(-\eta + \eta^2 \right) l \end{array} \right\}^T \tag{2.67}$$

For torsion, which includes a mid-element torsional displacement:

$$\mathbf{H}_\phi \left(x \right) = \left\{ \begin{array}{c} 1 - 3\eta + 2\eta^2 \\ 4\eta - 4\eta^2 \\ -\eta + 2\eta^2 \end{array} \right\}^T \tag{2.68}$$

The chord, beam, and torsion displacements within any finite element, and thus any portion of the beam, can be written as a product of a displacement function and known displacements at the nodes of the finite element.

$$v(x,t) = \mathbf{H}_v(x)\mathbf{y}_v(t) \tag{2.69}$$

$$w(x,t) = \mathbf{H}_w(x)\mathbf{y}_w(t) \tag{2.70}$$

$$\phi(x,t) = \mathbf{H}_v(x)\mathbf{y}_\phi(t) \tag{2.71}$$

where the vector y contains nodal displacements:

$$\mathbf{y}_v(t) = \begin{Bmatrix} v_0 \\ v_{0x} \\ v_1 \\ v_{1x} \end{Bmatrix} \qquad \mathbf{y}_w(t) = \begin{Bmatrix} w_0 \\ w_{0x} \\ w_1 \\ w_{1x} \end{Bmatrix} \qquad \mathbf{y}_\phi(t) = \begin{Bmatrix} \phi_0 \\ \phi_{0.5} \\ \phi_1 \end{Bmatrix} \qquad (2.72)$$

Here, subscript 0 refers to the inboard end of the finite element, and subscript 1 refers to the outboard end. Subscript x refers to the slope (spatial derivative) at the node. The temporal portion of the displacement vectors (Eqns. (2.69-2.71)) and their derivatives are contained in the system state vector, and are obtained from the solution to the beam finite element equations and are available at all times from the solver. The spatial portion of the displacement vectors are given by Eqns. (2.67-2.68) and their spatial derivatives. This assumed displacement in space between beam nodal elements converts the beam equations of motion from PDE into ODE form. The displacement vector is third order in space for beamwise and chordwise bending, meaning displacements within finite elements are limited to be at most cubic in nature. For torsion, the displacement are limited to follow a quadratic shape. Using equations Eqns. (2.69-2.71) and their appropriate space and time derivatives provides all the necessary variables to obtain a solution to the beam equation of motion.

Gaussian quadrature using Legendre Polynomials is performed on eight collocation points within each beam finite element to provide maximum integral accuracy for elements that have a varying structural, aerodynamic, or inertial spanwise forc-

ing. The Legendre polynomial integration points and weights are given in Table 2.1.

The standard interval of integration is changed to be the size of the mapping function

within the finite element and goes from 0 to 1.

Table 2.1: Legendre polynomial quadrature points and weights for interval $(-1,+1)$

Point	Weight
$+/-0.1834$	0.3627
$+/-0.5255$	0.3137
$+/-0.7967$	0.2224
$+/-0.9603$	0.1012

The total nodal forcing vector for each finite element can now be expressed as

a sum over the gaussian points within each element. For chord and beam bending:

$$\mathbf{F}_{v,w} = \int_{x=0}^{l} \mathbf{f}_{v,w}(x,t)\mathbf{H}_{v,w}^{T}(x)dx \tag{2.73}$$

$$\mathbf{F}_{v,w} = \sum_{i=1}^{NG} w_{i}\mathbf{f}_{v,w}(x_{i},t)\mathbf{H}_{v,w}^{T}(x_{i}) \tag{2.74}$$

The torsion bending moment has a similar formulation:

$$\mathbf{M}_{\phi} = \int_{x=1}^{l} \mathbf{m}_{\phi}(x,t)\mathbf{H}_{\phi}^{T}(x)dx \tag{2.75}$$

$$\mathbf{M}_{\phi} = \sum_{i=1}^{NG} w_{i}\mathbf{m}_{\phi}(x_{i},t)\mathbf{H}_{\phi}^{T}(x_{i}) \tag{2.76}$$

Here, w_{i} is the quadrature weight at each gauss point and $\mathbf{H}(x_{i})$ is the value

of the shape function at that point. $\mathbf{f}_{v,w}$ are the chord and beam forcing vector

per unit span and are the same quantities shown in Eqn. (2.66). During the code

execution, the components of Eqn. (2.66) are determined individually and summed

after integration along the element. In the moment equation, $\mathbf{m}_\phi$ is the torsional moment per unit span. This summation is repeated over all finite elements to produce the total nodal loading on the elastic beam. The force and moment forcing equations are obtained for inertial, structural, and aerodynamic loading. If the system is in equilibrium, these loads will cancel out, otherwise there is a resulting motion in the flexible beam.

2.5.6 Inertial Loads

Beam inertial loads are due to the local acceleration of a point on the beam and are obtained using the quadrature outline in the previous section. If the beam contains a lump mass or other localized masses such as the nacelle, there is no associated quadrature weight. These masses also do not have any contribution to the aerodynamic or structural loads. Their contribution is multiplied by the appropriate shape function value and is added directly to the integral over the beam represented by the summations in Eqn. (2.74) and Eqn. (2.76). To determine the contribution of any mass element, be it a lumped mass or distributed mass, the acceleration vector must be know.

Inertial loads are based on finding the absolute acceleration of a mass. The full acceleration vector in the undeformed coordinate system is given in Eqn. 2.54 as:

$$\mathbf{a}_B = a_x \mathbf{n}_1^b + a_y \mathbf{n}_2^b + a_z \mathbf{n}_3^b \tag{2.77}$$

Once the acceleration of the point is known, the inertial forces follow.

$$\mathbf{f}_I = -m \, \mathbf{a}_B \tag{2.78}$$

Displacements in the deformed coordinate system to the center of mass of the beam or tip element in the chordwise and vertical directions, n_2^f and n_3^f, respectively, create moments at the blade section.

$$\mathbf{m}_I = -m \left[\left(y_0 \mathbf{n}_2^f + z_0 \mathbf{n}_3^f \right) \times \mathbf{a}_B \right] \tag{2.79}$$

The full moment vector is:

$$\mathbf{m}_I = -m \left[M_1 \mathbf{n}_1^b + M_2 \mathbf{n}_2^b + M_3 \mathbf{n}_3^b \right] \tag{2.80}$$

If the beam has a simple lumped mass that is located on the elastic axis, there are no moments at the cross section. For more complicated masses, such as a nacelle, moments of inertia are lumped into two radii of gyration, one along y_0 and the other along z_0.

Once the inertial forces and moments are known at given spanwise stations, they are integrated into the nodal forces for the given finite element using Eqn. (2.74) and Eqn. (2.76). This summation takes care of the second term in the beam equation of motion given by Eqn. (2.63).

2.5.7 Structural Loads

The structural load equations for the elastic wings do not differ from those of the elastic blades and are obtained from Ref. 83. These equations are in the "semi-implicit" form, where an ordering scheme has been used to simplify the equations

into a set of algebraic equations that are integrated by parts. The total moments in the beam bending, chord bending, and torsion directions are:

$$M_b(v, w, \phi) = M_{t1} + M_{t0} \tag{2.81}$$

$$M_c(v, w, \phi) = M_{c2} + M_{c1} \tag{2.82}$$

$$M_t(v, w, \phi) = M_{b2} + M_{b1} \tag{2.83}$$

with:

$$M_{t1} = GJ \left(\phi_{,x} + v_{,xx} w_x \right) \tag{2.84}$$

$$M_{t0} = \frac{1}{2} \left(EI_2 - EI_3 \right) \sin 2\theta_G \left(v_{,xx}^2 - w_{,xx}^2 \right) - \left(EI_2 - EI_3 \right) \cos 2\theta_G v_{,xx} w_{,xx} \tag{2.85}$$

$$M_{c2} = - \left[\left(EI_2 \cos^2 \theta_G + EI_3 \sin^2 \theta_G \right) v_{,xx} \right.$$
$$\left. + \frac{1}{2} \left(EI_2 - EI_3 \right) \sin 2\theta_G \left(w_{,xx} - 2\phi v_{,xx} \right) + \left(EI_2 - EI_3 \right) \cos 2\theta_G \phi w_{,xx} \right] \tag{2.86}$$

$$M_{c1} = - GJ \phi_{,x} w_{,xx} \tag{2.87}$$

$$M_{b2} = - \left[\frac{1}{2} \left(EI_2 - EI_3 \right) \sin 2\theta_G \left(v_{,xx} + 2\phi w_{,xx} \right) + \left(EI_2 - EI_3 \right) \cos 2\theta_G \phi v_{,xx} \right.$$
$$\left. + \left(EI_2 \sin^2 \theta_G + EI_3 \cos^2 \theta_G \right) w_{,xx} \right] \tag{2.88}$$

$$M_{b1} = GJ \phi_{,x} v_{,xx} \tag{2.89}$$

$$\tag{2.90}$$

In the equations above, θ_G represents the angle of the blades with respect to the undeformed coordinate system. The beam, chord and torsion stiffnesses are EI_3, EI_2, and GJ, respectively. It should be noted that if only the beam degree of freedom is used, the equations above simplify to the beam equation as written in Eqn. (2.66). These equations still must be integrated by parts as many times

as the subscript on the left hand side indicates. The evaluation of the boundary conditions in these integrations gives no additional contribution to the equations as written above. The structural components of the quadrature given in Eqns. (2.74) and (2.76) is:

$$\mathbf{F}_v = \sum_{i=1}^{NG} w_i \left(M_{c2}(x_i, t) \mathbf{H}_{v,xx}^T(x_i) + M_{c1}(x_i, t) \mathbf{H}_{v,x}^T(x_i) \right) \tag{2.91}$$

$$\mathbf{F}_w = \sum_{i=1}^{NG} w_i \left(M_{b2}(x_i, t) \mathbf{H}_{v,xx}^T(x_i) + M_{b1}(x_i, t) \mathbf{H}_{v,x}^T(x_i) \right) \tag{2.92}$$

$$\mathbf{M}_\phi = \sum_{i=1}^{NG} w_i \left(M_{t0}(x_i, t) \mathbf{H}_\phi^T(x_i) + M_{t1}(x_i, t) \mathbf{H}_{\phi,x}^T(x_i) \right) \tag{2.93}$$

2.5.8 Aerodynamic Loads

The aerodynamic forcing is formulated in essentially the same manner as the inertial forcing for the elastic blade, except instead of accelerations, local velocities are needed. Section velocities and angles of attack are developed as in Ref. 57. Aerodynamics act as an external non-conservative force into the equations of motion, and go into the final term in the Galerkin beam equation of equilibrium, Eqn (2.63).

The blade velocities were obtained in Sec. 2.5.2. The total velocity is obtained by adding the local inflow velocity V_I. Since the dynamic inflow model is used, $\mathbf{V}_I$ only contains the vertical component of velocity:

$$\mathbf{V}_T = \mathbf{V}_P \left\{ \mathbf{n}^b \right\} - V_I \left\{ \mathbf{n}^b \right\} \tag{2.94}$$

$$\mathbf{V}_I = \lambda \mathbf{n}_3^b \tag{2.95}$$

$\mathbf{V}_T$ contains the total velocity of the blade as it moves through the air. To obtain velocities of the airmass, $\mathbf{V}_A$, as needed at the deformed blade, the transformation

from Sec. 2.1.6 is used.

$$V_A = \sqrt{(U_T^2 + U_P^2 + U_R^2)} \tag{2.96}$$

$$\alpha = \tan^{-1}\left[\frac{(U_T \tan\theta_G + U_P)\,|\cos\gamma|}{(U_T - U_P \tan\theta_G \cos^2\gamma)}\right] \tag{2.97}$$

Here U_P, U_T, and U_R are the perpendicular, tangential, and radial components of local blade velocities including all flexibility and freestream contributions. θ_G is the geometric blade pitch at the current azimuth location and includes twist, blade control pitch, and flexibility effects. $\cos\gamma$ is the yaw angle of flow and is defined as follows:

$$\cos\gamma = \frac{|U_T|}{\sqrt{U_T^2 + U_R^2}} \tag{2.98}$$

Generally, airfoil tables are functions of mach number and angle of attack.

$$C_L = C_L(\alpha, M) \tag{2.99}$$

$$C_D = C_D(\alpha, M) \tag{2.100}$$

$$C_M = C_M(\alpha, M) \tag{2.101}$$

2.5.8.1 Quasisteady Aerodynamics

Quasi-steady aerodynamics helps account for shed wake effects as non-circulatory effects in the creation of lift [85] [86]. Within these equations, the acceleration terms for a plunging, $\ddot{h}$, and pitching, $\ddot{\alpha}$, airfoils are neglected. Heave velocity, $\dot{h}$ terms are included in the look up table determination of C_L given above.

The total lift at at a blade section, including quasi-steady effects may be

written as:

$$L_Q = \frac{1}{2}\rho V_A^2 c \left[C_L + \frac{a\dot{\alpha}}{V_A} \left(\frac{c}{2} - x_A \right) \right] \tag{2.102}$$

$$L = L_Q + \frac{1}{2}\rho V_A^2 c \left[\frac{ac\dot{\alpha}}{4V_A} \right] \tag{2.103}$$

The total drag is:

$$D = \frac{1}{2}\rho V_A^2 c C_D \tag{2.104}$$

The forcing in the local coordinate system is

$$F_P = \frac{1}{V_A} \left[L\frac{U_T}{\cos\gamma} + DU_P \right] \tag{2.105}$$

$$F_T = \frac{1}{V_A} \left[DU_T - LU_P \cos\gamma \right] \tag{2.106}$$

$$F_R = \frac{1}{V_A} \left[DU_R - L\frac{U_P \cos\gamma U_R}{U_T} \right] \tag{2.107}$$

$$\mathbf{p}_a = \begin{bmatrix} F_R & F_T & F_P \end{bmatrix} \{\mathbf{n}^a\} \tag{2.108}$$

The total moment in the local coordinate system is:

$$M = M_S + M_Q + M_{\dot{\alpha}} \tag{2.109}$$

$$M_S = \frac{1}{2}\rho V_A^2 c^2 C_M \tag{2.110}$$

$$M_Q = F_P\, x_A \cos\theta_G + F_R\frac{L_Q}{L}x_A \sin\theta_G \tag{2.111}$$

$$M_{\dot{\alpha}} = -\frac{1}{8}\rho a V_A c^2 \dot{\alpha} \left(\frac{c}{2} - x_A \right) \tag{2.112}$$

$$\mathbf{q}_a = M\, \mathbf{n}_1^a \tag{2.113}$$

In the moment equations M_S is the steady state pitch moment, M_Q is the quasi-steady moment due to the offset of the aerodynamic center from the elastic axis, and $M_{\dot{\alpha}}$ represents non-circulatory contributions.

Other components in the equations above are ρ, air density; c, blade chord; a, local blade lift curve slope; and x_A, the offset of the aerodynamic center from the elastic axis. Local blade aerodynamic forces are integrated in the same manner as structural and inertial loads using Gaussian quadrature. Aerodynamics are not included in beam mode determination.

Once the loads are obtained above, they are transformed back to the unde-formed blade coordinate system using the inverse of the matrix given in Sec. 2.1.6. The aerodynamic loads may now be added to the beam equation of motion (Eqn. (2.63) through the quadratures given in Eqn. (2.74) and (2.76).

$$\mathbf{f}_a = \left[S^{ab} \right]^{-1} \mathbf{p}_a \tag{2.114}$$

$$\mathbf{m}_a = \left[S^{ab} \right]^{-1} \mathbf{q}_a \tag{2.115}$$

2.5.9   External Loads

External loads are loads that are passed onto the current body from bodies upstream. The wing has loads passed it it from the nacelle, and the rotors impart loads onto the nacelle. These loads are also treated as external non-conservative point forces in much the same manner as aerodynamics. External vertical and lateral forces go into the beam and chord residual equation, and external axial torques go

into the moment equation.

In the Gaussian quadratures shown by Eqns. (2.74) and (2.76), there is no quadrature weight associated with point forces and moment and the value of the shape functions, $\mathbf{H}^T(x_i, j)$ depends on the placement of the connection point of the upstream body within the current element.

Within the finite element that the external force is located, the external force adds the following contribution to the quadrature given in Eqn. (2.74):

$$\mathbf{F}_{v,w} = F_{v,w}^{\text{ext}}(x_i)\mathbf{H}_{v,w}^T(x_i) \tag{2.116}$$

The external moment is added as follows:

$$\mathbf{F}_{v,w} = M_{v,w}^{\text{ext}}(x_i)\mathbf{H}_{v,w,\mathbf{x}}^T(x_i) \tag{2.117}$$

For the torsion degree of freedom, the external moment contributions is:

$$\mathbf{M}_{\phi} = M_{\phi}^{\text{ext}}(x_i)\mathbf{H}_{\phi}^T(x_i) \tag{2.118}$$

2.5.10 Tension Induced Loads

The loading vectors described so far can be integrated in any order. For example, aerodynamic loads at the root are independent of the loading at the wing tip. Tensile loads at the inboard end of a rotating beam, however, are dependent on the forcing at the outer portions of the beam. These loads generate bending moments along the beam span and must be calculated from the outermost portion of the beam inwards.

The tensile load at any point along the beam comes from the summation of

axial forcing from that point outwards. The axial degree of freedom is not included in this analysis, but axial loads are transmitted to other bodies and cause a restorative flap moment for helicopter rotors. Within this formulation developed, beams may be connected to other bodies at any nodal location. Therefore, axial forcing may need to be integrated from both ends of the beam inboard to the connection point to the previous body in the multi-body system. For example, a tiltrotor's nacelle is connected at its center point to the wing. Therefore, tensile loads are calculated from both ends to this connection point.

2.5.11 Component Specific Treatment
2.5.11.1 Wings

The wing loading retains much of the same formulation of the rotor blades, including the quasi-steady components. For wings, rotor speed and blade precone, β_P is set to zero. As mentioned previously, aerodynamics for each component of the system is determined based on knowledge of the aerodynamic environment of the component.

In cruise, ailerons are used for roll control. Effects of flap deflections on lift and moment coefficients are given in Ref. 87. The same concepts are used here for aileron effects on lift and pitch coefficients.

$$C_{L_a} = C_L + \Delta C_{L_a} \delta_a \tag{2.119}$$

$$C_{M_a} = C_M + \Delta C_{M_a} \delta_a \tag{2.120}$$

where:

$$\Delta C_{L_a} = a\tau\eta \tag{2.121}$$

$$\tau = 1 - \frac{\theta_a - \sin\theta_a}{\pi} \tag{2.122}$$

$$\theta_a = \cos^- 1\left(2c_a/c - 1\right) \tag{2.123}$$

$$\eta = 0.85 - \frac{0.15}{20}\delta_a \tag{2.124}$$

$$\Delta C_{M_a} = -\Delta C_{L_a}\frac{2\sin\theta_a - \sin 2\theta_a}{8\left(\pi - \theta_a + \sin\theta_a\right)} \tag{2.125}$$

Where c_f/c is the aileron chord ratio to the airfoil section chord; δ_a is aileron deflection; a is the lift curve slope of the airfoil; and η is a linear approximation of the flap effectiveness factor for a slotted flap from $0 - 20$ deg. of deflection.

2.5.11.2 Nacelles

Nacelle aerodynamics are excluded in the calculations by setting all aerodynamic coefficients to zero and setting the aerodynamic center on the elastic axis. The nacelles are pinned at the connection to the wing, and thus contain a rigid-body rotational mode. This rotational mode produces displacements and slopes along the elastic axis from the undeformed nacelle coordinate system. These rigid displacements are used in the equations above to determine loading.

2.5.12 First-Order Form

The equations of motion for the beam require nodal displacement, velocity, and acceleration information, and so are second order in nature. The solution process requires first order equations, so a re-structuring of the nodal states is required. The

replacement of the second order states with two sets of first order states accomplishes the task.

$$x_1 = \dot{y} \tag{2.126}$$

$$x_2 = y \tag{2.127}$$

and

$$\dot{x}_1 = \ddot{y} \tag{2.128}$$

$$\dot{x}_2 = x_1 \tag{2.129}$$

For a homogenous second order system the conversion is as follows:

$$\ddot{y} + 2\zeta\omega\dot{y} + \omega^2 y = 0 \tag{2.130}$$

$$\begin{Bmatrix} \dot{x}_1 \\ \dot{x}_2 \end{Bmatrix} + \begin{bmatrix} 2\zeta\omega & \omega^2 \\ 1 & 0 \end{bmatrix} \begin{Bmatrix} x_1 \\ x_2 \end{Bmatrix} = \begin{Bmatrix} 0 \\ 0 \end{Bmatrix} \tag{2.131}$$

2.6 Inflow Equations of Motion

A three state Pitt-Peters type dynamic inflow model provides local velocities for air load determination [88]. The inflow at any point of the rotor can be written as:

$$\lambda(r, \psi) = \lambda_0 + \lambda_c r \cos\psi + \lambda_s r \sin\psi \tag{2.132}$$

Where λ_0, λ_s, and λ_c are the unknowns in the inflow equations, given in the tip-path plane:

$$\frac{1}{\Omega} M \begin{Bmatrix} \dot{\lambda}_0 \\ \dot{\lambda}_s \\ \dot{\lambda}_c \end{Bmatrix} + L_{nl}^{-1} \begin{Bmatrix} \lambda_0 \\ \lambda_s \\ \lambda_c \end{Bmatrix} = \begin{Bmatrix} C_T \\ -C_L \\ -C_M \end{Bmatrix} \tag{2.133}$$

The matrices M and L_{nl} contain the apparent mass terms and the non-linear inflow gains and are given in Ref. 89. The right hand side of the equations give the rotor thrust and pitching and rolling moments from the integration of blade aerodynamic loads. For multi-rotor configurations, each rotor has its own independent set of dynamic inflow equations.

As with the rigid-body and beam equations, all forcing is brought to the same side, and a residual value of the inflow equation is passed to the solver.

2.7   Root Force and Moment Summation

The forcing as described so far goes into the flexible beam equations of motion. The total forcing, including all degrees of freedom, must also get transmitted through the beam to the hub and the aircraft itself to drive the motion of the aircraft through the rigid-body equations of motion (Eqns.(2.22)-(2.27)).

A force summation method is used at the blade root to determine loads caused be inertial and aerodynamic loads. The loads at the blade root are:

$$\mathbf{F}_R = \int_e^1 \left(\mathbf{f}_A + \mathbf{f}_I \right) dx_0 \tag{2.134}$$

$$\mathbf{M}_R = \int_e^1 \mathbf{R}_C \times \left(\mathbf{f}_A + \mathbf{f}_I \right) + \left(\mathbf{m}_A + \mathbf{m}_I \right) dx_0 \tag{2.135}$$

Only aerodynamic and inertial pitching moments are transferred in the second term in the moment equation. $\mathbf{R}_C$ is the position vector of the deformed blade with respect to the hub.

$$\mathbf{R}_C = x_0\mathbf{n}_1^b + u\mathbf{n}_1^f + v\mathbf{n}_2^f + w\mathbf{n}_3^f \qquad (2.136)$$

For an articulated helicopter, flap and lag moments are not transferred to the hinge. The moments undergo further manipulation if there is a elastic offset. The total moments at the hub are:

$$\mathbf{M}_H = \mathbf{M}_R + \mathbf{R}_e \times \mathbf{F}_R \qquad (2.137)$$

Where $\mathbf{R}_e$ is the elastic offset

$$\mathbf{R}_e = e\mathbf{n}_1^b \qquad (2.138)$$

The forces and moments are then converted to the coordinate system of the downstream body, and act as external forcing on that body. For the blades, this includes inverse transformations from the preconed coordinate system to the rotating shaft system and finally to the non-rotating (hub) shaft system.

$$\mathbf{F}_H = \left[S^{NR,R}\right]^{-1}\left[S^{R,b}\right]^{-1}\mathbf{F}_R \qquad (2.139)$$

$$\mathbf{M}_H = \left[S^{NR,R}\right]^{-1}\left[S^{R,b}\right]^{-1}\mathbf{M}_R \qquad (2.140)$$

As well as acting as external forcing vectors on beam equations of motion, these forces and moments are also passed down to the root of the downstream body as additional forces and moments in the overall force and moment summation. At the

root they are summed with the inertial and aerodynamic forcing from that beam (Eqns. (2.134) and (2.135)). $\mathbf{M}_R$ has another component, the cross product of the displacement $\mathbf{R}_C$ to the external applied force.

Force and moment transfer in the multi-body system is independent of beam flexibility. Rigid portions of the multi-body model must also pass forcing to whatever body they are connected to, terminating at the CG.

2.8 Assembly of System Degrees of Freedom

The system equations of motion are written in first order ODE form. The equations are set up so that all forcing is brought to one side, for example, the X-Force equation is:

$$m\left(\dot{u} + qw - rv\right) + mg\sin\theta - X = 0 \tag{2.141}$$

or generally:

$$\mathbf{f}(\dot{\mathbf{x}}, \mathbf{x}, \mathbf{u}; t) = 0 \tag{2.142}$$

This formulation and solution of this form of equations is described in Ref. [90]. Note that this relation is not generally true unless exact solution to the system of equations has been found. This relation is usually equal to a residual value that is minimized.

The full state vector is created from the components described above. Beginning with the rigid-body states:

$$\mathbf{x}_{rb} = \{u \quad v \quad w \quad p \quad q \quad r \quad \phi \quad \theta \quad \psi\}^T \tag{2.143}$$

These states have their associate differential equations, given by Eqns. (2.22)-(2.30).

The next set of states represent inflow dynamics. One set of three inflow states and equations (Eqn. (2.133)) is present for each rotor.

$$\mathbf{x}_\lambda = \{\lambda_0 \quad \lambda_s \quad \lambda_c\}^T \tag{2.144}$$

The full state including the rigid-body states and states for inflows of rotors $1 \ldots N_R$ is:

$$\mathbf{x} = \left\{ \begin{array}{c} x_{rb} \\ \\ x_{\lambda 1} \\ \\ \vdots \\ \\ x_{\lambda N_R} \end{array} \right\} \tag{2.145}$$

Next come the flexible beam states. The flexible beam's degrees of freedom are dependent on the number of finite elements used. For the four element finite-element model, they are shown in Fig. 2.9. Each four element beam has the following degrees of freedom:

$$\mathbf{x}_{str} = \{v_1 \quad v_{1x} \quad w_1 \quad w_{1x} \quad \phi_1 \quad \phi_2 \quad v_2 \quad v_{2x} \quad w_2 \quad w_{2x} \quad \phi_3 \quad \phi_4 \quad v_3 \quad v_{3x}$$

$$w_3 \quad w_{3x} \quad \phi_5 \quad \phi_6 \quad v_4 \quad v_{4x} \quad w_4 \quad w_{4x} \quad \phi_7 \quad \phi_8 \quad v_5 \quad v_{5x} \quad w_5 \quad w_{5x} \quad \phi_9\}^T$$

$$\tag{2.146}$$

The differential equations associated with these degrees of freedom are the differential nodal loading equations given in Eqns. (2.74) and (2.76). The nodal states are converted to first order form, giving a state vector that has both the displacement and velocity of the nodes as states. The full state vector including flexible bodies 1

... N_B is:

$$\mathbf{x} = \left\{ \begin{array}{c} \mathbf{x}_{rb} \\[2mm] \mathbf{x}_{\lambda 1} \\[2mm] \vdots \\[2mm] \mathbf{x}_{\lambda N_R} \\[2mm] \mathbf{x}_{str1} \\[2mm] \vdots \\[2mm] \mathbf{x}_{strN_B} \\[2mm] \dot{\mathbf{x}}_{str1} \\[2mm] \vdots \\[2mm] \dot{\mathbf{x}}_{strN_B} \end{array} \right\} \tag{2.147}$$

Each state in the vector above has an associated equation. These equations have been described within this chapter. They are ordered in the same manner as the states are.

2.9 Chapter Summary

This chapter reviews the theoretical development of the math model. Multibody kinematics are retained to formulate position, velocity, and acceleration vectors of different parts of the multi-body system. Structural, inertial and aerodynamic forcing of the wing, blade, and other flexible components are discussed. Detailed expressions for the development of the system math model are given. For the multibody system, bodies downstream of the current body add external forces and mo-

ments. These forces and moments are integrated to provide the forcing function for the beam equations of motion as well as the overall aircraft dynamics.

Chapter 3:   Model Development and Solution

This chapter discusses in more depth the creation of the aircraft multi-body model from its components and various other capabilities of the software including trim and linearization. A formulation similar to a full multi-body analysis is used to connect the bodies and create the coupled equations of motion. Structural flexibility effects the kinematics of all bodies upstream of the current one. Modal coordinate transformations are used to reduce the system degrees of freedom and help retain only key modes in the analysis.

3.1   Tree Structure Management

At each time step, the only information each individual body has is that of the connection to the bodies just upstream of itself. This information contains the displacement vector $\mathbf{q}$ to the connection point of that next body, and the set of rotations needed to get to the coordinate system of the next body. This allows for components of the system to be easily swapped out with other components with minimal changes to the inputs. Information regarding each body is stored individually with that body in derived types, allowing for large systems to be constructed with minimal creation of vectors that must be passed through each subroutine. A tree array is formed to join the system of individual bodies into the full multi-body
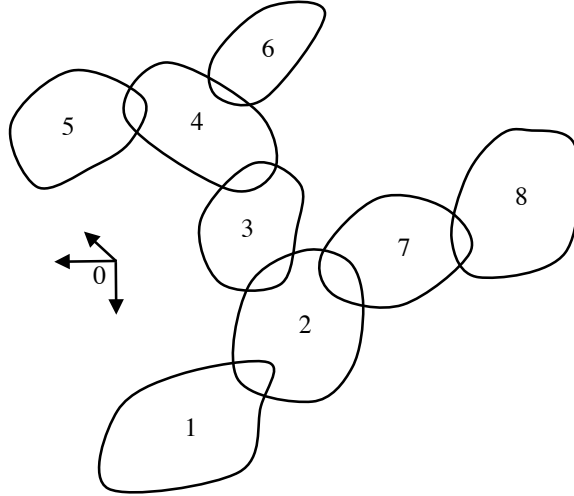
Figure 3.1:   Generic set of interconnected bodies

Table 3.1:   Tree array connecting the components of Fig. 3.1

k	1	2	3	4	5	6	7	8
Γ_1	0	1	2	3	4	4	2	7
Γ_2		0	1	2	3	3	1	2
Γ_3			0	1	2	2	0	1
Γ_4				0	1	1		0
Γ_5					0	0		

system of the aircraft and contains pointers to each of the derived types. A tree array for a generic set of interconnected bodies, shown in Fig. 3.1, is given in Table 3.1. The top line of the table contains a numerical assignment for each body in the system. The columns of the table indicate the path from that body to the reference frame. For the tilt rotor example, the fuselage, wings, and nacelles each have their own derived type. A tree array is formed and assigns body numbers to each component of the aircraft. Since some components are used twice, some body numbers are composed of the same derived type. As the kinematics of the system are created, the appropriate body is extracted from the set of all available bodies using the tree array.

The formulation of all components of the tree structure, including the coordinate system transformation matrices, kinematic relations, and kinematic vector transformations are done in unison in loops based on the length of each branch of the tree. All loops begin at the reference frame and branch out depending on the number of connections each individual body has. To obtain the kinematics of the final body in the tree system, the kinematic relations of all other bodies downstream of that one must be created first. This formulation reduces the number of matrix multiplications needed to model the entire system.

3.2   Modal Coordinate Transformation

One of the key features of the analysis is the modal coordinate transformation. The degrees of freedom for the model as described so far include all nodes for each flexible object, as shown in Figure 2.9. The modal coordinate transformation allows for the reduction of the beam degrees of freedom to a few key modes.

3.2.1   Mode Shapes

Full mass and stiffness matrices for each beam are only formulated once at the beginning of execution. For a tiltrotor example, this includes rotor blades, wings, and the dynamic nacelle. The mass matrix is obtained from a central difference approximation to perturbations of the second time derivative of the nodal degrees of freedom. The stiffness matrix comes from a central difference approximation to perturbations in displacement of the nodal degrees of freedom. The blade modes are obtained in a vacuum, i.e. aerodynamic loads are not included. The matrices

are approximations because the beam equations are generally nonlinear. The linear matrices can be written as:

$$[\mathbf{M}]\,\ddot{\mathbf{n}} + [\mathbf{K}]\,\mathbf{n} = 0 \tag{3.1}$$

Where $\mathbf{n}$ are the nodal degrees of freedom.

Eigen analysis produces a matrix of mode shapes, $[\mathbf{V}]$, which consists of columns of eigenvectors, along with a vector of the square of the corresponding modal frequencies, $\{\omega^2\}$, such that:

$$-\omega_i^2\,[\mathbf{M}]\,\{\mathbf{v}_i\} + [\mathbf{K}]\,\{\mathbf{v}_i\} = 0 \tag{3.2}$$

Here, $\mathbf{v}_i$ is the eigenvector associated with mode i and w_i is its frequency. Each column in the matrix of mode shapes gives the nodal displacements for the mode associated with that column. Four finite elements are used for the formulation of each blade, wing, and nacelle. The maximum number of modes retained is therefore 29 per beam.

Modal reduction greatly reduces the overall degrees of freedom of the system. The total nodal displacement can be written as the product of the columns of the $[\mathbf{V}]$ matrix associated with retained modal displacements $\mathbf{q}$:

$$\mathbf{n} = [\mathbf{V}]\,\mathbf{q} \tag{3.3}$$

Throughout the remainder of execution, any beam motion is limited to summed contributions from the retained modes. Only the lowest frequency modes are retained since the dominant response of the system comes from the low frequency

modes. Generally, two modes are retained for the blades, a flap mode and a lag mode. Three modes are retained for the wings so that there is a dominant mode in all three bending axes. Only the first rigid-body rotation mode is retained for the nacelles. This mode is obtained by constraining the displacement of the center node to be zero. This allows the nacelle to rotate about its connection to the wing. This summed contribution from the retained modes also goes into determining the displacements and angles that flexibility add to the kinematics of the multi-body system, given in Eqn. (A.10).

Beam mode shapes can also be read as inputs from files. Higher fidelity models can be used to obtain the mode shapes for each beam. These models could be higher fidelity beam models, or even 2 or 3-D mesh models. Mode shapes from these models would need to give displacements and rotations at the nodes of the beam used in the current analysis. Once the mode shapes are read into the matrix $[\mathbf{V}]$, they would be used throughout execution to constrain the beam deformation as described above.

3.2.2   Modal Forcing

The distributed forces along the wing, blade, or nacelle, are integrated across each finite element to produce nodal loads. The nodal loads are reduced to modal loads using the modal transformation matrix. For example,

$$\mathbf{F}_I = \sum_{k=1}^{N_E} [\mathbf{V}_k]^T \mathbf{p}_{Ik} \tag{3.4}$$

81

In this example, $\mathbf{F}_I$ are the modal inertial loads and $\mathbf{p}_I$ are nodal loads, the components of which show up in the Galerkin beam finite element equilibrium equation, Eqn. (2.63).

The sum of the modal inertial, aerodynamic, structural, and external loads produce the equilibrium equation for that mode. This equilibrium equation drives the motion of the beam modes, which are comprised of the nodal degrees of freedom. Artificial modal damping was added to the wing equations to produce stable modes with ~6% damping ratios. The majority of the flexible bodies in the system are connected to other bodies which also produce forces and moments at the connection point to the current body. These external forces and moments are also reduced to modal forcing. In equilibrium, the blade modal equations can be written as:

$$\mathbf{F}_I + \mathbf{F}_A + \mathbf{F}_S + \mathbf{F}_D + \mathbf{F}_E = \mathbf{0} \tag{3.5}$$

or, for each mode:

$$f\left(\dot{\mathbf{x}}, \mathbf{x}, \delta, t\right) = 0 \tag{3.6}$$

3.2.3 Transformed State Vector

Once each beam has been passed through the coordinate transformation, the state vector (Eqn. (2.147)) can be reconstructed with the new modal degrees of

freedom as opposed to the nodal degrees of freedom. The state vector looks identical:

$$
\mathbf{x} = \left\{
\begin{array}{c}
\mathbf{x}_{rb} \\[6pt]
\mathbf{x}_{\lambda 1} \\[6pt]
\vdots \\[6pt]
\mathbf{x}_{\lambda N_R} \\[6pt]
\mathbf{x}_{str1} \\[6pt]
\vdots \\[6pt]
\mathbf{x}_{strN_B} \\[6pt]
\dot{\mathbf{x}}_{str1} \\[6pt]
\vdots \\[6pt]
\dot{\mathbf{x}}_{strN_B}
\end{array}
\right\}
\tag{3.7}
$$

But now, the structural states have the following form instead of the form of Eqn. (2.146):

$$
\mathbf{x}_{str} = \left\{ x_1 ... x_{N_M} \right)^T
\tag{3.8}
$$

Where N_M is the number of retained modes for the current beam.

3.3   Structural Measurements

Available structural measurements include accelerations at any point in the aircraft, or strain measurements at the root of flexible bodies. Accelerations at the wing tip are used in the feedback of the linear model and root strain measurements

83

are used to measure structural motion.

Wing acceleration is available immediately from the kinematic relation equations, Eqn. (2.77). The offsets from the elastic axis now represent the sensor location as opposed to the location of the next body in the chain.

Strain measurements require additional work. In the "semi-implicit" form of the structural formulation, the strains are not directly solved for. To obtain the strains, a "fully-implicit" structural formulation is included, in which one of the first steps is the determination of strains from displacements. The derivation for the strains comes from Ref. 83 and is given more directly in Ref. 91. The strain vector has the form:

$$\epsilon = \epsilon_1 + \epsilon_2 y_0 + \epsilon_3 z_0 + \epsilon_4 y_0^2 + \epsilon_5 y_0 z_0 + \epsilon_6 z_0^2 \tag{3.9}$$

The values for y_0 and z_0 are offsets of the strain gauges from the elastic axis. The strain-displacement relation is:

$$\epsilon_{xx} = \frac{1}{2}(G_x \cdot G_x - 1) \tag{3.10}$$

G_x comes directly from the elastic displacement of the beam.

$$G_x = (1 + u_x)e_x + v_x e_y + w_x e_z + y_0(-\kappa_y e_x' + \tau e_z') + z_0(-\kappa_z e_x' - \tau e_y') \tag{3.11}$$

The curvatures, κ_y, κ_z, and τ are obtained from components of the transformation matrix from the blade undeformed to blade deformed coordinate system, along with

it's spatial derivative [83]:

$$\kappa_y = -\left(S_{11}S_{21,x} + S_{12}S_{22,x} + S_{13}S_{23,x}\right) \tag{3.12}$$

$$\kappa_z = -\left(S_{11}S_{31,x} + S_{12}S_{32,x} + S_{13}S_{33,x}\right) \tag{3.13}$$

$$\tau = -\left(S_{21}S_{31,x} + S_{22}S_{32,x} + S_{23}S_{33,x}\right) \tag{3.14}$$

3.4 Trim

The trim formulation defines an equilibrium point for the aircraft for a given steady flight condition, and consists of the solution of a set of algebraic equations. The trim problem is formulated for a steady, coordinated, helical turn. For a given aircraft weight and altitude, the flight condition is defined be a speed, V_0, turn rate $\dot{\psi}_0$, and flight path angle γ_0. Straight and level flight is a special case of a climbing turn with $\dot{\psi}_0 = \gamma_0 = 0$. Hover is a special case of straight and level flight with $V_0 = 0$. The trim algorithm follows the formulation given in Ref. 92, and additional details are given in Ref. 93. The algorithm is summarized here and additional details are given here for flexible wing and nacelle trim.

The trim unknowns can be partitioned into rigid-body, inflow, beam, and

nacelle segments.

$$\mathbf{y} = \begin{Bmatrix} \mathbf{y}_{rb} \\ \mathbf{y}_{\lambda} \\ \mathbf{y}_{str} \\ \mathbf{y}_{nac} \end{Bmatrix} \tag{3.15}$$

Each component will be described below

3.4.1 Aircraft Trim

Aircraft trim is defined by setting all aircraft accelerations to zeros, leading to constant (time invariant) values for the rigid-body states in the force and moment equations.

$$X_0 = m \left(q_0 w_0 - r_0 v_0 \right) + mg \sin \theta_0 \tag{3.16}$$

$$Y_0 = m \left(r_0 u_0 - p_0 w_0 \right) - mg \sin \phi_0 \cos \theta_0 \tag{3.17}$$

$$Z_0 = m \left(p_0 v_0 - q_0 u_0 \right) - mg \cos \phi_0 \cos \theta_0 \tag{3.18}$$

$$L_0 = - \left(I_{yy} - I_{zz} \right) q_0 r_0 - I_{xz} \left(p_0 q_0 \right) \tag{3.19}$$

$$M_0 = - \left(I_{zz} - I_{xx} \right) p_0 r_0 - I_{xz} \left(p_0^2 - r_0^2 \right) \tag{3.20}$$

$$N_0 = - \left(I_{xx} - I_{yy} \right) p_0 q_0 - I_{xz} q_0 r_0 \tag{3.21}$$

The Euler relations in trim are:

$$p_0 = \dot{\phi}_0 - \dot{\psi}_0 \sin \theta_0 \tag{3.22}$$

$$q_0 = \dot{\theta}_0 \cos \phi_0 + \dot{\psi}_0 \cos \theta_0 \sin \phi_0 \tag{3.23}$$

$$r_0 = \dot{\psi}_0 \cos \theta_0 \cos \phi_0 - \dot{\theta}_0 \sin \phi_0 \tag{3.24}$$

Note that in the rigid-body force equations, if ϕ_0 and θ_0 are not constants, the forcing due to gravity changes and the force equilibrium equations are no longer time invariant. Therefore, trim is also defined by zero aircraft roll and pitch Euler rates ($\dot{\phi}_0 = \dot{\theta}_0 = 0$), which lead to constant Euler angles. The only remaining unknown from the equations above is $\dot{\psi}_0$, the turn rate as defined by the trim condition. The yaw angle, ψ, can be reconstructed if its initial value ψ_0 is known from $\psi(t) = \dot{\psi}t + \psi_0$, where t is the elapsed time since the beginning of the turn. Therefore, the yaw angle state may be removed from the trim vector. The Euler equations reduce to:

$$p_0 = -\dot{\psi}_0 \sin \theta_0 \tag{3.25}$$

$$q_0 = \dot{\psi}_0 \sin \phi_0 \cos \theta_0 \tag{3.26}$$

$$r_0 = \dot{\psi}_0 \cos \phi_0 \cos \theta_0 \tag{3.27}$$

and a steady-state solution can now be found. Substituting the kinematic trim relations into the 6 rigid-body equations leaves the following unknowns (stick inputs

are also unknowns as they appear in the forcing terms in the rigid-body equations).

$$\mathbf{y}_{rb} = \{\delta_{lat} \quad \delta_{lon} \quad \delta_{col} \quad \delta_{ped} \quad u_0 \quad v_0 \quad w_0 \quad \phi_0 \quad \theta_0\}^T \tag{3.28}$$

The linear velocity components of the trim vector can be rewritten using the trim aircraft velocity.

$$u_0 = V_0 \cos \alpha_0 \cos \beta_0 \tag{3.29}$$

$$v_0 = V_0 \sin \beta_0 \tag{3.30}$$

$$w_0 = V_0 \sin \alpha_0 \cos \beta_0 \tag{3.31}$$

The final unknowns are:

$$\mathbf{y}_{rb} = \{\delta_{lat} \quad \delta_{lon} \quad \delta_{col} \quad \delta_{ped} \quad \alpha_0 \quad \beta_0 \quad \phi_0 \quad \theta_0\}^T \tag{3.32}$$

The first four unknowns are the pilot stick inputs. α and β are angles of attack and sideslip of the fuselage, respectively. These angles help define the trim velocities. ϕ_0 and θ_0 are roll and pitch Euler angles. The aircraft can have these attitudes while maintaining a trim condition. There are total of 8 unknowns in the trip problem, requiring 8 equations.

The first six equations consist of the the rigid-body equations, rewritten using Eqns. (3.25)-(3.27) and Eqns. (3.29)-(3.31). The two additional equations are the turn coordination and flight path equations. Turn coordination ensures that lateral

acceleration of the CG is zero. This is different from the Y-Force equation, which only ensures the left and right hand sides of the Y-Force equation are equal. The flight path equation states that the aircraft's vertical velocity in the z inertial axis equal to a constant value, $V_0 \sin \gamma_0$. Along with V_0 and $\dot{\psi}_0$ given above, γ_0 is the final trim condition that is set before execution. Converting body velocities to inertial velocities, and only retaining the z component gives the relation.

$$V_0 \sin \gamma_0 = \begin{bmatrix} u_0 & v_0 & w_0 \end{bmatrix} \begin{bmatrix} () & () & -\sin \theta_0 \\ () & () & \sin \phi_0 \cos \theta_0 \\ () & () & \cos \phi_0 \cos \theta_0 \end{bmatrix} \begin{Bmatrix} \mathbf{n}_1^I \\ \mathbf{n}_2^I \\ \mathbf{n}_3^I \end{Bmatrix} \tag{3.33}$$

$$= \left[-u_0 \sin \theta_0 + v_0 \sin \phi_0 \cos \theta_0 + w_0 \cos \phi_0 \cos \theta_0 \right] \mathbf{n}_3^I \tag{3.34}$$

$$= V_0 \left[-\cos \alpha_0 \cos \beta_0 \sin \theta_0 + \sin \beta_0 \sin \phi_0 \cos \theta_0 + \sin \alpha_0 \cos \beta_0 \cos \phi_0 \cos \theta_0 \right] \mathbf{n}_3^I$$

$$\tag{3.35}$$

V_0 can be removed from both sides of the above equation giving the final flight path angle trim equation. Components in the transformation matrix that are () are not necessary for the solution so are left out.

All forcing is brought to the same side of the algebraic trim equations, so they may be written as:

$$0 = \mathbf{f_{rb}} \left(\mathbf{y}, t \right) \tag{3.36}$$

These trim equations uphold trim at any point in time. Since rotorcraft have periodic forcing, the trim equations are integrated around the azimuth to ensure a

89

trim state for a full rotor revolution. The left hand side of Eqn. (3.36) is generally not equal to zero unless the algebraic solver has found the exact trim solution. The residual value is integrated around the azimuth.

$$\mathbf{f_{rb}}\left(\mathbf{y}; \psi\right) = \mathbf{res_{rb}}\left(\mathbf{y}; \psi\right) \tag{3.37}$$

$$\int_0^{2\pi} \mathbf{res_{rb}}\left(\mathbf{y}; \psi\right) \, d\psi = 0 \tag{3.38}$$

The trim equations using the residuals for the three force and moment equations are:

$$\int_0^{2\pi} \mathrm{res}_X \, d\psi = 0 \tag{3.39}$$

$$\int_0^{2\pi} \mathrm{res}_Y \, d\psi = 0 \tag{3.40}$$

$$\int_0^{2\pi} \mathrm{res}_Z \, d\psi = 0 \tag{3.41}$$

$$\int_0^{2\pi} \mathrm{res}_L \, d\psi = 0 \tag{3.42}$$

$$\int_0^{2\pi} \mathrm{res}_M \, d\psi = 0 \tag{3.43}$$

$$\int_0^{2\pi} \mathrm{res}_N \, d\psi = 0 \tag{3.44}$$

The final two equations are the turn coordination and flight path equations. These are integrated around the azimuth as well. The turn coordination sets Eqn. 3.17 equal to zero.

$$\int_0^{2\pi} \frac{\dot{\psi}_0 V_0}{g} \left(\cos \phi_0 \cos \alpha_0 + \tan \theta_0 \sin \alpha_0\right) \cos \beta_0 - \sin \phi_0 \, d\psi = 0 \tag{3.45}$$

For straight flight with $\dot{\psi}_0 = 0$, this equation reduces to:

$$\int_0^{2\pi} \sin \phi_0 \, d\psi = 0 \tag{3.46}$$

The turn coordination equation integrated around the azimuth is:

$$\int_0^{2\pi} \sin \gamma_0 + [\cos \alpha \cos \beta \sin \theta_0 - \cos \theta_0 (\sin \beta_0 \sin \phi_0 + \sin \alpha_0 \cos \beta_0 \cos \phi_0)] \, d\psi = 0 \tag{3.47}$$

These eight aircraft trim equations are grouped into a vector containing all trim equations:

$$\mathbf{Y} = \{\mathbf{Y}_{rb}\}^T \tag{3.48}$$

3.4.2   Flexible Beam Trim

The beam equations of motion are second order in time. To convert the differential beam equations into algebraic equations, periodicity is assumed around the azimuth. The assumption of periodicity gives produces approximate beam displacements since actual beam motion may include higher harmonics. The trimmed modal displacements have the following form:

$$\mathbf{x} \approx \mathbf{x}_{\text{app}} = \mathbf{y}_0 + \sum_{k=1}^{N_h} (\mathbf{y}_{kc} \cos k\psi + \mathbf{y}_{ks} \sin k\psi) \tag{3.49}$$

The above equation can be easily differentiated twice to produce the needed modal velocities and accelerations (it is assumed rotor speed is constant in trim, Ω):

$$\dot{\mathbf{x}} \approx \dot{\mathbf{x}}_{\text{app}} = \Omega \sum_{k=1}^{N_h} k \left(-\mathbf{y}_{kc} \sin k\psi + \mathbf{y}_{ks} k \cos k\psi \right) \tag{3.50}$$

$$\ddot{\mathbf{x}} \approx \ddot{\mathbf{x}}_{\text{app}} = \Omega^2 \sum_{k=1}^{N_h} k^2 \left(-\mathbf{y}_{kc} \cos k\psi - \mathbf{y}_{ks} \sin k\psi \right) \tag{3.51}$$

The trim unknowns in the trim algebraic solution are the steady state and harmonic coefficients. Any number of harmonics of motion are retainable. The equations above give the harmonic coefficients for a single mode. If multiple beam modes are retained, each mode's motion will be reduced to harmonic motion.

The total vector of structural unknowns for N_B flexible beams (rotor blades or wings), each with N_h harmonics:

$$\mathbf{y}_{beam} = \left\{ y_0 \quad y_{1c} \quad y_{1s} \dots y_{N_h c} \quad y_{N_h s} \right\}^T \tag{3.52}$$

$$\mathbf{y}_{str} = \left\{ \begin{array}{c} \mathbf{y}_{beam1} \\ \vdots \\ \mathbf{y}_{beamN_B} \end{array} \right\} \tag{3.53}$$

As with the rigid-body equations, the equilibrium equations for each beam mode are also integrated around the azimuth. They are based on a harmonic balance of residuals as described in Section 3.4.1. Generally, the modal equilibrium equation, Eqn. (3.6) is not equal to 0, but rather a residual that is dependent on the current trim guess and azimuth position, $\mathbf{res}_{\text{str}}(\mathbf{y}; \psi)$. From Eqn. (3.59), there are $2N_h + 1$

unknowns for each mode of each beam, so $2N_h + 1$ trim equations are needed. The trim equations for the beam modal unknowns aim to minimize this residual and its harmonics as follow.

$$\int_0^{2\pi} \mathbf{res_{beam}}\left(\mathbf{y}; \psi\right) \ d\psi = 0$$

$$\int_0^{2\pi} \mathbf{res_{beam}}\left(\mathbf{y}; \psi\right) \cos i\psi \ d\psi = 0 \quad i = 1, \ldots, N_h \qquad (3.54)$$

$$\int_0^{2\pi} \mathbf{res_{beam}}\left(\mathbf{y}; \psi\right) \sin i\psi \ d\psi = 0 \quad i = 1, \ldots, N_h$$

The equations above represent the beam trim equations for a single mode of a single beam. Adding additional modes makes the trim equation vector:

$$\mathbf{Y}_{beam} = \{Y_0 \quad Y_{1c} \quad Y_{1s} \ldots Y_{N_h c} \quad Y_{N_h s}\}^T \qquad (3.55)$$

$$(3.56)$$

Where Y_0 represents the first the trim equation and $Y_{N_h c}$ and $Y_{N_h s}$ represent the N_h harmonc cosine and sine equations. The beams are all grouped together to give the full vector of beam trim equations.

$$\mathbf{Y}_{str} = \begin{Bmatrix} \mathbf{Y}_{beam1} \\ \vdots \\ \mathbf{Y}_{beamN_B} \end{Bmatrix} \qquad (3.57)$$

93

3.4.2.1 Nacelle Trim

The trim solution for the nacelle is treated differently. Here, the nacelle angle (i.e modal deflection $\mathbf{x}_{nac}$) is a trim condition, much like aircraft velocity, flight path, or turn rate. The trim unknown is the torque required to keep the nacelle at that trim condition. δ_{nac} represent input torques at the nacelle connection to the wing and are the unknowns for the nacelle trim equations.

$$\mathbf{y}_{nac} = \{\delta_{nac1} \quad \delta_{nac2}\}^T \tag{3.58}$$

The nacelle trim equation is similar to the residuals for other elastic beams. Only a constant deflection is allowed for each nacelle:

$$\mathbf{x} \approx \mathbf{x}_{\mathrm{app}} = \mathbf{y}_0 \tag{3.59}$$

$$\dot{\mathbf{x}} \approx \dot{\mathbf{x}}_{\mathrm{app}} = 0 \tag{3.60}$$

$$\ddot{\mathbf{x}} \approx \ddot{\mathbf{x}}_{\mathrm{app}} = 0 \tag{3.61}$$

The deflection goes into the nacelles modal equation, Eqn. (3.6), and the nacelle torque required to maintain trim equilibrium is determined. Since only a single unknown exists per nacelle, the nacelle trim equation is:

$$\int_0^{2\pi} \mathbf{res_{nac}} \left(\mathbf{y}; \psi\right) \ d\psi = 0 \tag{3.62}$$

94

Since tiltrotors have two nacelles, each with its own trim equation, the full nacelle trim equation vector is:

$$\mathbf{Y}_{nac} = \left\{ Y_{nac1} \quad Y_{nac2} \right\}^T \tag{3.63}$$

3.4.3 Inflow Trim

Dynamic inflow trim equations and unknowns are included in the trim procedure. Each rotor has a constant coefficient and first harmonic sine and cosine inflow distribution. The dynamic inflow equations for each rotor are given in Eqn. (2.133), and are converted to algebraic equations as follows. In trim the time derivative of the inflow equations must be zero when integrated around the azimuth, which implies that only the steady-state component of inflow is present. The inflow trim equations are therefore:

$$L_{nl}^{-1} \left\{ \begin{matrix} \lambda_0 \\ \lambda_s \\ \lambda_c \end{matrix} \right\} = \left\{ \begin{matrix} C_T \\ -C_L \\ -C_M \end{matrix} \right\} \tag{3.64}$$

As with aircraft and beam equations, all forcing is brought to the left hand side. The unknowns for each rotor are the inflow coefficients. There are as many sets of these unknowns as there are rotors.

$$\mathbf{y}_\lambda = \{\lambda_{10} \quad \lambda_{1s} \quad \lambda_{1c} \dots \lambda_{N_R 0} \quad \lambda_{N_R s} \quad \lambda_{N_R c}\}^T \tag{3.65}$$

The harmonic balance approach assures equilibrium over a rotor revolution:

$$\int_0^{2\pi} \mathbf{res}_{\lambda_0}\left(\mathbf{y};\psi\right)\ d\psi = 0$$

$$\int_0^{2\pi} \mathbf{res}_{\lambda_s}\left(\mathbf{y};\psi\right)\ d\psi = 0 \qquad (3.66)$$

$$\int_0^{2\pi} \mathbf{res}_{\lambda_c}\left(\mathbf{y};\psi\right)\ d\psi = 0$$

These equations are collected for all rotors:

$$\mathbf{Y}_\lambda = \begin{Bmatrix} \mathbf{Y}_{\lambda_{10}} \\[6pt] \mathbf{Y}_{\lambda_{1s}} \\[6pt] \mathbf{Y}_{\lambda_{1c}} \\[6pt] \vdots \\[6pt] \mathbf{Y}_{\lambda_{N_R0}} \\[6pt] \mathbf{Y}_{\lambda_{N_Rs}} \\[6pt] \mathbf{Y}_{\lambda_{N_Rc}} \end{Bmatrix} \qquad (3.67)$$

3.4.4   Summary

The full trim unknown vector is then comprised of the each components unknowns as discussed above.

$$\mathbf{y} = \begin{Bmatrix} \mathbf{y}_{rb} \\ \mathbf{y}_{\lambda} \\ \mathbf{y}_{str} \\ \mathbf{y}_{nac} \end{Bmatrix} \tag{3.68}$$

The full trim equation vector is:

$$\mathbf{Y} = \begin{Bmatrix} \mathbf{Y}_{rb} \\ \mathbf{Y}_{\lambda} \\ \mathbf{Y}_{str} \\ \mathbf{Y}_{nac} \end{Bmatrix} \tag{3.69}$$

To find the trim solution, a nonlinear equation solver is used. This solver uses a modification of the Powell hybrid method to obtain a solution, where a Jacobian matrix is calculated using a forward-difference approximation [94].

3.5   Coordinate Transformations

It often serves to transform beam motion to different coordinates to allow for better comparisons to other analyses. These transformations include the wing mode

transformation, which converts individual wing motion to symmetric and antisymmetric motion, and the multi-blade coordinate transformation, which transforms individual blade motion into sine and cosine harmonic motion around the azimuth. These transformations are generally implemented on the linearized system (discussed later), but can easily transform the state vector of the non-linear model as well.

The mode shapes of the elastic beams generally contain coupled beamwise, chordwise, and torsion bending. The mode is named after the dominant response. Therefore, a beamwise mode will contain mostly beamwise bending but could also contain chordwise and torsion bending.

3.5.1   Wing Mode Transformation

Figure 3.2 shows the beam modes and nomenclature used in this analysis. The motion of the left and right wing are independent in the formulation and therefore symmetric and asymmetric modes are not explicitly formed. The following coordinate transformation is used to transform from the independent wing degrees of freedom to symmetric and asymmetric degrees of freedom.

$$\begin{Bmatrix} x_{1l} \\ x_{1r} \end{Bmatrix} = \begin{bmatrix} 1 & 1 \\ 1 & -1 \end{bmatrix} \begin{Bmatrix} x_{1s} \\ x_{1a} \end{Bmatrix} \tag{3.70}$$

x_{1l} and x_{1r} are the modal deflections of the left and right wing for the first mode and x_{1a} and x_{1s} are the same deflections given in terms of antisymmetric and symmetric modes. Since this conversion matrix contains only constants, there are no additional components for transformations of time derivatives of states. Both the rate and

acceleration states are also converted using Eqn. (3.70).
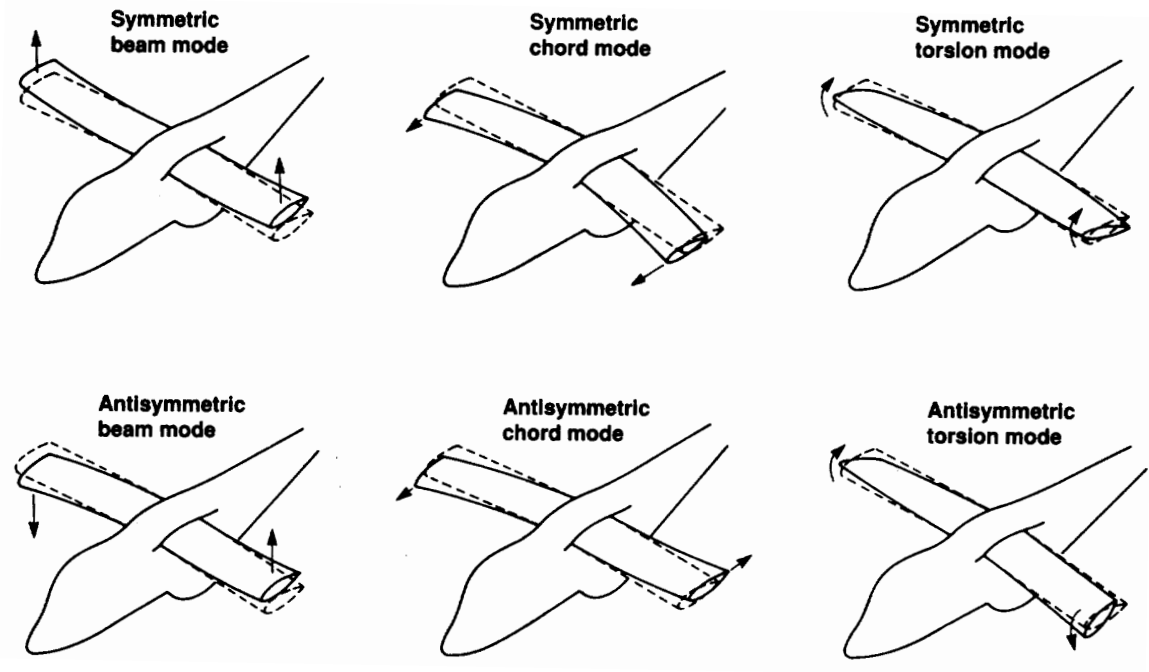
Figure 3.2: Tilt-rotor beam mode shapes [20]

3.5.2 Multi-Blade Coordinate Transformation

The multi-blade coordinate transformation (MCT) converts individual rotor blade motion in the rotating frame to sine and cosine harmonics around the rotor azimuth in the non-rotating frame. Each rotor has its own transformation. It is assumed that blade motion has already been reduced using the modal coordinate transformation to dominant modes. Each mode is independently transformed using the multi-blade coordinate transformation. This transformation allows for analysis using lateral, longitudinal, and collective flapping as opposed to individual blade motion. Let $\left[T^{RF}\right]$ be the matrix transformation that converts the state vector

from the fixed frame to the rotating frame.

$$\mathbf{x}_R = \left[T^{RF} \right] \mathbf{x}_F \tag{3.71}$$

The state vectors time derivative:

$$\dot{\mathbf{x}}_R = \left[\dot{T}^{RF} \right] \mathbf{x}_F + \left[T^{RF} \right] \dot{\mathbf{x}}_F \tag{3.72}$$

Beam equations in first order form contain the displacement and rate state in the state vector, so the transformations above are composed of sets of transformations. For a single rotor, with four blades, the displacement, rate, and acceleration components of the transformation matrices are:

$$\left[T^D \right] = \begin{bmatrix} 1 & \cos \psi & \sin \psi & -1 \\ 1 & -\sin \psi & \cos \psi & 1 \\ 1 & -\cos \psi & -\sin \psi & -1 \\ 1 & \sin \psi & -\cos \psi & 1 \end{bmatrix} \tag{3.73}$$

$$\left[T^R \right] = \begin{bmatrix} 0 & -\Omega \sin \psi & \Omega \cos \psi & 0 \\ 0 & -\Omega \cos \psi & -\Omega \sin \psi & 0 \\ 0 & \Omega \sin \psi & -\Omega \cos \psi & 0 \\ 0 & \Omega \cos \psi & \Omega \sin \psi & 0 \end{bmatrix} \tag{3.74}$$

100

$$[T^A] = \begin{bmatrix} 0 & -\Omega^2 \cos\psi - \dot{\Omega}\cos\psi & -\Omega^2 \sin\psi + \dot{\Omega}\cos\psi & 0 \\ 0 & \Omega^2 \sin\psi - \dot{\Omega}\cos\psi & -\Omega^2 \cos\psi - \dot{\Omega}\sin\psi & 0 \\ 0 & \Omega^2 \cos\psi + \dot{\Omega}\sin\psi & \Omega^2 \sin\psi - \dot{\Omega}\cos\psi & 0 \\ 0 & -\Omega^2 \sin\psi + \dot{\Omega}\cos\psi & \Omega^2 \cos\psi + \dot{\Omega}\sin\psi & 0 \end{bmatrix} \tag{3.75}$$

With the components known, the full transformation matrices may be created

$$\left[T^{RF}\right] = \begin{bmatrix} T^D & T^R \\ 0 & T^D \end{bmatrix} \tag{3.76}$$

$$\left[\dot{T}^{RF}\right] = \begin{bmatrix} T^R & T^A \\ 0 & T^R \end{bmatrix} \tag{3.77}$$

The linear systems (described in later section) will also require $\left[T^{RF}\right]^{-1}$, so this matrix will be created here for consistency. This matrix consists of the components $\left[T^{DI}\right]$ and $\left[T^{RI}\right]$.

$$\left[T^{DI}\right] = \frac{1}{4} \begin{bmatrix} 1 & 1 & 1 & 1 \\ 2\cos\psi & -2\sin\psi & -2\cos\psi & 2\sin\psi \\ 2\sin\psi & 2\cos\psi & -2\sin\psi & -2\cos\psi \\ 1 & 1 & 1 & 1 \end{bmatrix} \tag{3.78}$$

$$[T^{RI}] = \frac{\Omega}{4} \begin{bmatrix} 0 & 0 & 0 & 0 \\ -2\sin\psi & -2\cos\psi & 2\sin\psi & 2\cos\psi \\ 2\cos\psi & -2\sin\psi & -2\cos\psi & 2\sin\psi \\ 0 & 0 & 0 & 0 \end{bmatrix} \tag{3.79}$$

and finally:

$$\left[T^{RF}\right]^{-1} = \begin{bmatrix} T^{DI} & T^{RI} \\ 0 & T^{DI} \end{bmatrix} \tag{3.80}$$

Blade flap and lag modes are generally retained. The formulation given above is only for a single mode, so transformation matrices will need to be stacked and grouped properly for multiple modes to be transformed.

3.6 Linearization

The full aircraft equations of motion are written as a system of nonlinear ODEs in first order form. The coefficients generally have periodic coefficients. Linearization is obtained numerically by expanding the equations of motion in a first order Taylor series approximation. The resulting system of linearized ODEs describes the aircraft small perturbation motion about the trim condition. Although linear models are rigorously valid only for small perturbations, linear models are used to routinely develop aircraft flight control systems and generally represent aircraft behavior well even for moderate to large perturbations from the trim condition. A

discussion of linearization of output equations is also included.

3.6.1 Linearization of Equations of Motion

Linearization is based on a Taylor series expansion of the nonlinear equations of motion about the trim condition, denoted by $()_0$. The equations are written as:

$$0 = \mathbf{f}\left(\dot{\mathbf{x}}, \mathbf{x}, \mathbf{u}, t\right) \tag{3.81}$$

and in trim:

$$0 = \mathbf{f}\left(\dot{\mathbf{x}}_0, \mathbf{x}_0, \mathbf{u}_0, t\right) \tag{3.82}$$

$$
\begin{aligned}
\mathbf{f}\left(\dot{\mathbf{x}}, \mathbf{x}, \mathbf{u}, t\right) = & \mathbf{f}\left(\dot{\mathbf{x}}_0, \mathbf{x}_0, \mathbf{u}_0, t\right) + \frac{\partial \mathbf{f}\left(\dot{\mathbf{x}}_0, \mathbf{x}_0, \mathbf{u}_0, t\right)}{\partial \dot{\mathbf{x}}} \Delta \dot{\mathbf{x}} + \frac{\partial \mathbf{f}\left(\dot{\mathbf{x}}_0, \mathbf{x}_0, \mathbf{u}_0, t\right)}{\partial \mathbf{x}} \Delta \mathbf{x} + \\
& \frac{\partial \mathbf{f}\left(\dot{\mathbf{x}}_0, \mathbf{x}_0, \mathbf{u}_0, t\right)}{\partial \mathbf{u}} \Delta \mathbf{u} + \underbrace{O\left(||\Delta \dot{\mathbf{x}}||^2, ||\Delta \mathbf{x}||^2, ||\Delta \mathbf{u}||^2\right)}_{O(\epsilon^2)}
\end{aligned} \tag{3.83}
$$

where:

$$\Delta \dot{\mathbf{x}} \equiv \dot{\mathbf{x}} - \dot{\mathbf{x}}_0 \tag{3.84}$$

$$\Delta \mathbf{x} \equiv \mathbf{x} - \mathbf{x}_0 \tag{3.85}$$

$$\Delta \mathbf{u} \equiv \mathbf{u} - \mathbf{u}_0 \tag{3.86}$$

The linear model results in the creation of three matrices. The state vector and its time derivative perturbation matrices are $n \times n$, and the control perturbation matrix is $n \times m$, where n is the number of states and m is the number of controls. Perturbations of the time derivative of the state vector produce a mass matrix which is dependent on the current azimuth, $E(\psi)$. Perturbations to the state vector produce a matrix of stability derivatives, $F(\psi)$. Perturbations to the control vector produce control derivatives, $G(\psi)$, such that:

$$[E_{ij}(\psi)] = \frac{\partial f_i(\dot{\mathbf{x}}_0, \mathbf{x}_0, \mathbf{u}_0)}{\partial \dot{x}_j} \tag{3.87}$$

$$[F_{ij}(\psi)] = \frac{\partial f_i(\dot{\mathbf{x}}_0, \mathbf{x}_0, \mathbf{u}_0)}{\partial x_j} \tag{3.88}$$

$$[G_{ij}(\psi)] = \frac{\partial f_i(\dot{\mathbf{x}}_0, \mathbf{x}_0, \mathbf{u}_0)}{\partial u_j} \tag{3.89}$$

A central difference scheme is used for the derivative approximations. These matrices are then converted to standard linear form.

$$[E(\psi)]\dot{\mathbf{x}}(\psi) = [F(\psi)]\mathbf{x}(\psi) + [G(\psi)]\mathbf{u}(\psi) \tag{3.90}$$

or

$$\dot{\mathbf{x}}(\psi) = \underbrace{[E(\psi)]^{-1}[F(\psi)]}_{[A(\psi)]}\mathbf{x}(\psi) + \underbrace{[E(\psi)]^{-1}[G(\psi)]}_{[B(\psi)]}\mathbf{u}(\psi) \tag{3.91}$$

The $A(\psi)$ and $B(\psi)$ matrices are functions of azimuth, are may expanded into a Fourier series containing n harmonics.

$$[A(\psi)] = [A_0] + \sum_{k=1}^{n} \left([A_{kc}]\cos k\psi + [A_{ks}]\sin k\psi\right) \tag{3.92}$$

$$[B(\psi)] = [B_0] + \sum_{k=1}^{n} \left([B_{kc}]\cos k\psi + [B_{ks}]\sin k\psi\right) \tag{3.93}$$

The multi-blade coordinate transformation is applied at this point and the constant terms of the Fourier series above will provide a linear time-invariant representation of aircraft motion. The transformation is as follows using equations developed in Section 3.5.2. Here, $[A_R]$ is the constant component from Eqn. (3.92), and $[B_R]$ is the constant component from Eqn. (3.93), where $()_R$ signifies rotating frame.

$$\dot{\mathbf{x}}_R = [A_R]\,\mathbf{x}_R + [B_R]\,\mathbf{u} \tag{3.94}$$

$$\left[\dot{T}^{RF}\right]\mathbf{x}_F + \left[T^{RF}\right]\dot{\mathbf{x}}_F = [A_R]\left[T^{RF}\right]\mathbf{x}_F + [B_R]\,\mathbf{u} \tag{3.95}$$

$$\dot{\mathbf{x}}_F = \underbrace{\left[T^{RF}\right]^{-1}\left([A_R]\left[T^{RF}\right] - \left[\dot{T}^{RF}\right]\right)}_{[A_F]}\mathbf{x}_F + \underbrace{\left[T^{RF}\right]^{-1}[B_R]}_{[B_F]}\mathbf{u}$$

$$\tag{3.96}$$

3.6.2   Linearization of Outputs

Much like the creation of the state matrices, a central difference scheme is used to linearize the structural measurements. This produces matrices due to perturbations in the time derivative of the state vector ($\left[\dot{C}(\psi)\right]$), the state vector itself

$([C(\psi)])$, and the control vector $([D(\psi)])$.

The output matrices may also be expanded in Fourier series, as the state matrices were in Eqns. (3.92) and (3.93). The constant component is retained for a LTI system and a multi-blade coordinate transformation is applied to these constant matrices.

The standard state space output form is:

$$\mathbf{y} = [C]\,\mathbf{x} + [D]\,\mathbf{u} \tag{3.97}$$

The matrices must be converted to the fixed frame and this standard form using the MCT. As in the state matrix calculations, $\left[\dot{C}_R\right]$ $[C_R]$, and $[D_R]$ represents the constant component of the Fourier transform of the output matrices.

$$\mathbf{y} = \left[\dot{C}_R\right]\dot{\mathbf{x}}_R + [C_R]\,\mathbf{x}_R + [D_R]\,\mathbf{u} \tag{3.98}$$

$$\mathbf{y} = \left[\dot{C}_R\right]\left[\dot{T}^{RF}\right]\mathbf{x}_F + \left[\dot{C}_R\right]\left[T^{RF}\right]\dot{\mathbf{x}}_F + [C_R]\left[T^{RF}\right]\mathbf{x}_F + [D_R]\,\mathbf{u} \tag{3.99}$$

$$\mathbf{y} = \left[\dot{C}_R\right]\left[\dot{T}^{RF}\right]\mathbf{x}_F + \left[\dot{C}_R\right]\left[T^{RF}\right]\left([A_F]\,\mathbf{x}_F + [B_F]\,\mathbf{u}\right) + [C_R]\left[T^{RF}\right]\mathbf{x}_F + [D_R]\,\mathbf{u}$$

$$\tag{3.100}$$

$$\mathbf{y} = \underbrace{\left(\left[\dot{C}_R\right]\left[\dot{T}^{RF}\right] + \left[\dot{C}_R\right]\left[T^{RF}\right][A_F] + [C_R]\left[T^{RF}\right]\right)}_{[C_F]}\mathbf{x}_F + \tag{3.101}$$

$$\underbrace{\left([D_R] + \left[\dot{C}_R\right]\left[T^{RF}\right][B_F]\right)}_{[D_F]}\mathbf{u}$$

3.7   Comparisons with Multi-Body Solutions

A full multi-body formulation is generally characterized by:

106

1. *Numerical kinematics* — Position vectors, velocities, and accelerations are all built numerically with no algebraic manipulations, ordering schemes, or limitations on magnitude of displacements and rotations. Furthermore, the kinematic formulation can be extended in an automated way to any number of bodies in a chain.

2. *Enforcement of connectivity through explicit equations of constraint* — The equations are generally algebraic, resulting in an overall model that is formulated as a system of Differential Algebraic Equations (DAEs) rather than a system of Ordinary Differential Equations (ODEs).

The present model implements numerical kinematics, but does not include explicit equations of constraint. The bodies are rigidly constrained together, and motion only enters the system through structural motion (flexible or rigid-body), which is governed by differential equations, preserving the ODE structure.

The lack of explicit constraint equations makes the model less flexible than full multi-body formulations. The topology is limited to tree-like arrangements without loops. Since motion is modeled through structural flexibility, mode shapes are required and can be determined within the software, or read in as inputs. In determining mode shapes, certain nodes are constrained. The location of the constrained node along the beam element must also function as a connection point between bodies. Connectivity that cannot be described by adding or removing nodal degrees of freedom requires changes to the software implementation. Moreover, the formulation is less suitable for software interfaces in which users assemble the model from

point-and-click selections of element libraries.

On the other hand, the model naturally results in a system of ODEs, modal coordinate transformations are easily implemented, and there is no need to solve DAE systems (typically of index 3 or higher) or use techniques to condense out algebraic equations of constraints or convert them to ODEs. If necessary, equations of constraints could simply be added to the present formulation through the use of Lagrange multipliers and suitable DAE solvers. All structural and inertial couplings are rigorously modeled. The aerodynamic couplings need to be analyzed on a configuration-by-configuration basis, and may require additional configuration-specific modeling, but this is also true for full multi-body formulations. For example, rotor to wing interference effects are added with knowledge of the wing location with respect to the rotor. Because the present formulation allows for an arbitrary number of rotors of arbitrary position and orientation, and any number of flexible aerodynamic surfaces located anywhere on the aircraft, it is still sufficiently general to formulate flight dynamic models for all configurations envisioned for future rotorcraft with little or no recoding.

The model is formulated as a series of nested loops (from outermost to innermost: over rotors, blades or wings, finite elements, and Gauss points within elements), uses modal coordinate transformations, and contains no coupled algebraic equations. With the exception of the blade inertia load calculations (because of the centrifugal force), all loops can be traversed in any order, and can be easily parallelized. As a result, real-time execution is achievable on off-the-shelf workstations with no approximations for models of realistic complexity. Software granularity is

also sufficient for CUDA/GPU-based real time implementations.

Details of the baseline blade equations of motion can be found in Ref. 84, and serve as a starting point for the discussion regarding the wing equations. The equations of motion can be broken down into three key components; inertial, structural, and aerodynamic loads.

3.8   Free Flight Response

Starting from a set of consistent initial conditions (i.e. Eqn. (2.142) is met), the non-linear equations of motion can be integrated in time to form a free flight response of the aircraft. A trimmed solution is used as the set of initial conditions and pilot inputs are used as inputs to the system.

3.8.1   Initial Conditions

The trim solution must be converted to the system states as given in Eqn. (3.7) along with the state time derivatives. The rigid-body components of the trimmed initial condition are given in Section 3.4.1. The conversion to flexible beam states from trim states is given in Section 3.4.2. Finally, inflow states are obtained from trim states as described in Section 3.4.3.

3.8.2   Integration

Once the initial condition is set, the equations can be integrated. Since the trim condition provides a feasible solution to the equations of motion, the trim

starting point should be valid for the ODEs as well, and the convergence criteria should be met at the initial time point. The solver uses backwards differentiation formulas of variable orders to solve the equations of motion for a given time span [95]. The solver can be variable or fixed-step in time, though the variable step solution is solved faster. The states and their time derivatives are provided at each time step as outputs.

Pilot controls do not appear in Eqn. (2.142), but they are still present and variable at each time step. Controls alter blade pitch or other aerodynamic surfaces on the aircraft, and a new equilibrium point must be determined if they are changed. For example, blade pitch changes will alter the aerodynamic loads over rotor blades. The corresponding beam equation of motion will obtain a new equilibrium point where these loads are countered by the other forcing loads for the beam. These change will also propagate to the forcing at the CG which will change the dynamic response at the CG.

3.9   Chapter Summary

The linking of the various components of an aircraft model using a tree array has been shown. Modal analysis significantly reduces the system degrees of freedom and provides a representation for modal deflections of the entire aircraft structure. Finally, trim and linearization of the aircraft model was discussed.

Chapter 4: Validation

An important first step was to validate the model against flight data for a known configuration to test its fidelity. The model was validated against the XV-15 before being applied to the LCTR.

4.1   Validation with XV-15

The XV-15 was chosen because simulation input data, such as aerodynamic tables, and flight responses that can be used for validation were readily available in the public domain. XV-15 input data were obtained from the GTRSIM manual and sample code inputs. Blade structural data was not a part of the GTRSIM simulations and was derived from a UH-60 blade input block.

4.1.1   Model Description

The model includes rigid wings and nacelles. Only the first structural mode was retained for the blade, which was a rigid body flapping mode. Since the first blade mode contained only rigid deflections, blade structure contributions due to flexibility do not affect the model. The first order model contains 27 states. There are 9 rigid body aircraft states, and 3 inflow states per rotor. Since the XV-15

111

has three blades, flapping is reduced to coning and first harmonic sine and cosine components, giving 6 states per rotor. Formulation of the aircraft state vector is described in Sec. 2.8.

To trim the aircraft, there are a total of 28 unknows. There are 8 aircraft rigid-body trim unknowns. Each rotor has 3 inflow trim unknowns. Rotor blade flapping is allowed a constant component and three harmonics of sine and cosine flapping, giving 7 unknowns per rotor. Trim unknowns and equations are described in Sec. 3.4.

Airframe aerodynamics, including impingement of the downwash on the wing surfaces, and inflow effects on the elevator and rudders, are modeled using the flight test-derived data tables in Ref. 11.

4.1.2   Hover

Figure 4.1 shows a frequency response comparison of the XV-15 roll rate to lateral stick inputs in hover. The curve labeled "HeliUM" represents the model developed in the present study. The curve marked "ID Model" comes from a state space model derived from flight test data using system identification. The "GTRSIM" model represents a state space model derived from the GTRSIM software. Stability and control derivatives for both comparison curves can be found in Ref. 96. "Flight Data" curves are derived from frequency sweeps performed during test flights. The roll response is measured in rad/sec, while the input is degrees of aileron deflection. Control surface deflections are downstream of the stability and control augmenta-
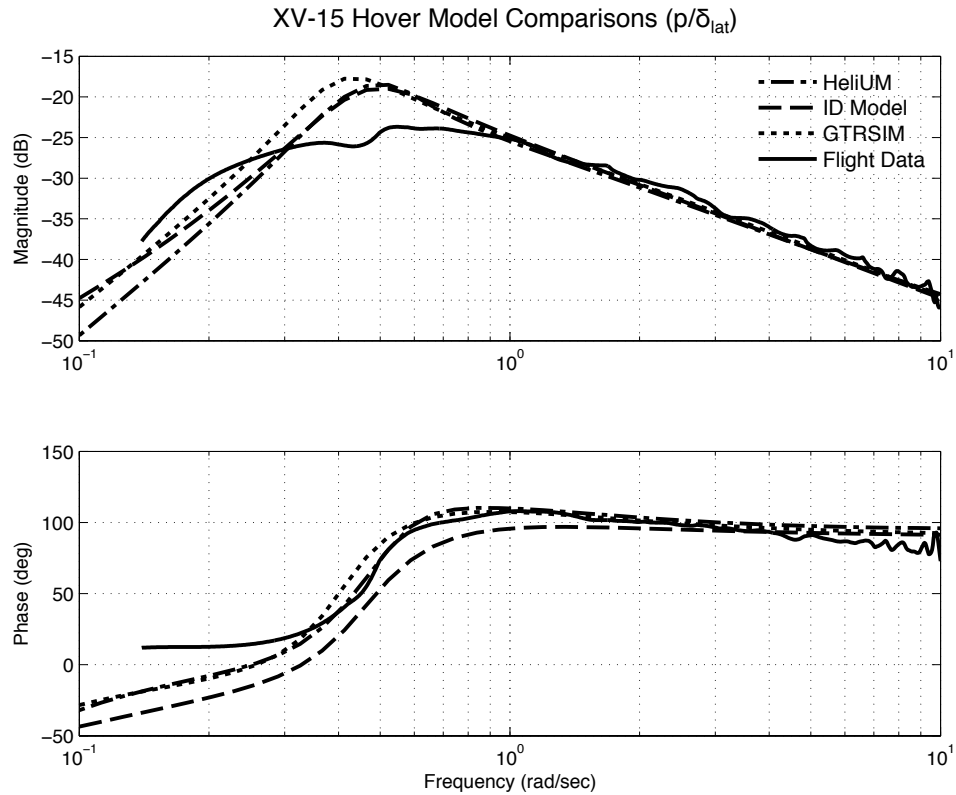
Figure 4.1: XV-15 hover roll rate response to lateral stick inputs.

tion systems and are geared with swashplate inputs. They are used to measure

the input for the bare airframe responses. The roll response curve is dominated by

the low frequency lateral phugoid mode. Overall, there is good agreement between

the HeliUM curve and the GTRSIM and ID models. While the unstable phugoid

frequency agrees well with flight test data, there is a 5 dB over prediction of the

roll response by the models as compared to flight data. This could be attributed to

poor coherence at the phugoid frequency for the flight data.

The hover yaw rate response is shown in Fig. 4.2. Here, the units are rad/sec

of yaw rate for degrees of rudder deflection input. Rudder inputs are is geared with

antisymmetric longitudinal swashplate inputs. The yaw response is essentially a first
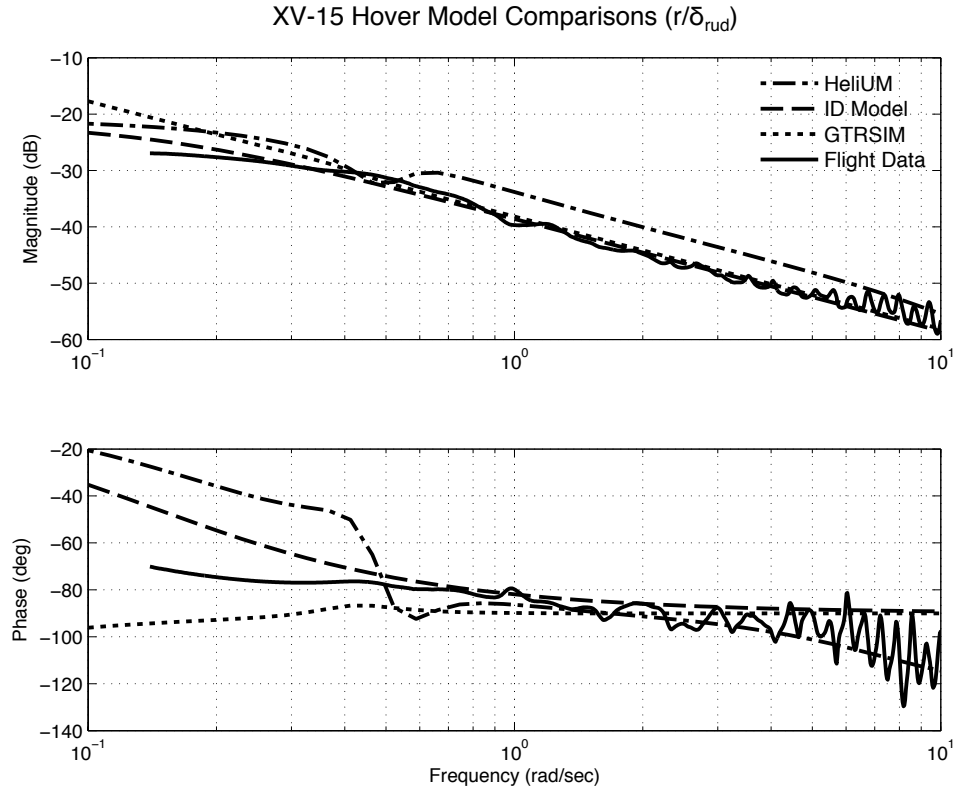
Figure 4.2: XV-15 hover yaw rate response to pedal inputs.

order system that has a pole at low frequency, giving a constant -20 db/dec slope at the frequencies shown in the figure. The offset in the HeliUM magnitude response above 0.6 rad/sec can be attributed to the modeling of the hub. The XV-15 has a gimbaled hub, while the present model has an articulated hub, with the gimbal behavior approximated through flapping springs. Yaw behavior is dependent on longitudinal flapping, so small discrepancies in modeling could have larger impacts on the dynamic response of the aircraft.

Figure 4.3 shows the pitch rate response to longitudinal inputs. Here the curve marked "TF Model" comes from low order transfer functions found in Ref. 18. Flight data were not available for the pitch or heave responses, but the transfer function
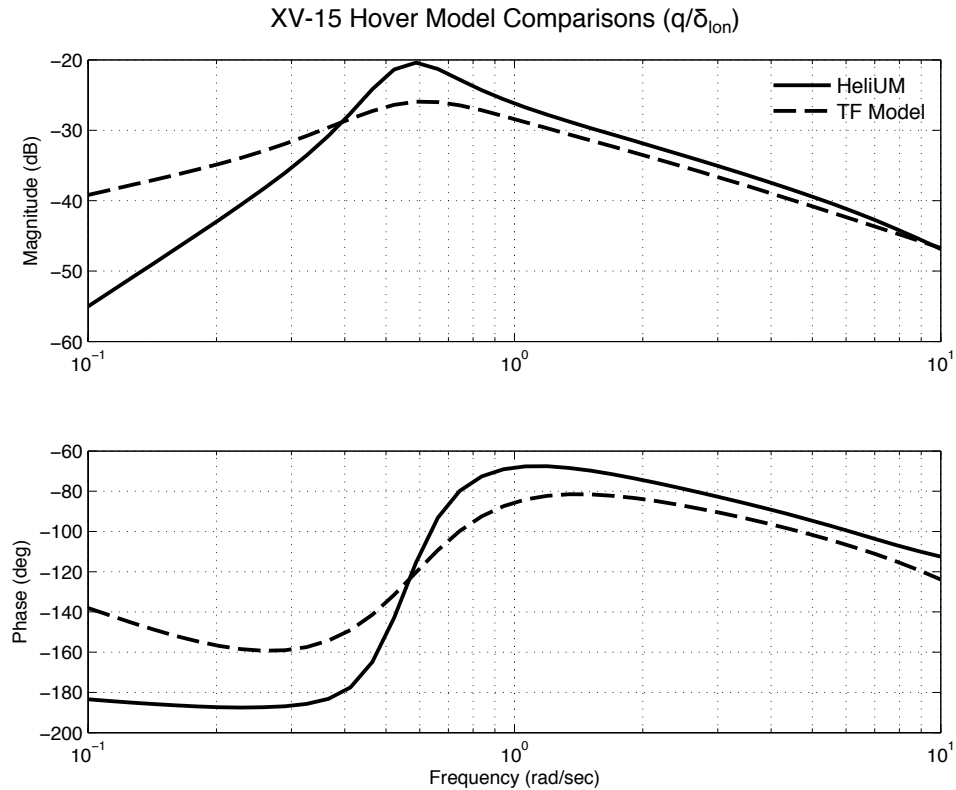
Figure 4.3: XV-15 hover pitch rate response to longitudinal stick inputs.

models were fit to flight data. The pitch response is measured in rad/sec and the input is degrees of elevator deflection, which are geared with symmetric longitudinal cyclic swashplate commands. Much like the roll response, this curve is dominated by the low frequency phugoid pole. There is a difference in the low frequency slope of the curves; the TF Model predicts a 20 dB/dec slope, while the HeliUM model predicts a 40 dB/dec slope. This difference is again attributed to the modeling of the hub. The pitch response of the rotorcraft is a product of longitudinal flapping of each rotor and variations in hub type should produce different results. This is not seen in the roll response, Fig. 4.1 or heave repsonse, Fig. 4.4, because these responses come from collective and rotor coning.

Figure 4.4 shows the heave response to collective stick inputs. The HeliUM curves match well with the low order transfer function model. The slight difference in magnitude plots represents an error of less than 5%. The portions of the magnitude and phase curves between 1 and 10 rad/sec show a consistent heave response to commanded inputs at these frequencies. The transfer function model has a flat magnitude response because the effects of dynamic inflow are not included, although they are present in the HeliUM model.
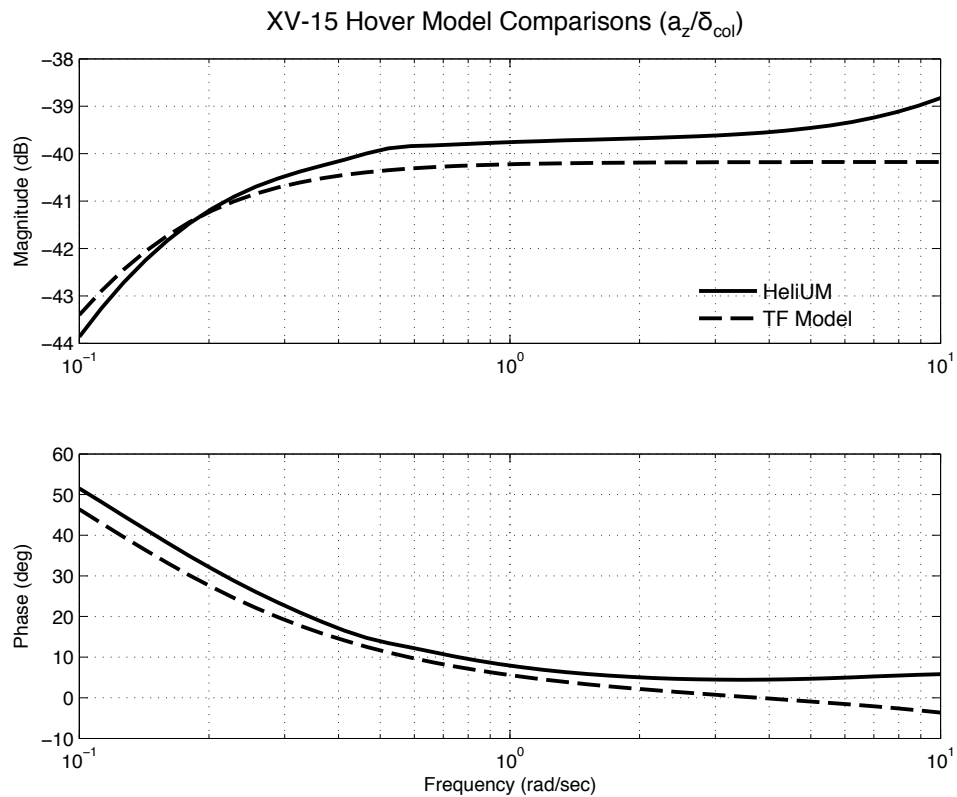
Figure 4.4: XV-15 hover heave response to collective stick inputs.

4.1.3 Cruise

In cruise mode, the XV-15 behaves much like a fixed wing aircraft. Through transition to cruise, rotor symmetric and antisymmetric lateral cyclic controls are reduced based on nacelle angle. At the cruise nacelle angle, the pilot lacks lateral cyclic control, and controls the roll of the aircraft through the ailerons. The cruise speed for validation is 180 knots.

XV-15 Cruise Model Comparisons (p/δ_{lat})
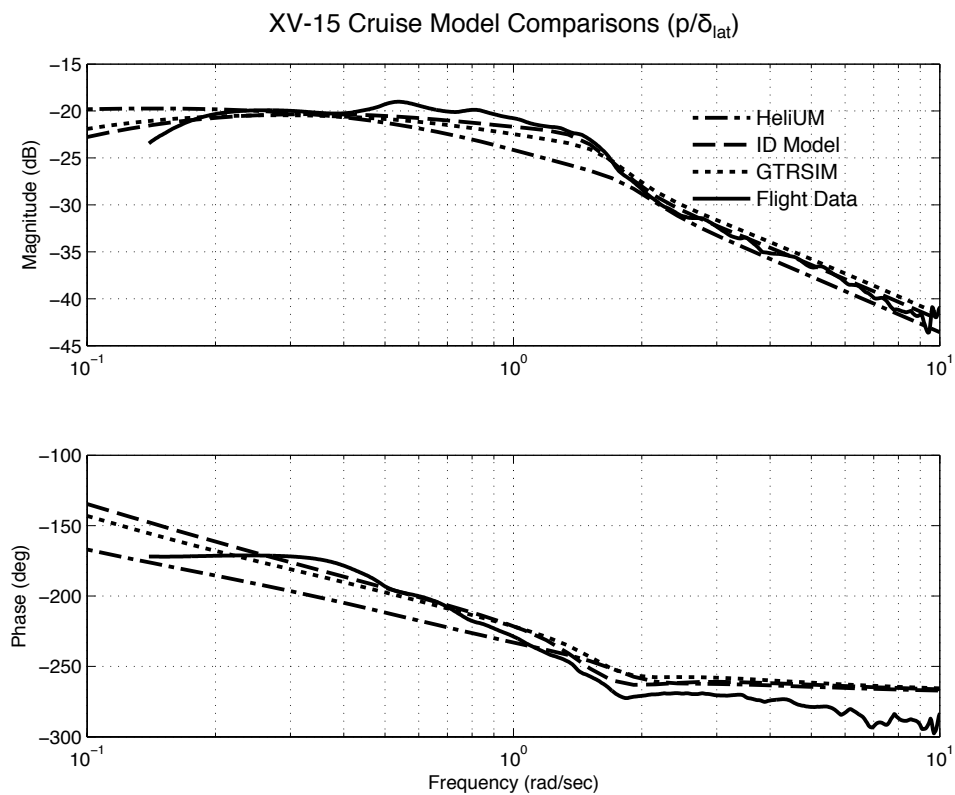
Figure 4.5: XV-15 cruise roll rate response to lateral stick inputs.

Figure 4.5 shows the roll rate response to lateral stick commands. The units are the same as the hover configuration. The roll response is dominated by the Dutch roll mode at around 1.5 rad/sec, with a corresponding magnitude drop and phase

decrease. The HeliUM model shows a slightly more damped Dutch roll oscillation, but the overall response matches well.

The yaw response, Fig. 4.6, shows the yaw rate response in rad/sec to measured rudder inputs in degrees. The lightly damped zero at 0.45 rad/sec is followed by the Dutch roll peak, again at around 1.5 rad/sec. The damping of the zero for the HeliUM model is predicted slightly unstable while the other models predict a stable zero. Overall the curve fits well with the other models and flight data.
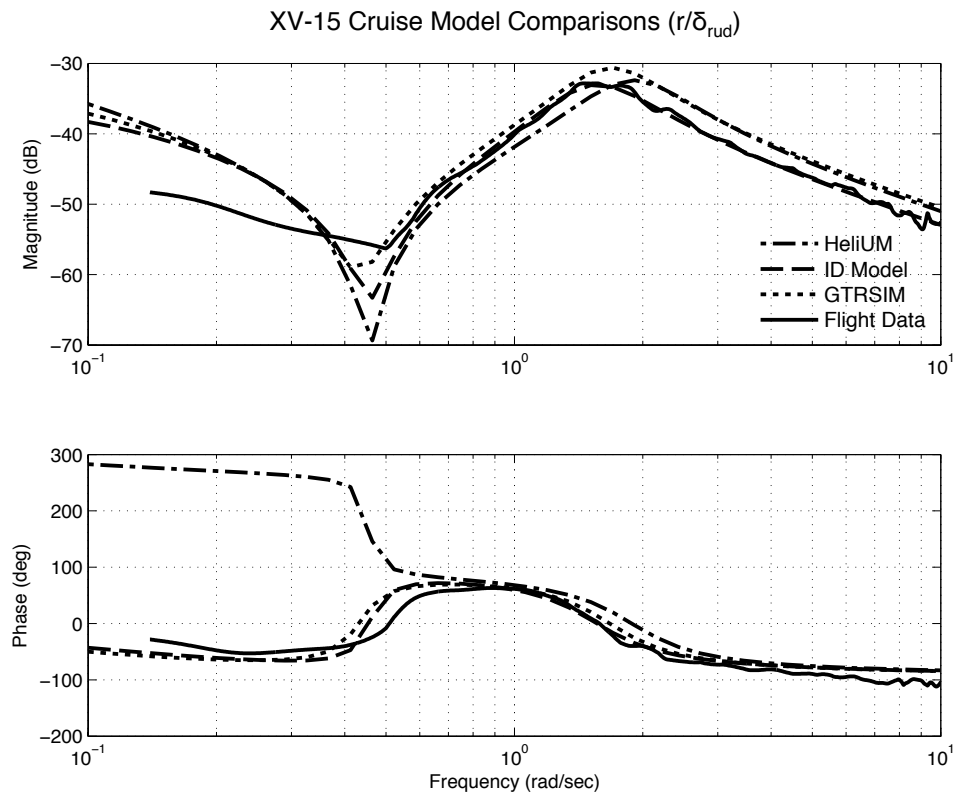
Figure 4.6: XV-15 cruise yaw rate response to pedal inputs.

The pitch response in Fig. 4.7 shows the pitch response in rad/sec to measured elevator inputs in degrees. The transfer function model is a low order fit of the physical response and only includes the lightly damped short period mode near 2

118

rad/sec. The short period mode occurs at a slightly lower frequency in the transfer function model than it does in the HeliUM case. The gain and phase offset at low frequency can be attributed to phugoid dynamics which are not included in the low order transfer function model.
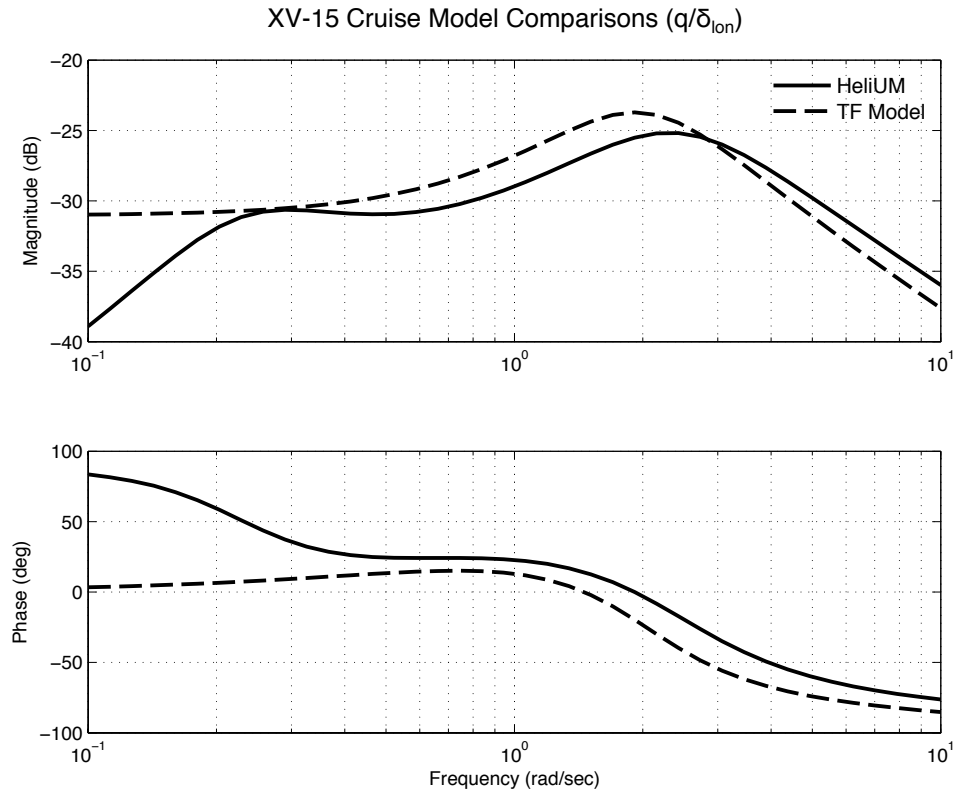
Figure 4.7: XV-15 cruise pitch rate response to longitudinal stick inputs.

Overall, there is good agreement between the XV-15 HeliUM model, prior models, and flight data, validating the modeling approach taken. The hover validation affirms that rotor dynamics have the appropriate effect on the system response, while the cruise validation affirms correct airframe aerodynamics.

119

4.2 LCTR Dynamics

The LCTR dynamics are next validated against CAMRAD. These models are then reduced to include only lateral/directional and wing bending states.

4.2.1 Model Description

The models contained rotor, inflow, and rigid body states for a total of 59 states. As with the XV-15 there are 9 rigid-body aircraft states, and 3 inflow states per rotor. In the LCTR analysis, blades are allowed flap and lag displacements. The LCTR also has 4 blades, meaning a multi-blade coordinate transformation results in a constant, sine and cosine first harmonic, and differential flap and lag displacements, giving 16 states per rotor. The HeliUM models also contain wing bending states. Each retains three modes, giving 6 flexibility states per wing.

In trim there are a total of 48 unknowns. The first set of unknowns are 8 rigid-body unknowns. Each rotor inflow has 3 unknowns, for a total of 6 inflow unknowns. Each rotor has 7 unknowns per retained blade mode, including a constant deflection (coning, or constant lag angle) plus three harmonics of sine and cosine, giving a total of 28 rotor unknowns. The wings are allowed a constant deflection for each mode, giving 3 unknowns per wing and 6 unknowns total.

Downwash impingement on the wing is modeled. The wing is approximately 1/3 R below the main rotor and is assumed to be immersed in the wake of the rotor. The components of the inflow velocity are obtained from the dynamic inflow coefficients of the rotor at the 270 deg azimuth position, approximately the azimuth

position of blade passage over the wing. These inflow velocities are then augmented by the nacelle angle to find the local velocity at the wing section.

The same wing airfoil data is used for the LCTR as was available for the XV-15. This airfoil data includes aerodynamic coefficients for very large angles of attack as are needed by a wing experiencing downwash in hover. The XV-15 aerodynamic coefficient look up tables are functions of angle of attack, mach number, nacelle angle, and flap setting. For the LCTR hover case, the portions of the look up tables with the nacelle in the vertical position and flaps retracted were used. The total download as a fraction of gross weight in hover was similar to that of the XV-15 in hover. Aerodynamic contributions from the empennage are neglected in hover.

Since, the LCTR model involves flexible wings, modeling in the multi-body formulation becomes important. Figure 4.8 shows the multi-body LCTR setup, including coordinate systems and displacement vectors between bodies from the CG to the one rotor hub. A similar set of transformations and vectors exists for the other rotor. Figure 4.9 shows the effects of wing flexibility to the displacements and coordinate systems.
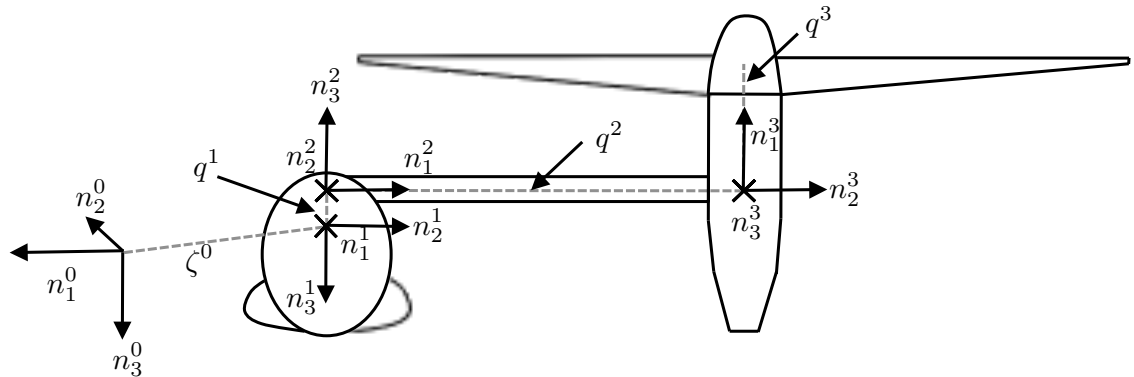
Figure 4.8: LCTR multi-body setup
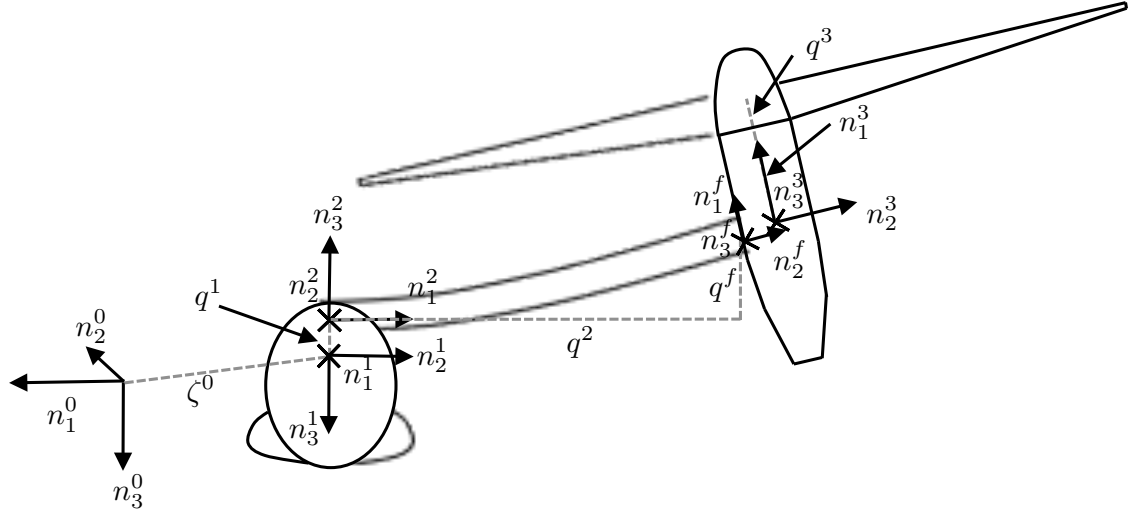
Figure 4.9: Flexed LCTR multi-body formulation

The nacelles are added onto the deformed wing coordinate system, and the rotor system is added to the deformed (rotated) nacelles.

4.2.2 Full Order Validation

Full order LCTR models derived from HeliUM are compared to full order rigid-body CAMRAD models. The majority of the inputs for HeliUM come directly from the CAMRAD model. The HeliUM model contains two rotor modes; flap and lag.

Wing flexibility was also included in the validation (Figs. 4.12-4.15) as a separate curve since the CAMRAD linear model did not include wing flexibility. The wing structural frequencies were derived to match those of Ref. 2, and structural damping was set to 6 %. Wing beamwise bending stiffness was modified until the antisymmetric beamwise bending mode occurred at approximately 16.5 rad/sec. Likewise, chordwise stiffness was modified until a frequency of 14.5 rad/sec was reached for the antisymmetric chordwise bending mode. Finally, torsion stiffness

was also changed so that torsion modes matched with the nacelles held fixed. The pylon is centered vertically along the elastic axis so the chordwise and torsion modes are fairly decoupled. Mode shapes for the LCTR are shown in Figs. 4.10 and 4.11. Torsion modes are not shown, but couple pitch motion to wing torsion motion. Each mode has a symmetric and antisymmetric component.The wing modes show up as second order poles and are accompanied by decreases in phase. The validation results look at both the longitudinal as well as lateral/direction axes.
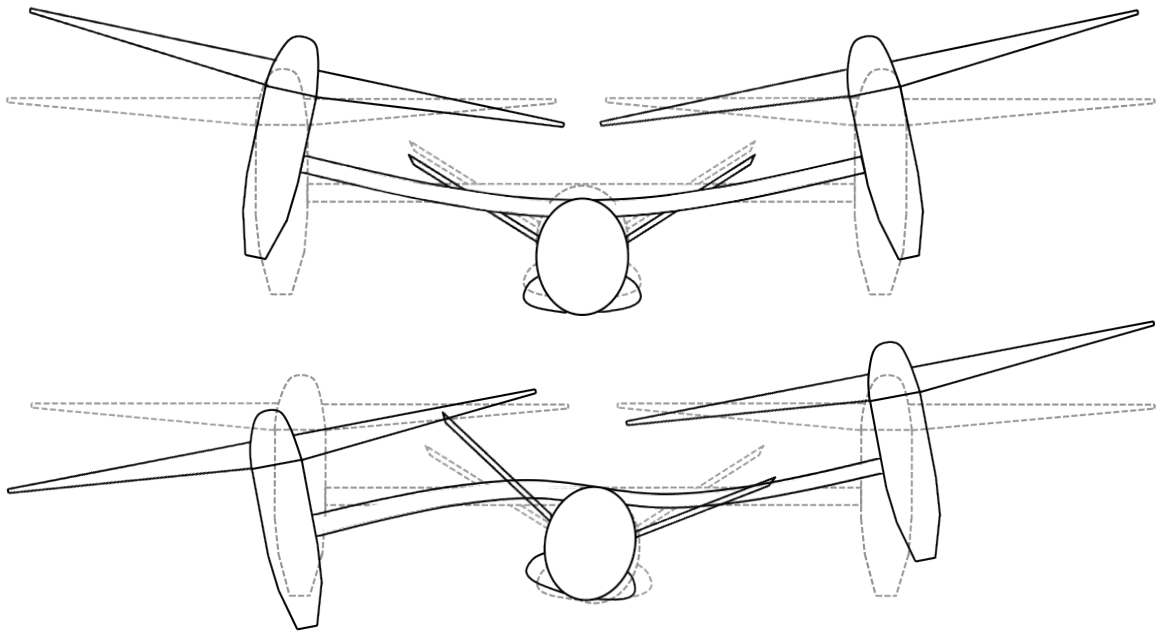
Figure 4.10: LCTR symmetric and antisymmetric beamwise bending mode shapes

The LCTR modal frequencies could also be estimated if the XV-15 structural modes are known. Froude scaling suggests that the structural frequencies of the aircraft will reduce with the square root of the vehicle size ratio [97]. The LCTR has a rotor radius of 32.5 feet, and the XV-15 rotor had a 12.5 foot radius, giving a ratio of 0.38. The first symmetric structural mode, derived from XV-15 flight test
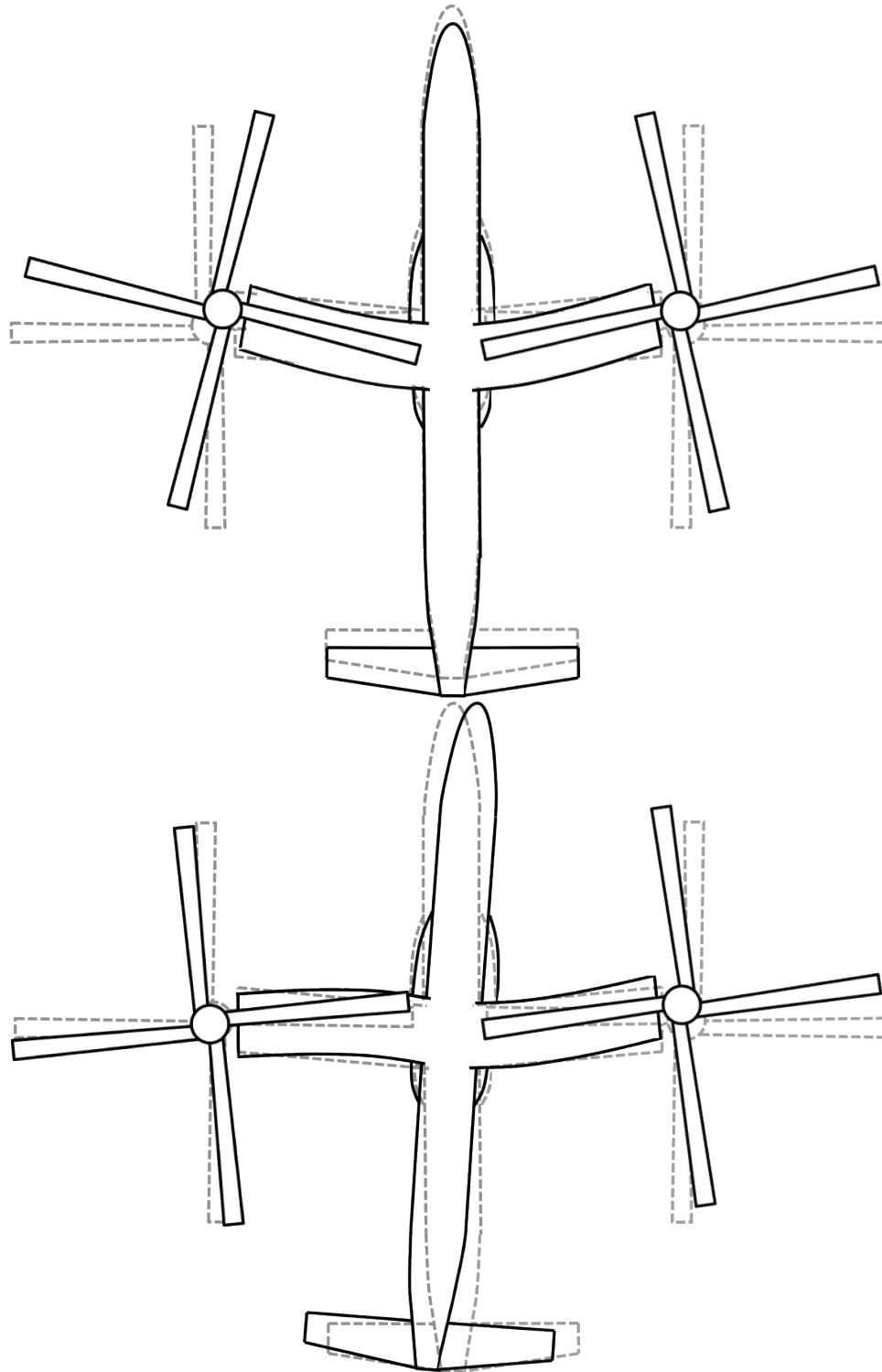
Figure 4.11: LCTR symmetric and antisymmetric chordwise bending mode shapes

results, occurs at 20.7 rad/sec, giving an estimate of 12.8 rad/sec for the LCTR. The first symmetric coupled rigid-body/wing mode from the model occurs at 9.9 rad/sec. Using Froude scaling alone would suggest that including the structural frequencies of the LCTR would be important for flight controls applications. The scaling isn't exact, but provides a good rule of thumb estimation for mode scaling.

Figures 4.12 through 4.15 compare the CAMRAD and HeliUM models. Overall there is good agreement in all axes for the rigid wing HeliUM and the CAMRAD models up to about 30 rad/sec. The rigid wing plots (*HeliUM Rigid Wing*) don't include any structural flexibility, while the flex wing plots (*HeliUM Flex Wing*)have a rigid fuselage with flexible wings. The output magnitudes are expressed in deg/sec or ft/sec. Inputs are inches of stick deflection. Rotor modes also match well. The first flap mode from HeliUM is at 1.44/rev and for CAMRAD is at 1.43/rev. The models all match well at low frequency and diverge at the frequency of the wing mode, as expected, because flexible wing modes are highly coupled to fuselage states.

The roll response, Fig. 4.12, is dominated by the lateral phugoid at low frequency. When comparing the CAMRAD and rigid wing HeliUM curves, there are offsets only at the higher frequencies corresponding to rotor dynamics. The large peak in the magnitude in the flexible wing response around 16 rad/sec is the wing antisymmetric beam mode. It will be shown that this mode corresponds to the anti-symmetric beamwise bending mode mentioned earlier. At frequencies above the wing mode, the flexible wing HeliUM curve has characteristics similar to the other curves.

The yaw response, Fig. 4.13, is similar to that of the XV-15, Fig. 4.2, and
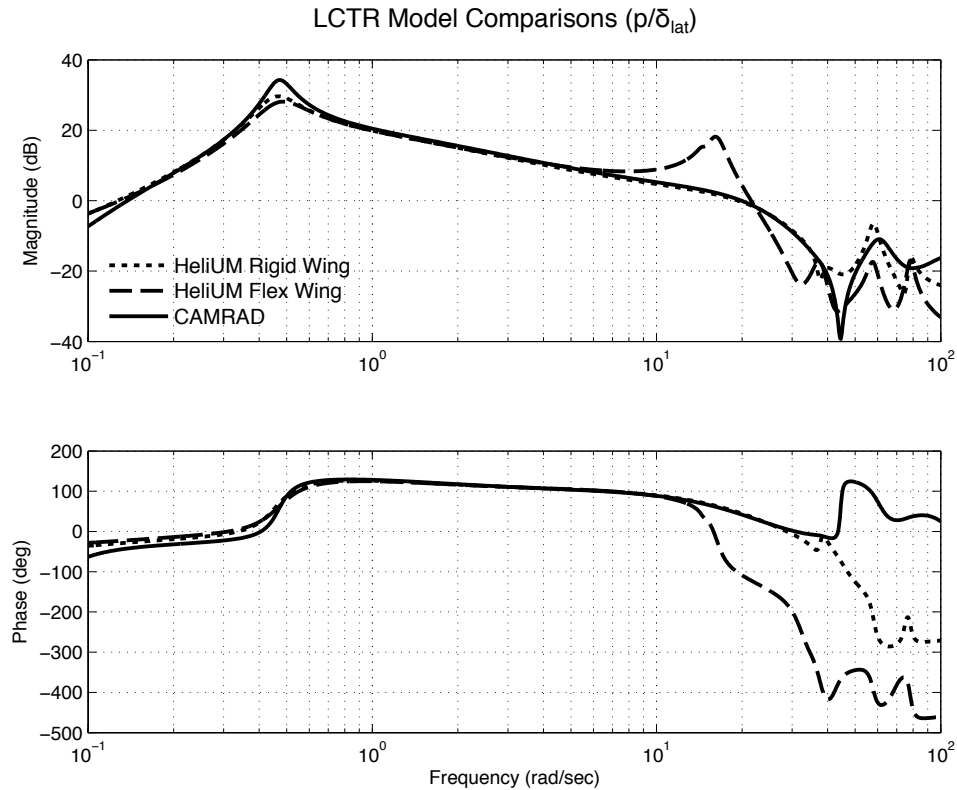
Figure 4.12: LCTR hover roll rate response to lateral stick inputs.

shows a fairly constant -20 dB/dec slope in the magnitude plot. The low frequency first order yaw mode causes the slope change in the magnitude plot and associated 90 deg phase decrease. As with the roll case, and with the rest of the plots, rotor dynamics start to have a dominant effect at around 30 rad/sec. The wing structural peak, at around 14 rad/sec, is associated with the antisymmetric chordwise wing bending mode as indicated earlier.

The HeliUM model was not able to capture the low frequency XV-15 pitch response well (Fig. 4.3), and this was attributed to the rotor hub modeling. The LCTR has a hingeless rotor system which forces the blades to behave as cantilevered beams. HeliUM models this type of blade boundary condition and the response
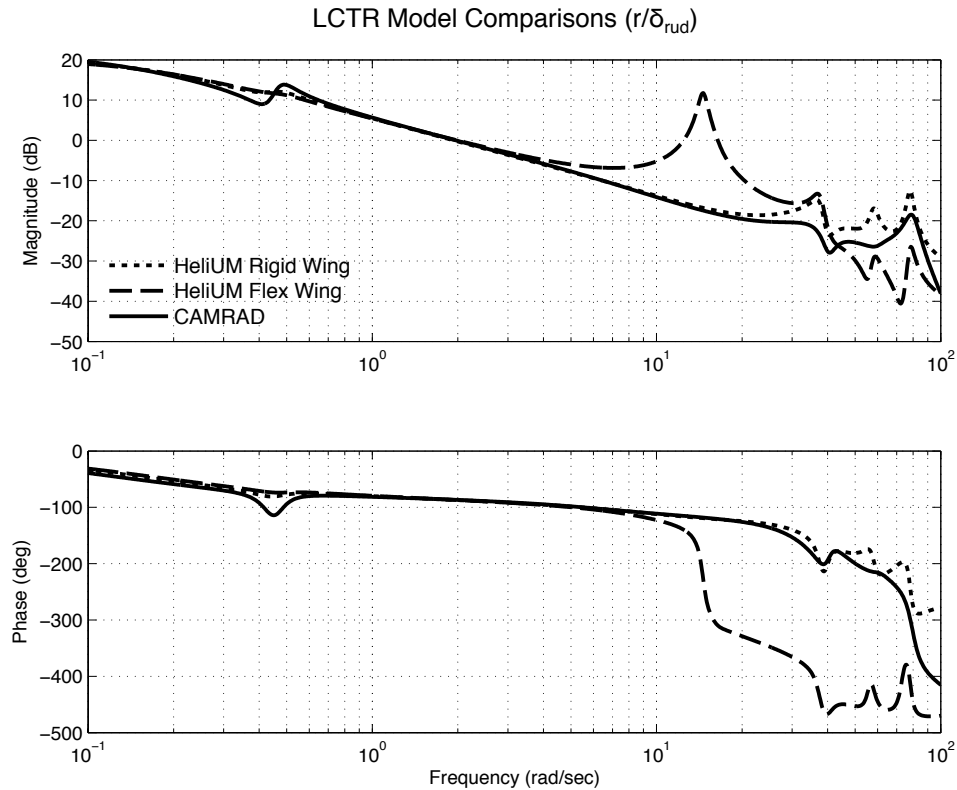
Figure 4.13: LCTR hover yaw rate response to pedal inputs.

now matches well with CAMRAD results (Fig. 4.14). The low frequency phugoid mode frequency and damping is matched almost exactly between the models. The HeliUM rigid wing model matches the CAMRAD model almost exactly over the entire frequency range shown. The wing flexibility contribution here comes from coupled symmetric chordwise beam bending and torsional displacements. This mode is the symmetric counterpart to the wing mode in the yaw response.

The vertical velocity response of the rigid body HeliUM case matches well with the CAMRAD plot, and is shown in Fig. 4.15. The wing bending mode excited here is a symmetric beamwise bending mode, the counterpart to the antisymmetric mode in the roll response. The rigid wing HeliUM model matches CAMRAD almost
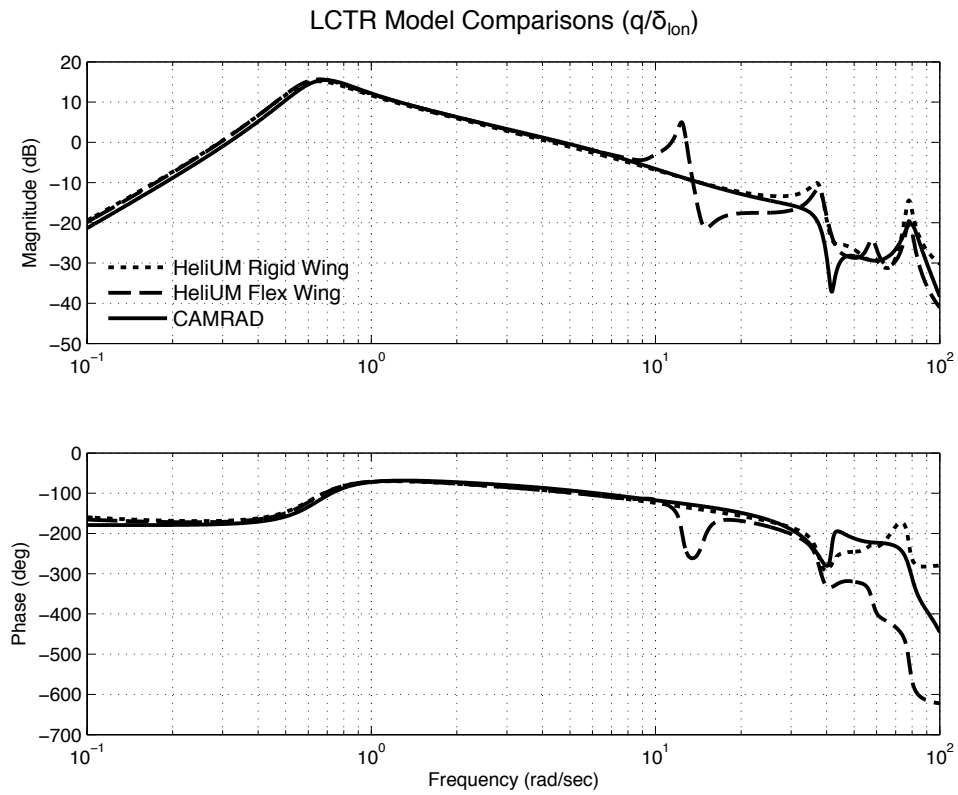
Figure 4.14: LCTR hover pitch rate response to longitudinal stick inputs.

exactly up to 100 rad/sec.
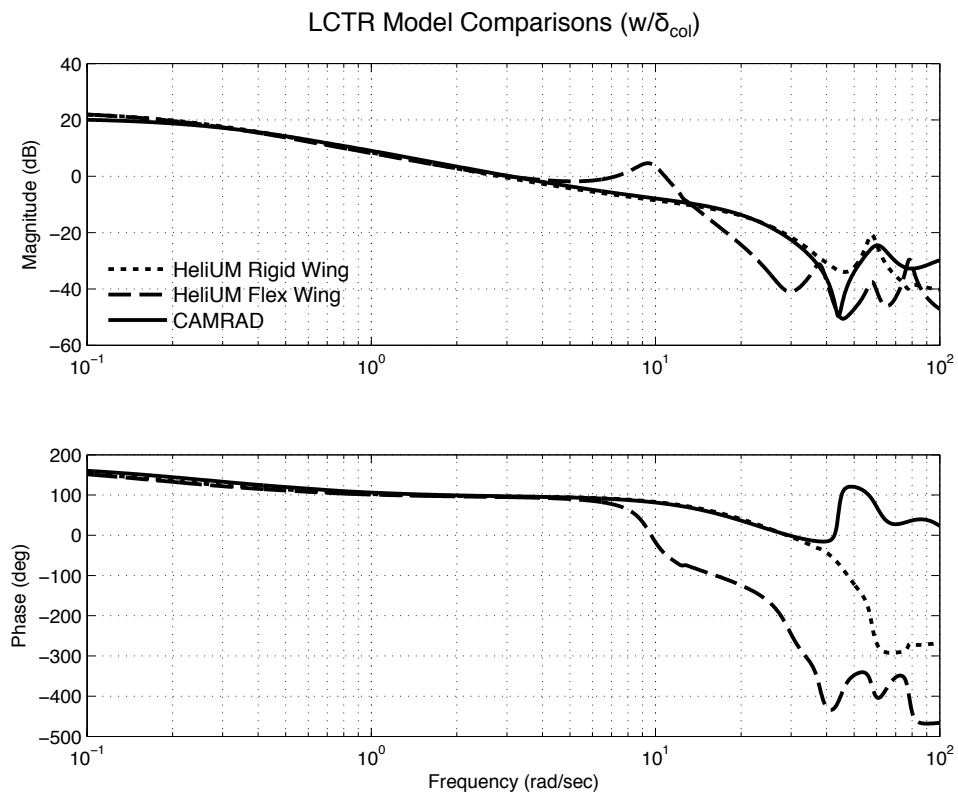
Figure 4.15: LCTR hover vertical velocity to collective inputs

4.2.3 Reduced Order Models

Reduced order models offer the ability to evaluate the overall aircraft response in terms of conventional stability and control derivatives. In the reduced order models shown, only lateral/directional rigid body states are retained along with the relevant wing structural modes if wing flexibility is included. All the models used come from HeliUM. Table 4.1 summarizes the states kept and the nomenclature used for the reduced models. Longitudinal rigid body, rotor, inflow, and non-relevant wing states are reduced out using a quasi-static reduction. The *Rigid Wing* model contains 47 states, while the *Lat/Dir Rigid Wing* model contains only 5 total states (including yaw angle, ψ) . The *Flex Wing* model contains 55 states, all the states of the Rigid Wing model and an additional 8 wing structural states. The *Lat/Dir Flex Wing* model contains 9 states, including 5 rigid body states and 4 states associated with two antisymmetric wing bending modes. The lateral axis excites, almost exclusively, the antisymmetric beamwise bending mode, while the directional axis excites the antisymmetric chordwise/torsion mode. Figures 4.16 and 4.17 show reduced order models. The full order curves are retained for comparison.

Table 4.1: Reduced order model nomenclature

	Longitudinal Rigid Body	Lateral/Directional Rigid Body	Inflow	Rotor	Symmetric Structural	Antisymmetric Structural
Rigid Wing	√	√	√	√		
Flex Wing	√	√	√	√	√	√
Lat/Dir Rigid Wing		√				
Lat/Dir Flex Wing		√				√

The Lat/Dir Rigid Wing roll response matches well with the full order Rigid Wing model, which also includes rotor dynamics, at low frequency, meaning the system is well decoupled from longitudinal dynamics, as expected for a tiltrotor in hover. Divergence occurs in the magnitude plot around 8 rad/sec, well within the frequency range of interest for control systems design. Rotor modes are important even at this low frequency and using a reduced order model might lead to an inaccurate stability and handling qualities analysis. The Lat/Dir Rigid Wing phase response diverges from the full order response at higher frequency than the magnitude plot. The wing mode excited in the Lat/Dir Flex Wing case is the anti-symmetric beamwise bending mode. The other wing modes have a negligible impact on the roll response. The included wing bending mode captures well the dynamics around the frequency of the wing mode. There are only slight gain and phase differences around the frequency range of the mode. These differences could be attributed to effects from the other flexible wing modes, but clearly, the dominant response is captured.

The Lat/Dir Rigid wing yaw response matches well at low frequency in the magnitude plot. Pedal inputs produce differential longitudinal cyclic commands to the rotor. The tip path plane must realign in order to produce differential longitudinal forces and thus yaw moments. This realignment produces a time delay, and thus the phase diverges at lower frequencies than the roll response since the rotor responds to lateral stick commands through collective inputs which achieve a response from the system much faster than cyclic inputs. The phase difference in the rigid wing reduced model could be accounted for with a time delay. The time delay is
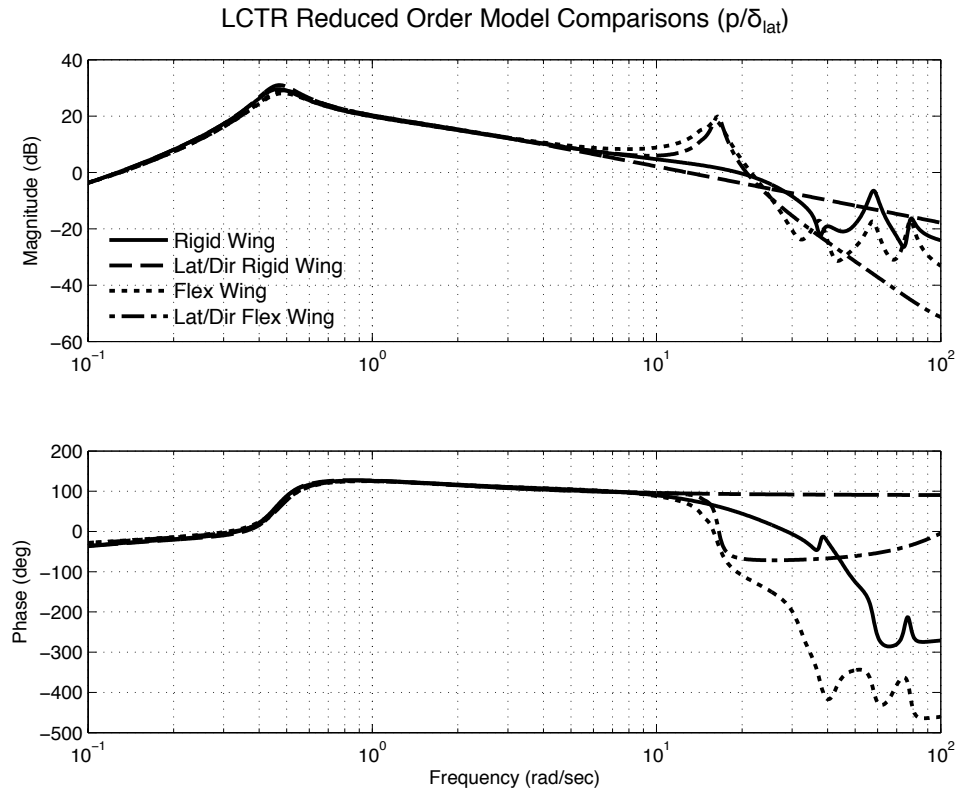
Figure 4.16: LCTR reduced order hover roll response comparisons with full order models

approximately 0.04 seconds. For the LCTR rotor with a flap frequency of 1.44/rev, a 1/rev input leads to a delay of approximately 0.04 seconds before realignment of the tip path plane, which matches the time delay estimate from the phase offset. Rotor dynamics therefore play a large role in the yaw response. Time delays could be used to improve the phase difference if low order models are needed. Magnitude plots, however, are not affected by time delays, so large variations between the reduced order and full order magnitude plots would still produce significant error in flight control applications. The Lat/Dir Flex Wing case contains the antisymmetric chordwise/torsion bending mode. This is the only mode significantly excited by this

response.
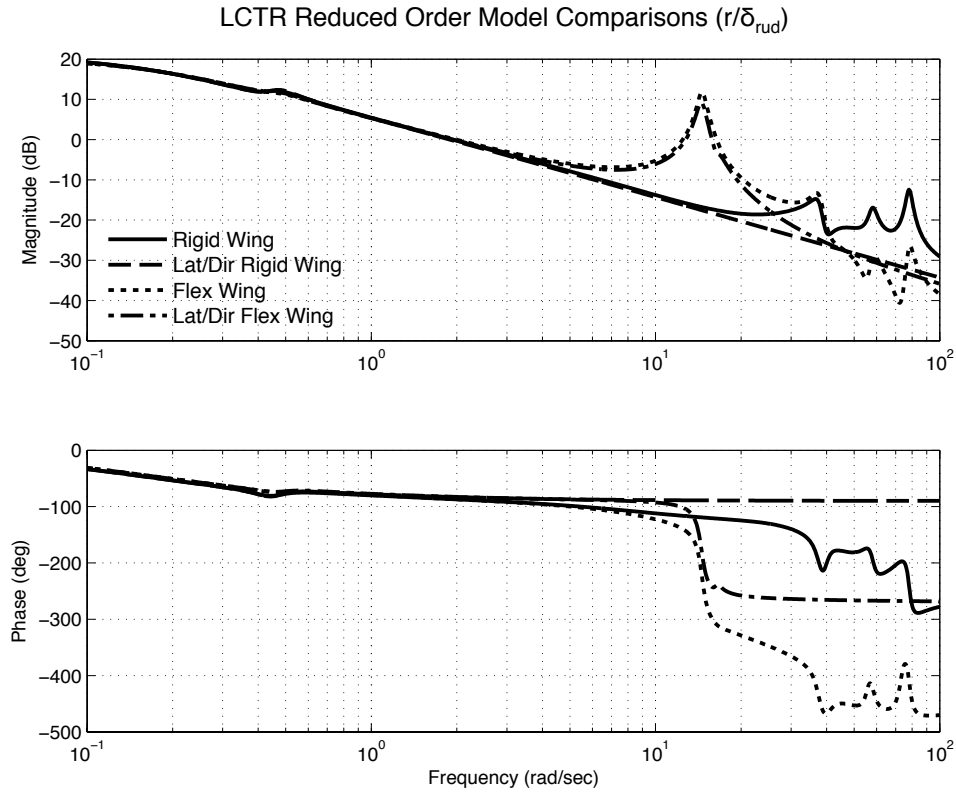
Figure 4.17: LCTR reduced order hover yaw response comparisons with full order models

4.3 LCTR Nacelle Validation

4.3.1 Model Setup

The LCTR model with a dynamic nacelle is set up in the same manner as the model described in Sec. 4.2.1 with the addition of nacelle dynamics. The nacelles add four additional states to the state vector. In trim, there are two additional unknowns, the nacelle input torques.

4.3.2 Validation

Nacelle dynamics for the HeliUM model of the LCTR are next validated against a CAMRAD model with a dynamic nacelle. The implementation of nacelle motion is implemented differently in HeliUM than in CAMRAD. The CAMRAD model offers direct control of the nacelle angle, while in HeliUM nacelle control comes through a torque motor at the wing connection and the nacelle angle comes of the solution to the second order differential equation. A proportional-integral-derivative (PID) control system is included for the nacelle so that the pilot commands a nacelle angle, much like the CAMRAD case. The validation below includes this control system in the HeliUM model. Figure 4.18 shows the longitudinal velocity response of the aircraft to nacelle angle commands. This HeliUM nacelle control system's gains were changed until the nacelle mode at 60 rad/sec matched the CAMRAD model. The dynamics match well for a broad frequency range. The steady state velocity to nacelle commands is essentially zero. There is an aircraft dynamic mode around 0.6 rad/sec which matches the phugoid frequency for this aircraft. The near zero steady state velocity value can be explained by Fig. 4.19, the aircraft pitch response to nacelle inputs. This figure shows that at steady state, the aircraft pitch response is equal in magnitude to the commanded nacelle angle, but opposite in phase. Positive nacelle displacement is define aft. If the nacelle is rotated aft, the nose will pitch down to realign the nacelle vertically in the inertial frame. The result is an aircraft that has changed pitch attitude, but remains in hover since the rotors remain vertical in the inertial frame. The figures show slight disagreement
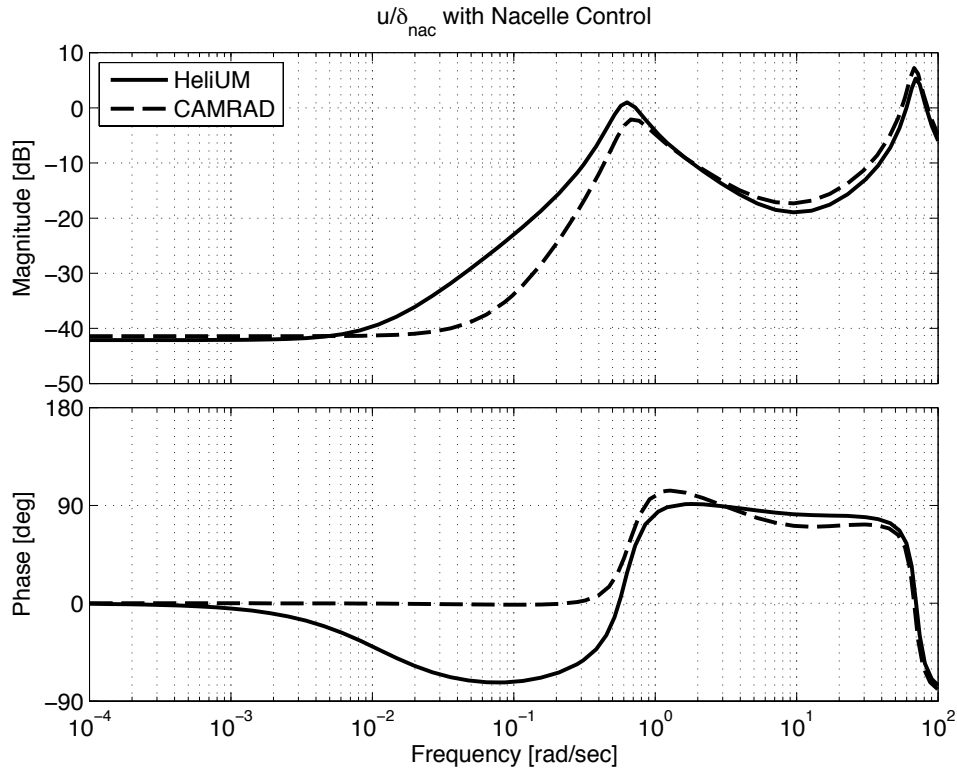
Figure 4.18: Longitudinal velocity changes to nacelle angle commands

at mid-frequencies, but overall have the same dynamics. There is a second order

pole-zero combination around 1 rad/sec, with the pole being the unstable phugoid.

There is also a nacelle mode at higher frequency. The final bare-airframe validation

response is shown in Fig. 4.20. This figure shows the aircraft velocity response to

longitudinal inputs. The unstable phugoid dynamics are again visible, as is the high

frequency nacelle mode.

Along with the bare-airframe validation shown so far, coupling numerators

were used to constrain the pitch attitude with longitudinal stick inputs [98]. The

nacelle could now be tilted to move the aircraft fore or aft without the aircraft

pitching, as if it were on a rail. The state-space coupling numerator approach,

described in Ref. 99 was used to constrain pitching motion. With pitch removed
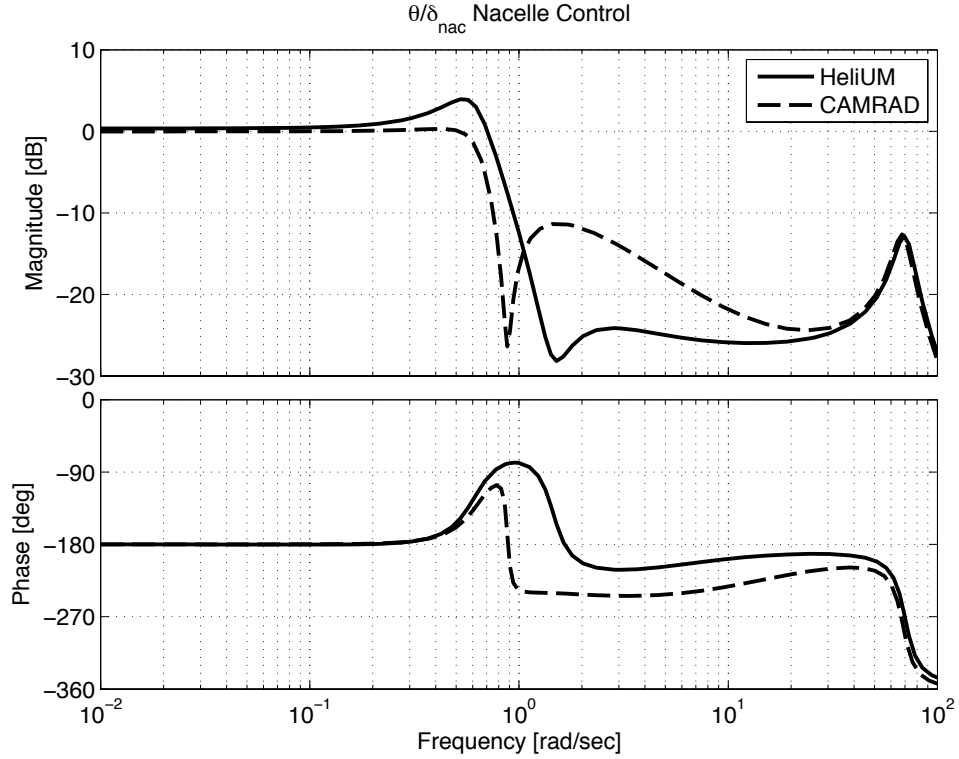
Figure 4.19: Pitch angle changes to nacelle angle commands

from the equation, the longitudinal velocity transfer function is first order.

$$\dot{x} = X_u u - g\theta_{nac} \tag{4.1}$$

$$\frac{u}{\theta_{nac}} = \frac{-g}{s - X_u} \tag{4.2}$$

This gives a first order response with a break at X_u and a $-g/s$ response at high frequency. X_u is change in x-force for perturbations in velocity, and for fixed wing aircraft is associated with fuselage drag. For rotorcraft, most of this stability derivative comes from the rotor response to perturbations as fuselage drag is small in hover. The full order ($\sim$60 states) constrained responses, along with their simplified counterparts (2 state) given by Eqn. (4.2) are shown in Fig. 4.21

The HeliUM simple transfer function model and full-order models match very

136
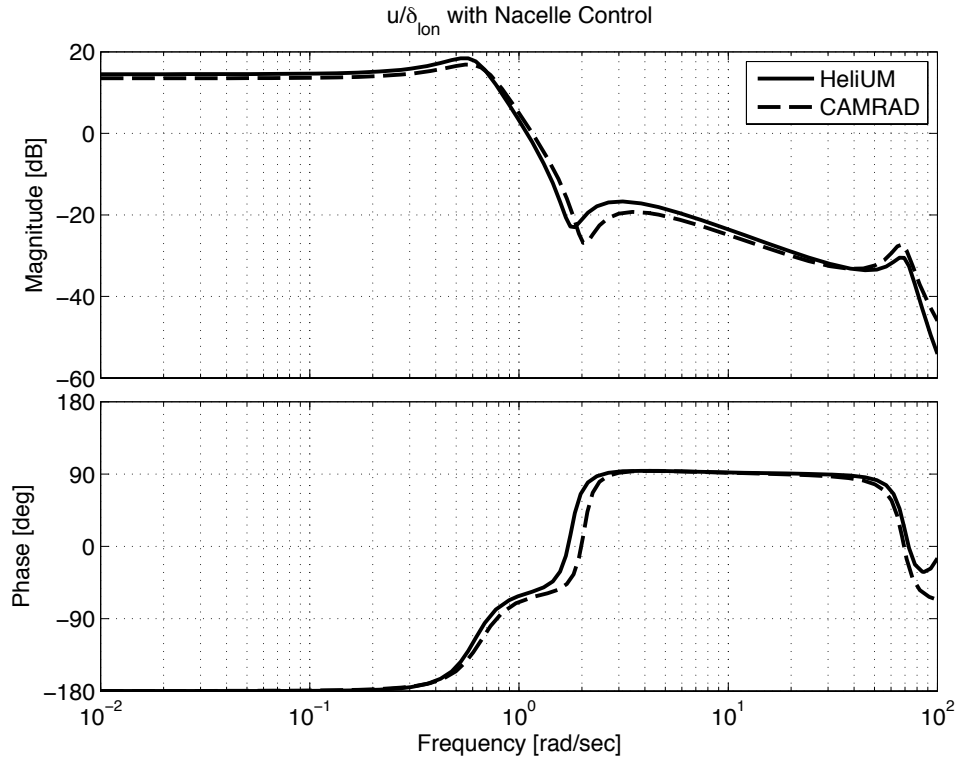
Figure 4.20: Longitudinal velocity changes to longitudinal stick commands

well at mid and low frequencies meaning the simple first order transfer function is
an accurate simplification of the equations of motion. There are slight differences in
the low frequency pole location, but overall the CAMRAD and HeliUM responses
match very well.

4.4 Validation of Four Element FEM Beam

Four finite elements are used to model the wings, blades, and nacelles. Addi-
tional and fewer elements were used to ensure the validity of using four elements.
Figure 4.22 clearly shows that four finite elements produce accurate results over the
full frequency range. Using two finite elements gives nearly identical results to four
and eight. As described previously, beam and chord bending shape functions allow
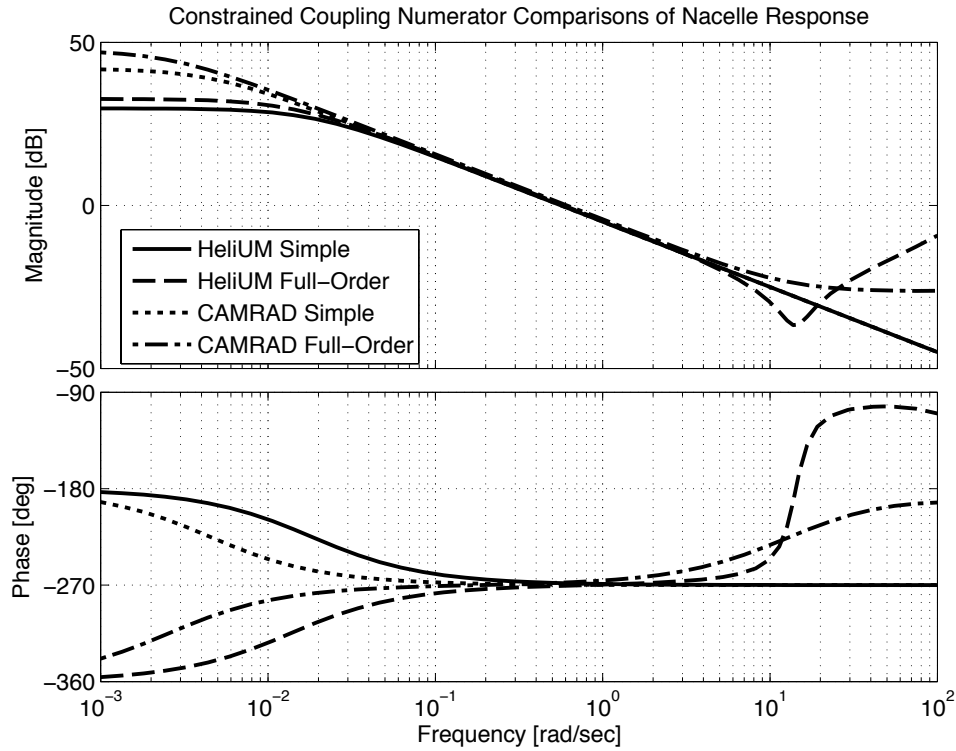
Figure 4.21: Longitudinal velocity response to nacelle inputs with pitch attitude constrained

for a cubic beam displacement over each finite element. Given the similarity of the roll response using any amount of finite elements shows that the wing and blade displacements are low order and easily approximated with few finite elements. This could be inferred from the model setup. The majority of wing forcing comes from the nacelle, a point force on the tip of the wing. This gives simple beam deflections. If the nacelle were located inboard of the wing tip, the wing bending could be more complex. Adding additional finite elements would only slow the solution process without improving model accuracy.
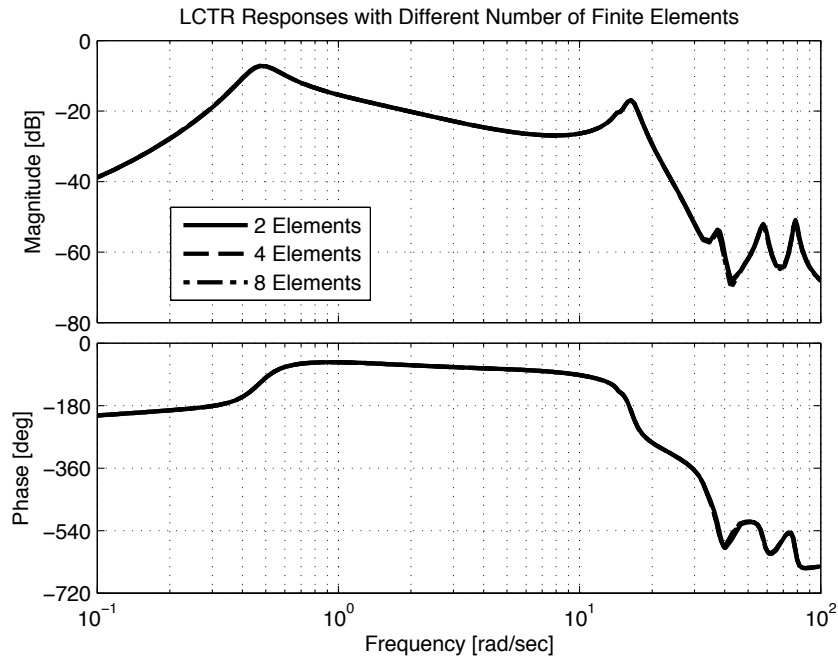
Figure 4.22: Comparisons of roll response using different numbers of finite elements for the wings and rotor blades.

4.5 Number of Wing Modes Retained

The number of wing modes retained for each wing was also varied to determine the minimum number needed to accurately model aircraft dynamics up to about 20 rad/sec. Figures 4.23-4.26 show the on-axis responses obtained retaining two to five wing modes. When two wing modes are retained for each wing, a total of four structural modes are obtained for the aircraft. Checking system eigenvalues shows that after two wing modes, all natural frequencies are above 60 rad/sec. The figures also show that the system responds essentially identically after the first two modes for each wing are included.

139
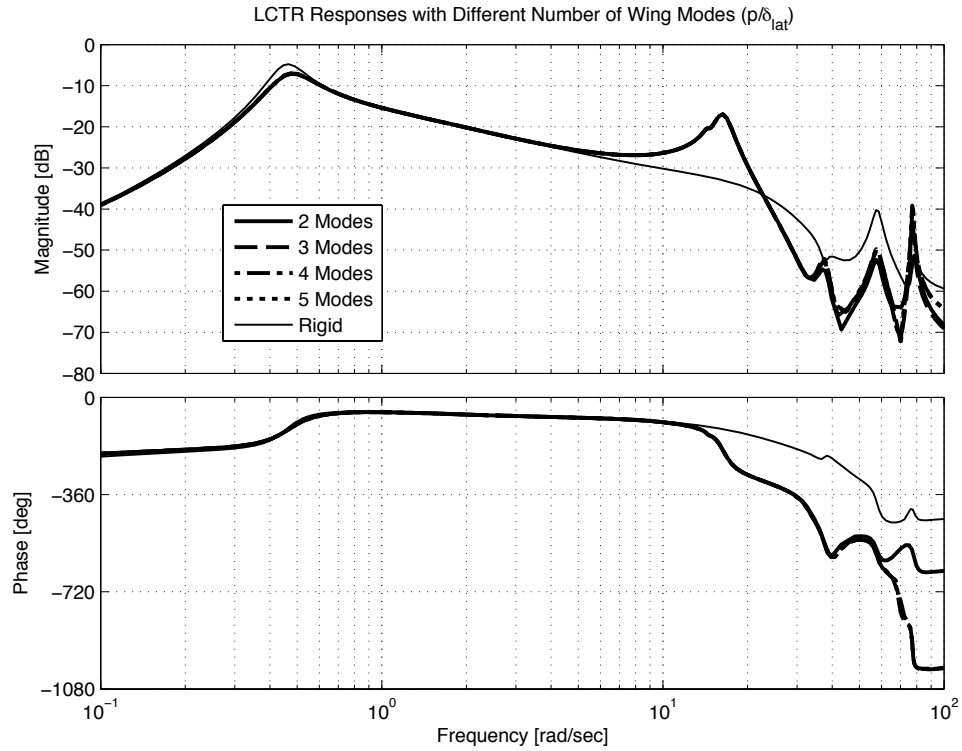
Figure 4.23: Comparisons of roll response with different amounts of wing modes retained

4.6 Chapter Summary

The model has been validated with the XV-15 and LCTR. Differences in XV-15 dynamics when compared to other models and flight data are attributed to rotor hub modeling. The validation with a LCTR model shows almost identical dynamics in the bare airframe. The validation also showed that four low frequency structural modes occur below 20 rad/sec, and thus need to be included for control law development and analysis. The nacelle dynamics have also been validated. Slight differences in the response with the dynamic nacelle are attributed to potential differences in the model input parameters.
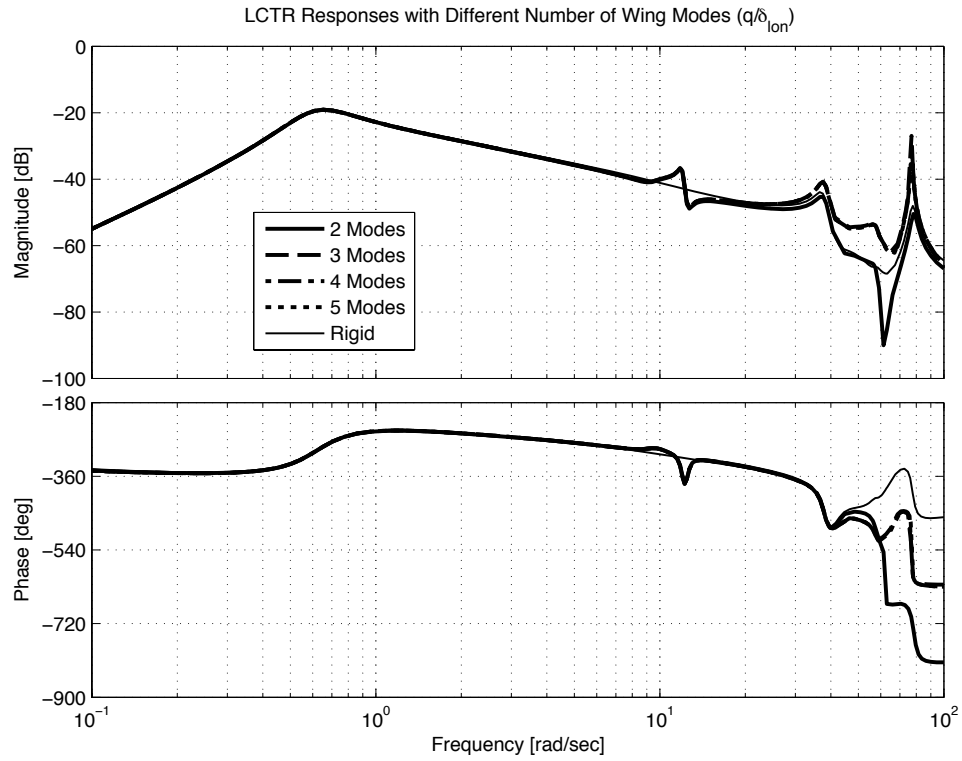
Figure 4.24: Comparisons of pitch response with different amounts of wing modes retained
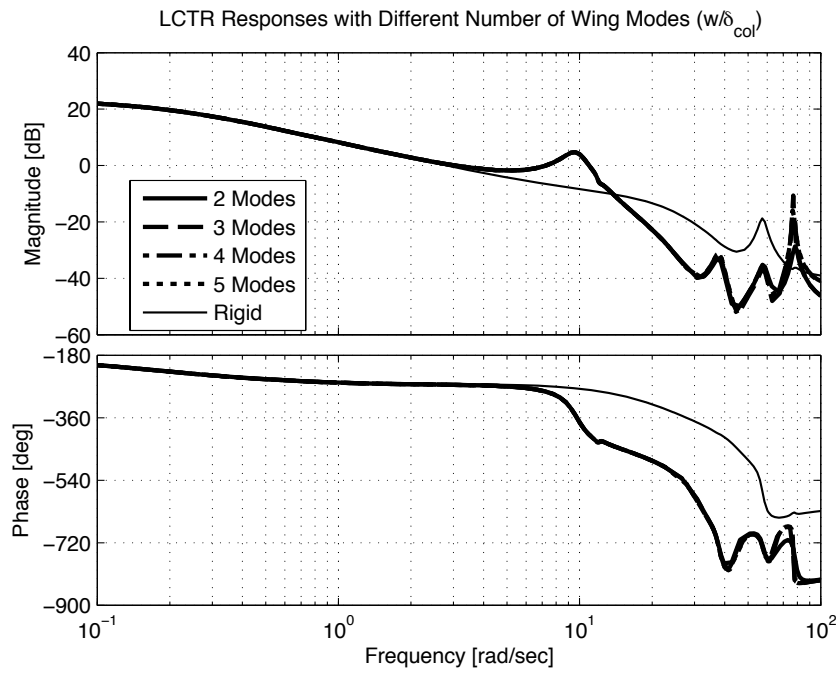
Figure 4.25: Comparisons of heave response with different amounts of wing modes retained
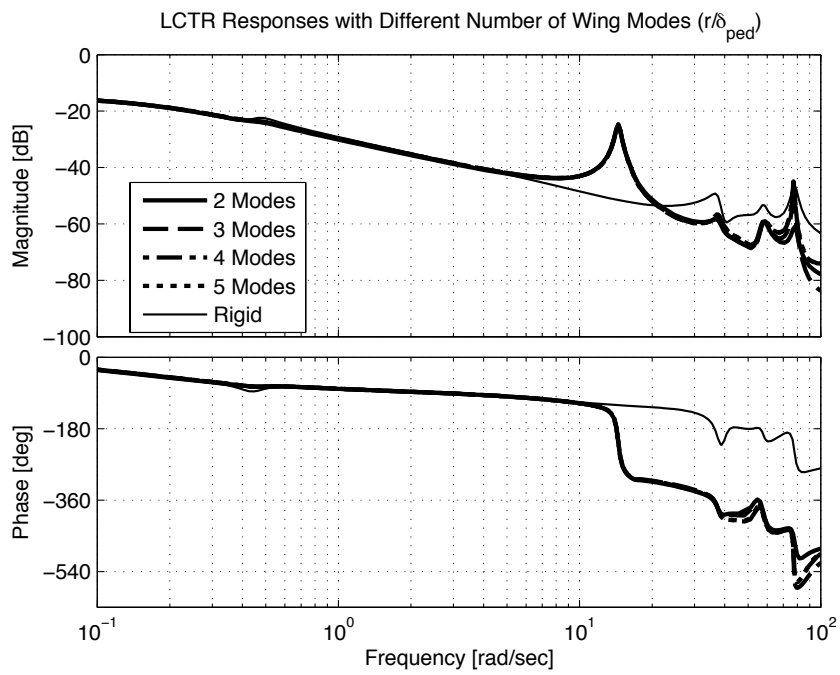
Figure 4.26: Comparisons of yaw response with different amounts of wing modes retained

Chapter 5:   Structural Coupling Analysis

This chapter serves to draw comparisons between the HeliUM linear model and other elastic models commonly used. The model structures will be presented and compared with each other. Two example cases, hover and cruise, using the LCTR model will be given. The model includes two structural modes and no nacelle dynamics.

5.1   Introduction

The HeliUM model fully couples the rigid-body and elastic states, giving a multi-body appearance to the equations of motion. The model does not need to come from an actual multi-body construction. As long as the model is formed by connecting bodies that have individual inertial, structural, and aerodynamic properties, it is referred to herein as *multi-body*. Specific comparisons are giving to the formulation given by Schmidt (Ref. 77), herein called the *mean-axis* formulation. The mean-axis model assumes there are no inertial changes within a flexible structure and adds only aerodynamic effects due to elasticity to the rigid body equations. The rigid-body portion remains the same with or without the inclusion of structural flexibility.   When developing linear models directly from rigid-body models, the

equations of motion generally undertake this form. Next, a model given by Tischler (Ref. 97), particularly useful for system identification, is discussed. This *hybrid-flexible* model couples the rigid body response with the elastic states in the output equations, reducing the problem size for system identification significantly. Finally, comparisons are given to a model in which the rigid-body and structural states are fully *decoupled*, with the structural response again modifying the output only.

As well as the elastic models introduced above, there are models which only contain rigid-body states. A *rigid-body* model is obtained from an aircraft that does not exhibit any structural motion whatsoever. This aircraft is not allowed to deform in any manner from its original configuration. This type of model is non-physical, but is generally obtained from modeling software, or rigid wind tunnel models. A *static-elastic* model also contains only rigid-body states, but with the effects of structural flexibility absorbed into the stability and control derivatives. Such a model is obtained from system identification of flight data since aircraft are flexible in nature and undergo structural oscillations with perturbations and are also deflected in their trim configuration. This model is also obtained from a quasi-static reduction of a model that contains elastic states. A comparison of the static-elastic model to the rigid-body model would produce *flex factors*, or the changes in the vehicles rigid-body dynamics due to flexibility. If the flex factors are unity, elastic motion does not alter the aerodynamics of the vehicle, and the rigid-body and static-elastic models are the same.

The elastic model types are now described in order of descending complexity, starting from the multi-body model and finishing with the decoupled model.

5.2   Multi-Body Flexible Formulation: Current Development

The multi-body like linear model most rigorously captures couplings between different aircraft components. A model with a sensor at the center of mass has the following structure:

$$\begin{Bmatrix} \dot{x}_R \\ \dot{x}_E \end{Bmatrix} = \begin{bmatrix} A_R & A_{RE} \\ A_{ER} & A_E \end{bmatrix} \begin{Bmatrix} x_R \\ x_E \end{Bmatrix} + \begin{bmatrix} B_R \\ B_E \end{bmatrix} \begin{Bmatrix} u \end{Bmatrix} \tag{5.1}$$

$$y = x_R$$

In this formulation, the rigid-body states (x_R) represent the motion of a point "o" within the fuselage, while the structural states (x_E) give each modes deflection with respect to the fuselage. This point serves as the origin for the building up of the multi-body aircraft components and is chosen to represent the center of mass of the undeformed aircraft. The model is built up one component at a time, meaning each individual component (i.e. fuselage, wing, etc.) has its own mass and aerodynamic properties. Since total aircraft mass is an integrated quantity, the center of mass and mass moments of inertia of the aircraft change after deformation, but the origin, "o", remains the same as it is a physical location within the aircraft fuselage. There is no "mean-axis assumption" in this model. The mean-axis assumption states that the rigid-body components of the state-vector follow the overall, or "mean" aircraft motion and neglect inertial couplings [81]. Within the multi-body model, the rigid-body components of the state vector measure the states of the origin point within

the fuselage. The output of the system is simply a fuselage state as defined by the origin point "o". This output contains any structural bending contributions local to the origin point. For a large tiltrotor in hover, the wings in trim deflect upward 18 inches resulting in a center of mass shift of ∼4.5 inches. This shift is relatively small compared to the scale of the aircraft (rotor radius of 32.5 feet).

In the multi-body model there is no overall rigid-body frame that elastic deflections are added onto, instead the fuselage is part of the flexible system and can deflect within an elastic mode; see Fig. 5.1 for a tilt-rotor asymmetric mode and Fig. 5.2 for an initial condition response showing fuselage roll rate and wing tip rate for the same asymmetric bending mode. The final curve in the plot $(p/(d\eta/dt))$ shows the ratio of roll rate to wing tip rate remains constant throughout the time history, as expected. This figure shows the ratio of the roll rate state to the modal displacement rate state of the eigenvector associated with the antisymmetric beam mode. The fuselage itself is rigid, and its involvement in a mode can be thought of as a rigid rotation of the fuselage when accounting for a coupled wing-fuselage system. The structural contributions to the motion of the aircraft are coupled into a set of eigenmodes, of which only a small set are retained, up to the maximum frequency range of interest.
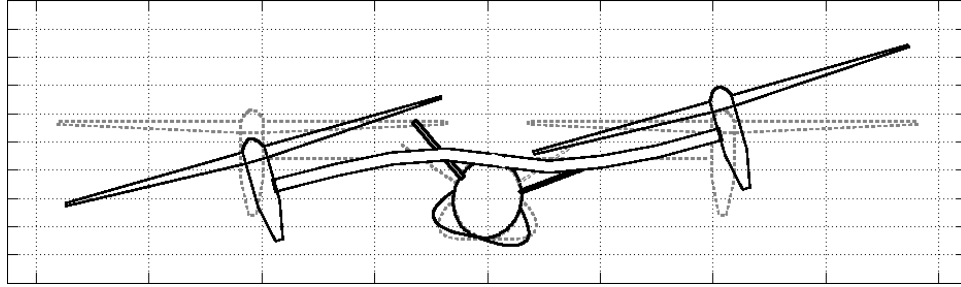
Figure 5.1: LCTR elastic mode shape
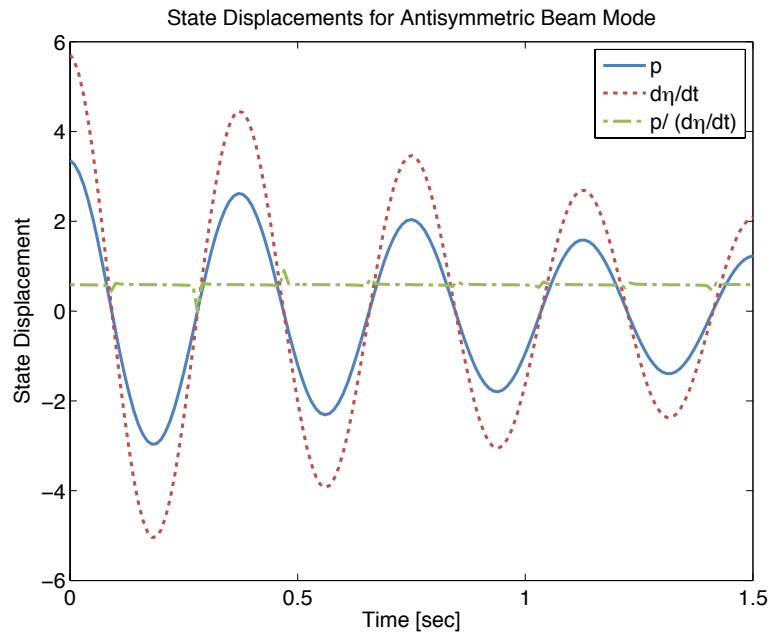
Figure 5.2: LCTR elastic mode shape time history

Since the first set of states (x_R) in Eqn. (5.1) represent the fuselage and its motion, the stability and control derivatives are much different than the standard rigid-body derivatives. For example, there is no control input that directly and instantaneously acts on the fuselage. This gives control derivatives that are essentially zero in the B_R portion of the control derivative matrix. The pilot inputs to the rotor must propagate down the flexible wing, and then they impact the fuselage through

wing bending. The rotor forcing is dominant in the structural portion of the control vector. The same can be said for the A_R portion of the stability derivative matrix. Again, the first set of states represent the fuselage and its motion, and these derivatives have different meaning than the standard rigid-body stability derivatives. For example, roll moments are transferred through wing bending, therefore, the predominant stability derivative in the roll equation is that of the structural displacement state in the A_{RE} portion of the state matrix. There must be structural bending of the wing to create forces and moments at the wing root, the connection point to the fuselage. Without structural bending, there is no transfer of forces or moments to the root. For example, the moment at the wing root can be derived from either a force summation or modal method, and must give the same result both ways. In the force summation method, all external forces and moments are summed to give the total forcing on the body downstream (i.e. fuselage). In the modal method, wing bending at the fuselage connection can be used to give the full forcing on the downstream body. Wing deflection is assumed to be a linear combination of a set of eigenmodes, so using the modal method where the curvature is a summation over all the modes gives the following moment:

$$M = EI \frac{d^2 w}{dx^2} \tag{5.2}$$

Clearly, bending must occur in order for a moment to be transferred. Since the wing has mass, it cannot bend instantaneously, giving a near zero rigid-body control derivative. If there were control surfaces directly on the fuselage, their effects would pass through to these control derivatives. Any model which follows this type of

formulation is referred to as a multi-body model.

If the structural states were reduced out of the multi-body model, the result would be the static-elastic model.

Comprehensive flight mechanics models generally take on a multi-body formulation. Examples include tilt-rotor models developed using software tools such as MBDyn (Refs. 45, 46), CAMRAD (Ref. 2), and HeliUM (Ref. 100). Another multi-body model commonly used is FLIGHTLAB (Ref. 47).

5.3   Mean-Axis Flexible Formulation

A commonly used approach to derive the equations of motion for a flexible aircraft is to build flexibility effects onto the rigid-body dynamics [101] [77] [102]. The equations of motion are built upon the mean-axis assumption, that is, structural deflections are assumed small enough that the mass distribution with respect to the center of mass of the aircraft is considered constant. This gives mass moments and products of inertia which are constant. It is also assumed that structural deflections can be lumped into sets of eigenmodes, of which only a finite amount are retained.

Elastic modes are coupled with rigid-body motion solely due to aerodynamic changes. The airframe is allowed to bend due to an elastic mode, and the resulting changes in aerodynamic forcing on the wing (lift, drag, etc.), are added to the rigid-body forcing equations. Changes in rigid-body states also add to the forcing of the elastic degrees of freedom, creating a fully coupled system. For example, aircraft roll motion creates airflow over the wing which adds forcing onto the elastic degrees

of freedom.

The aircraft motion at the sensor location is gained in the output matrix by summing the rigid-body motion with the elastic motion at the sensor location. The rigid-body states for this aircraft do not have a physical realization for the elastic aircraft, but are rather a reference frame that follows the equivalent rigid-body motion of the aircraft. The elastic motion refers to elastic vibrations around the rigid-body vehicle reference axes and elastic contributions to the output is multiplied by an *influence coefficient*, Φ_{ma}, which determines the motion of the sensor not caused by aerodynamics (e.g. caused my inertial coupling). The influence coefficient treats the elastic vibration as a sensor displacement from the reference axes. All aerodynamic influences are retained in A_{RE} in this model type. If the structural mode contains angular displacements, this influence coefficient will capture the relative rotation of the center of mass relative to the reference vehicle axes. The mode shape is assumed to be know before hand. The formulation used is similar to Eqn. (5.1), with the addition of the influence coefficient term in the output.

$$\left\{ \begin{matrix} \dot{x}_R \\ \dot{x}_E \end{matrix} \right\} = \begin{bmatrix} A_R & A_{RE} \\ A_{ER} & A_E \end{bmatrix} \left\{ \begin{matrix} x_R \\ x_E \end{matrix} \right\} + \begin{bmatrix} B_R \\ B_E \end{bmatrix} \left\{ u \right\} \tag{5.3}$$

$$y = x_R + \Phi_{\text{ma}} x_E$$

The state vector has two components, x_R and x_E, corresponding to the rigid-body and elastic states, respectively. The elastic states in the example give the modal angular displacement and rates at the nose of the fuselage where a sensor is

located. Even if the sensor was at the center of mass, there would be a structural contribution added to it if the center of mass was involved in the modal response. This is in contrast to the multi-body formulation already described. A_R and B_R are the standard rigid-body stability and control derivatives and remain unchanged from a purely rigid-body formulation. This means that the aeroelastic coupling, A_{RE}, component above is solely due to changes in the vehicle aerodynamics due to structural deformations. The A_{ER}, or rigid-body coupling, portion comes from changes in aerodynamic forcing on the elastic degrees of freedom due to changes in the rigid body states. Finally A_E is the structural mode. The elastic portion of the control matrix contains forcing on the elastic states due to pilot inputs, or changes in control effectiveness due to structural bending. This would capture, for example, aileron control reversal if the aircraft's wings were highly flexible. The measured output of the aircraft is simply the sum of the rigid body output as well as the local output at the sensor, which contains contributions from elasticity. The vehicle is essentially a rigid-body modified to include elastic aerodynamic effects.

This building up of the aircraft states is one method often employed to obtain linear models including elastic states, especially when a rigid-body linear model is used as the starting point. References 103 and 104 provide an excellent example in the development of this type of model and associated comparisons with flight data in the time domain for a flexible glider. Reference 103 also gives comparison between the gliders rigid-body and elastic aerodynamic parameters. A flexible B-1 model is developed using this architecture in Ref. 101. Reference 79 develops flexible equations of motion for a generic transport using this formulation.

5.4 Hybrid-Flexible Model

The hybrid-flexible model structure, proposed by Tischler in Ref. 97, is a derivative of the coupled models described so far and is well suited for system identification from flight data with a limited number of structural sensors. It will be shown later that the A_{RE} portion of the stability derivative matrix, as well as the influence coefficient, Φ, are fully correlated and cannot be separated from a system identification point of view if the shape of the structural modes is not known or if multiple sensors are not present to accurately identify the mode shape of the structural mode. In other words, the motion of the aircraft at a sensor location can come from either the involvement of the sensor location in a structural mode or effective rigid-body dynamics of the aircraft. If multiple sensors are located along the wings and fuselage, the structural mode can be identified, and the equations of motion would take on the form of Eqn. (5.3).

Provided there is adequate frequency separation between the structural and rigid-body modes, the structural mode's effect on rigid body dynamics can be assumed to be quasi-static. The aero-elastic coupling terms are dropped and their influence is absorbed into the stability derivatives, giving static-elastic stability and control derivatives. Reference 97 gives the following guideline:

$$\frac{\omega_{\mathrm{str}}}{\omega_{\mathrm{rb}}} \geq 5 \tag{5.4}$$

The hybrid-flexible model structure contains the static-elastic stability and control derivatives in the A_R and B_R portion of the state-space model, and no aero-elastic

coupling, or A_{RE}. The A_{ER} portion is still retained to provide coupling of the rigid-body states back into the structural states. The damping of the eigenvalue pair associated with the structural modes is set to match the full-order multi-body model since the overall dynamics must remain the same. Since the aeroelastic terms are dropped, any structural influence on the rigid-body modes is included in the influence coefficient.

Theodore et al. (Ref. 105) and Tischler (Ref. 97) present the identification of a large flexible transport aircraft using the hybrid-flexible model. Sahasrabudhe (Ref. 69) generates a model of a large helicopter where the measured response is a sum of rigid-body dynamics and structural dynamics. The structural response includes forcing from the rigid-body motion of the aircraft, giving a hybrid-flexible architecture.

5.5   Decoupled Model

The final elastic model is a one where the structural and rigid-body states are decoupled from one another, meaning the off diagonal components (A_{RE} and A_{ER}) of the stability derivative matrix are set to 0. This model type is a further simplification of the coupled models and also relies on the output equations to add influence of the structural modes to motion of the aircraft. As with the hybrid-flexible, this model also uses the static-elastic rigid-body stability and control derivatives.

This model structure is demonstrated by Najmabadi et al (Ref. 75) for a identification of a large transport aircraft. This model structure is used to integrate

elastic effects into a rigid-body simulator of an F/A-18 (Ref. 68). Powers (Ref. 63) also used a decoupled model to incorporate a first structural bending mode into an SR-71 identification problem.

5.6   Model Comparisons

There are two key differences between the multi-body and mean-axis models.

1. The transfer of forcing from the wing to the fuselage in the multi-body model is not instantaneous and occurs through wing bending. For example, forcing from the control derivative matrix in the mean-axis model can occur in the rigid-body components of the state vector; it does not in the multi-body case. Elastic motion is coupled to the fuselage motion inertially and aerodynamically, while in the mean-axis formulation they are coupled solely due to aerodynamics. In the multi-body model, aerodynamic and inertial forcing on the flexible body are treated identically in the creation of the equations of motion. They have an identical influence in the linear model and are thus fully correlated.

2. The reference axis for the mean-axis model is the equivalent rigid-body axes anchored at the nominal CG for trimmed flight, onto which elastic motion is added. The reference axes for the multi-body model are fuselage axes which describe the motion and location of the fuselage only.

The multi-body model can be converted to the mean-axis model if a rigid-body model is available, either from simulation, wind-tunnel testing, or system identifi-

cation with multiple structural sensors. To convert the multi-body model to the mean-axis model, the rigid-body stability and control derivatives are taken from the rigid-body model, and the coupling terms can be identified to create the same static-elastic model as is created by a direct reduction of the elastic states from the flexible HeliUM model. The only assumption in doing so is that the changes in the inertial properties of the aircraft while it flexes are small enough to be negligible. This conversion is performed herein to highlight the equality between the two models even if the individual stability and control derivatives are much different. Steps given to convert the mean-axis model to the hybrid-flexible are also given. Finally, steps in converting from the hybrid-flexible to the decoupled model are given. Starting from the multi-body model, the conversions are as follows:

Note: For a given stability or control derivative, say L_p, the nomenclature used in the discussion given in Table 5.1. The derivative name remains italicized, but the abbreviation for the model type is not.

Table 5.1: Control and stability derivative nomenclature for L_p

Models without flexibility	
Derivative Name	Model Name
L_{prb}	Rigid-body model
L_{pse}	Static-elastic model

Models with flexibility	
Derivative Name	Model Name
L_{pmb}	Multi-body model
L_{pma}	Mean-axis model
L_{phf}	Hybrid-flexible model
L_{pd}	Decoupled model

As has been mentioned, the upper left quadrant of the stability derivative matrix, A_R, and the upper section of the control derivative matrix, B_R, are repeated in some of the models and are defined to come from models that do not include structural flexibility. The off-diagonal portion and the output portion of the models is where differences occur. Table 5.2 shows these equalities.

Table 5.2: A_R and B_R definitions for different models

Stability Derivative Matrix	Control Derivative Matrix	Model
$A_{Rma} \equiv A_{Rrb}$	$B_{Rma} \equiv B_{Rrb}$	Mean-axis model
$A_{Rhf} \equiv A_{Rse}$	$B_{Rhf} \equiv B_{Rse}$	Hybrid-flexible model
$A_{Rd} \equiv A_{Rse}$	$B_{Rd} \equiv B_{Rse}$	Decoupled model

Multi-body to mean-axis conversion:

1. Replace the A_R and B_R portion of the multi-body model with the rigid-body (*not* static-elastic) model of the same aircraft.

2. A quasi-steady reduction of the mean-axis model must produce the same

static-elastic model as a quasi-steady reduction of the flexible multi-body model. For a roll response, the key coupling term in the A_{RE} portion of the state matrix is L_η. The following equations, based on derivations shown in Ref. 97, give the relationship between the rigid-body and static-elastic L_p stability derivative and the L_δ control derivative for a simple three degree of freedom model. The degrees of freedom are roll rate and two degrees of freedom associated with the structural mode.

$$L_{p\mathrm{se}} = L_{p\mathrm{rb}} + \frac{L_\eta}{\omega^2}\eta_p \tag{5.5}$$

$$L_{\delta\mathrm{se}} = L_{\delta\mathrm{rb}} + \frac{L_\eta}{\omega^2}\eta_\delta \tag{5.6}$$

The unknowns in the equations above are the coupling terms, L_η and η_p, as well as the structural control derivative, η_δ. The system has more unknowns than equations, so it cannot be solve uniquely. The rigid-body coupling term, η_p, or structural control derivative, η_δ can be retained from the flexible model, reducing the degrees of freedom and providing a solution. The frequency of the structural mode, ω, is retained from the multi-body model. If the flexible and rigid multi-body models are set up appropriately, the equations should produce the same coupling term. For larger systems, or with systems with sensor outputs, the coupling terms and structural control derivative may be identified using system identification software.

3. Once an aerodynamic L_η is identified for the mean-axis model ($L_{\eta\mathrm{ma}}$) from the previous step, it is placed back into A_{RE} to form the complete mean-axis

model. This $L_{\eta\mathrm{ma}}$ comes purely from changes in aerodynamic forcing due to changes in structural flexibility. The identified η_p and η_δ are also placed back into the state matrix.

4. The remainder of the aircraft measured response comes from forcing other than aerodynamics and is lumped into an influence coefficient, $\Phi_{p\mathrm{ma}}$. This coefficient is an equivalent displacement of the sensor from a structural node (see Eqn. (5.3)). It has the form:

$$\Phi_{p\mathrm{ma}} = \frac{-\left(L_{\eta\mathrm{mb}} - L_{\eta\mathrm{ma}}\right)}{\omega^2} \tag{5.7}$$

Here, $L_{\eta\mathrm{mb}}$ comes from the multi-body model and $L_{p\mathrm{ma}}$ is the identified value from the mean-axis solution.

5. The influence coefficient multiplies the structural rate term in the output matrix. For example:

$$p_{\mathrm{ma}} = p + \Phi_{p\mathrm{ma}}\dot{\eta}_{str} \tag{5.8}$$

Here p is the rigid-body roll response and $\Phi_{p\mathrm{ma}}\dot{\eta}_{str}$ is the response due to the structural mode deflection. The full response, p_{ma}, accounts for the offset of the sensor from the structural node. This response should match the mult-body response exactly.

Hybrid-Flexible Model

1. Starting with either the multi-body or mean-axis model, replace the A_R and B_R portion of the model with the static-elastic model of the same aircraft.

2. Drop the aeroelastic coupling terms A_{RE}.

3. Determine the *effective* influence coefficient, Φ, of the response on the rigid-body stability derivatives. The influence coefficient can be thought of as an *equivalent* sensor displacement which picks up all local modal bending effects. Determination of the influence coefficient is described in subsequent sections, but is of the form shown here (see also Ref. 97). If starting from the mean-axis model:

$$\Phi_{p\mathrm{hf}} = \frac{-L_{\eta\mathrm{ma}}}{\omega^2} + \Phi_{p\mathrm{ma}} \qquad (5.9)$$

If starting from the multi-body model:

$$\Phi_{p\mathrm{hf}} = \frac{-L_{\eta\mathrm{mb}}}{\omega^2} \qquad (5.10)$$

If starting from the mean-axis model, $\frac{-L_{\eta\mathrm{ma}}}{\omega^2}$ is the equivalent displacement, with the aeroelastic coupling term, $L_{\eta\mathrm{ma}}$, coming from A_{RE} and ω being the structural mode frequency. $\Phi_{p\mathrm{ma}}$ (see Eqn. (5.7)) is a physical displacement of a sensor from a structural mode node. If the multi-body model is served as the starting point, there is no physical sensor displacement and the influence coefficient comes from the equivalent displacement. The effective influence coefficient $\Phi_{p\mathrm{hf}}$, beginning with either method, will be the same value.

4. The frequency and damping of the eigenvalue related to the structural mode must be preserved throughout the model reduction. Therefore, the A_E components are modified to produce the same eigenvalues as the fully coupled

system.

5. The influence coefficient again multiplies the structural rate term in the output matrix.

$$p_{\text{hf}} = p' + \Phi_{phf}\dot{\eta}_{str} \tag{5.11}$$

Here p' is the static-elastic roll response and $\Phi_{phf}\dot{\eta}_{str}$ is the influence coefficient from Eqn. (5.9) or (5.10).

Decoupled Model:

1. Retain the static-elastic A_R and B_R portion of the flexible model.

2. Drop the off-diagonal components of the stability derivative matrix (A_{RE} and A_{ER}).

3. Ensure that the frequency and damping of the structural mode eigenvalue matches that of the original model

4. The same output equation, Eqn. (5.11), as the hybrid-flexible model is used.

The main difference between the mean-axis model and the hybrid-flexible and decoupled models presented here is the use of the rigid-body vs. the static-elastic stability derivatives. The reduction of the structural modes from the mean-axis model would produce the static-elastic rigid-body stability derivatives of the hybrid-flexible and decoupled models.

5.7   Implications for Model Identification from Flight Data

The model type identified from flight data is determined by the parameters left free in the identification. The mean-axis form of the flexible model relies on the influence coefficient to couple the sensor response to the rigid-body response. It has been shown, Eqn. (5.9), that $\Phi_{p\mathrm{ma}}$ and the aeroelastic coupling term, $L_{\eta\mathrm{ma}}$, are fully correlated, meaning this model type would not be identified well if only a single sensor is used. Reference 97 provides an example for a Harrier VSRA aircraft in which the two components of $\Phi_{p\mathrm{hf}}$ (Eqn. (5.9)) were not individually identifiable because only a single sensor was used. Multiple sensors were present in the glider example of Refs. 103 and 104, meaning the influence coefficient, Φ_{ma}, and the aeroelastic coupling terms in A_{RE} were able to be identified separately. Φ_{ma} could also be determined from ground shake tests or flexible model analysis leaving only $L_{\eta\mathrm{ma}}$ as an unknown.

For a multi-body type model, there is no influence coefficient to identify, and all aeroelastic coupling and sensor information is contained in the coupling terms. However the aeroelastic coupling and rigid-body coupling terms are also correlated. Multiple sensor information could also be used to resolve these correlation issue.

In contrast to the multi-body model, a hybrid-flexible model fully relies on a lumped influence coefficient in the output and has no aeroelastic coupling terms to identify. This model type is the simplest to identify while retaining the majority of the key dynamics. An important assumption in this model type however is that there is adequate separation between the structural and rigid body modes.

Possibly the simplest model to identify, the decoupled model, assumes no coupling terms and accounts for all flexibility effects in the influence coefficients of the output equation. The influence coefficient accounts for all aerodynamic and inertial coupling as well as any influence from sensor displacements. This identified model would have the static-elastic rigid-body states in the A_R position and zeros on the off-diagonal terms.

5.8   Influence Coefficients

Φ_p can be determined using a partial fraction expansion of a fully coupled model (as the multi-body or static-elastic model) into a decoupled one, where the decoupled model contains a summed rigid-body and elastic response. If compared to a summation of a purely rigid-body response and an isolated structural mode, the difference between the two models results in the influence coefficient.

The influence coefficient can also be determined by analyzing the eigenvector corresponding to the structural mode. Continuing with the example above for a roll rate response , Φ_p would be the component of the structural mode eigenvector corresponding to a roll displacement or rate, divided by the component corresponding to the structural deflection or rate. This gives the mode shape slope for a given response. The same could be said in structural dynamics, where the eigenvector of a mode represents the nodal displacements, or a mode shape, and ratios of the nodal displacements can be used to determine relative displacements of nodes to each other. Here, the mode shape contains fuselage and wing bending displacements and

rates.

The full aircraft output, as expressed by any of the models presented, represents the sum of rigid-body rate plus the contributions of the components of the structural mode. The partial fraction method as well as eigenvector method are now analyzed for a simplified 3-DOF roll response, following Ref. 97. The states are roll rate, p, as well as structural states associated with the first structural mode, $\dot{\eta}$ and η. Assuming there is no sensor offset, meaning the sensor is on a node of a mode ($\Phi_{\text{ma}} = 0$), the linear model initially has the following form *Note*: There is no implication on the form of the model, it can be an mean-axis type model or multi-body type model.

$$
A = \begin{bmatrix} L_p & L_{\dot{\eta}} & L_{\eta} \\ \eta_p & -2\zeta\omega & -\omega^2 \\ 0 & 1 & 0 \end{bmatrix} \qquad B = \begin{bmatrix} L_{\delta} \\ \eta_{\delta} \\ 0 \end{bmatrix} \qquad \text{with} \qquad x = \begin{Bmatrix} p \\ \dot{\eta} \\ \eta \end{Bmatrix} \qquad (5.12)
$$

The model above is simplified to ease creating an analytical solution by assuming an undamped oscillatory structural mode ($\zeta = 0$). Damping adds additional terms to the eigenvectors obscuring the dominant terms that are derived below. Also, the rigid-body coupling term, η_p, and aeroelastic coupling term, $L_{\dot{\eta}}$, term are neglected. Rigid-body coupling can be ignored if there is negligible effect of rigid-body motion on the structural mode. $L_{\dot{\eta}}$ also has a negligible impact on the dynamics when

compared to L_η

$$A = \begin{bmatrix} L_p & 0 & L_\eta \\ 0 & 0 & -\omega^2 \\ 0 & 1 & 0 \end{bmatrix} \qquad B = \begin{bmatrix} L_\delta \\ \eta_\delta \\ 0 \end{bmatrix} \qquad (5.13)$$

The eigenvalues and eigenvectors associated with the structural mode are: $\lambda_{str} = \pm i\omega$, with:

$$v_{str+} = \begin{Bmatrix} L_\eta \\ i\omega\,(i\omega + L_p) \\ -(i\omega + L_p) \end{Bmatrix} \quad \text{and} \quad v_{str-} = \begin{Bmatrix} L_\eta \\ -i\omega\,(-i\omega + L_p) \\ -(-i\omega + L_p) \end{Bmatrix} \qquad (5.14)$$

Assuming a large frequency separation between the structural mode and the rigid-body mode, L_p can be assumed to have minimal influence, giving the following eigenvectors.

$$v_{str+} = \begin{Bmatrix} L_\eta \\ -\omega^2 \\ -i\omega \end{Bmatrix} \quad \text{and} \quad v_{str-} = \begin{Bmatrix} L_\eta \\ -\omega^2 \\ i\omega \end{Bmatrix} \qquad (5.15)$$

The influence coefficient of the structural mode to the rigid body motion of the aircraft has been stated to be the mode shape slope, here it is the ratio of the rigid-body rate component of the to the structural rate component. Using either eigenvector in the above equation, this gives:

$$\Phi_p = \frac{\partial p}{\partial \eta} = -\frac{L_n}{\omega^2} \qquad (5.16)$$

In determining Φ_p from a partial fraction expansion, the p/δ transfer function is

164

expanded [97]:

$$\frac{p}{\delta} = \frac{L_\delta \left(s^2 + \omega^2\right) + L_\eta \eta_\delta}{\left(s - L_p\right)\left(s^2 + \omega^2\right)} = \frac{A}{s - L_p} + \frac{B_1 s + B_0}{s^2 + \omega^2} \tag{5.17}$$

Solving for A, B_0, and B_1 yields:

$$A = L_\delta + \frac{L_n \eta_\delta}{\omega^2 + L_p^2} \tag{5.18}$$

$$B_1 = -\frac{L_n \eta_\delta}{\omega^2 + L_p^2} \tag{5.19}$$

$$B_0 = -\frac{L_p L_n \eta_\delta}{\omega^2 + L_p^2} \tag{5.20}$$

Again, with the large frequency separation, L_p^2 can safely be ignored in the denominator. Furthermore, B_0 term is small and adds a negligible quantity to the steady state response. Removing these terms gives a total response of:

$$\frac{p}{\delta} \cong \underbrace{\frac{L_\delta + \frac{L_\eta}{\omega^2}\eta_\delta}{s - L_p}}_{p'} + \underbrace{\frac{-L_\eta}{\omega^2}}_{\Phi_p} \underbrace{\frac{\eta_\delta s}{s^2 + \omega^2}}_{\dot{\eta}_{str}} \tag{5.21}$$

$$\cong p' + \Phi_p \dot{\eta}_{str} \tag{5.22}$$

The static-elastic rigid body response summed with isolated structural rate response ($\dot{\eta}_{\text{str}}$). Note that Φ_p is the same ($-L_\eta/\omega^2$) using both the partial fraction expansion method as well as the eigenvector method. If a more coupled model is used than that presented, the influence coefficient would not have such a simple analytical solution. It would still, however, have the same form; most easily identifiable from an eigenvector analysis.

5.9   Static-Elastic Model

The static-elastic model is obtained by performing a quasi-steady reduction of the structural states into the rigid-body states by setting the rate and acceleration terms of the structure mode to zero (i.e. they are static), and solving for the remaining states. The static-elastic model, when compared to the purely rigid-body model, differs when the flex factors are not unity. Starting from the simplified linear model, a quasi-steady reduction is performed. There is no sensor displacement, so $\Phi = 0$. There is no implication on the model form and the reduction is valid starting from a multi-body like or mean-axis like model. Note: Starting from the hybrid-flexible model the following reduction would not change the rigid-body states since the aeroelastic coupling terms are zero. Therefore, the hybrid-flexible model uses static-elastic rigid-body stability derivatives.

$$A_{se} = A_R - A_{RE}A_E^{-1}A_{ER} \tag{5.23}$$

$$B_{se} = B_R - A_{RE}A_E^{-1}B_E \tag{5.24}$$

A_R is the quadrant of retained states. A_{RE} and A_{ER} represent the off-diagonal components to be eliminated and A_E is the quadrant composed of states to be eliminated.

$$\begin{Bmatrix} \dot{p} \\ 0 \\ 0 \end{Bmatrix} = \begin{bmatrix} L_p & L_{\dot{\eta}} & L_{\eta} \\ \eta_p & 0 & -\omega^2 \\ 0 & 1 & 0 \end{bmatrix} \begin{Bmatrix} p \\ \dot{\eta} \\ \eta \end{Bmatrix} + \begin{bmatrix} L_{\delta} \\ \eta_{\delta} \\ 0 \end{bmatrix} \begin{Bmatrix} \delta \end{Bmatrix} \tag{5.25}$$

and:

$$\dot{p}' = L_{p_{se}}p' + L_{\delta_{se}}\delta \tag{5.26}$$

where:

$$L_{p_{se}} = \underbrace{L_p}_{A_R} - \underbrace{\begin{bmatrix} L_{\dot{\eta}} & L_{\eta} \end{bmatrix}}_{A_{RE}} \underbrace{\begin{bmatrix} 0 & -\omega^2 \\ 1 & 0 \end{bmatrix}^{-1}}_{A_E^{-1}} \underbrace{\begin{bmatrix} \eta_p \\ 0 \end{bmatrix}}_{A_{ER}} \tag{5.27}$$

$$L_{p_{se}} = L_p + \frac{L_{\eta}}{\omega^2}\eta_p = L_p - \Phi_p\eta_p \tag{5.28}$$

and similarly:

$$L_{\delta_{se}} = L_{\delta} + \frac{L_{\eta}}{\omega^2}\eta_{\delta} = L_{\delta} - \Phi_p\eta_{\delta} \tag{5.29}$$

The same influence coefficient and thus control derivative is seen in the quasi-steady reduction as in converting the system to output form (Eqn. (5.21)). It should be mentioned again that the rigid-body, or fuselage, control derivatives are generally near zero in the multi-body flexible model since the aircraft forcing comes at the end of the flexible wings. Since forcing comes through structural bending, the aeroelastic coupling term L_{η} is large, whereas it is smaller for the mean-axis case where only aerodynamic forcing is transferred with wing bending. Once the quasi-steady reduction is performed, the control derivatives take their more familiar form, where a control perturbation elicits an instantaneous roll response of the aircraft through L_{δ}. In other words, a reduction of the multi-body model will create large influence coefficients, while the reduction of the mean-axis model will generally have smaller

influence coefficients.

Flex factors have been defined (Ref. 97) to give the changes in rigid-body dynamics due to structural flexibility. For example, using Eqns. (5.28) and (5.29):

$$ff_{L_\delta} = \frac{L_{\delta_{se}}}{L_{\delta_{rb}}} = \frac{L_\delta - \Phi_p \eta_\delta}{L_{\delta_{rb}}} \tag{5.30}$$

$$ff_{L_p} = \frac{L_{p_{se}}}{L_{p_{rb}}} = \frac{L_p - \Phi_p \eta_p}{L_{p_{rb}}} \tag{5.31}$$

5.10 Tilt-Rotor Example: Hover

The multi-body model is now taken from its standard form and converted to mean-axis form, hybrid-flexible form, as well as decoupled form. We start with the lateral/directional multi-body model which includes the anti-symmetric beamwise wing bending mode. Lateral stick inputs excite the wing anti-symmetric beam mode through differential collective of the rotors. Pedal inputs are also retained to keep a full lateral/directional model. Pedal inputs do not excite this structural mode significantly.

Note: The subscripts detailing which model the control and stability derivatives come from are omitted where the model structure is presented for clarity. They are re-introduced when the derivatives are given numerical values.

5.10.1 Multi-Body Model

$$
\begin{Bmatrix} \dot{v} \\ \dot{p} \\ \dot{r} \\ \dot{\phi} \\ \ddot{\eta} \\ \dot{\eta} \end{Bmatrix} =
\left[\begin{array}{cccc|cc}
Y_v & Y_p & Y_r & g & Y_{\dot{\eta}} & Y_\eta \\
L_v & L_p & L_r & 0 & L_{\dot{\eta}} & L_\eta \\
N_v & N_p & N_r & 0 & N_{\dot{\eta}} & N_\eta \\
0 & 1 & \sin\theta_0 & 0 & 0 & 0 \\
\hline
\eta_v & \eta_p & \eta_r & 0 & -2\zeta\omega & -\omega^2 \\
0 & 0 & 0 & 0 & 1 & 0
\end{array} \right]
\begin{Bmatrix} v \\ p \\ r \\ \phi \\ \dot{\eta} \\ \eta \end{Bmatrix} +
\left[\begin{array}{cc}
Y_{\delta_{lat}} & Y_{\delta_{ped}} \\
L_{\delta_{lat}} & L_{\delta_{ped}} \\
N_{\delta_{lat}} & N_{\delta_{ped}} \\
0 & 0 \\
\hline
\eta_{\delta_{lat}} & \eta_{\delta_{ped}} \\
0 & 0
\end{array} \right]
\begin{Bmatrix} \delta \end{Bmatrix}
$$

$$(5.32)$$

$$
p_{\text{measured}} = \begin{bmatrix} 0 & 1 & 0 & 0 & 0 & 0 \end{bmatrix}
\begin{Bmatrix} v \\ p \\ r \\ \phi \\ \dot{\eta} \\ \eta \end{Bmatrix} +
\begin{bmatrix} 0 \end{bmatrix} \begin{Bmatrix} \delta \end{Bmatrix}
$$

$$(5.33)$$

with $\theta_0 = -0.039$ rad.

For the hovering tilt-rotor example, the stability and control derivatives are :

$$
\begin{array}{ccc|cc}
Y_{v\mathrm{mb}} = -0.0778 & Y_{p\mathrm{mb}} = -4.75 & Y_{r\mathrm{mb}} = 0.853 & Y_{\dot{\eta}\mathrm{mb}} = 2.04 & Y_{\eta\mathrm{mb}} = 102 \\[2mm]
L_{v\mathrm{mb}} = 0.0170 & L_{p\mathrm{mb}} = 0.785 & L_{r\mathrm{mb}} = -0.061 & L_{\dot{\eta}\mathrm{mb}} = -1.73 & L_{\eta\mathrm{mb}} = -163 \\[2mm]
N_{v\mathrm{mb}} = 0.00013 & N_{p\mathrm{mb}} = 0.0254 & N_{r\mathrm{mb}} = -0.179 & N_{\dot{\eta}\mathrm{mb}} = 0.0385 & N_{\eta\mathrm{mb}} = 3.93 \\[2mm]
\hline
\eta_{v\mathrm{mb}} = 0.0434 & \eta_{p\mathrm{mb}} = 3.02 & \eta_{r\mathrm{mb}} = -0.541 & \zeta_{\mathrm{mb}} = 0.112 & \omega = 16.6
\end{array}
$$

$$(5.34)$$

$$
\begin{array}{cc}
Y_{\delta_{lat}\mathrm{mb}} = -0.375 & Y_{\delta_{ped}\mathrm{mb}} = -0.528 \\[2mm]
L_{\delta_{lat}\mathrm{mb}} = 0.0175 & L_{\delta_{ped}\mathrm{mb}} = 0.120 \\[2mm]
N_{\delta_{lat}\mathrm{mb}} = 0.0205 & N_{\delta_{ped}\mathrm{mb}} = 0.030 \\[2mm]
\hline
\eta_{\delta_{lat}\mathrm{mb}} = 0.414 & \eta_{\delta_{ped}\mathrm{mb}} = 0.286
\end{array}
$$

5.10.2 Rigid-Body Models

A purely rigid-body model of the same aircraft (without any elastic motion) has the following form:

$$
\begin{Bmatrix} \dot{v} \\ \dot{p} \\ \dot{r} \\ \dot{\phi} \end{Bmatrix} =
\begin{bmatrix}
Y_v & Y_p & Y_r & g \\
L_v & L_p & L_r & 0 \\
N_v & N_p & N_r & 0 \\
0 & 1 & \sin\theta_0 & 0
\end{bmatrix}
\begin{Bmatrix} v \\ p \\ r \\ \phi \end{Bmatrix} +
\begin{bmatrix}
Y_{\delta_{lat}} & Y_{\delta_{ped}} \\
L_{\delta_{lat}} & L_{\delta_{ped}} \\
N_{\delta_{lat}} & N_{\delta_{ped}} \\
0 & 0
\end{bmatrix}
\{\delta\}
\qquad (5.35)
$$

$$
p_{\text{measured}} = \begin{bmatrix} 0 & 1 & 0 & 0 \end{bmatrix} \begin{Bmatrix} v \\ p \\ r \\ \phi \end{Bmatrix} + \begin{bmatrix} 0 \end{bmatrix} \{\delta\} \tag{5.36}
$$

$$
\begin{aligned}
& Y_{v\text{rb}} = -0.0799 \quad && Y_{p\text{rb}} = -3.21 \quad && Y_{r\text{rb}} = -1.28 \\
& L_{v\text{rb}} = -0.00824 \quad && L_{p\text{rb}} = -1.02 \quad && L_{r\text{rb}} = 0.255 \\
& N_{v\text{rb}} = 0.0010 \quad && N_{p\text{rb}} = 0.0628 \quad && N_{r\text{rb}} = -0.194
\end{aligned} \tag{5.37}
$$

$$
\begin{aligned}
& Y_{\delta_{lat}\text{rb}} = 0.045 \quad && Y_{\delta_{ped}\text{rb}} = -0.382 \\
& L_{\delta_{lat}\text{rb}} = -0.229 \quad && L_{\delta_{ped}\text{rb}} = -0.0504 \\
& N_{\delta_{lat}\text{rb}} = 0.0281 \quad && N_{\delta_{ped}\text{rb}} = 0.0357
\end{aligned}
$$

There are large changes in rigid-body portion of the stability derivatives between the rigid-body and multi-body models, with some derivatives even changing sign. The rigid-body portion of the multi-body model place the fuselage, so these stability and control derivatives lack meaning in the classical linear model sense. Note especially the large aeroelastic coupling term, L_η as well as small rigid body roll control derivative, $L_{\delta_{lat}}$, when comparing the multi-body model to the rigid-body model. The lateral control derivative is small because this input excites wing bending, so the control comes from the structural control derivative. Wing bending does not impart yaw moments, so the multi-body and rigid-body yaw control derivatives, $N_{\delta_{ped}}$, are nearly identical. If a anti-symmetric chordwise bending mode was included, the

yaw control would come through that mode's bending and the rigid-body control derivative in the multi-body model would be small. Performing a quasi-steady reduction of the flexible model gives the following static-elastic stability and control derivatives.

$$Y_{vse} = -0.0617 \quad Y_{pse} = -3.63 \quad Y_{rse} = 0.653$$

$$L_{vse} = -0.00869 \quad L_{pse} = -1.003 \quad L_{rse} = 0.259 \tag{5.38}$$

$$N_{vse} = 0.00075 \quad N_{pse} = 0.0685 \quad N_{rse} = -0.186$$

$$Y_{\delta_{lat}se} = -0.222 \quad Y_{\delta_{ped}se} = -0.422$$

$$L_{\delta_{lat}se} = -0.228 \quad L_{\delta_{ped}se} = -0.0495$$

$$N_{\delta_{lat}se} = 0.0264 \quad N_{\delta_{ped}se} = 0.0341$$

The static-elastic model is similar to the rigid-body model, meaning there are only slight alterations the the rigid-body dynamics caused by structural flexibility. The flex factors for key stability and control derivatives are:

$$ff_{L_p} = 0.98$$

$$ff_{L_v} = 1.055$$

$$ff_{Y_v} = 0.773$$

$$ff_{N_r} = 0.96 \tag{5.39}$$

$$ff_{N_v} = 0.736$$

$$ff_{L_{\delta_{lat}}} = 0.995$$

$$ff_{N_{\delta_{ped}}} = 0.954$$

These flex factors further illustrate the similarity between the two models. The large flex factors for Y_v and N_v are caused by the rotor being pointed slightly inboard due to structural bending. When the system is perturbed in the lateral direction, the large changes in these two stability derivatives come from the changes in rotor forcing.

5.10.3   Mean-Axis Model

Converting the multi-body model to mean-axis form, the rigid-body stability derivatives are placed in the upper-left quadrant. The rigid-body coupling terms in the lower-left quadrant and the aeroelastic coupling terms in the upper-right quadrant are identified so that the static-elastic model is obtained upon reduction of structural modes. The structural control derivative is also left in the identification. Expanding upon the simple example shown in Eqn. (5.27), the aeroelastic coupling stability derivatives important in the static-elastic reduction are those which multiply the structural displacement degree of freedom.

$$
\begin{aligned}
A_{se} &=
\begin{bmatrix}
Y_v & Y_p & Y_r & g \\
L_v & L_p & L_r & 0 \\
N_v & N_p & N_r & 0 \\
0 & 1 & \sin(\theta) & 0
\end{bmatrix}
-
\begin{bmatrix}
Y_{\dot{\eta}} & Y_\eta \\
L_{\dot{\eta}} & L_\eta \\
N_{\dot{\eta}} & N_\eta \\
0 & 0
\end{bmatrix}
\begin{bmatrix}
0 & 1 \\
-\frac{1}{\omega^2} & -\frac{2\zeta}{\omega}
\end{bmatrix}
\begin{bmatrix}
\eta_v & \eta_p & \eta_r & 0 \\
0 & 0 & 0 & 0
\end{bmatrix} \\[2em]
&=
\begin{bmatrix}
Y_v & Y_p & Y_r & g \\
L_v & L_p & L_r & 0 \\
N_v & N_p & N_r & 0 \\
0 & 1 & \sin(\theta) & 0
\end{bmatrix}
+ \frac{1}{\omega^2}
\begin{bmatrix}
Y_\eta \eta_v & Y_\eta \eta_p & Y_\eta \eta_r & 0 \\
L_\eta \eta_v & L_\eta \eta_p & L_\eta \eta_r & 0 \\
N_\eta \eta_v & N_\eta \eta_p & N_\eta \eta_r & 0 \\
0 & 0 & 0 & 0
\end{bmatrix}
\end{aligned}
\tag{5.40}
$$

similarly:

$$
B_{se} =
\begin{bmatrix}
Y_{\delta_{lat}} & Y_{\delta_{ped}} \\
L_{\delta_{lat}} & L_{\delta_{ped}} \\
N_{\delta_{lat}} & N_{\delta_{ped}} \\
0 & 0
\end{bmatrix}
+ \frac{1}{\omega'^2}
\begin{bmatrix}
Y_\eta \eta_{\delta_{lat}} & Y_\eta \eta_{\delta_{ped}} \\
L_\eta \eta_{\delta_{lat}} & L_\eta \eta_{\delta_{ped}} \\
N_\eta \eta_{\delta_{lat}} & N_\eta \eta_{\delta_{ped}} \\
0 & 0
\end{bmatrix}
\tag{5.41}
$$

The aeroelastic coupling terms which multiply the structural rate term (i.e. $L_{\dot{\eta}}$) do not appear in the final expression and can be dropped and left out of the identification. The aeroelastic coupling and rigid-body coupling terms are correlated, so there is no simple expression to identify individual derivatives as in the derivations presented before when roll was the only rigid-body degree of freedom. Since these values are correlated, multiple responses should be used in the process to identify these values. If sensor measurements exist, they can help identify structural modes
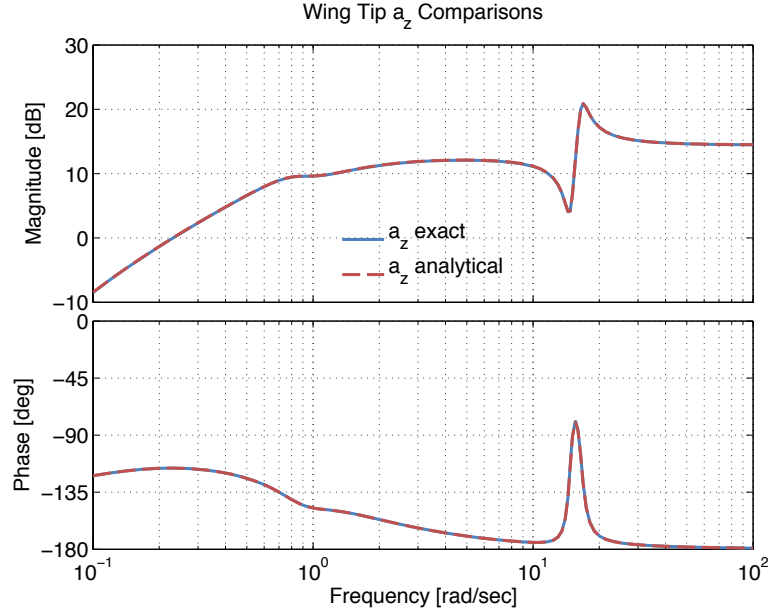
Figure 5.3: $\frac{a_z}{\delta}$: wing tip accelerations to lateral stick inputs

and structural influences on rigid-body motion. Wing-tip and mid-span accelerometers are used here as well as wing root strain. Since wing acceleration is a function of time-derivatives of states, the output matrices are unknown functions of the state and control matrices. It is desirable to make a simplified expression for wing tip acceleration based on linear combinations of states and their time derivatives. The wing tip acceleration is simplified to be a sum of the roll acceleration multiplied by the distance to the sensor (x_{sens}) and the acceleration caused by structural bending of the wing.

$$a_z = \dot{p} x_{\mathrm{sens}} + \Phi_\eta \ddot{\eta} \tag{5.42}$$

The influence coefficient on the structural acceleration term simply adds units to the non-dimensional acceleration. In the multi-body tiltrotor example, this value is 32.5. The mean-axis influence coefficient is left in the identification since the mode

175

in this model has different meaning than in the multi-body model. The response comparisons of the full acceleration and the simplified expression, shown in Fig. 5.3, show the simplified model is essentially identical to the full response and thus adequate for system identification. The primary focus of the identification is on the roll response to lateral stick inputs. Lateral velocity and yaw responses as well as responses to pedal inputs were also used. This array of responses helps ensure that the non-dominant terms in roll are still well identified and gives better Cramer-Rao bounds and reduces parameter insensitivity. More information on system identification can be found in Ref. 97. The identification results are presented in Appendix B.

The identified $L_\eta = -0.668$ is much smaller than its original value of $L_\eta = -163$ (Eqn. (5.34)) from the multi-body model. The aeroelastic coupling terms in the multi-body model transmit not only forcing and moments from wing aerodynamic changes as in the mean-axis model, but all forcing transmitted to the fuselage. In this model, no forcing is being transmitted to the fuselage without wing bending. In the mean-axis model, rigid-body forcing is already being transmitted through, only changes based on aerodynamics are not. The near zero identified L_η means that in hover, wing bending produces insignificant aerodynamic changes on the aircraft. This is a fairly intuitive response as the wings in hover do not produce lift, so changing the wings angle of attack through wing bending is meaningless. The wings are only affected by the rotor downwash. The rotor also does not produce large changes in lift due to changes in wing bending. The identified mean-axis model has

the form:

$$Y_{vma} = -0.0798 \quad Y_{pma} = -3.21 \quad Y_{rma} = -1.28 \quad \bigg| \quad Y_{\dot{\eta}ma} = 0.0 \quad Y_{\eta ma} = 25.5$$

$$L_{vma} = -0.00824 \quad L_{pma} = -1.02 \quad L_{rma} = 0.255 \quad \bigg| \quad L_{\dot{\eta}ma} = 0.0 \quad L_{\eta ma} = -0.668$$

$$N_{vma} = 0.0010 \quad N_{pma} = 0.0628 \quad N_{rma} = -0.194 \quad \bigg| \quad N_{\dot{\eta}ma} = 0.0 \quad N_{\eta ma} = -0.237$$

$$\eta_{vma} = 0.268 \quad \eta_{pma} = 0.00 \quad \eta_{rma} = 0.00 \quad \bigg| \quad \zeta_{ma} = 0.0647 \quad \omega = 16.7$$

$$(5.43)$$

$$Y_{\delta_{lat}ma} = -0.228 \quad Y_{\delta_{ped}ma} = -0.382$$

$$L_{\delta_{lat}ma} = -0.229 \quad L_{\delta_{ped}ma} = -0.0504$$

$$N_{\delta_{lat}ma} = 0.0281 \quad N_{\delta_{ped}ma} = 0.0357$$

$$\eta_{\delta_{lat}ma} = 0.414 \quad \eta_{\delta_{ped}ma} = 0.286$$

The output equation now contains the sensor's response to local bending due to the structural mode:

$$p_{\text{measured}} = \begin{bmatrix} 0 & 1 & 0 & 0 & \Phi_{pma} & 0 \end{bmatrix} \begin{Bmatrix} v \\ p \\ r \\ \phi \\ \dot{\eta} \\ \eta \end{Bmatrix} + \begin{bmatrix} 0 \end{bmatrix} \begin{Bmatrix} \delta \end{Bmatrix} \qquad (5.44)$$

The full Φ is first determined by the eigenvector (Eqn. (5.16)) or time history plot showing the motion of the fuselage and wing tip. The full Φ (Eqn. 5.9) from the eigenvector ($\Phi = 0.5918$) matches closely to the $L_{\eta \text{mb}}/\omega^2$ approximation

177

($\Phi = 0.5915$), and shows that even for a larger degree of freedom system, the simplifications used to derivation of the influence coefficient were valid. The influence coefficient as determined in Eqn. (5.7) becomes:

$$\Phi_{p\mathrm{ma}} = 0.5891 \tag{5.45}$$

The identified value of this influence coefficient is $\Phi_{p\mathrm{ma}} = 0.5947$. This $\Phi_{p\mathrm{ma}}$ contains all elastic bending contributions except those due to aerodynamics. The relative similarity of this value to the full value of Φ and the near zero value of the identified $L_{\eta\mathrm{ma}}$ shows that in hover, wing bending produces negligible effects on the rigid-body roll response of the aircraft. Therefore, the roll sensor, located at the CG in this case, picks up elastic bending effects through the influence coefficient. The influence coefficients not changing means that the measured response is not affected by wing bending due to aerodynamics and forcing on the structural mode comes from elsewhere. The aerodynamic effects of wing bending have thus been effectively isolated from the model.

The static-elastic model has been defined as a model with rigid-body degrees of freedom that retains static-elastic effects of aerodynamic changes due to structural bending on rigid-body motion. It is obtained from a quasi-static reduction of the structural modes. The reduction of the structural modes from the mean-axis model should produce the same static-elastic model as the reduction of the structural modes from the multi-body model, Eqn (5.46). The reduction of the structural modes from

Eqn. (5.43) produces the following stability and control derivatives:

$$Y_{v\text{se}} = -0.0554 \quad Y_{p\text{se}} = -3.21 \quad Y_{r\text{se}} = 1.279$$

$$L_{v\text{se}} = -0.00888 \quad L_{p\text{se}} = -1.024 \quad L_{r\text{se}} = 0.255 \qquad (5.46)$$

$$N_{v\text{se}} = 0.00079 \quad N_{p\text{se}} = 0.0628 \quad N_{r\text{se}} = -0.194$$

$$Y_{\delta_{lat}\text{se}} = -0.190 \quad Y_{\delta_{ped}\text{se}} = -0.355$$

$$L_{\delta_{lat}\text{se}} = -0.230 \quad L_{\delta_{ped}\text{se}} = -0.0511$$

$$N_{\delta_{lat}\text{se}} = 0.0278 \quad N_{\delta_{ped}\text{se}} = 0.0355$$

This gives the following flex factors:

$$ff_{L_p} = 1.00$$

$$ff_{L_v} = 1.078$$

$$ff_{Y_v} = 0.694$$

$$ff_{N_r} = 1.00 \qquad (5.47)$$

$$ff_{N_v} = 0.777$$

$$ff_{L_{\delta_{lat}}} = 1.004$$

$$ff_{N_{\delta_{ped}}} = 0.993$$

Comparing these flex factors with those of the multi-body reduction (Eqn.(5.39)) shows very similar trends. Almost all flex factors are near one, except ff_{Y_v} and ff_{N_v}, which are in the range of 0.7 to 0.8. The mean-axis identification produced $\eta_p = 0$ and $\eta_r = 0$. These terms appear in the static-elastic reduction of the columns associated with p and r states (see Eqn. (5.40)). Since they are zero, the second and third columns of the static-elastic model above (from mean-axis reduction) will
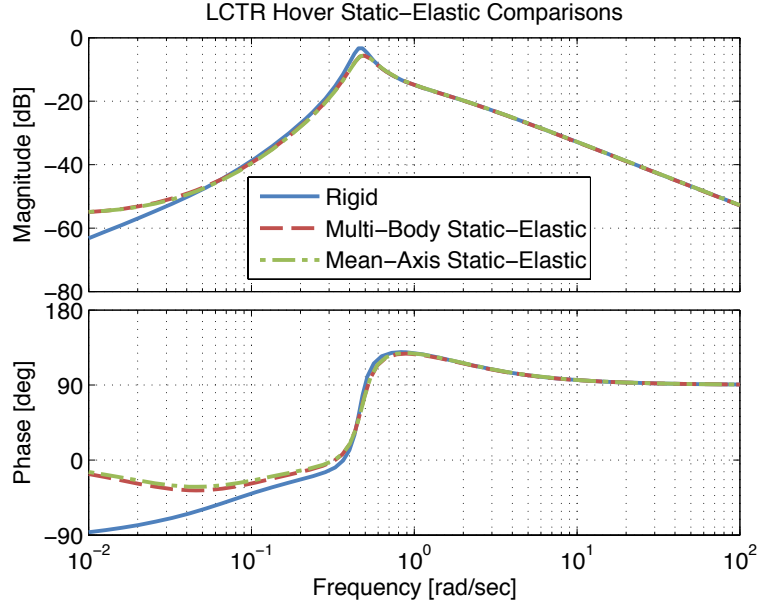
Figure 5.4: $\frac{p}{\delta_{lat}}$: multi-body and mean-axis static-elastic model comparisons for hovering LCTR

be unchanged from the rigid-body model and will have a flex factor of one, hence $ff_{L_p} = 1$ and $ff_{N_r} = 1$. The static-elastic response for the multi-body and mean-axis models are compared with the rigid response and are shown in Fig. 5.4. These static-elastic models match well, meaning the coupling terms are well identified and recreate the key control and stability derivatives during reduction.

5.10.4   Hybrid-Flexible and Decoupled Models

The hybrid-flexible model contains the static-elastic stability derivatives in the upper-left quadrant and has no aeroelastic coupling in the upper-right quadrant. Since this model has no aeroelastic coupling, the static-elastic reduction of this model does not alter any of the control or stability derivatives. The rigid-body response is decoupled from the elastic states and the elastic mode sensed comes

purely from the output equation. The rigid-body coupling terms from the mean-axis identification are retained. If no mean-axis model exists, these terms could be identified. The stability and control derivatives are as follows:

$$
\begin{array}{lll|ll}
Y_{v\text{hf}} = -0.0617 & Y_{p\text{hf}} = -3.63 & Y_{r\text{hf}} = 0.653 & Y_{\dot{\eta}\text{hf}} = 0.0 & Y_{\eta\text{hf}} = 0.0 \\[2mm]
L_{v\text{hf}} = -0.00869 & L_{p\text{hf}} = -1.003 & L_{r\text{hf}} = 0.259 & L_{\dot{\eta}\text{hf}} = 0.0 & L_{\eta\text{hf}} = 0.0 \\[2mm]
N_{v\text{hf}} = 0.00075 & N_{p\text{hf}} = 0.0685 & N_{r\text{hf}} = -0.186 & N_{\dot{\eta}\text{hf}} = 0.0 & N_{\eta\text{hf}} = 0.0 \\[2mm]
\hline
\eta_{v\text{hf}} = 0.268 & \eta_{p\text{hf}} = 0.00 & \eta_{r\text{hf}} = 0.00 & \zeta_{\text{hf}} = 0.0647 & \omega = 16.7
\end{array}
$$

$$(5.48)$$

$$
\begin{array}{ll}
Y_{\delta_{lat}\text{hf}} = -0.222 & Y_{\delta_{ped}\text{hf}} = -0.422 \\[2mm]
L_{\delta_{lat}\text{hf}} = -0.228 & L_{\delta_{ped}\text{hf}} = -0.0495 \\[2mm]
N_{\delta_{lat}\text{hf}} = 0.0264 & N_{\delta_{ped}\text{hf}} = 0.0341 \\[2mm]
\hline
\eta_{\delta_{lat}} = 0.414 & \eta_{\delta_{ped}} = 0.286
\end{array}
$$

The output equation is modified to include the full influence of the modal bending on the equivalent rigid body response as well:

$$
p_{\text{measured}} = \begin{bmatrix} 0 & 1 & 0 & 0 & \Phi_{p\text{hf}} & 0 \end{bmatrix} \begin{Bmatrix} v \\ p \\ r \\ \phi \\ \dot{\eta} \\ \eta \end{Bmatrix} + \begin{bmatrix} 0 \end{bmatrix} \begin{Bmatrix} \delta \end{Bmatrix} \tag{5.49}
$$

181

where:

$$\Phi_{phf} = \frac{-L_{\eta ma}}{\omega^2} + \Phi_{pma} = \frac{0.668}{16.7^2} + 0.5891 = 0.5915 \tag{5.50}$$

or directly from the eigenvector of the system:

$$\Phi_p = \frac{\partial p}{\partial \dot{\eta}} = 0.5918 \tag{5.51}$$

The decoupled model is the same as the hybrid-flexible model with the rigid-body coupling terms, A_{ER} dropped as well.

The roll rate frequency response to lateral stick inputs, the primary response of interest of the systems described above, is given in Fig. 5.5. Off-axis and pedal responses are also shown in Figures 5.6 - 5.10. For the roll response, all four models match extremely well over a broad frequency range. The large separation of the structural mode from the rigid body modes ($\omega_{\min \text{ flex}}/\omega_{\max \text{ rb}} > 10$) is well within the guideline set by Eqn. (5.4). If the modes were closer together, the responses might differ more in the frequency range of interest. The slight differences at high-frequency in the phase plot for the decoupled model suggest that the rigid-body coupling terms are important for accurate identification of the dynamics around the structural mode. The hybrid-flexible and mean-axis models fully capture the dynamics of the multi-body model. The hybrid-flexible model, however, contains fewer stability derivatives and would be easier to identify from flight data. It is also a simpler model to recreate using the steps above. The added complexity of identifying the mean-axis model is not justified if the frequency separation in the

182

modes is adequate as in the given example. This model form may be necessary if the frequency separation is smaller than that given in the inequality in Eqn. (5.4). In analyzing the off-axis and pedal responses, similar trends to the roll response are seen. Generally, the reduced complexity of the hybrid-flexible and decoupled models are sufficient for obtaining linear models accurate up to, and even above, the structural modes for the LCTR configuration in hover.

Figure 5.5: $\frac{p}{\delta_{lat}}$: roll rate response comparisons of LCTR to lateral stick inputs in hover
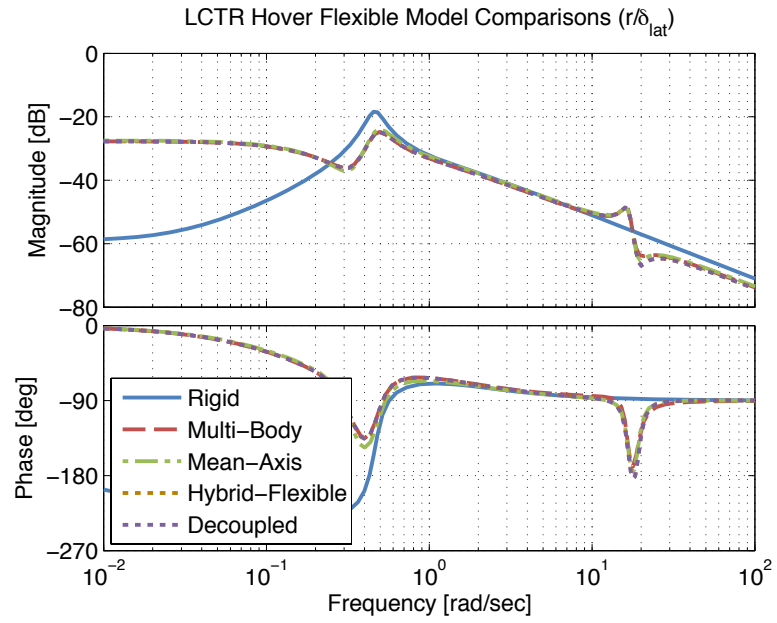
Figure 5.6: $\frac{r}{\delta_{lat}}$: yaw rate response comparisons of LCTR to lateral stick inputs in hover

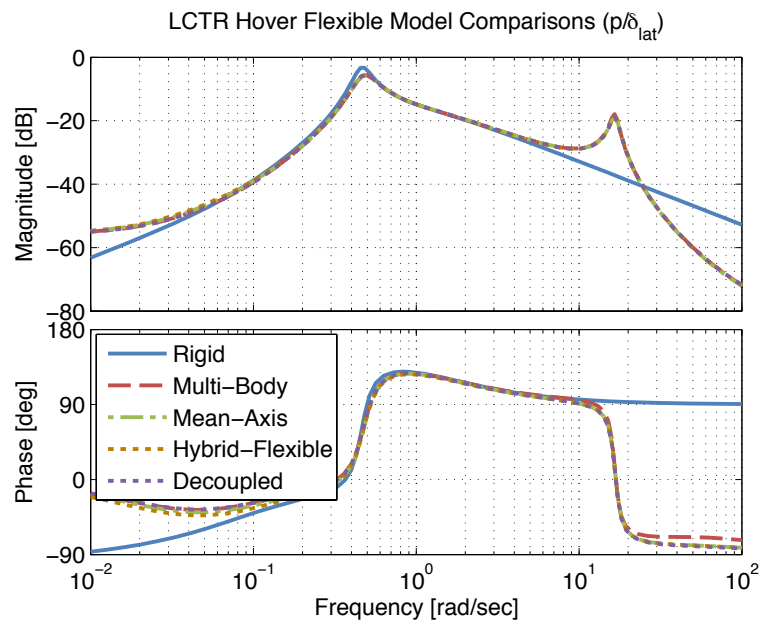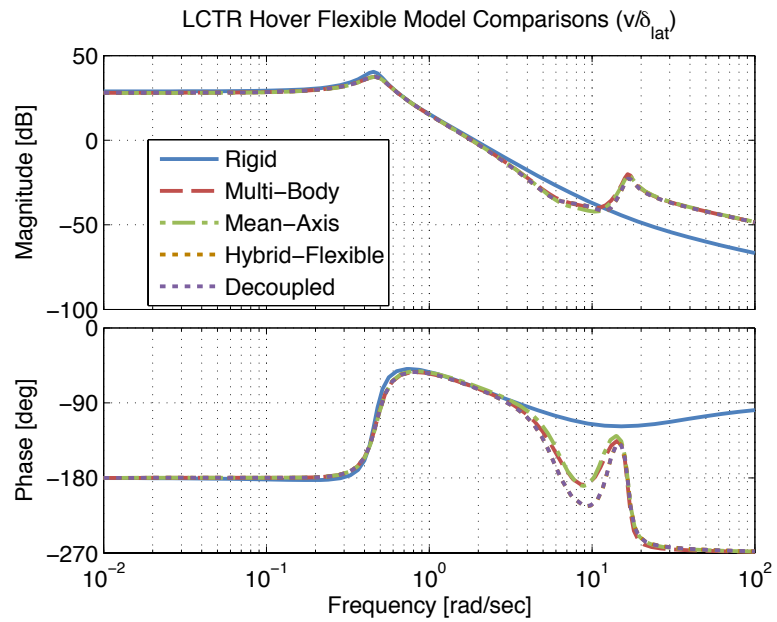Figure 5.7: $\frac{v}{\delta_{lat}}$: lateral velocity response comparisons of LCTR to lateral stick inputs in hover
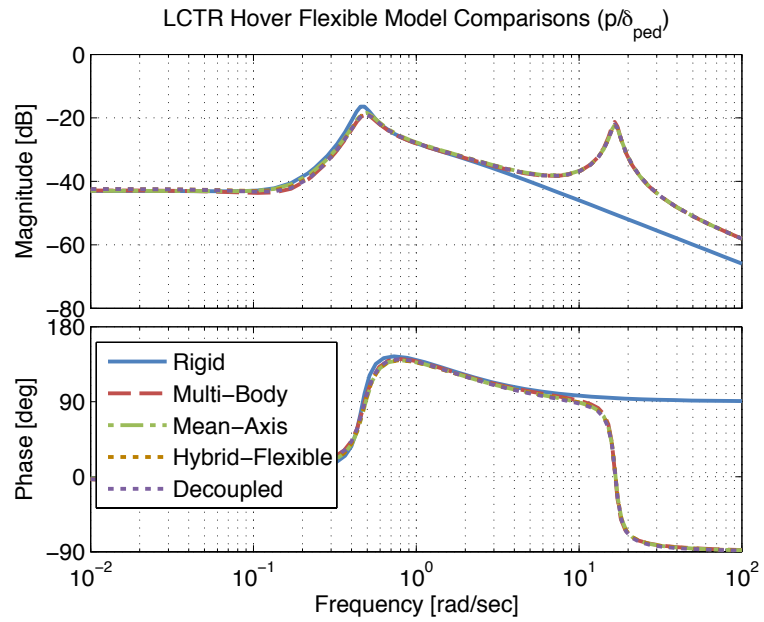
Figure 5.8: $\frac{p}{\delta_{ped}}$: roll rate response comparisons of LCTR to pedal inputs in hover
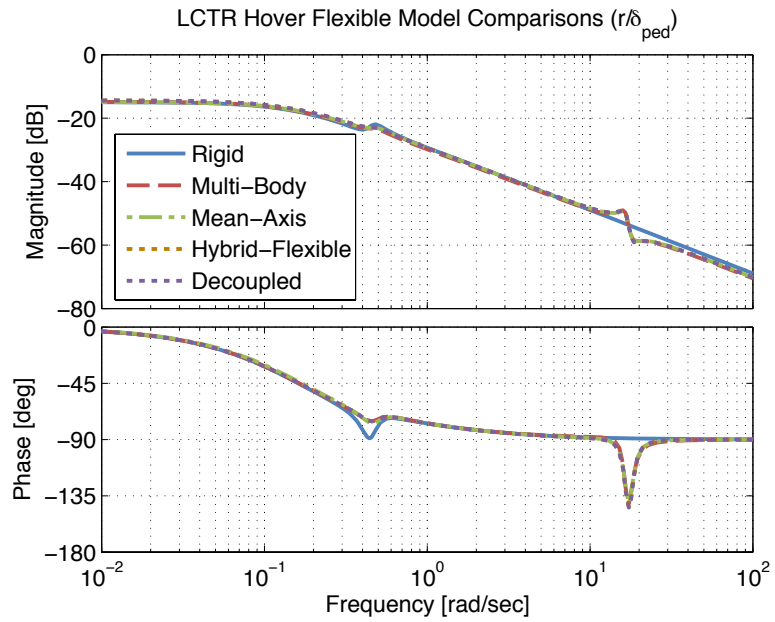
Figure 5.9: $\frac{r}{\delta_{ped}}$: yaw rate response comparisons of LCTR to pedal inputs in hover
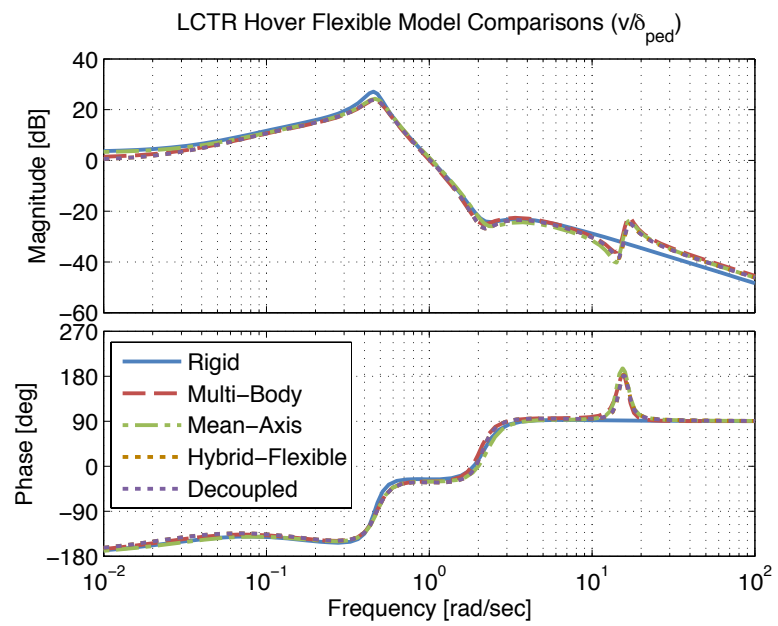
Figure 5.10: $\frac{v}{\delta_{ped}}$: lateral velocity response comparisons of LCTR to pedal inputs in hover

5.11 Tilt-Rotor Example: Cruise

The same steps above are recreated for the tilt-rotor in a 160 knot cruise condition.

5.11.1 Multi-Body Model

Starting again from the multi-body form of Eqn. (5.32):

$$
\begin{array}{lll|ll}
Y_{v\mathrm{mb}} = -0.272 & Y_{p\mathrm{mb}} = 36.86 & Y_{r\mathrm{mb}} = -264.7 & Y_{\dot{\eta}\mathrm{mb}} = 2.00 & Y_{\eta\mathrm{mb}} = 86.37 \\[4pt]
L_{v\mathrm{mb}} = -0.0173 & L_{p\mathrm{mb}} = 0.095 & L_{r\mathrm{mb}} = 0.360 & L_{\dot{\eta}\mathrm{mb}} = -1.107 & L_{\eta\mathrm{mb}} = -161.5 \\[4pt]
N_{v\mathrm{mb}} = 0.0032 & N_{p\mathrm{mb}} = 0.191 & N_{r\mathrm{mb}} = -0.280 & N_{\dot{\eta}\mathrm{mb}} = -0.096 & N_{\eta\mathrm{mb}} = 4.57 \\[4pt]
\hline
\eta_{v\mathrm{mb}} = -0.0278 & \eta_{p\mathrm{mb}} = 1.890 & \eta_{r\mathrm{mb}} = -0.384 & \zeta_{\mathrm{mb}} = 0.0895 & \omega = 16.5
\end{array}
$$

$$(5.52)$$

$$
\begin{array}{ll}
Y_{\delta_{lat}\mathrm{mb}} = -0.144 & Y_{\delta_{ped}\mathrm{mb}} = -1.355 \\[4pt]
L_{\delta_{lat}\mathrm{mb}} = -0.044 & L_{\delta_{ped}\mathrm{mb}} = -0.258 \\[4pt]
N_{\delta_{lat}\mathrm{mb}} = -0.019 & N_{\delta_{ped}\mathrm{mb}} = 0.140 \\[4pt]
\hline
\eta_{\delta_{lat}\mathrm{mb}} = 0.110 & \eta_{\delta_{ped}\mathrm{mb}} = -0.334
\end{array}
$$

with $\theta_0 = 0.151$ rad.

The aero-elastic coupling term $L_{\eta\mathrm{mb}} = -161.5$ has a similar value to the hover case ($L_{\eta\mathrm{mb}} = -163$). This is expected because wing bending imparts moments at the wing root. If the wing bends the same amount, the moment at the root should be equal, regardless if the wing is in cruise or hover. This value can also be obtained

from a simple derivation. For the hover case, roll moments come from rotor forcing and impact the wing at the tip. In cruise, roll moments come from the ailerons, which span the outer portion of the wing. The following derivation assumes all forcing to be at the wing tip. Taking the static wing deflection, w, given a wing tip forcing "P" and solving for the wing deflection given a moment:

$$w = \frac{PL^3}{3EI} = \frac{ML^2}{3EI} \tag{5.53}$$

$$M = \frac{3EIw}{L^2} \tag{5.54}$$

This moment provides a roll acceleration to the fuselage.

$$M = \dot{p}I_{xx} \tag{5.55}$$

Equating the two moment equations and solving for $\dot{p}$ gives the roll acceleration caused by a quasi-static deflection of one of the wings.

$$\dot{p} = -\frac{3EIw}{I_{xx}L^2} \tag{5.56}$$

Values for the LCTR can be substituted into the equation above. Since $L_{\eta\mathrm{mb}}$ is for a wing antisymmetric mode, the total moment created by wing bending is multiplied by two, one for each wing. The moment is also negated since positive antisymmetric bending (right wing up), creates a negative roll moment. The value of I_{xx} is for the fuselage only, as wing bending only impacts moments transferred to the fuselage. Also, wing modal bending, η, is non-dimensional so the displacement

188

must be dimensionalized (multiplied by rotor radius, 32.5').

$$\dot{p} = -2 \left(\frac{3 \times (5.073 \times 10^8)}{(4.16 \times 10^5) \times 38.71^2} \right) 32.5\eta \tag{5.57}$$

$$\dot{p} = -158.7\eta \tag{5.58}$$

This value closely matches the values for the LCTR in hover and cruise, further verifying the model.

5.11.2   Rigid-Body Models

The purely rigid-body model of the same aircraft (without any elastic motion) has the following form:

$$
\begin{aligned}
Y_{v\mathrm{rb}} &= -0.2887 & Y_{p\mathrm{rb}} &= 39.29 & Y_{r\mathrm{rb}} &= -264.5 \\
L_{v\mathrm{rb}} &= 0.0005 & L_{p\mathrm{rb}} &= -1.136 & L_{r\mathrm{rb}} &= 0.567 \\
N_{v\mathrm{rb}} &= 0.0034 & N_{p\mathrm{rb}} &= -0.073 & N_{r\mathrm{rb}} &= -0.280
\end{aligned}
\tag{5.59}
$$

$$
\begin{aligned}
Y_{\delta_{lat}\mathrm{rb}} &= 0.006 & Y_{\delta_{ped}\mathrm{rb}} &= -1.508 \\
L_{\delta_{lat}\mathrm{rb}} &= -0.110 & L_{\delta_{ped}\mathrm{rb}} &= -0.061 \\
N_{\delta_{lat}\mathrm{rb}} &= -0.018 & N_{\delta_{ped}\mathrm{rb}} &= 0.135
\end{aligned}
$$

The static-elastic stability and control derivatives.

$$
\begin{aligned}
Y_{v\mathrm{se}} &= -0.281 & Y_{p\mathrm{se}} &= 37.46 & Y_{r\mathrm{se}} &= -264.8 \\
L_{v\mathrm{se}} &= -0.0007 & L_{p\mathrm{se}} &= -1.03 & L_{r\mathrm{se}} &= 0.589 \\
N_{v\mathrm{se}} &= 0.0027 & N_{p\mathrm{se}} &= 0.223 & N_{r\mathrm{se}} &= -0.286
\end{aligned}
\tag{5.60}
$$

$$Y_{\delta_{lat}\text{se}} = -0.109 \quad Y_{\delta_{ped}\text{se}} = -1.461$$

$$L_{\delta_{lat}\text{se}} = -0.110 \quad L_{\delta_{ped}\text{se}} = -0.059$$

$$N_{\delta_{lat}\text{se}} = -0.017 \quad N_{\delta_{ped}\text{se}} = 0.135$$

The rigid-body and static-elastic models above give the following flex factors.

$$ff_{Y_v} = 0.973$$

$$ff_{L_p} = 0.907$$

$$ff_{Y_p} = 0.953$$

$$ff_{N_r} = 1.022 \tag{5.61}$$

$$ff_{N_v} = 0.787$$

$$ff_{L_{\delta_{lat}}} = 0.994$$

$$ff_{N_{\delta_{ped}}} = 1.00$$

The flex factors for cruise also show the influence of structural bending on the rigid-body stability derivatives. These values are generally of the same magnitude in cruise as they are for hover, meaning the frequency responses are not anticipated to alter too much between the flexible and rigid cases at low frequencies.

5.11.3   Mean-Axis Model

The identification of the cruise model proved to be more challenging than the hover model and is described in Appendix B in Section B.2. The final identified model becomes:

$$Y_{v\text{ma}} = -0.2887 \quad Y_{p\text{ma}} = 39.29 \quad Y_{r\text{ma}} = -264.5 \quad \Big| \quad Y_{\dot{\eta}\text{ma}} = 0.0 \quad Y_{\eta\text{ma}} = 0.0$$

$$L_{v\text{ma}} = 0.00054 \quad L_{p\text{ma}} = -1.136 \quad L_{r\text{ma}} = 0.5671 \quad \Big| \quad L_{\dot{\eta}\text{ma}} = 0.0 \quad L_{\eta\text{ma}} = -41.32$$

$$N_{v\text{ma}} = 0.0034 \quad N_{p\text{ma}} = -0.073 \quad N_{r\text{ma}} = -0.28 \quad \Big| \quad N_{\dot{\eta}\text{ma}} = 0.0 \quad N_{\eta\text{ma}} = -49.29$$

$$\eta_{v\text{ma}} = 0.0062 \quad \eta_{p\text{ma}} = -1.250 \quad \eta_{r\text{ma}} = -0.204 \quad \Big| \quad \zeta_{\text{ma}} = 0.0603 \quad \omega = 16.65$$

$$(5.62)$$

$$Y_{\delta_{lat}\text{ma}} = -0.278 \quad Y_{\delta_{ped}\text{ma}} = -3.007$$

$$L_{\delta_{lat}\text{ma}} = -0.096 \quad L_{\delta_{ped}\text{ma}} = -0.097$$

$$N_{\delta_{lat}\text{ma}} = 0.0 \quad N_{\delta_{ped}\text{ma}} = 0.064$$

$$\eta_{\delta_{lat}\text{ma}} = 0.113 \quad \eta_{\delta_{ped}\text{ma}} = -0.334$$

The identified aeroelastic coupling L_η stability derivative is much larger here than in hover. This means bending of the antisymmetric wing bending mode produces significant aerodynamic rolling moment, whereas it was seen to be negligible in hover. This large value of L_η also means the influence coefficient Φ_{p_a} will not be the same as the full Φ as was the case for hover.

$$\Phi_{p_a} = \Phi + \frac{L_\eta}{\omega^2} = 0.5932 + \frac{41.32}{16.65^2} = 0.4442 \tag{5.63}$$

The identified value of Φ_{p_a} (Table B.5, parameter Phip) is 0.4439, a very good match with the derived value. The influence coefficient changing means that the bending within this mode is caused by aerodynamics.

The difference in influence coefficient from the hover case to the cruise case is now discussed. The antisymmetric mode is essentially identical in hover or cruise, and looks like the mode in Figure 5.1 in either case. The different mean-axis influence coefficient means that the *equivalent* rigid-body motion of the aircraft is different. The influence coefficient is then added to the equivalent rigid-body motion to obtain the actual motion at the sensor location. The multi-body case can be thought of one where the influence coefficient is zero. The sensor dynamics are picked up in the fuselage states fully as the fuselage participates in the mode. For the mean-axis model in hover, the influence coefficient was essentially L_η/ω^2 and the identified mean-axis L_η was zero. This means the equivalent rigid-body is not active in the mode, and the influence of the mode must be fully regained using the influence coefficient. In the cruise case, the equivalent rigid-body still participates in the mode as it is excited by wing bending. The influence coefficient is only partly responsible for regaining the response at the sensor location. This also means that the static-elastic response in cruise will be different than the rigid-body response. In hover, they were nearly identical.

The static-elastic reduction of the mean-axis model gives:

$$
\begin{aligned}
Y_v &= -0.289 & Y_p &= 39.29 & Y_r &= -264.5 \\
L_v &= -0.0004 & L_p &= -0.950 & L_r &= 0.598 \\
N_v &= 0.0023 & N_p &= 0.149 & N_r &= -0.244
\end{aligned}
\tag{5.64}
$$

$$Y_{\delta_{lat}} = -0.278 \quad Y_{\delta_{ped}} = -3.007$$

$$L_{\delta_{lat}} = -0.113 \quad L_{\delta_{ped}} = -0.048$$

$$N_{\delta_{lat}} = -0.02 \quad N_{\delta_{ped}} = 0.123$$

The flex factors are as follows:

$$ff_{Y_v} = 1.00$$

$$ff_{L_p} = 0.836$$

$$ff_{Y_p} = 1.00$$

$$ff_{N_r} = 0.871 \tag{5.65}$$

$$ff_{N_v} = 0.678$$

$$ff_{L_{\delta_{lat}}} = 1.021$$

$$ff_{N_{\delta_{ped}}} = 0.913$$

As for the hover case, these flex factors compare well with the static-elastic reduction of the multi-body model. The only flex factor that shows a significant differences is ff_{N_r}. In the identification, the parameter Y_η was set to zero, meaning the first row of the static-elastic reduction of the mean-axis form remains unchanged from the rigid-body values as per Eqn. (5.40).

In this cruise model, there are large flex factors for key stability derivatives of the roll response. Specifically, L_p changes between the rigid and flexible models and is the cause of the low frequency magnitude difference between the two models and the break in the response (around 1 rad/sec) occurring at slightly lower frequency in the cruise model. Static-elastic comparisons of the mean-axis and multi-body models are show in Fig. 5.11. As with the hover response, the static-elastic responses match

well together. The off-diagonal terms are well identified so that a reduction of the structural terms produces similar quasi-static dynamics (i.e. static bending produces the same result for both models). There are larger differences when compared to the rigid model in cruise than there were in hover. These differences were predicted by the large aeroelastic coupling terms in the cruise mean-axis model.
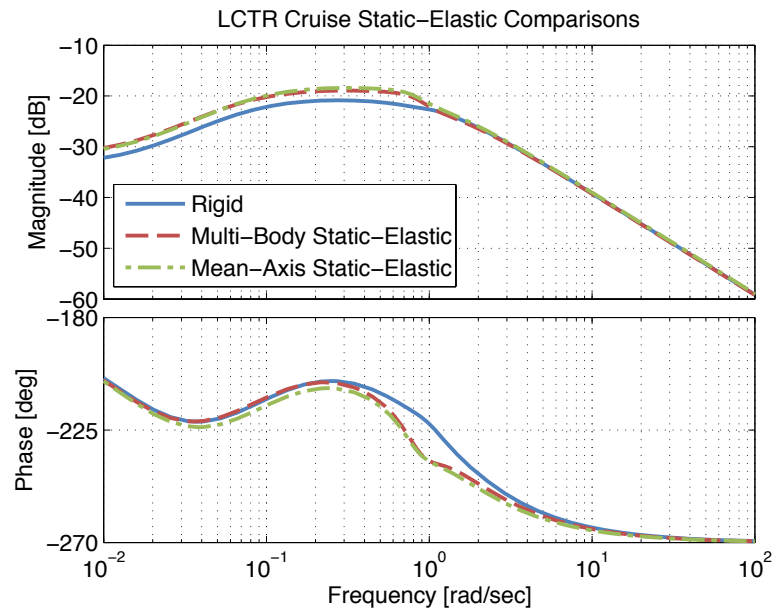

Figure 5.11: $\frac{p}{\delta_{lat}}$: multi-body and mean-axis static-elastic model comparisons for the LCTR in cruise

5.11.4   Hybrid-Flexible and Decoupled Models

The hybrid-flexible model is of the form:

$$
\begin{array}{lll|ll}
Y_v = -0.281 & Y_p = 37.46 & Y_r = -264.8 & Y_{\dot\eta} = 0.0 & Y_\eta = 0.0 \\[2mm]
L_v = -0.0007 & L_p = -1.03 & L_r = 0.589 & L_{\dot\eta} = 0.0 & L_\eta = 0.0 \\[2mm]
N_v = 0.0027 & N_p = 0.223 & N_r = -0.286 & N_{\dot\eta} = 0.0 & N_\eta = 0.0 \\[1mm]
\hline
\eta_v = 0.0062 & \eta_p = -1.250 & \eta_r = -0.204 & \zeta = 0.0603 & \omega = 16.65
\end{array}
\tag{5.66}
$$

$$
\begin{array}{ll}
Y_{\delta_{lat}} = -0.278 & Y_{\delta_{ped}} = -3.007 \\[2mm]
L_{\delta_{lat}} = -0.096 & L_{\delta_{ped}} = -0.097 \\[2mm]
N_{\delta_{lat}} = 0.0 & N_{\delta_{ped}} = 0.064 \\[1mm]
\hline
\eta_{\delta_{lat}} = 0.113 & \eta_{\delta_{ped}} = -0.334
\end{array}
$$

The decoupled model is the same as the hybrid-flexible model with the rigid-body coupling terms set to zero.

The final models are compared in Figures 5.12 - 5.17. The models are plotted for a large frequency range ($\omega = 0.01 - 100$ rad/sec) to capture the rigid-body and structural dynamics, even though the identification for many of these models occurred over a much smaller range. For the roll response to lateral stick inputs, the primary model of concern, there are slight differences between the models around the structural mode. Generally, the models match well at low frequency, but diverge around the structural mode. Aerodynamics has a much larger impact on cruise dynamics and the identified mean-axis model is not able to capture the dynamics

both in the rigid-body range as well as the structural range. The pedal responses for the hybrid-flexible and decoupled models are significantly different than the other responses, showing that aeroelastic coupling has a large impact on these responses. A new model was not identified for the hybrid-flexible model, it is a derivative of the mean-axis model. If a new model was identified to create new rigid-body coupling terms, the responses might match better. The hybrid-flexible and decoupled models are essentially identical for many of the responses, meaning rigid-body coupling does not have a large affect on the responses. These plots further validate the fact that the cruise model is significantly altered by aerodynamic changes due to wing bending, whereas the hover response is not.

Figure 5.12: $\frac{p}{\delta_{lat}}$: roll rate response of LCTR to lateral stick inputs in cruise (ID from $\omega = 0.01 - 22.0$ rad/sec)

196

Figure 5.13: $\frac{r}{\delta_{lat}}$: yaw rate response of LCTR to lateral stick inputs in cruise (ID from $\omega = 0.01 - 4.0$ rad/sec)

Figure 5.14: $\frac{v}{\delta_{lat}}$: lateral velocity response of LCTR to lateral stick inputs in cruise (ID from $\omega = 0.01 - 4.0$ rad/sec)

Figure 5.15: $\frac{p}{\delta_{ped}}$: roll rate response of LCTR to lateral stick inputs in cruise (ID from $\omega = 0.3 - 100.0$ rad/sec)
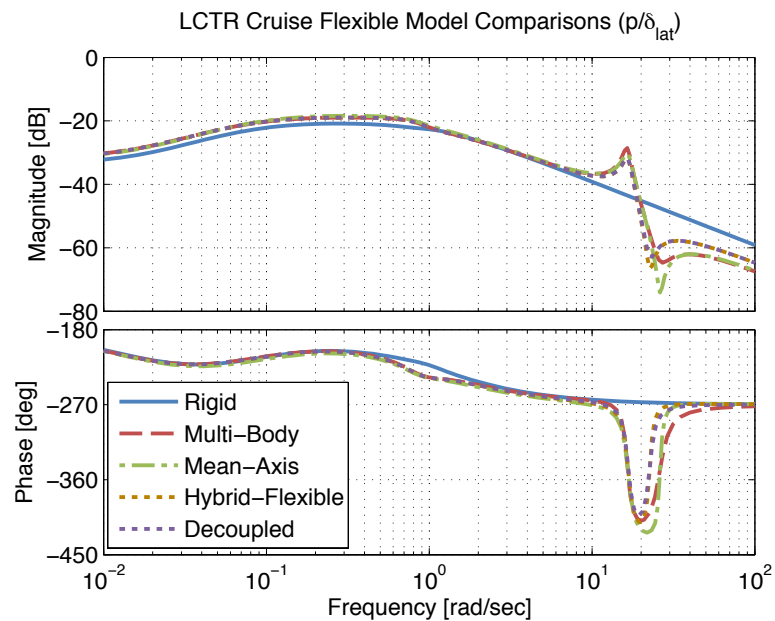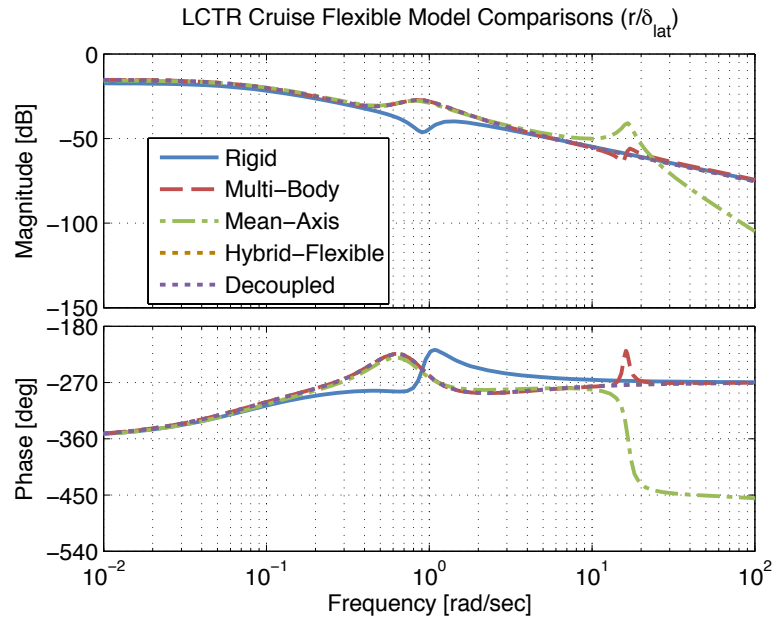

Figure 5.16: $\frac{r}{\delta_{ped}}$: yaw rate response of LCTR to lateral stick inputs in cruise (ID from $\omega = 0.01 - 4.0$ rad/sec)
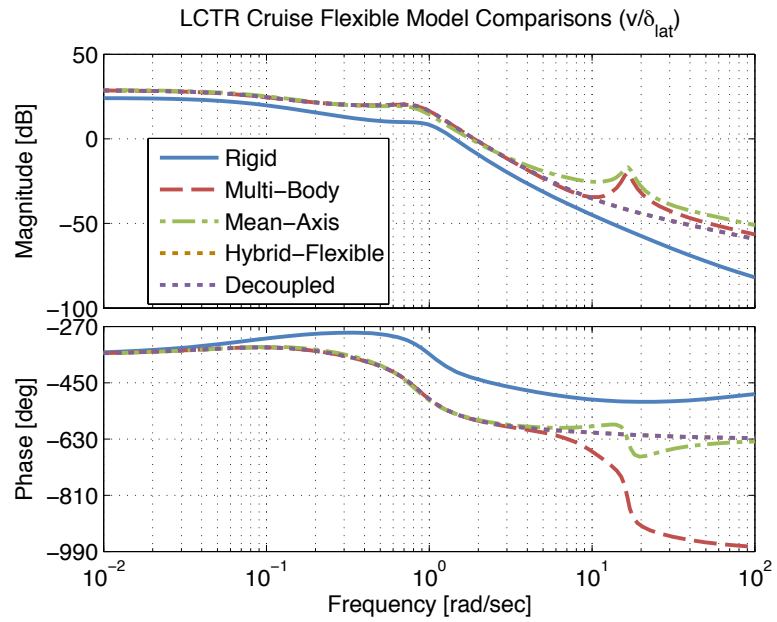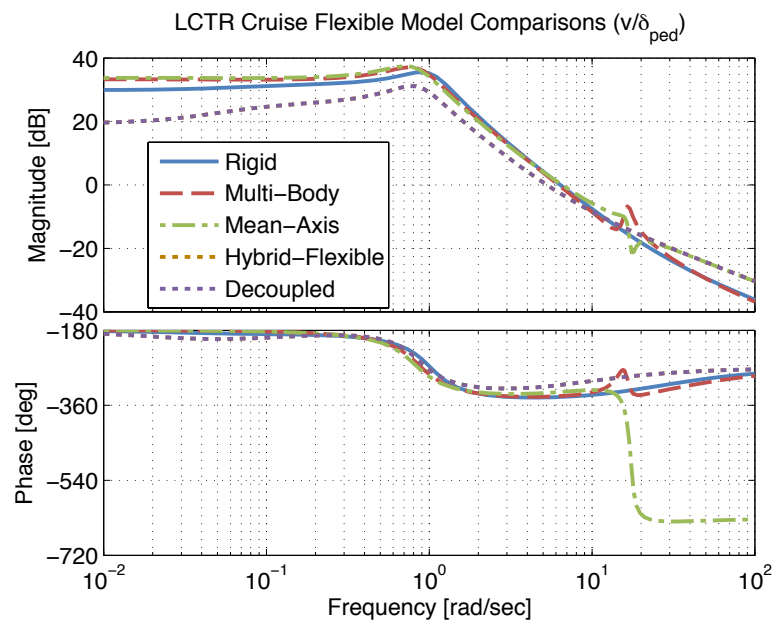
Figure 5.17: $\frac{v}{\delta_{ped}}$: lateral velocity response of LCTR to lateral stick inputs in cruise (ID from $\omega = 0.01 - 4.0$ rad/sec)
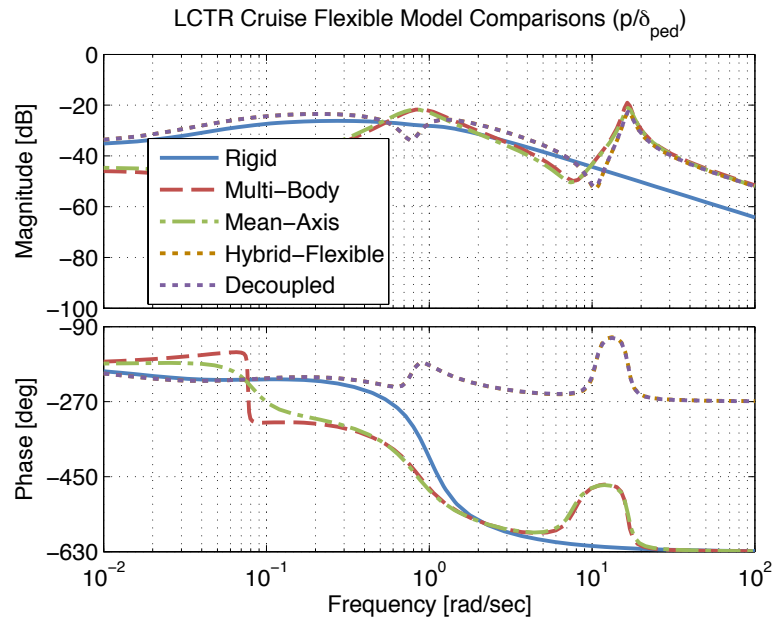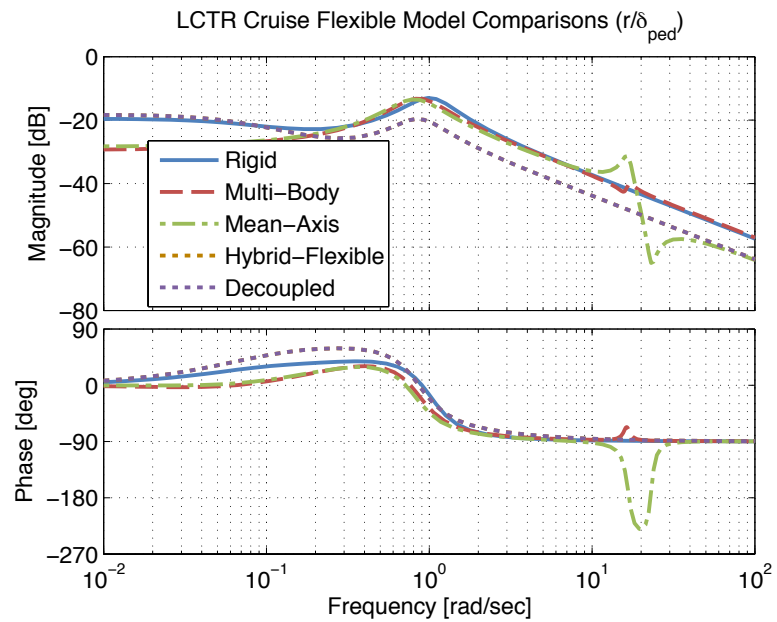
5.12 High Frequency Asymptotes

The high frequency roll acceleration response has an asymptote of L_δ. As previously mentioned, L_δ is near zero in the multi-body case as rotor forcing must first pass through the wing structure. However, the mean-axis, hybrid-flexible, and output models have the rigid-body or static-elastic L_δ, which is several orders of magnitude larger than the flexible case. It will be shown that the influence coefficient in the output of the flexible response serves to reduce the high frequency value of the rigid-body response back to the original flexible L_δ.

Starting from the multi-body model, the static-elastic model is obtained using Eqns. (5.5) and (5.6). Here L_δ and L_p without subscripts represent the original multi-body or mean-axis values. Once converted from multi-body form the response contains the structural mode multiplied by the influence coefficient. The decoupled model takes the following form:

$$\frac{\dot{p}}{\delta} = \frac{sp}{\delta} = \frac{sL_{\delta_{se}}}{s - L_{p_{se}}} + \Phi\frac{\dot{\eta}_\delta s^2}{s^2 + \omega^2} = \frac{s\left(L_\delta + \frac{L_n}{\omega^2}\dot{\eta}_\delta\right)}{s - \left(L_p + \frac{L_n}{\omega^2}\dot{\eta}_p\right)} + \frac{-L_\eta}{\omega^2}\frac{\dot{\eta}_\delta s^2}{s^2 + \omega^2} \tag{5.67}$$

At high frequency (s large), the transfer function approaches:

$$\frac{\dot{p}}{\delta} = \left(L_\delta + \frac{L_n}{\omega^2}\dot{\eta}_\delta\right) - \frac{L_\eta\dot{\eta}_\delta}{\omega^2} = L_\delta \tag{5.68}$$

Where L_δ is the original flexible model control derivative. See Fig. 5.18 for a comparison of the hovering LCTR, where a multi-body model response gave $L_\delta = 0.0175$, and the decoupled model gave $L_\delta = -0.228$. The high frequency

200
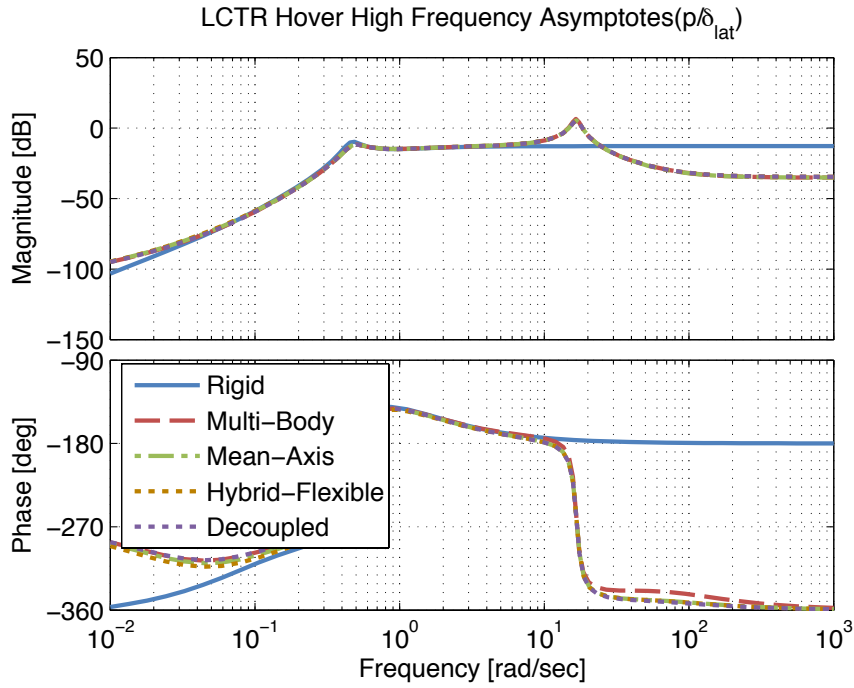
Figure 5.18: $\frac{\dot{p}}{\delta}$: roll acceleration response of LCTR to lateral stick inputs

approaches -34 dB, the value of the multi-body L_δ, as expected.

5.13   Chapter Summary

Different flexible model architectures have been analyzed. These include the multi-body model, which is formed by summing the effects of aircraft component independently; the mean-axis model, which assumes a rigid aircraft whose dynamics are altered by changes in aerodynamic forcing due to structural bending; the hybrid-flexible model, a simplification of the multi-body and mean-axis models which only includes coupling effects from rigid-body motion onto the structural modes; and the decoupled model, which assumes no coupling between the rigid-body and structural dynamics.

Multi-body models capture both inertial and aerodynamic changes to the aircraft as it flexes. Mean-axis models only capture the aerodynamic changes and assume the inertial properties of the aircraft don't change as it flexes. The inertial changes are generally quite small and can be ignored, providing a pathway to convert the multi-body model to the mean-axis model. The multi-body model can be converted to the mean-axis model through identification of off diagonal coupling terms. These terms are highly correlated and system identification software must be used to ensure a valid response.

The states of the mean-axis, hybrid-flexible and decoupled models, when compared to the multi-body model, take on different meanings. In the multi-body model, the rigid-body states place the fuselage. In the other models, they place the equivalent rigid-body of the aircraft. The response at the fuselage in the mean-axis, hybrid-flexible and decoupled models is then regained through an influence coefficient, based on the local structural bending at the sensor location.

The influence coefficients for each output are factors of the modal displacement at the sensor location. Influence coefficients can be determined by evaluating the eigenvectors for modes present in a response and are functions of modal natural frequency and components from the aero-elastic coupling matrix.

Hybrid-flexible and decoupled models are reductions of the multi-body and mean-axis models. They preserve the dynamics of the original responses well, but may diverge if coupling terms are important in the response or if there is a significant difference between the static-elastic and rigid-body response.

The hover analysis shows that there is not a large effect of elastic motion on

the response of the aircraft. The flex-factors for this case are generally near one, and aeroelastic and rigid-body coupling terms are small as well. The cruise, flex-factors became larger and aeroelastic coupling terms become significant to the response. If a static wing deflection is given to the simulation models, the change in aerodynamic roll moment in the cruise configuration is significantly larger than in hover. This further validates that in hover elastic effects do not alter aerodynamics significantly, whereas in cruise they do.

The static-elastic reduction of the mean-axis model shows similar trends to the original static-elastic reduction of the multi-body model. The flex-factors that remained unaffected in multi-body reduction remained so in the mean-axis reduction, and the ones that changed in the multi-body reduction did so as well in the mean-axis reduction.

Chapter 6: Flexible LCTR Control Design

This chapter develops a control system for the flexible LCTR. The control system aims to reduce the structural oscillations to improve both fatigue life of aircraft components and the passenger ride quality. Wing tip acceleration is fed back and structural motion, as measured using wing root strain gauges, is minimized.

6.1 Model Description

The same control architecture is used as described in Refs. [27–29] and is shown in Fig. 6.1 with the addition of a structural feedback path. The structural feedback portion of this block diagram is developed within this dissertation.
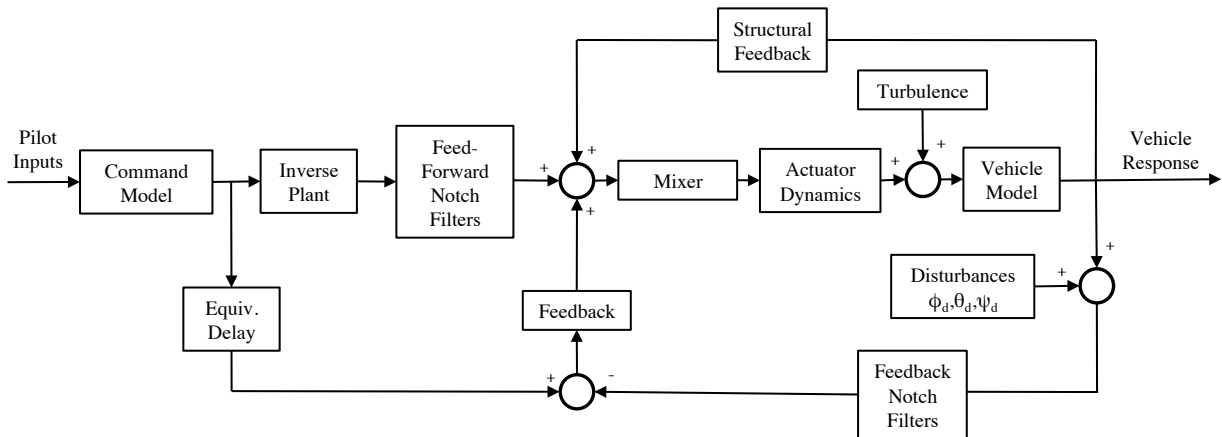
Figure 6.1: Model following control system architecture

6.1.1 Model Overview

This control system architecture is referred to as a model following control system, in that the desired closed loop performance of the system is set by the command model. The command model gives either an attitude command attitude hold (ACAH) or translational rate command (TRC) response type in the lateral and longitudinal axes and rate command in the yaw and vertical axes.

The inverse plant contains first order fits of the short-term aircraft on-axis response between 1 and 10 rad/sec. The inverse and the vehicle model cancel for low frequency inputs, and the resulting aircraft motion follows the command model. Notch filters are used to remove structural excitation from the commanded response and the feedback. Notch filters in the command path prevent the pilot from exciting the structural modes and in the feedback path they prevent the control system from exciting the modes. The mixer block aims to remove off-axis responses. For example, roll and yaw may be coupled, and the mixer would add pedal inputs to piloted lateral stick pilot inputs so that the aircraft response is decoupled. Actuator dynamics limit the allow actuator motion using actuator displacement and rate saturation. The primary actuators are modeled as second order systems with an 8 Hz natural frequency and a damping ratio of 0.7. Having actuator limits also allows for evaluation of PIO tendencies. Turbulence is input into the system at the actuator level using the CETI model [106]. This form of turbulence input results in realistic aircraft motion.

The bare-airframe vehicle model used includes three wing degrees of freedom

as well as nacelle motion and contains a total of 63 states. Disturbances are added to the system outputs and represent measurement errors. Disturbances input to the system at the outputs also allow for disturbance rejection criteria to be evaluated. The equivalent time delay block is introduced to avoid overdriving actuators and other higher order dynamics that are not modeled by the first order inverse block. The time delays are equal to the system response delays to command inputs. The feedback block converts the error signals into actuator motion.

Additional details are now given for the components of the control system.

6.1.2   Nacelle Controller

The bare-airframe dynamics include active nacelles. Each nacelle has an associated control which generates torques at the nacelle's connection point to the wing to rotate it. Without these control inputs, the nacelles' rotation about the wing would simply be the solution to the nacelle differential equation. The nacelle control acts as an additional non-conservative force in these equations of motion.

A nacelle control system, shown in Fig. 6.2 was developed so the nacelle response matched that found most desirable by pilots [31], namely an 8 rad/sec natural frequency and a high damping ratio. Nacelle angle and rate are fed back to the nacelle torque motor to create the control system. In the figure, the the gain blocks represent proportional gains, integral gain ratio (ratio of integral to proportional gain), and derivative gains. The nacelles are also rate limited to 7.5 rad/sec and have 9 degree displacement limits from the 86 degree trim position. This allowed

the nacelles to rotate aft of vertical for longitudinal control.
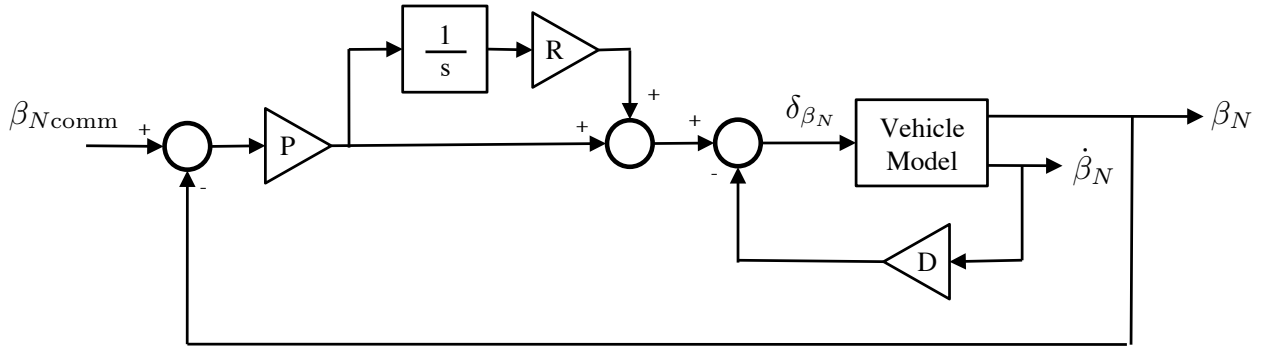
Figure 6.2: Nacelle angle control system

6.1.3   Command Model

6.1.3.1   ACAH Command Model

Different command models were developed for ACAH and TRC modes. In ACAH mode, pilot stick position commands aircraft attitudes. Lateral stick motion causes antisymmetric collective changes in the rotors and longitudinal commands cause symmetric longitudinal cyclic inputs to the rotors. The command model responses for ACAH mode are second order for the lateral/longitudinal axes, and first order for the pedal and heave axes. Command model time constants, natural frequencies, damping ratios and control sensitivities are based on findings from the NASA simulation studies [28, 29, 31]. Attitude commands in both axes are second order and command 0.2 radians of attitude/inch of stick deflection and have natural frequencies of 1 rad/sec. The damping for the lateral axis is 1.0 and longitudinal

axis is 1.45. The generic form for the ACAH system is:

$$\frac{\phi}{\delta_{lat}}, \frac{\theta}{\delta_{lon}} = \frac{K\omega^2}{s^2 + 2\zeta\omega s + \omega^2} \qquad (6.1)$$

Collective stick commands vertical velocity through symmetric collective changes and pedal inputs command yaw rates through antisymmetric longitudinal cyclic changes. Both the vertical and directional axes commands are first order. The vertical axis commands 10 feet per second/inch of collective stick deflection, with a time constant of 0.76 seconds. The directional axis commands 0.15 rad/second of yaw rate per inch of pedal deflection with a time constant of 0.7 seconds. The first order heave and yaw responses may be written as:

$$\frac{w}{\delta_{col}}, \frac{r}{\delta_{ped}} = \frac{K}{Ts + 1} \qquad (6.2)$$

The nacelles are commanded to remain vertical in this mode and symmetric lateral cyclic inputs are not used. Time delays are added to the command model signals that are sent to the feedback to avoid overdriving actuators.

6.1.3.2 TRC Command Model

The translational rate command (TRC) system is a control system designed with the faster ACAH system active. All commanded responses are first order and stick position commands either lateral or longitudinal velocity with attitudes commanded to remain zero. The ACAH control loop remains closed in order to

drive the attitudes to zero. Different inceptors are used for TRC commands versus ACAH commands. Lateral translational rate is obtained using symmetric lateral cyclic, whereas antisymmetric collective is used for roll attitude commands. In the longitudinal axis, symmetric longitudinal cyclic is used for attitude commands, and nacelle angle is used for TRC commands. Both axes command 10 feet/second velocities per inch of stick deflection and have 5 second time constants.

$$\frac{u}{\delta_{lon}}, \frac{v}{\delta_{lat}} = \frac{10}{5s + 1} \tag{6.3}$$

The vertical and directional axes remain unchanged from ACAH mode. The low-order inverse of the TRC system assumes that the ACAH loop is closed and tightly constrained since the ACAH loop is faster than the TRC loop (natural frequency of 1 rad/sec for ACAH versus a time constant of 5 seconds for TRC).

6.1.4   Inverse Plant

The inverses block contains only on-axis inverses. Each inverse is first order and captures the short term aircraft response. Integral gains are used in the feedback system to remove steady state errors. The inverse of the TRC system assumes that the ACAH loop is closed and tightly constrained since the ACAH loop is faster than the TRC loop (natural frequency of 1 rad/sec for ACAH versus a time constant of 5 seconds for TRC).

6.1.5   Notch Filters

As mentioned, notch filters are used in the feedforward and rigid-body feedback paths as shown in Fig. 6.1. The notch filters used are shown in Fig. 6.3, and have the following form:

$$N(s) = \frac{s^2 + 2\zeta_{\text{num}}\omega s + \omega^2}{s^2 + 2\zeta_{\text{den}}\omega s + \omega^2} \tag{6.4}$$

The damping of the numerator and denominator of each filter are hand tuned so that the frequency matched that of the structural mode. As can be seen in this figure, notch filters remove magnitude content at their respective frequency. The penalty is a reduction of phase at lower frequencies. This phase reduction can directly lead to lower stability margins. Notch filters are used often by fixed-wing aircraft control system designers to account for structural modes [107, 108].

The notch filters in the feedback path serve to remove structural oscillation from the rigid-body feedback signals. They are only placed on the roll rate, yaw rate, and vertical velocity signals as measured at the CG. With structural feedback active, these filtered signals are added to wing acceleration signals to create the total feedback signal. This allows for the wing tip acceleration signals to be used for structural control, and rigid-body feedback signals to be used for lower frequency airframe dynamics. Without structural feedback, the notch filters serve simply to avoid excitation of the modes by the control system.
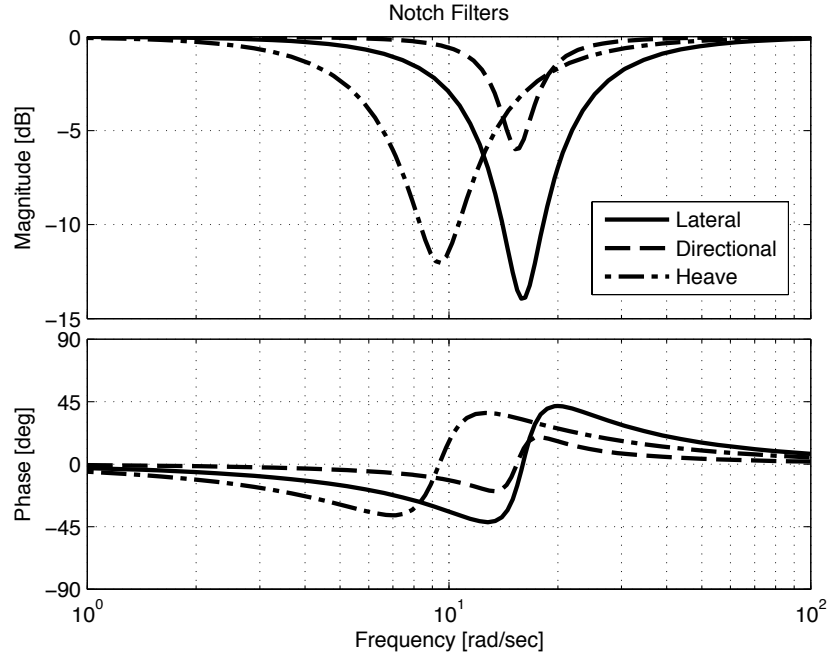
Figure 6.3: Notch filters for the lateral, directional, and heave axes

6.1.6 Mixer

Crossfeeds within the mixer are used in the feedforward path to remove unwanted off-axis response without using feedback. Generally, the crossfeed signals are simple gains. Crossfeeds are determined using coupling numerators as in Ref. [109]. The gain value is determined by looking at the off-axis response to bare-airframe stick inputs and dividing it by the on axis response. For example, the lateral stick to pedal crossfeed (to remove yaw coupling to lateral stick inputs) has the following form.

$$
G_{\text{lat}}^{\text{ped}} = \frac{\left. \dfrac{r}{\delta_{lat}} \right|_{\substack{w \to \delta_{col} \\ \theta \to \delta_{lon}}}}{\left. \dfrac{r}{\delta_{ped}} \right|_{\substack{w \to \delta_{col} \\ \theta \to \delta_{lon}}}} \tag{6.5}
$$

211

These transfer functions are generally flat for low to mid frequencies, giving the gain of the crossfeed. The sign of the crossfeed is determined by the phase curve of the signal. The only crossfeed that is not a pure gain is the nacelle motion to longitudinal stick. This crossfeed is a ratio of second order transfer functions and is also passed through a low pass filter. This crossfeed was identified to be critical in removing uncommanded pitch motion as a result of longitudinal inputs in TRC mode [30].

6.1.7 Feedback

Using rigid-body as well as structural feedback allows the optimization to focus independently on both low frequency rigid-body dynamics through the rigid-body feedbacks as well as structural motion through the gains on the isolated structural responses. The complete feedback pathway for the lateral axis is shown in Fig. 6.4. Proportional-integral-derivative (PID) feedback on the rigid-body signals is passed through the notch filter, then summed with the structural feedback.

6.1.7.1 Rigid-body

Standard rigid-body feedback signals exist, including aircraft attitudes and linear and angular rates. All rigid-body integral ratio gains are constrained to be 1/5th of the expected crossover frequency for that axis. This minimizes phase loss in the broken loop response while still giving good steady-state tracking.
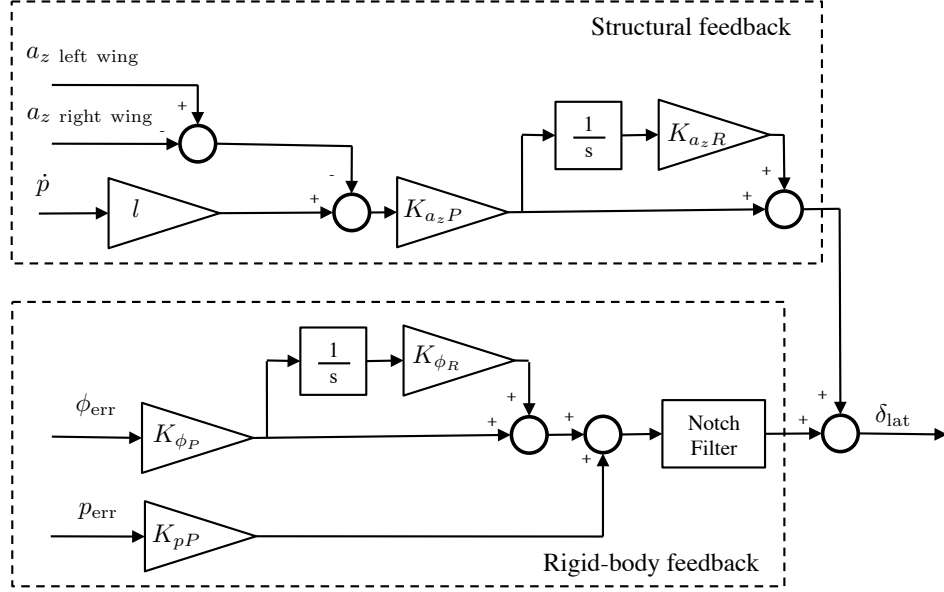
Figure 6.4: Lateral axis rigid-body and structural feedback

6.1.7.2 Structural

Historically [64,66,71,72,74,75], accelerometer measurements are available for either structural feedback or load monitoring.

As described previously, modal acceleration is fed back for structural mode control. Wing tip accelerometer signals are combined to isolate certain structural modes; for example, symmetric versus antisymmetric beamwise bending can be obtained by either summing or subtracting wing tip vertical acceleration signals. The CG response is then scaled by the wing length and subtracted from these signals to isolate structural motion (see Fig. 6.5).

$$\frac{\ddot{\eta}}{\delta_{lat}} = \dot{p}_{CG} l - \frac{\left(a_{z \text{ left wing tip}} - a_{z \text{ right wing tip}}\right)}{2} \tag{6.6}$$

The structural feedback signals are included for the lateral, direction and vertical axes.
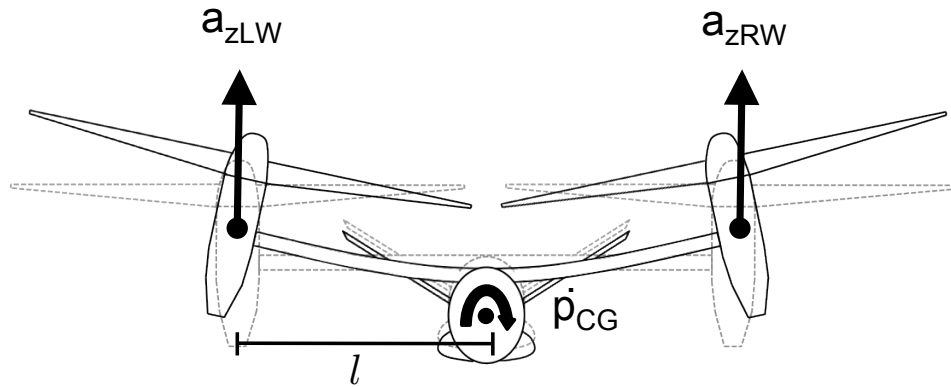
Figure 6.5: Modal acceleration isolation from accelerometer signals

Figure C.24 provides a good initial guess for the PI ratio used in the control law optimization process. The final structural PI ratios are between 3 and 15:

$$\frac{K_{I_{str}}}{K_{P_{str}}} \approx 3 - 15 \tag{6.7}$$

To reduce the number of parameters in the design optimization, the integral gains can be held fixed within this range. Refer to Appendix C for further details on structural gain selection.

Within the TRC mode, a PI control system is implemented on the lateral and longitudinal rigid-body velocity errors. As with the ACAH system, the integral ratio gain on the rigid-body feedback is hardwired to be 1/5th of crossover frequency in both TRC axes. Based on Ref. [110], the crossover in the TRC loops is about 1/5th the crossover of the faster ACAH loops. There is no structural feedback specific to TRC mode. Nacelle dynamics are too slow to be useful in structural control. All structural control is therefore implemented within the ACAH control system. Since the ACAH feedback loop remains active in TRC mode, structural control is

retained.

6.2 Gain Optimization

The gains are optimized using the CONDUIT$^®$ software tool [111]. CONDUIT$^®$ uses the feedback gains as variables in the optimization and strives to meet design specifications while ensuring stability and minimum actuator usage. The specifications are given numerical values and gradients for the optimization. A minimax optimization approach is used so that in a subsequent iteration no specification value will be degraded beyond the current worst value.

Table 6.1 presents the specifications used in the optimization. The specifications include various broken loop specifications from MIL-F-9490E [113], closed loop specifications from ADS-33E [32], among others. Specifications are broken up into different categories.

The optimization begins with *Hard* specifications. These ensure overall design stability and robustness and include stability margin, Nichols margin, and eigenvalue specifications from MIL-F-9490E. There are tighter stability margin requirements for frequencies near the structural modes, specifically, an increase to 8 dB of gain margin and 60 degrees of phase margin. These tighter requirements ensure stability if the structural modes are not well identified or they vary depending on loading, fuel quantity, etc. For the ACAH systems, any design with structural feedback also has specifications to ensure stability is retained if the structural feedback signals are lost. The structural feedback signals are cut out of the response and stability margins are reanalyzed. The hard specifications comprise the first portion of the optimization.

Table 6.1: Control system optimization specifications

Spec Type	Spec Name	Description	Axis
Hard	EigLcG1	Eignevalues in L.H.P	-
	StbMgG1	Gain/Phase Margin (6 dB, 45 deg)	All
	StbMgG2	Structural Gain/Phase Margin (8 dB, 60 deg)	All
	NicMgG1	Nichols Margin (6 dB, 45 deg)	All
	NicMgSt	Structural Nichols Margin (8 dB, 60 deg)	All
Soft	ModFoG2	Model Following [1]	All
	DstBwG1	Disturbance Rejection Bandwidth[2]	All
	DstPkG1	Disturbance Rejection Peak	All
	CrsMnG2	Minimum Crossover Frequency[3]	All
	OlpOpG1	Open Loop Onset Point (Cat II PIO) [112]	All
	RmsAcG1	Structural RMS to CETI Disturbance	All
	FreHeH1	Heave Response (using 1st order LOES fit)	Heave
	EigDpG1	Eigenvalue Damping (up to 5 rad/sec)	-
	EigDpG1	Eigenvalue Damping (5-10 rad/sec)	-
Summed Obj.	CrsLnG1	Crossover Frequency	All
	RmsAcG1	Actuator RMS	All
Check Only	BnwAtH1	Bandwidth (Other MTEs, UVE > 1)	Lat
	BnwYaH2	Bandwidth (Other MTEs)	Dir
	RisLoG1	Rise Time (using 1st order LOES fit)	Lon/Lat TRC
	EigDpG1	Eigenvalue Damping (10-18 rad/sec)	-

[1] Model following max frequency was reduced from 10 rad/sec to 4 rad/sec for both Flex Wing cases.
[2] Outer loop TRC DRB set using specifications from Ref. [110]
[3] Minimum crossover for outer loop set using specifications from Ref. [110]

The solver ignores all the other specifications until all the hard specifications are level 1. Once all hard specifications are level 1, the second stage of optimization begins.

The second stage consists of *Soft* constraints, which ensure good design performance. These specifications generally include model following, disturbance rejection bandwidth (DRB), disturbance rejection peak response (DRP), and eigendamping specifications. PIO tendencies are also evaluated in this category using the OLOP

specification [112]. The structural specifications (described in next section) were grouped into this category as well. Optimization to these specifications is performed after all hard constraints are in the level 1 region. Hard specifications must remain in the level 1 region throughout this portion, and the rest of the optimization process.

The final stage of optimization minimizes *Summed Objective* specification. Actuator RMS and crossover frequency are minimized as much as possible while ensuring that the soft and hard constraints remain in the level 1 region. This phase of optimization ensures minimal actuator and control system activity.

Check Only specifications are not involved in the optimization, but are evaluated by the solver as a check. Bandwidth and rise-time specifications fall within this category. The aircraft bandwidths and rise times are set by the command model to meet Level 1 requirements, so optimization to these values is not required. Additional details on the phases of the optimization can be found in Ref. 111.

6.2.1   TRC Gain Determination

The innermost loop in the control system stabilizes and controls the nacelles. Once the nacelle gains are determined, they remain fixed for the entire design process. The ACAH loop is built onto the nacelle loop. The TRC loop assumes the ACAH system is also active. The design criteria for the TRC loop comes from Ref. [110]. The crossover frequency requirement for velocity response is 1/5th of the faster ACAH response. The DRB is also set to 1/5th of the ACAH DRBs. The disturbance rejection peak response requirements are left unchanged.

Within the TRC mode, a PI control system is implemented on the lateral and longitudinal rigid-body velocity errors. As with the ACAH system, the integral ratio gain on the rigid-body feedback is hardwired to be 1/5th of crossover frequency in both TRC axes. There is no structural feedback specific to TRC mode. Nacelle dynamics are too slow to be useful in structural control. All structural control is therefore implemented within the ACAH control system. Since the ACAH feedback loop remains active in TRC mode, structural control is retained.

To determine the gains for the TRC mode, the ACAH gains are frozen, greatly reducing the optimization problem size. The results of this methodology were compared to freeing all the gains and re-optimizing [110]. Both methods produced similar results and freezing the inner loop gains led to a much quicker optimization solution.

6.2.2   Structural Specifications

Most specifications used during the optimization are requirements from accepted sources such as ADS-33E and MIL-9490E. Given that structural requirements do not exist in terms of allowed closed loop motion, a new specification, shown in Fig. 6.6, was developed to constrain structural motion.

The root mean square (RMS) value of beam strain in the beamwise and chordwise directions serve as the metric to be minimized. The RMS is obtained in the frequency domain by integrating the strain metric from 1 to 100 rad/sec:

$$RMS = \sqrt{\frac{1}{\pi} \int_1^{100} |F(\omega)|^2 d\omega} \tag{6.8}$$
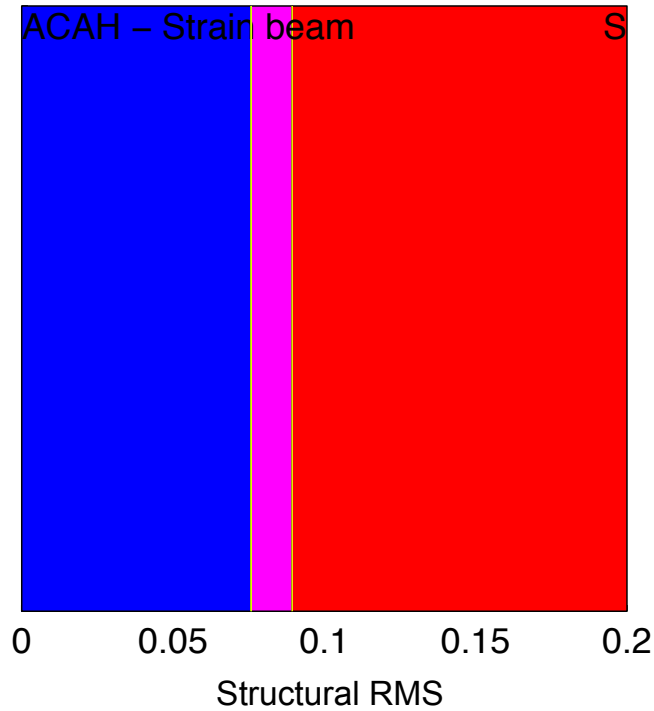
Figure 6.6: CONDUIT® structural specification

Lower frequency motion is attributed to the rigid-body dynamics and is ignored. The strain includes deflections of both the symmetric and antisymmetric bending modes. The specification is evaluated for CETI turbulence inputs [106] in order to ensure accurate excitation levels for each axis. The CETI turbulence model provides an accurate representation of atmospheric turbulence and captures the aircraft response to turbulence. For each design, the optimizer was allowed to minimize this specification to provide a best case solution for that design. The final level 1/2 boundary represents the minimum attainable strain with structural feedback turned on. The final level 2/3 boundary represents the lowest structural strain RMS without structural feedback.

6.2.3 Structural Control Tradeoffs

A tradeoff study was performed on the structural RMS specifications to determine the minimum structural RMS value attainable for the given control system design. The structural specification was used in the beam and chord axes, meaning total beamwise and chordwise motion were minimized. For this optimization, the structural specification boundaries are incrementally tightened (allowing less structural oscillation to turbulence) until the optimization routine is no longer able to find a feasible solution that simultaneously meets the tightened structural requirements and all other design criteria. This case on the boundary between the feasible and infeasible solution represents the Pareto optimal case. The full set of specifications for the ACAH control system from Table 6.1 are used to ensure the structural motion reduction still produces a stable control system with good handling qualities.

CONDUIT® specifications are divided into three levels as shown in Figure 6.6. Generally the boundaries between the levels represent the boundary of handling qualities. For example, the level 1/2 boundaries for bandwidth come from ADS-33E guidelines. Similarly low frequency stability margin specification level 1/2 boundaries are set to 45° for phase and 6 dB for gain as set by MIL-F-9490D. Level 2/3 boundaries similarly represent the shift from level 2 to level 3 handling qualities.

For the structural specification, the level 1/2 boundaries represent the structural RMS values obtained with the structural gains turned off. This boundary is independently determined for both the beam and chord axes. These values represent the "best" that the control system can do without structural feedback. The trade-

off study begins by moving the level 1/2 boundary further into the level 2 region, thereby loosening the requirements on structural RMS. This is done to investigate the effects of allowing the structural gains to be active across the full design space. The level 1/2 boundary is then set tightened incrementally into the level 1 region for all axes simultaneously. Once the boundary in one axis is no longer able to be reduced, the boundary value is fixed at this optimal value and the optimization continues on the other structural specifications to find optimal values for all axes.

This type of tradeoff study is called a design margin optimization (DMO). Another example of a DMO, used to increase the disturbance rejection bandwidth and crossover frequency of a UH-60 Blackhawk can be found in Ref. [110]. This reference also presents additional guidelines of performing a design margin optimization.

The structural strain RMS values obtained from this study are shown in Figure 6.7. The step between designs is based on a percentage of the size of the level 2 region and is labeled as a DMO step. The RMS values are normalized based on the the nominal case which is the best case structural performance without structural feedback, labeled DMO step 0. For each DMO design shown, a full optimization is completed. All hard and soft constraints must meet level 1 values while summed objective specifications minimize actuator usage and crossover frequency.

By design, the best case without structural feedback was set as the Level 1 (DMO=0) boundary, as shown in Fig. 6.7. Based on the chord axis, Fig. 6.7b, just turning on structural feedback shows an immediate improvement in RMS value as compared to the nominal design. The structural RMS is reduced to 84% of the nominal value. Structural gains are beneficial in minimizing actuator usage (final

221

step in optimization) in this axis, the byproduct of which is also a reduction in structural RMS. The final DMO design, with a design margin of 80%, represents the lowest structural RMS attainable with structural feedback, while meeting all stability and handling quality requirements. This design will be compared to other designs in a later section.
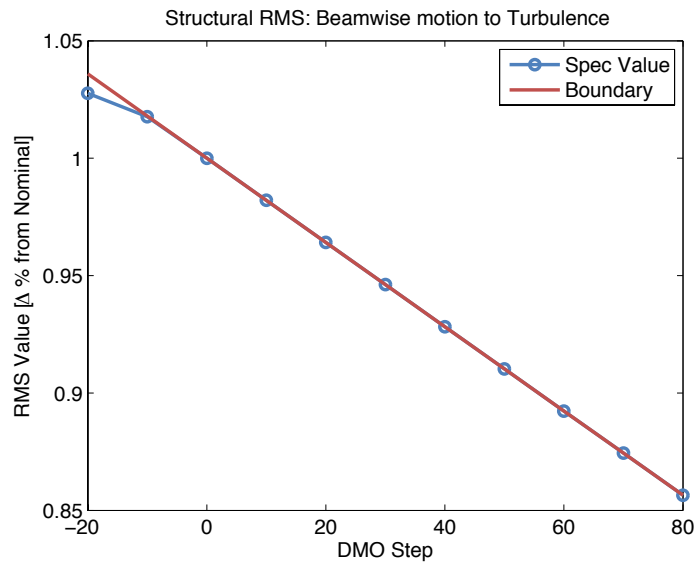
(a) Beam axis strain RMS per DMO step
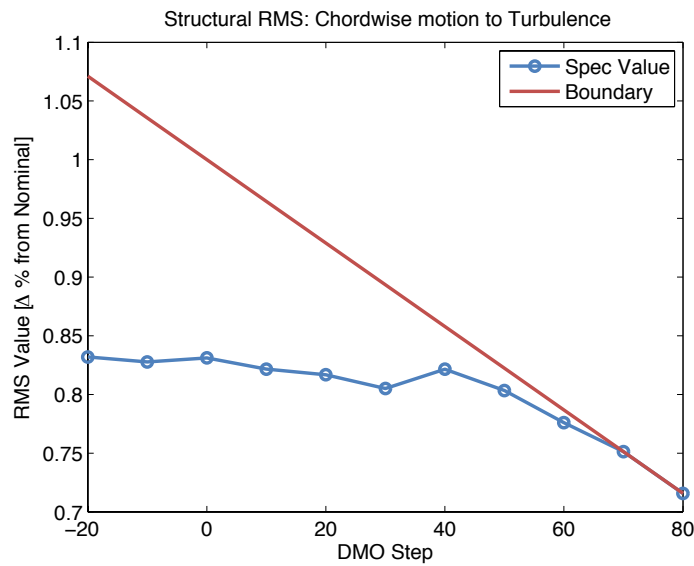
(b) Chord axis strain RMS per DMO step

Figure 6.7: Strain RMS requirements and optimized values for each DMO step

Figure 6.8 shows the structural gains for the design margin optimization shown in Fig. 6.7. The gains that act on the beam axis are the summed and differential wing tip vertical acceleration (a_z) gains, as shown by the dashed and dotted lines. The summed wing tip vertical acceleration gain shows an increase with nearly each DMO step. The increase in this gain is responsible for the reduction in structural RMS shown in Figure 6.7a. After the initial improvement in chordwise strain obtained by simply allowing the optimization engine to use the structural gains, the chord structural RMS values remain generally flat until approximately design margin 50%, when the RMS values approach the boundary again and begin to decrease. This decrease is accompanied by a rise in the gain in this axis at the same design margin.
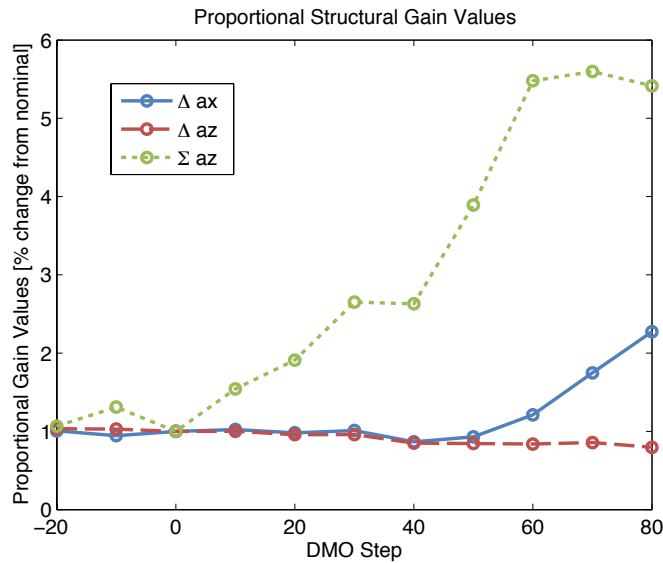

Figure 6.8: Proportional structural gain values for each DMO step

The gain on differential wing tip vertical acceleration remains fairly inactive during the optimization. As previously mentioned, the CETI turbulence model is an accurate representation of aircraft dynamics due to atmospheric turbulence,

which has large low frequency content. The antisymmetric beam mode occurs at 17 rad/sec and the symmetric beam mode occurs at 9 rad/sec. The symmetric mode is excited more in turbulence since it is at lower frequency, so this mode drives the specification for the beam axis more than the antisymmetric beam mode.

Figure 6.9 compares the strain RMS to the actuator RMS. The actuator RMS is a measure of swashplate actuator usage in each axis. Figure 6.9a shows that for the beam axis, which is excited by both lateral and heave inputs, much improvement in strain RMS is achievable with negligible changes in actuator usage.

At a design margin of 60%, the lateral actuator, which reflects antisymmetric collective on the rotors, begins to increase. The structural gain for the differential vertical acceleration remains flat in Fig. 6.8. More actuator usage is needed to continue reducing structural excitation above the 60% design margin since the gain does not change.

Figure 6.9a also contains the heave actuator RMS, a measure of rotor symmetric collective pitch changes. The actuator RMS for this axis remains fairly flat. Since the heave actuator RMS remains flat but the design margin requires reduced structural motion, the damping on the symmetric beamwise mode must improve. If the gain improves damping, the wing motion is reduced without increasing actuator motion.

In the chordwise direction, the gains increase for design margins of 50% or higher, but the actuator RMS (Fig. 6.9b) remains relatively flat.

Figure 6.10 shows the damping values of the three low frequency structural modes impacted by structural feedback. Increases in structural gain values tend to
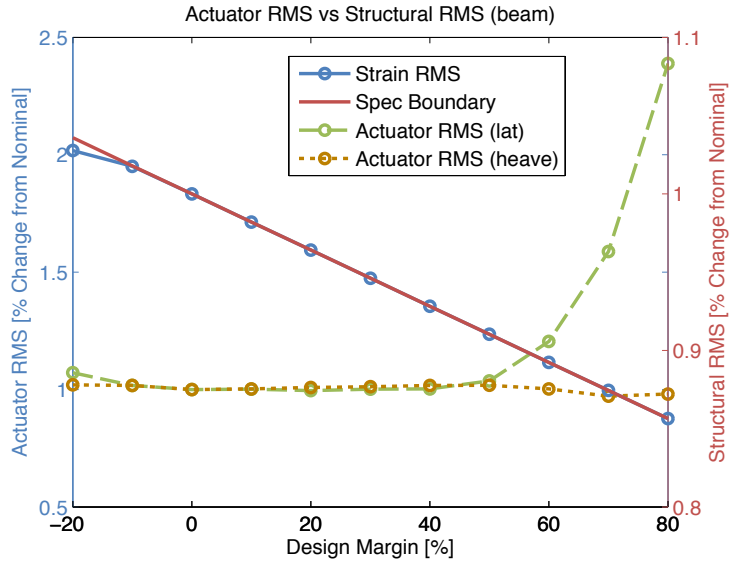
(a) Beam axis strain RMS compared to actuator RMS for each DMO step
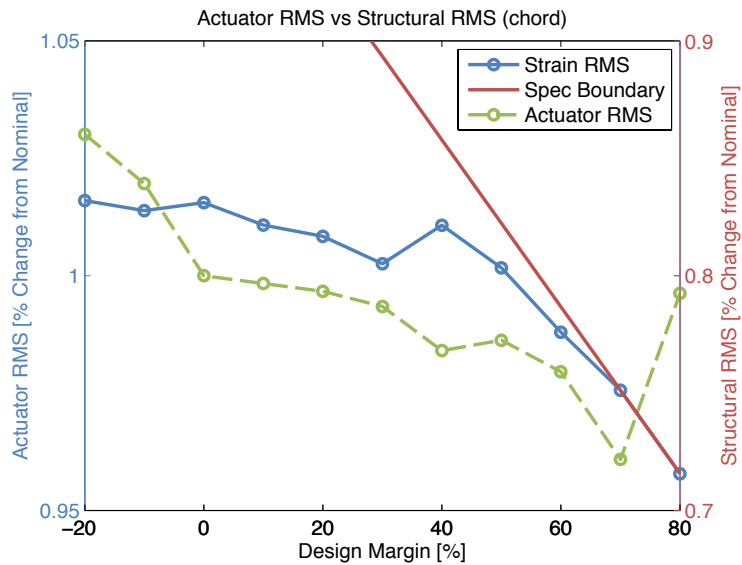
(b) Chord axis strain RMS compared to actuator RMS for each DMO step

Figure 6.9: Strain RMS compared to actuator RMS for each DMO step

accompany improvements in damping. The largest improvement in damping is for the symmetric beam mode, as expected since the summed vertical wing acceleration gain begins to increase for small design margins. The Antisymmetric beam mode shows slight decrease in damping for increases in design margin and the gain on this

mode did not change during the design margin optimization. Finally, the damping of the antisymmetric chord mode remains fairly flat. The structural gain for this axis was also relatively flat.
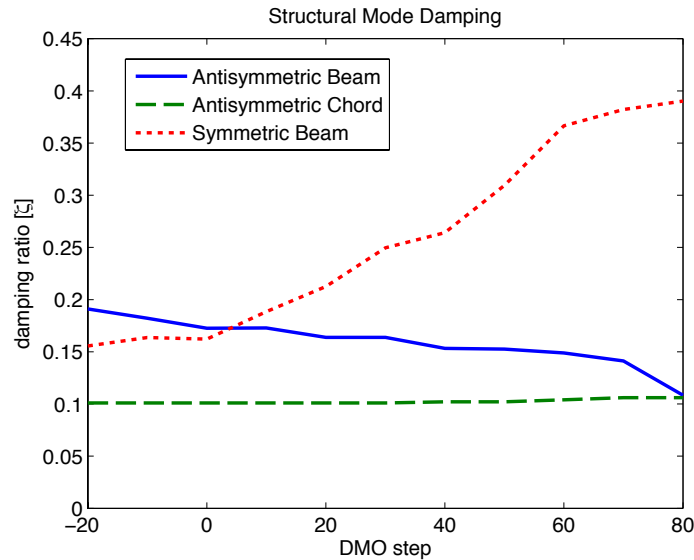
Figure 6.10: Structural mode damping ratios for each design margin

The key trade-offs determined by this design margin optimization include:

- Structural RMS improvements can be achieved with little additional actuator activity, except for the lowest strain RMS requirements, which come at the cost of additional actuator activity.

- Damping of the lowest frequency structural modes were improved, but the damping of the higher frequency antisymmetric beam mode was reduced.

6.2.4 Notch Filter and Static-Elastic Optimization

Additional designs were optimized to provide comparison points to the designs discussed in the design margin optimization, which provided optimal designs with

structural feedback. A static-elastic (see Chapter 5 for further details) design was optimized to show the effects of designing a control system for a rigid aircraft and implementing it onto a flexible one. The static-elastic bare-airframe model is obtained by a quasi-static reduction of the structural modes from the flexible model. Since this model is rigid, structural specifications were not used. A design with notch filters in the feedforward path was also optimized with and without structural feedback. The notch filters serve to reduce piloted excitation of the structural modes without structural feedback. The design with the notch filters and structural feedback also came from a design margin optimization as was described earlier for the case with only structural feedback.

6.3   ACAH Design Comparisons

The comparisons will focus on several designs, most of which have already been described and which are summarized in Table 6.2. The *StrFB* design comes from the design margin optimization and represents the design with maximum structural feedback that has the least structural excitation to turbulence. *noStrFB* is the design without any structural feedback. This design still includes the strain RMS specification, so it represents a "best case" scenario when not using structural feedback. The *SE* design is the static-elastic design. This is the design that would be obtained if the control system designer did not account for structural motion during the design of the control laws. All the designs described contain notch filters in the feedback path of the rigid-body response. They serve to isolate the structural motion to the structural feedbacks. The *NotchStrFB* design has notch filters in the

227

Table 6.2: Design summary

	feedforward notch filters	feedback notch filters	structural feedback	designed with flexible bare-airframe	designed with static-elastic bare-airframe
noStrFB	-	✓	-	✓	-
SE	-	✓	-	-	✓
StrFB	-	✓	✓	✓	-
NotchStr	✓	✓	✓	✓	-
NotchNoStr	✓	✓	-	✓	-

feedforward path as well. These notch filters removed pilot excitation of the structural modes. This design also contains structural feedback. Finally, *NotchNoStrFB* contains notch filters in the feedforward path, but does not have structural feedback. This methodology is often employed by control designers, to simply notch out the structural modes.

Table 6.3 summarizes the lateral/directional ACAH system performance and handling qualities for the described designs. Broken loop stability margins and closed loop components of these tables will be analyzed below. Table 6.4 presents the same information for the longitudinal and heave axes. The various control systems will now be compared in terms of their broken loop, disturbance rejection, and closed loop responses.

6.3.1 ACAH Broken Loop

Figures 6.11, 6.13, 6.15, and 6.17 show the broken loop responses of the controller. The loops were broken at the actuators. The broken loop responses are used to calculate the stability margins and crossover frequencies, given in Tables 6.3 and 6.4. The control systems are designed to have a broken loop crossover frequency of $\omega_c = 2.0$ rad/sec in the lateral, directional, and longitudinal axes and $\omega_c = 1.5$

Table 6.3: Lateral/Directional ACAH design comparison

	noStrFB	StrFB	SE	NotchStrFB	NotchNoStrFB
Lat ω_c [rad/sec]	2.56	2.69	2.23	2.57	2.66
Dir ω_c [rad/sec]	2.00	2.11	2.02	2.12	2.00
Lat PM_{rb} [rad/sec] [1]	59.7	52.8	71.22	58.5	50.6
Lat GM_{rb} [dB] [1]	8.07	8.79	6.88	9.02	9.64
Dir PM_{rb} [rad/sec] [2]	69.2	72.8	59.6	72.8	71.0
Dir GM_{rb} [dB] [2]	-	9.81	10.5	9.79	-
Lat PM_{str} [rad/sec]	-	71.6	-	78.1	-
Lat GM_{str} [dB]	36.6	11.2	34.5	11.4	37.9
Dir PM_{str} [rad/sec]	-	-	-	-	-
Dir GM_{str} [dB]	9.22	8.00	43.4	8.00	9.03
Lat ω_{BW} [rad/sec]	1.87	1.84	1.99	1.84	1.85
Lat τ_{PD} [sec]	0.21	0.10	0.21	0.12	0.11
Dir ω_{BW} [rad/sec]	1.10	1.10	1.11	1.10	1.10
Dir τ_{PD} [sec]	0.086	0.099	0.085	0.099	0.087
ϕ-DRB [rad/sec]	1.13	1.27	0.90	1.15	1.27
ϕ-DRP [dB]	3.33	4.37	2.33	3.79	4.30
ψ-DRB [rad/sec]	0.726	0.700	0.854	0.701	0.700
ψ-DRP [dB]	2.30	2.15	3.00	2.14	2.19

[1] Rigid-body frequency gain and phase margins (requirement 6dB/45 deg.).
[2] Gain and phase margins at structural frequencies (requirement 8dB/60 deg.).

rad/sec in heave.

The low frequency response of the lateral broken loop plots looks nearly identical for all designs. The dynamics in this frequency range are set by general aircraft requirements such as model following, crossover, and disturbance rejection, and do not change between the designs presented, which differ in their structural feedback characteristics. Above 10 rad/sec, the plots diverge into two groups of lines. The StrFB and NotchStrFB plots have higher magnitudes above 10 rad/sec, a direct result of the structural feedback. The peak near 17 rad/sec is the antisymmetric beamwise mode (see Fig. 4.10 for mode shape). With structural feedback engaged,

Table 6.4: Longitudinal/Heave ACAH design comparison

	noStrFB	StrFB	SE	NotchStrFB	NotchNoStrFB
Lon ω_c [rad/sec]	3.24	2.00	2.00	2.00	3.27
Heave ω_c [rad/sec]	1.50	2.03	1.54	1.99	1.50
Lon PM_{rb} [rad/sec][1]	58.9	54.2	58.0	53.4	59.8
Lon GM_{rb} [dB][1]	14.5	11.8	11.4	11.9	14.2
Heave PM_{rb} [rad/sec][1]	68.8	63.1	68.5	63.5	68.8
Heave GM_{rb} [dB][1]	11.7	8.34	11.4	8.27	11.65
Lon PM_{str} [rad/sec]	-	-	-	-	-
Lon GM_{str} [dB]	8.06	13.8	12.1	13.8	8.00
Heave PM_{str} [rad/sec]	-	85.7	-	89.9	-
Heave GM_{str} [dB]	50.3	8.18	50.0	8.15	50.3
Lon ω_{BW} [rad/sec]	2.44	2.69	2.56	2.69	2.44
Lon τ_{PD} [sec]	0.059	0.072	0.065	0.072	0.059
Heave $1/T_h$ [rad/sec]	1.18	1.04	1.17	1.05	1.18
Heave τ_h [sec]	0.00	0.03	0.00	0.026	0.00
θ-DRB [rad/sec]	0.634	0.738	0.696	0.745	0.613
θ-DRP [dB]	3.26	4.91	4.85	4.97	3.34
w-DRB [rad/sec]	1.09	1.00	1.12	1.00	1.09
w-DRP [dB]	2.97	4.11	3.01	4.14	2.98

[1] Rigid-body frequency phase and gain margins (requirement 6dB/45 deg.).
[2] Phase and gain margins at structural frequencies (requirement 8dB/60 deg.).

the control system is more active at the structural frequencies in an effort to reduce structural oscillation. This increase in magnitude is problematic from a stability margin standpoint as there are additional 0 dB crossings and the magnitude curve stays close to the 0 dB line for a larger frequency range. However, the increased requirements for stability margins in the structural frequency range serve to ensure system stability, even if there is uncertainty in the structural modes.

The increase in stability margins is also retained in the Nichols requirements, shown in Figure 6.12, through an increase in size of the exclusion zone for the structural frequency range (Fig. 6.12b). Nichols plots contain an exclusion zone centered
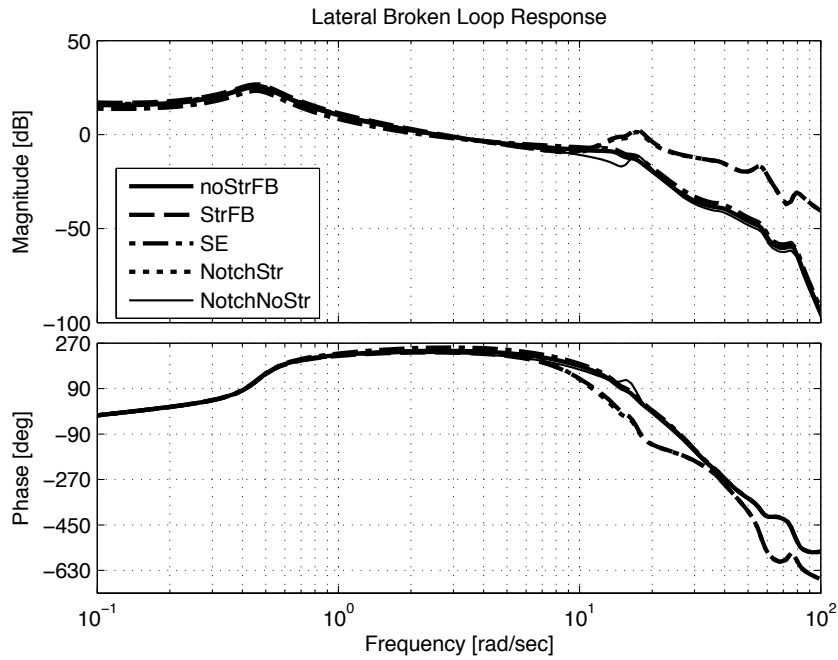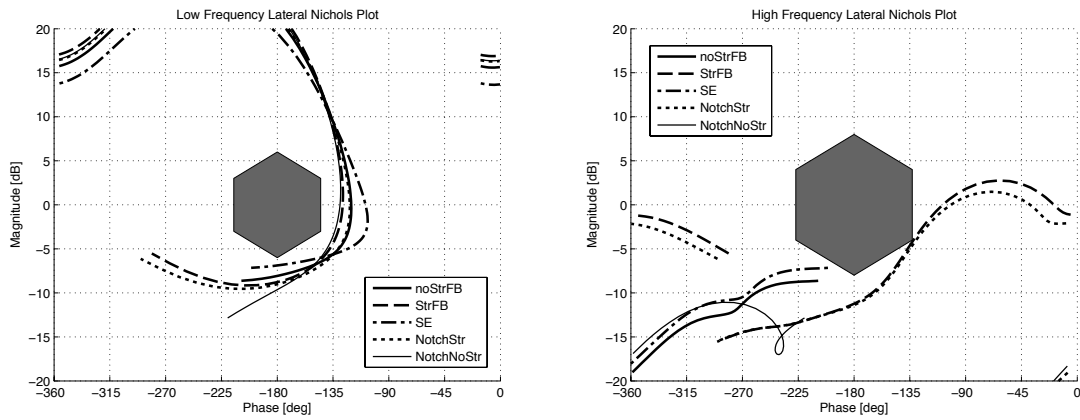
Figure 6.11: Lateral broken loop response

(a) Lateral axis Nichols plot for low frequency dynamics

(b) Lateral axis Nichols plot for dynamics in the structural frequency range

Figure 6.12: Lateral axis Nichols plots

around to 0 dB, -180 deg instability point. This exclusion zone prevents combinations of gain and phase margins from broken loop response from approaching instability and serves to add robustness to the system. The Nichols plot in the structural frequency range, Fig 6.12b, shows that the two designs with structural

231

feedback are on the boundary of the exclusion zone at -135 deg of phase. This boundary prevents the structural gains from increasing further and limits the effectiveness of the structural feedback. Without structural feedback, the noStrFB, SE, and NotchNoStr plots drop in magnitude above 10 rad/sec and there are no additional concerns about stability. All the designs developed had the same stability requirements. The noStr and SE designs were required to adhere to increased stability margins at the structural frequencies, even though they lacked structural feedback.

The directional broken loop response is plotted in Figure 6.13 and the Nichols margin plots are show in Figure 6.14. This plot has very similar characteristics to the lateral broken loop response, and here the structural mode is the antisymmetric chordwise mode at 14 rad/sec (see Fig. 4.11 for mode shape). Above the structural frequency, there are large gains in the designs with structural feedback, and the other designs drop off in magnitude. There is a broad frequency range where the response is near the 0 dB line, causing potential problems with stability margins. The Nichols plots show, however, that the exclusion zone is again not penetrated in any of the designs.

Figures 6.15 and 6.16 show the broken loop responses in the longitudinal axis. There is no structural feedback that enters the longitudinal control signal, so the responses all look similar, except for a gain offset. The two designs that have increased magnitude are the NotchNoStrFB and NoStrFB designs, and the increase is caused by a larger gains on the pitch rate error feedback. This increase in gain occurs even though during the final stage of optimization, the crossover frequency
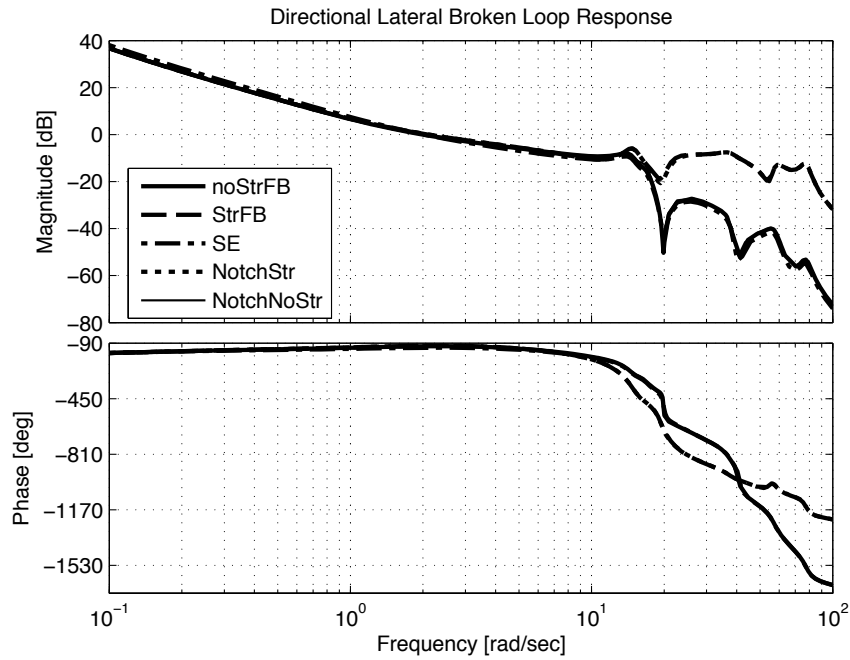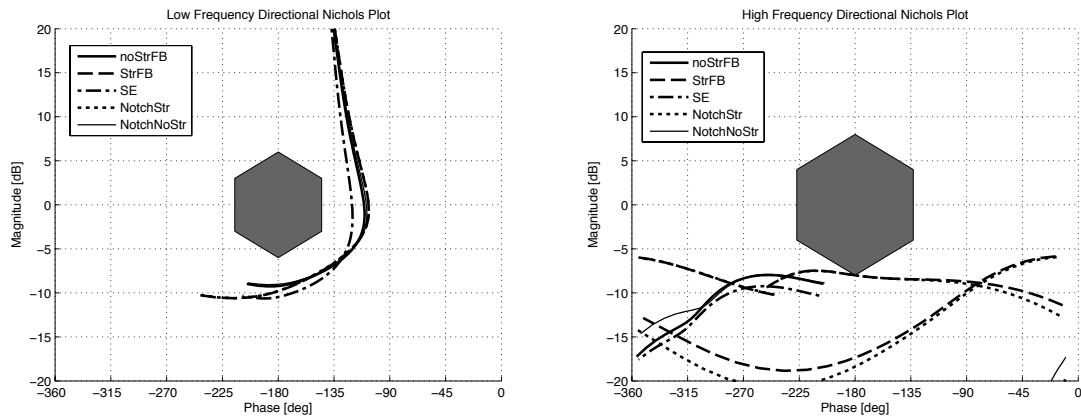
Figure 6.13: Directional broken loop response

(a) Directional axis Nichols plot for low frequency dynamics

(b) Directional axis Nichols plot for dynamics in the structural frequency range

Figure 6.14: Directional axis Nichols plots

is minimized, with 2 rad/sec being the allowed minimum.

The final set of broken loop figures are in heave, and are shown in Figures 6.17

and 6.18. There is significant structural feedback in this axis as shown by the large

magnitude increase at the structural frequency. The Nichols plot for the structural
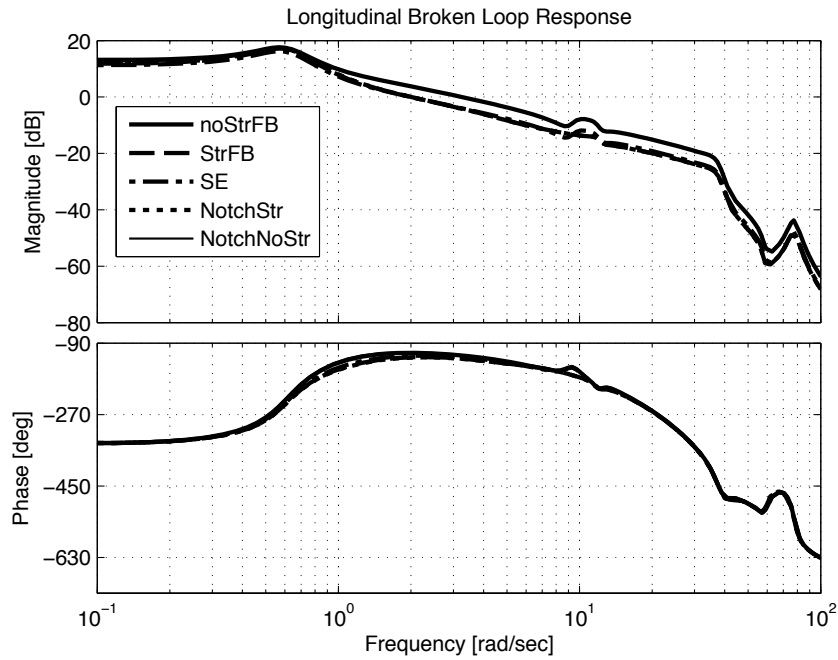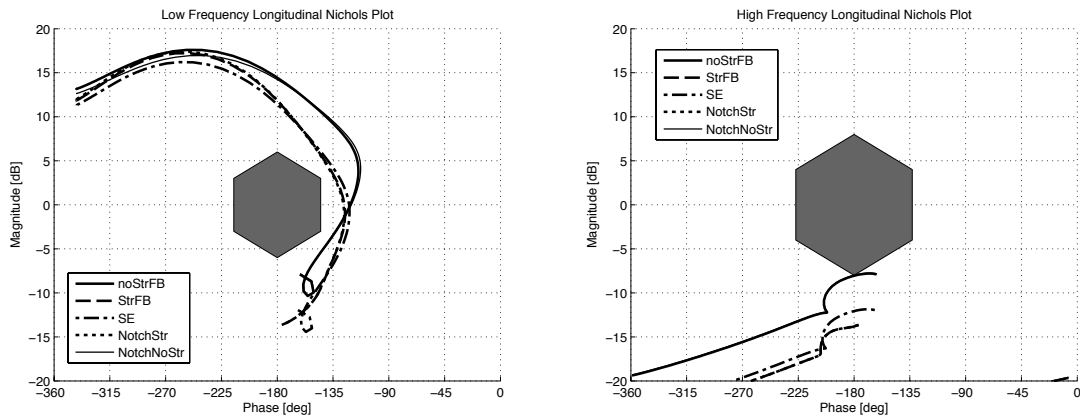
Figure 6.15: Longitudinal broken loop response

(a) Longitudinal axis Nichols plot for low fre-
quency dynamics

(b) Longitudinal axis Nichols plot for dy-
namics in the structural frequency range

Figure 6.16: Longitudinal axis Nichols plots

response, Fig 6.18b shows that the structural feedback designs are right on the exclu-

sion zone. The structural gains are therefore limited by the stability requirements.

The increase in the broken loop magnitude response coincides with the drop in the

phase curve to 0 deg (-360 in the figure). The magnitude curve drops when the

234

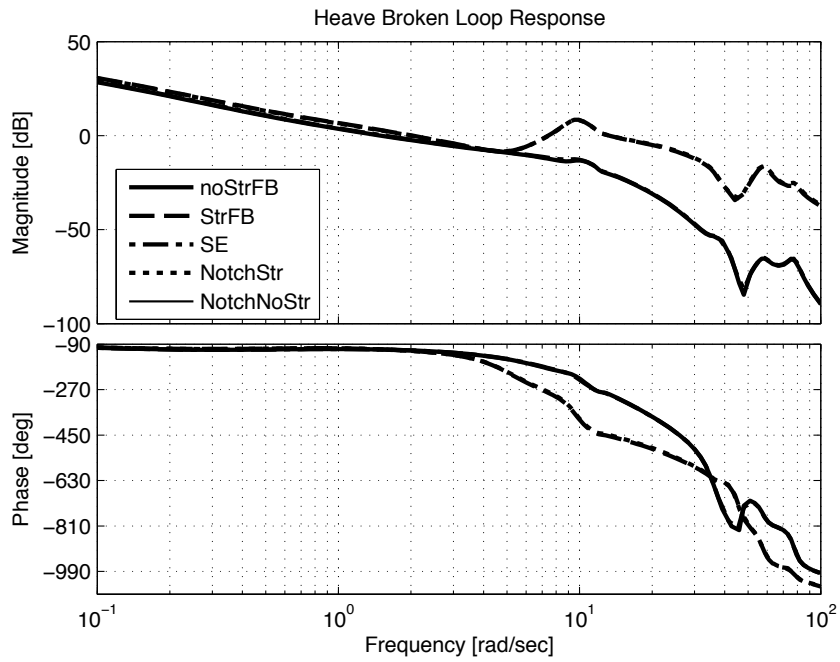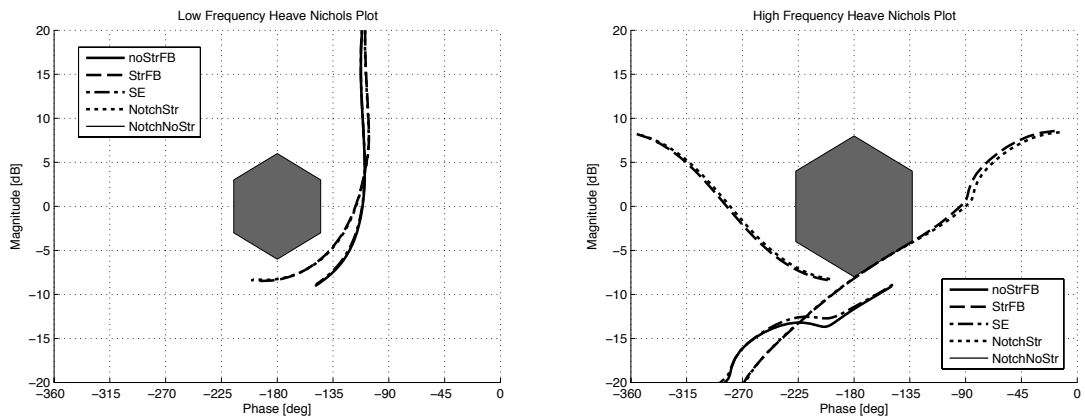phase reaches -180 deg points (-540 in the figure).

Figure 6.17: Heave broken loop response

(a) Heave Nichols plot for low frequency dynamics

(b) Heave Nichols plot for dynamics in the structural frequency range

Figure 6.18: Heave Nichols plots

6.3.2 ACAH Closed Loop

The closed loop roll responses are compared next. Magnitudes are expressed in degrees for roll and pitch attitude commands and deg/sec for yaw rate commands. Vertical velocity is expressed in feet per second. Inputs are inches of stick deflection for all axes.

The closed loop ACAH roll response to piloted inputs is shown in Figure 6.19. The responses are compared to commanded responses coming out of the command model. The Command Model line also includes the equivalent time-delay also shown in Fig. 6.1. The lateral axis has excellent model following up to 4 rad/sec. Above this frequency the phase curves depart slightly from the command model, but still track very well. Near the structural frequency, associated with the antisymmetric beamwise bending mode, the differences in the designs becomes apparent. Where for the broken loop response the designs could have been lumped into one of two curves, here they nearly all quite different. The NotchNoStr design follows the Command Model response the closest up to above 15 rad/sec. The NotchStr design, including both notch filters and structural feedback, actually suppresses the response at the structural mode when compared to the Command Model. There are slight oscillations in the phase curve, but for this design it does not completely diverge from the Command Model until above 20 rad/sec. The StrFB design attempts to suppress the structural feedback but is unable to bring the magnitude curve down to the Command Model as well as the notch filter designs. This design has the departure in the phase curve above 4 rad/sec. The final two curves, noStrFB

and SE, sit nearly on top of each other and have the worst overall performance when compared to the Command Model. There is no attempt to reduce structural oscillation in the design, and structural dynamics begin to have effect at around 4 rad/sec, well within the piloted frequency range of interest.
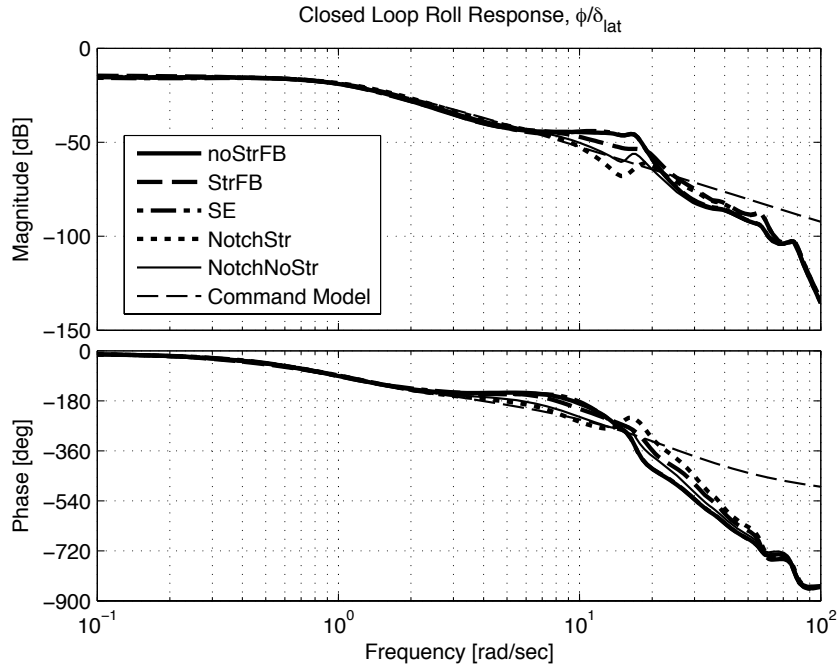

Figure 6.19:   Closed loop roll response to lateral stick inputs

The closed loop step responses are shown next in Figures 6.20. The attitude response shows the systems performance to commanded inputs over a duration of 10 seconds. All designs match well with each other and there is hardly any structural oscillation noticeable. None of the designs reach the steady state step commanded value, but all result in nearly identical attitude.

Figure 6.20b shows the roll rate response, which is faster than the attitude response and is useful for comparing the structural responses of the gain sets. The noStrFB design has the largest amount of oscillation. The SE design has nearly an
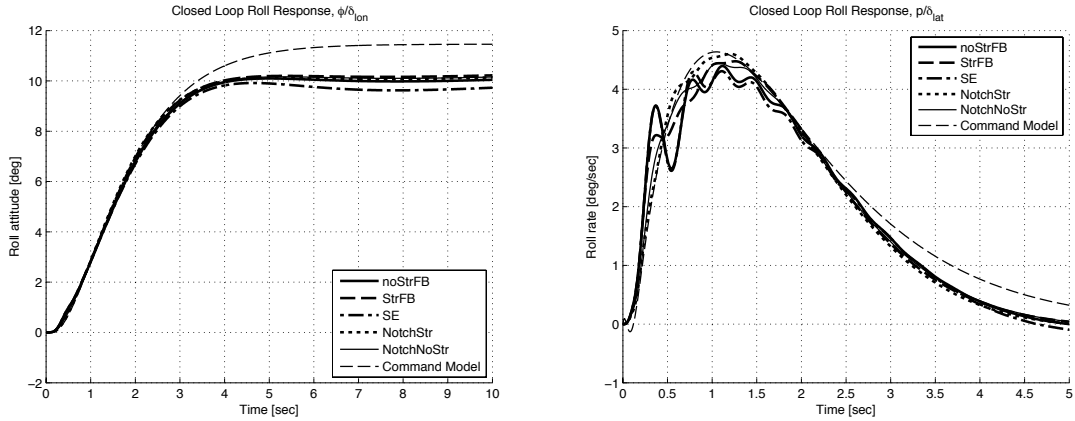
(a) Closed loop roll attitude response to lateral stick inputs

(b) Closed loop roll rate response to lateral stick inputs

Figure 6.20: Lateral axis closed loop step responses

identical response to the noStrFB design and sits on top of it for the first second in the figure. The StrFB curve also shows some excitation, but it is quickly damped with almost all structural oscillation being removed after 1.5 seconds. The Notch-Str and NotchNoStr designs have the best performance and follow the Command Model the best. The notch filter in the feedforward path removes piloted input at the structural frequency, greatly reducing structural excitation and giving the best performance. It should be noted again that all the designs contain notch filters on the rigid-body feedback signals. These notch filters serve to isolate the feedback at the structural frequencies to the structural feedback gains. Reference [100] shows closed loop response without notch filters in the feedback or feedforward path in roll and yaw.

The directional closed loop response is shown in Figure 6.21. As with the lateral response, there is good low frequency tracking of the command model, and the responses diverge at the structural mode. The SE and noStrFB designs have

nearly identical responses and have the largest magnitude increase at the structural mode, the antisymmetric chordwise mode. The other designs do not excite the structural mode in this axis.
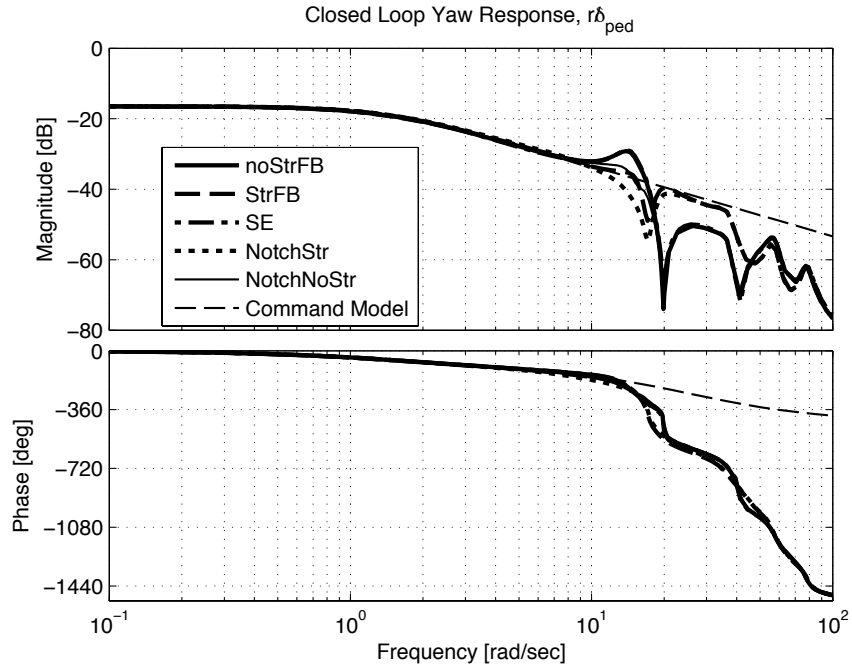

Figure 6.21: Closed loop yaw rate response to pedal inputs

The similarity of the designs is well represented in the step response shown in Figure 6.22. All the designs track the commanded response very well. The structural oscillation is slight and is barely noticeable even in the designs without structural feedback. The same trend for all plots in the lateral axis is noticeable. For pilot inputs, notch filters do an excellent job of reducing structural oscillation.

The closed loop pitch frequency response is shown in Figure 6.23. This response shows little structural oscillation excitation in any of the designs, and all the designs have nearly identical performance. The slight structural excitation near 10 rad/sec comes from the symmetric beamwise bending mode which shows up predom-
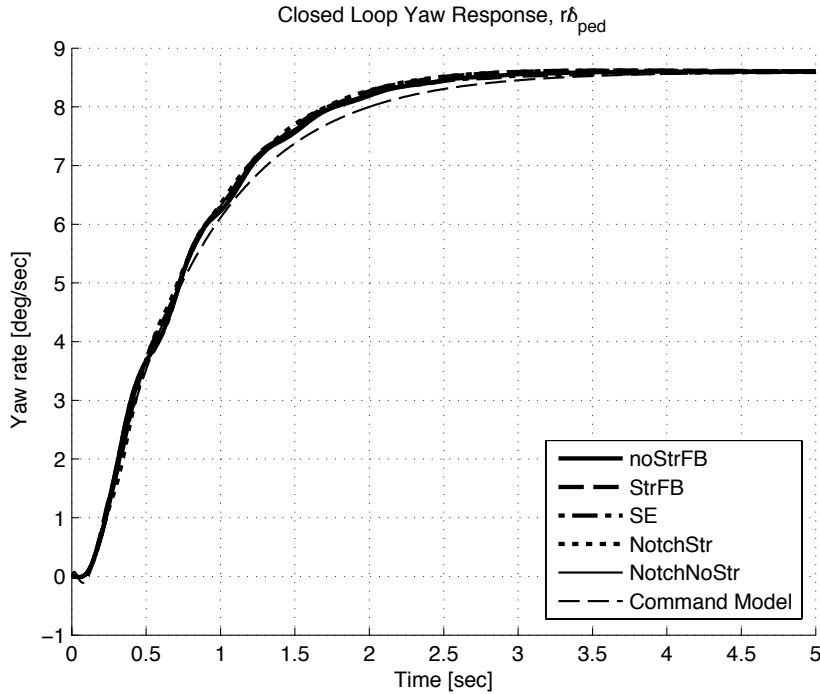
239

Figure 6.22: Directional axis closed loop step responses

inantly in the heave response. The heave axis structural gains remove the oscillation in this axis as well, as noted by the StrFB curve. There was no structural feedback present for this axis since longitudinal inputs do not directly excite any structural modes in ACAH mode.

The closed loop step response is shown next in Figures 6.24. This response, similar to the lateral response, shows a moderate steady state error after ten seconds for all the designs. The error could be do to the flap back of the rotor due to forward airspeed, resulting in lower steady-state velocities. As predicted by the frequency response, all the designs have nearly identical performance. In the pitch rate, Figure 6.24b, the noStrFB shows slight more oscillation than the other designs. The NotchNoStrFB curve is nearly identical to the noStrFB curve.

The final closed loop comparison is for the heave response to collective inputs,
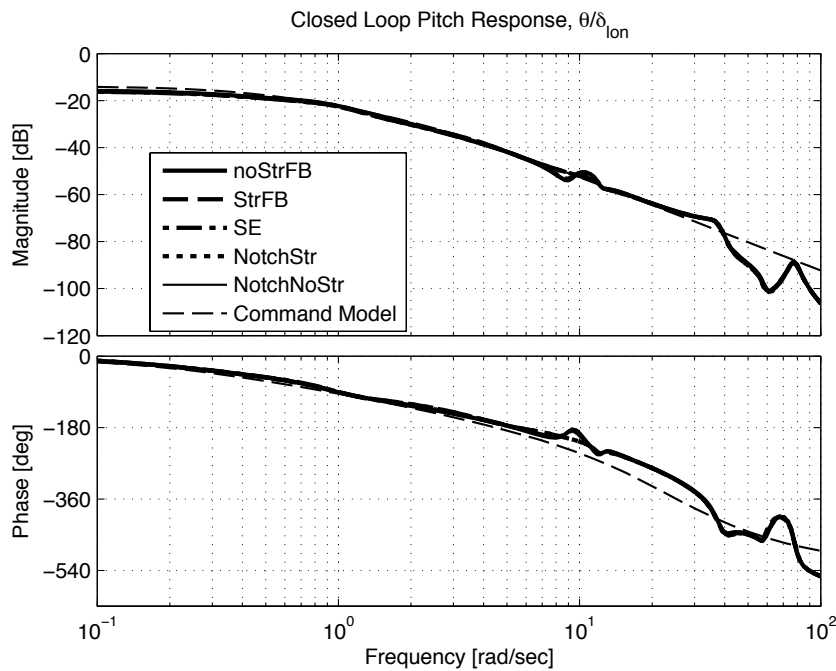
Figure 6.23: Closed loop pitch response to longitudinal stick inputs
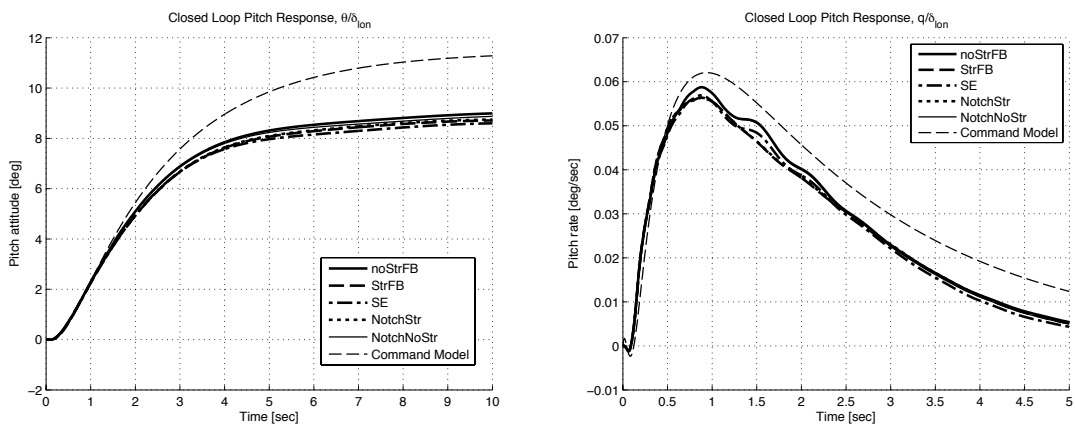
(a) Closed loop pitch attitude response to longitudinal stick inputs

(b) Closed loop pitch rate response to longitudinal stick inputs

Figure 6.24: Longitudinal axis closed loop step responses

shown in Figure 6.25. It is obvious from this frequency response that the noStrFB and SE responses will show large oscillation at the structural frequency, around 10 rad/sec. The StrFB response shows large improvements in damping at the structural frequency, as does the NotchNoStr design. The NotchStr design acts to inhibit

motion at the structural frequency and has a large reduction in magnitude at that frequency.
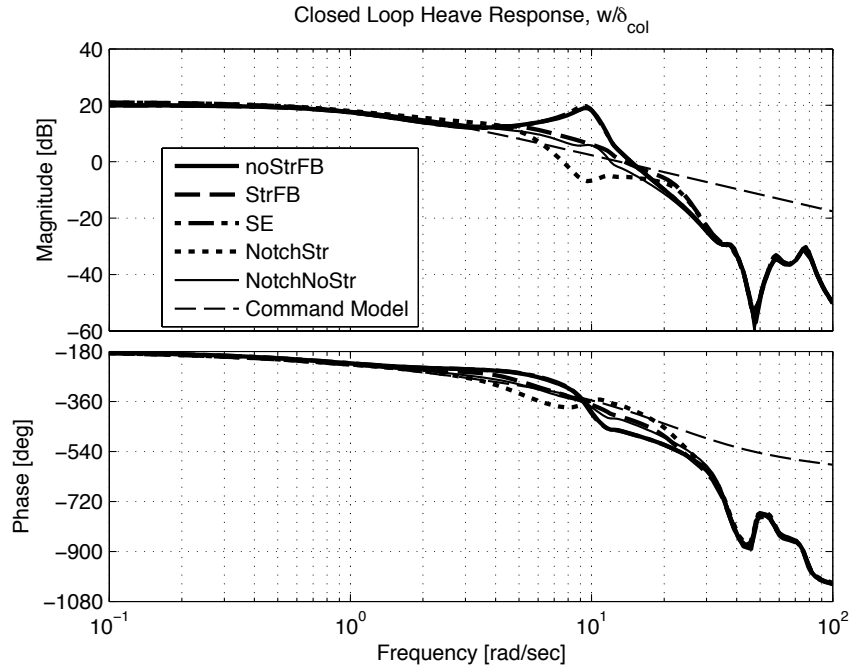
Figure 6.25: Closed loop pitch response to collective stick inputs

The step response is shown in Figure 6.26. The noStrFB and SE designs show large oscillation and have nearly identical responses. Their steady state value asymptotes to 10 feet/sec, as set by the Command Model. The NotchNoStr shows almost no oscillation and also asymptotes to the same rate as the Command Model. This response shows the closest alignment with the Command Model in this axis. The two designs with structural feedback exhibit nearly no oscillation, but the steady state response is greater than the Command Model.
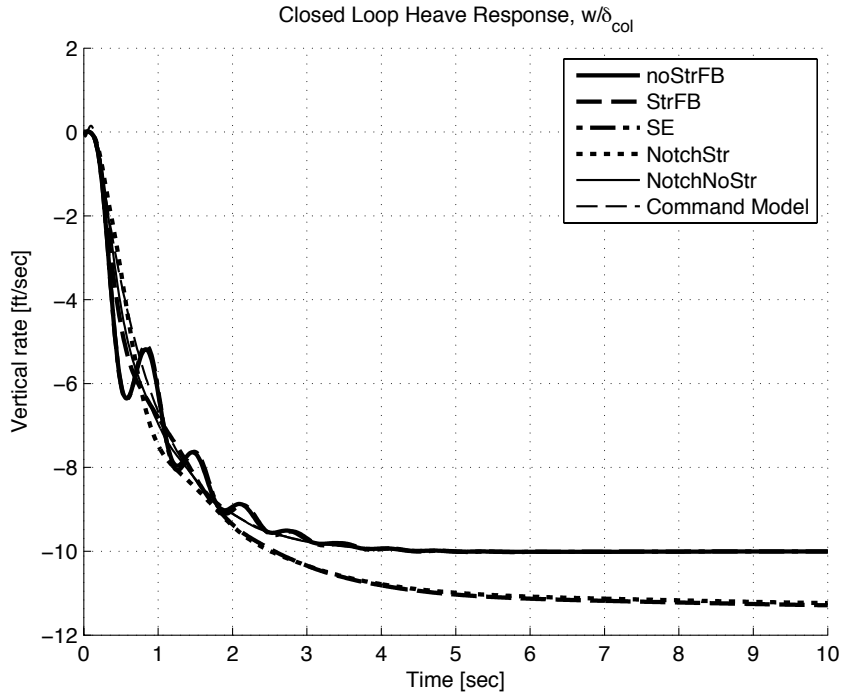
Figure 6.26: Closed loop heave response to a collective step input

6.3.3 Bandwidth

Even though the closed loop bandwidth may be tuned by the command model, it is useful to evaluate the closed loop performance by using the ADS-33E bandwidth criteria since it also incorporates system time delay. A NASA piloted simulation (Ref. 28) determined that the ADS-33E bandwidth specification boundaries were inaccurate for such a large aircraft. New boundaries were determined in this study, which are also presented here for comparison. The primary reason for the new boundaries is the large pilot station offset from the center of gravity. Higher bandwidth control systems produced large, objectionable accelerations at the pilot station and were thus poorly rated. For pitch and roll, the Level 1 boundary for the LCTR2 was roughly centered around a 1 rad/sec command model (same natural

243

frequency as used here).

The roll bandwidth plot is shown in Fig. 6.27. Since model following performance is good below 4 rad/sec, nearly all the designs have the same bandwidth. The difference in the designs comes from the phase delay. The designs with structural feedback, which effectively reduces structural phase lag, have smaller delays than the designs without. The designs without the feedback, however, lie in, or nearly in, the level 1 region of the proposed LCTR2 boundaries and are in the level 2 region of the ADS-33E boundaries. With structural feedback, the designs are in the level 2 region for both set of boundaries. The command model can be easily adjusted to meet the proposed LCTR boundaries given in Ref. 28.
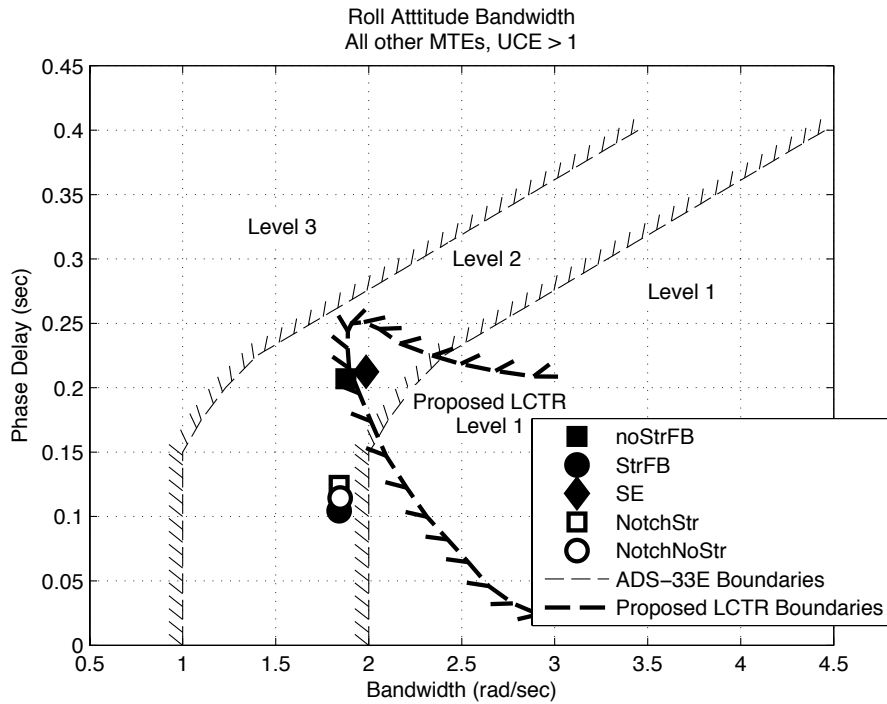
Figure 6.27: ADS-33 Roll Bandwidth specification for Hover, all other MTEs

The yaw bandwidth is shown next in Fig. 6.28. Here the proposed LCTR boundaries are drastically different than the classic ADS-33E boundaries. Lateral

244

pilot station acceleration is sensitive to yaw commands, so very low bandwidth cases performed the best in the piloted sims. All five of the designs have nearly the identical bandwidth and phase delay and are all in the level 1 region for the proposed boundaries and the level 2 region for the ADS-33E boundaries.
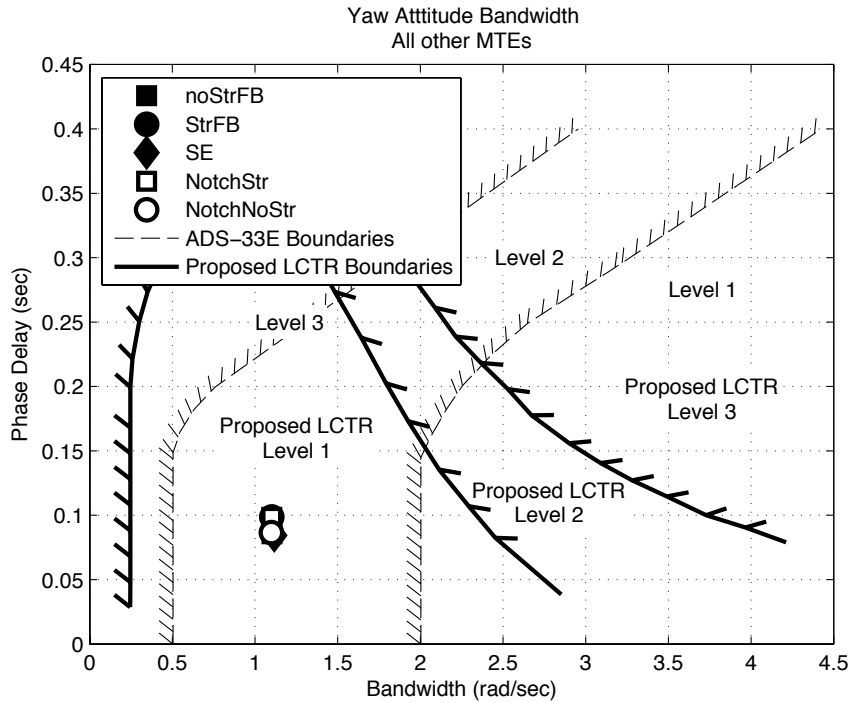
Figure 6.28: ADS-33 Yaw Bandwidth specification for Hover, all other MTEs

Figure 6.29 shows the pitch bandwidth specification. The proposed LCTR boundary in this axis looks similar to roll axis boundary, even though the pilot station offset suggests there should be large sensitivity to pitch inputs because of resulting heave accelerations. As with yaw, nearly all the designs produce the same bandwidth and time delay and lie nearly on top of each other in the specification. The designs lie on the level 1/2 border of the proposed boundaries and are well within level 1 for the classic ADS-33E boundaries.

Filters are generally associated with increased time delay. The bandwidth
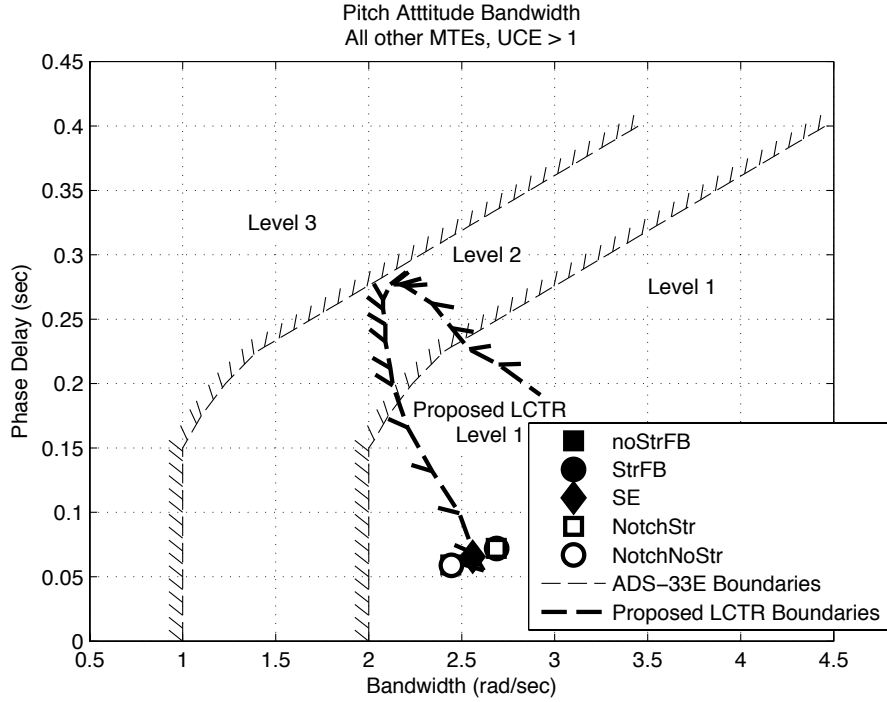
Figure 6.29: ADS-33 Pitch Bandwidth specification for Hover, all other MTEs

comparisons show that increases in time delay due to notch filters are generally

minor. The trend is true for all the bandwidth plots shown.

6.3.4 ACAH Disturbance Rejection

Disturbance rejection properties for the ACAH system are obtained from in-

jecting disturbances at the sensor level, so aircraft motion is not altered directly

(as with turbulence using the CETI model), but is altered by the control system

response to the disturbances. These types of disturbances occur when there are

erroneous sensor measurements. The disturbance rejection bandwidth (DRB) gives

the frequency up to which the control system can reject disturbances well, and is

taken at the -3 dB crossing of the magnitude plot. The disturbance rejection peak

(DRP) is taken from the maximum magnitude the aircraft obtains from a given

disturbance. Generally, systems with worse DRB (lower frequency crossing of -3 dB line) will have an improved DRP. This is true because the sensitivity plot, used to obtain DRB and DRP, must obey Bode's integral theorem for a SISO system. The integral of the sensitivity magnitude plot is conserved with different feedback gains. Even for this more highly coupled MIMO system, the trend is still present. So, if DRB is improved and pushed higher and higher, the drawback is that the peak response is also increased (see Fig. 6.30). Both specifications are included to ensure that the peak does not get too large for improved bandwidths and vice-versa. The DRB varies for each axis and is described below, but the maximum allowed DRP is 5 dB for any response.
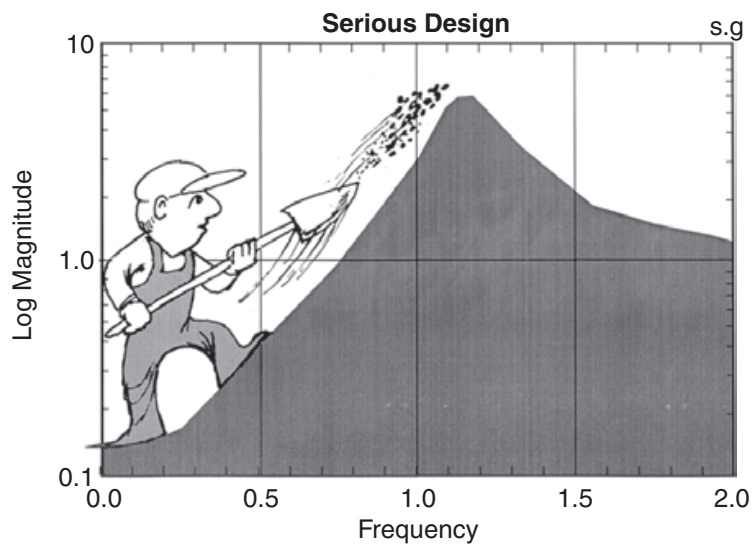
Figure 6.30: Sensitivity tradeoffs between DRB and DRP (from Ref. [114]).

The lateral disturbance rejection response is shown in Fig. 6.31. This response shows that the SE design has the lowest bandwidth, but also the lowest peak response. The ADS-33E requirement for bandwidth for ϕ disturbances is 0.9 rad/sec, and the SE design falls directly on this boundary. The noStrFB and NotchStr de-
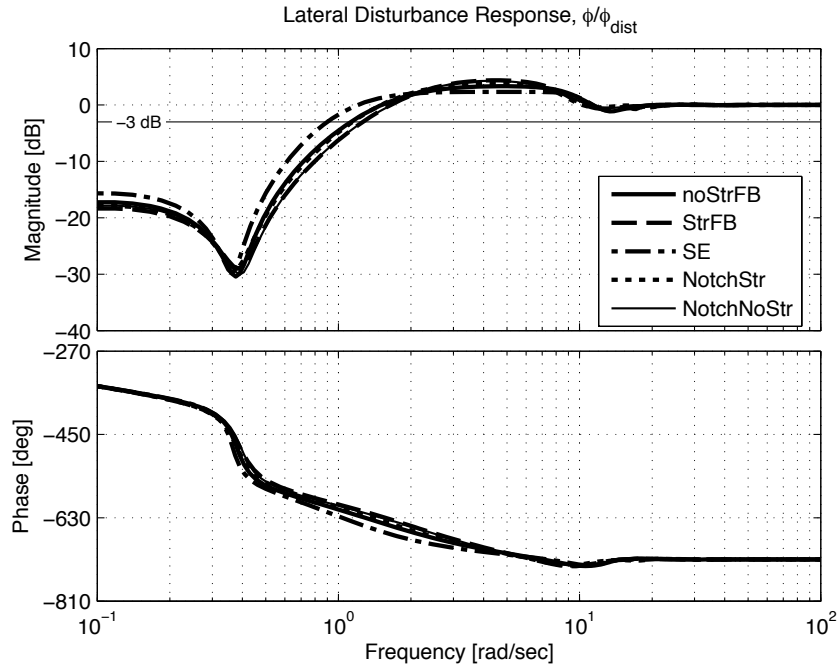
Figure 6.31: Lateral disturbance rejection response

signs have the next highest bandwidth and NotchNoStr and StrFB designs have the highest bandwidth.

The next figure, Fig 6.32 shows the disturbance response for disturbances injected into the ψ channel. The ADS-33E requirement is 0.7 rad/sec for these disturbances. This figure has the opposite trend when compared to lateral disturbances. The SE design has the highest bandwidth as well as the highest peak disturbance response, while the other designs all line up together and have a lower bandwidth, but a lower peak response.

The longitudinal response, shown in Fig. 6.33, shows that the noStrFB and NotchNoStr designs have nearly identical responses and have the worst DRB performance and the lowest DRP. The StrFB, SE, and NotchStr designs are all aligned and have better DRB. The ADS-33E requirement requires a minimum of 0.5 rad/sec
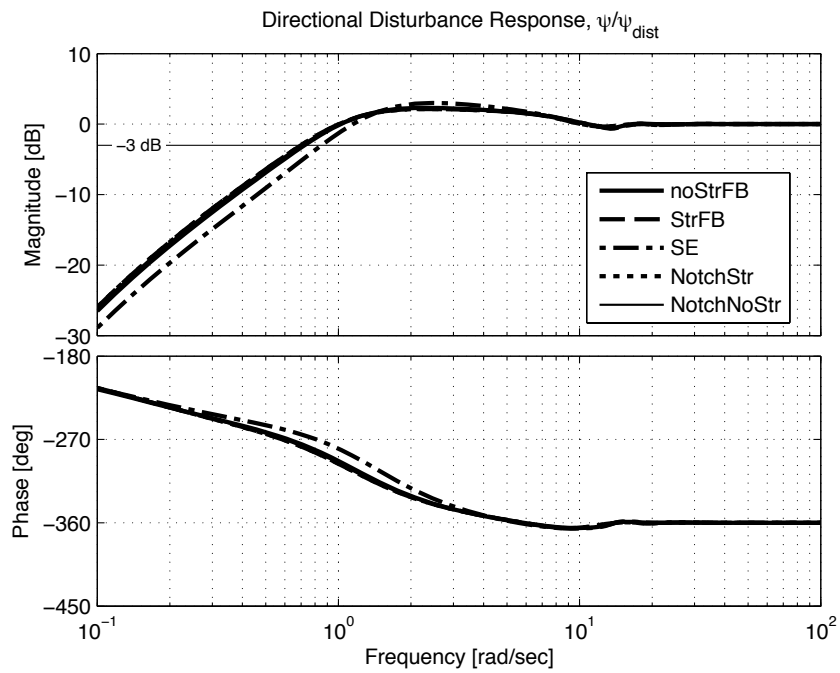
Figure 6.32: Directional disturbance rejection response

of DRB, which is met for all the designs.
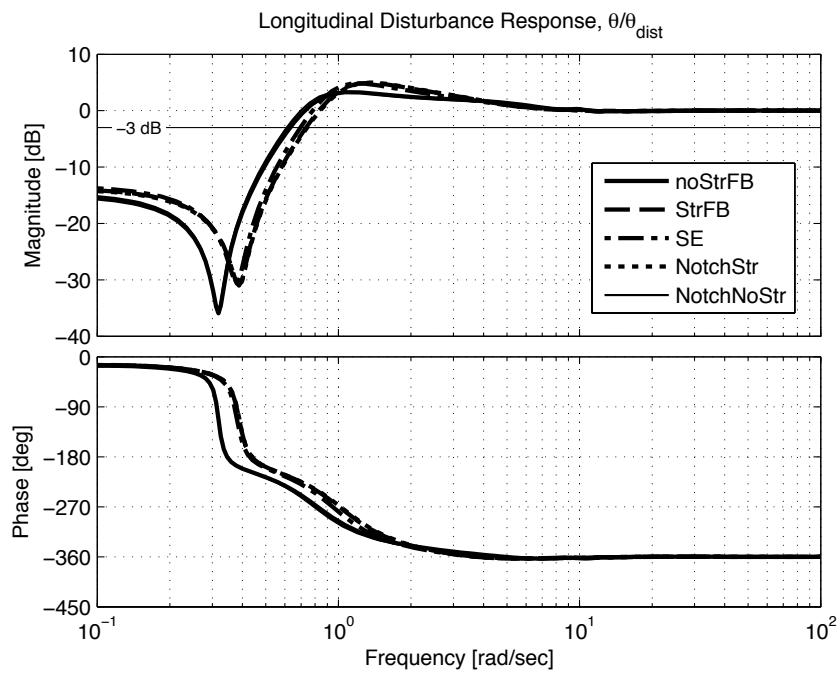
Figure 6.33: Longitudinal disturbance rejection response

The final disturbance rejection plot is in heave, where vertical velocity disturbances are injected into the measurements. Here, 1 rad/sec is the minimum required bandwidth. The two curves with structural feedback align with each other to have higher magnitude for low frequency disturbances and also have a higher peak response. The curves without structural feedback perform better at low frequency and also have lower peak responses.
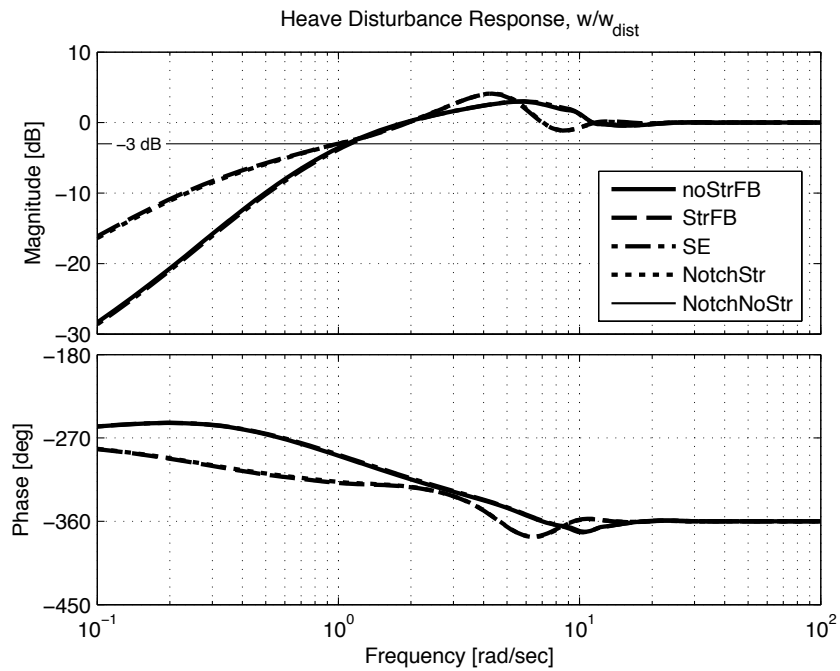
Figure 6.34: Vertical disturbance rejection response

6.4 TRC Design Comparisons

The translational rate command (TRC) system is designed with the ACAH system active. Only the longitudinal and lateral axes are altered and provide velocity responses to stick commands. The directional and heave axes remain unaltered from the ACAH design and will thus not be shown in this section. Stability margin and

disturbance rejection characteristics of the various control systems are shown in Table 6.5. Note that the disturbance rejection bandwidth is worse for this outer loop system than the faster ACAH inner loop. Since the crossover frequency for the TRC system is much lower than ACAH, the broken loop response tends to have much lower magnitude at the structural frequencies, giving good stability margins.

Table 6.5: Lateral/Longitudinal TRC design comparison

|	noStrFB	StrFB	SE	NotchStrFB	NotchNoStrFB
Lat ω_c [rad/sec]	0.4	0.4	0.4	0.4	0.4
Lon ω_c [rad/sec]	0.4	0.4	0.4	0.4	0.4
Lat PM_{rb} [rad/sec] [1]	78.1	76.7	80.5	77.4	78.2
Lat GM_{rb} [dB] [1]	-	-	-	-	-
Lon PM_{rb} [rad/sec] [2]	57.8	57.8	57.9	57.8	57.8
Lon GM_{rb} [dB] [2]	20.2	23.0	21.7	23.0	20.2
Lat PM_{str} [rad/sec]	-	-	-	-	-
Lat GM_{str} [dB]	33.3	34.6	33.7	34.7	33.3
Lon PM_{str} [rad/sec]	-	-	-	-	-
Lon GM_{str} [dB]	-	44.6	-	44.3	-
u-DRB [rad/sec]	0.239	0.240	0.240	0.240	0.239
u-DRP [dB]	1.08	1.08	1.08	1.08	1.09
v-DRB [rad/sec]	0.311	0.307	0.321	0.308	0.311
v-DRP [dB]	1.06	0.96	1.33	1.03	0.97

[1] Low frequency gain and phase margins (requirement 6dB/45 deg.).
[2] Gain and phase margins at structural frequencies (requirement 8dB/60 deg.).

As with the ACAH system, the comparisons between the designs will consist of broken loop frequency responses, closed loop step input time histories and frequency responses, and disturbance rejection responses.

6.4.1   TRC Broken Loop

Figure 6.35 show the lateral broken loop responses of the TRC system. Since the there is minimal magnitude content at the structural frequencies, it is not expected that the control system will excite the structural modes. In fact, the structural modes do not even appear in the broken loop plot, meaning they are not present in the aircraft response with the ACAH loops closed. All of the designs in the lateral TRC responses display the desirable -20 dB/dec slope which gives good low frequency model following of pilot inputs as well as high frequency disturbance attenuation. The Nichols plots (Fig. 6.36) confirm the benign characteristics in this axis. The magnitude response at the structural frequency is low enough to not even appear on the high frequency Nichols plot, Fig. 6.36b.
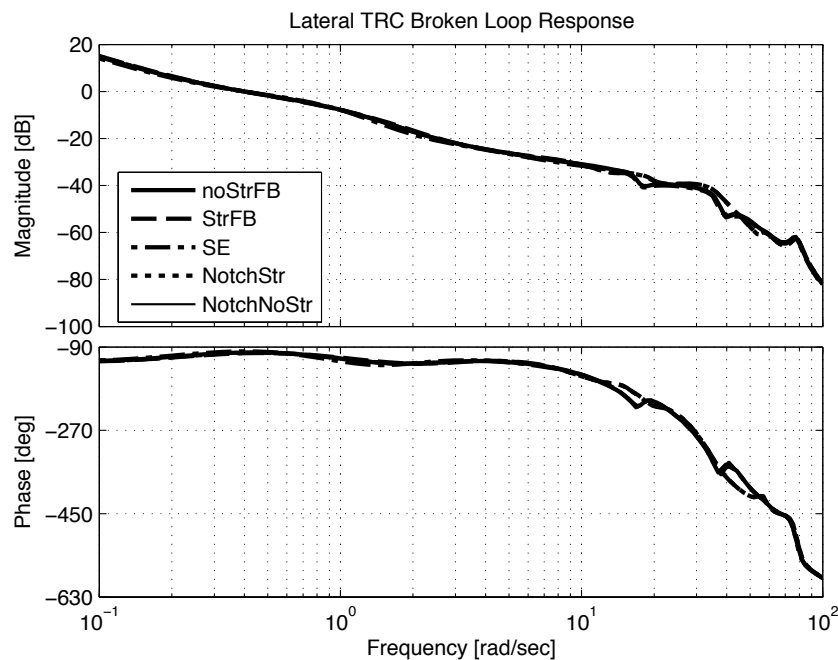
Figure 6.35: Lateral broken loop TRC response
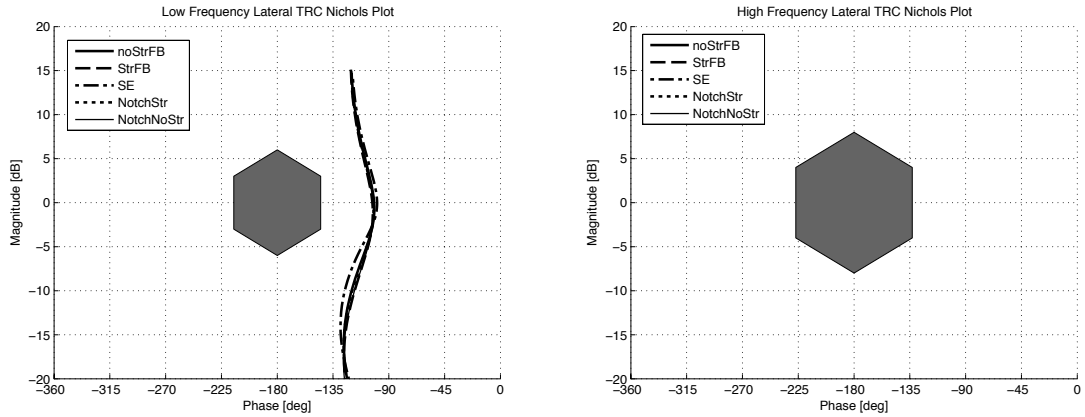
(a) Lateral axis Nichols plot for low frequency
dynamics

(b) Lateral axis Nichols plot for dynamics in
the structural frequency range

Figure 6.36: Lateral axis TRC Nichols plots
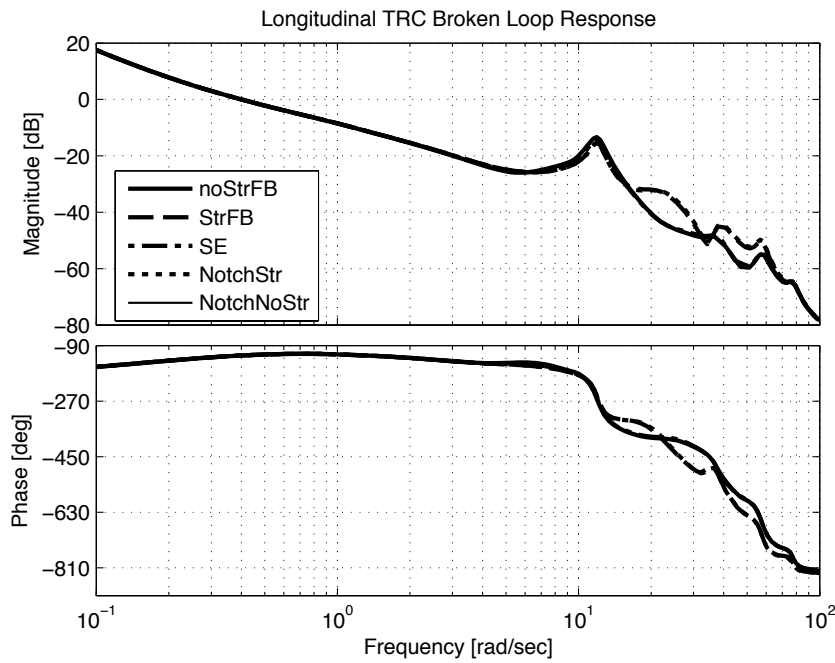
Figure 6.37: Longitudinal broken loop TRC response

The longitudinal axis is shown next in Fig. 6.37. There is a large peak near
12 rad/sec for all the designs. This peak comes from excitation of the symmetric
chordwise bending mode (see Fig. 4.11). There is no structural feedback for this
mode as is it not excited in any of the ACAH responses. All the designs have

identical performance and a -20 dB/dec slope giving good model following in the piloted frequency range. Above the nacelle peak, there is slight elevation in the magnitude peaks for the designs with structural feedback. Due to the low crossover frequency, it is not expected that the control system will excite any structural modes. The Nichols plots (Fig. 6.38) show that the stability margins are adequate at all frequency ranges. The structural peak shows up in the high frequency Nichols plot, but stays well clear of the exclusion zone.
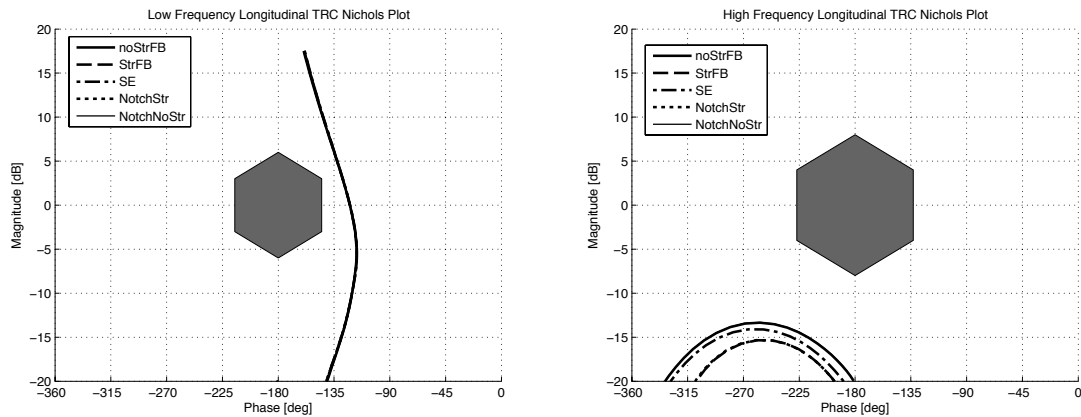
(a) Directional axis Nichols plot for low frequency dynamics

(b) Directional axis Nichols plot for dynamics in the structural frequency range

Figure 6.38: Longitudinal axis TRC Nichols plots

6.4.2   TRC Closed Loop

The closed loop TRC performance is best analyzed by both comparing the velocity response as well as the attitude response. The designed TRC system commands zero attitudes, requiring the aircraft to stay level for all inputs. The closed loop lateral frequency response is shown in Fig. 6.39 and the step input time history is shown in Fig. 6.40. Figure 6.41 shows the associate roll rate response to lateral stick inputs.
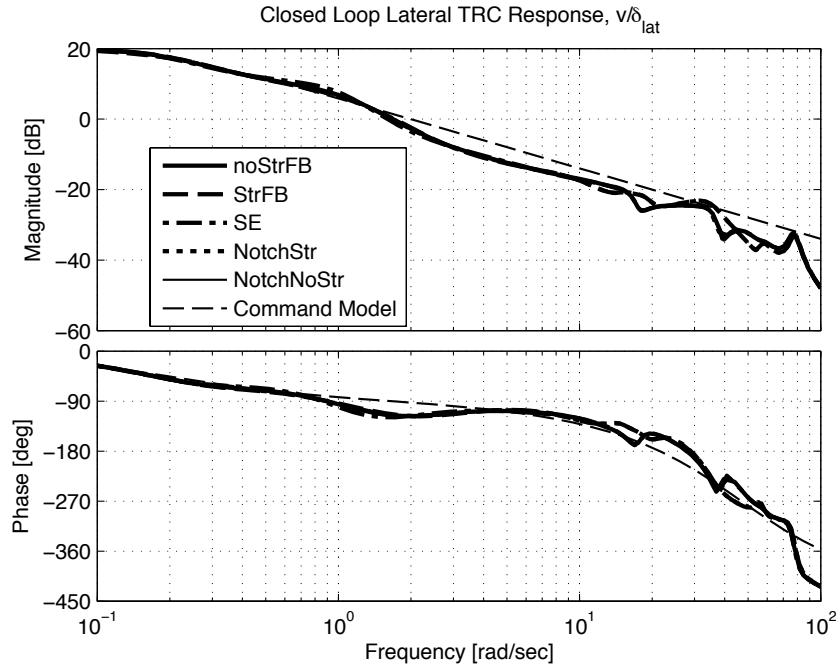
Figure 6.39: Closed loop lateral velocity TRC response to lateral stick inputs

The frequency response shows that the designs have nearly identical performance. There is slight degradation in the responses between 2 and 10 rad/sec, but overall the designs all follow the command response quite well. The model following specification for TRC focused on frequencies below 1 rad/sec, where TRC inputs are most common. There was also only a single rate gain for each TRC axis, with the integral gain being a fixed ratio of this gain. A derivative gain would have improved the model following at mid frequencies but was deemed unnecessary. The step response confirms the excellent model following, with almost no structural oscillation noticeable in any of the designs.

Since the closed loop ACAH roll response had excellent model following at low frequency (Fig. 6.19), the designs all do a good job of not exciting roll rates, as shown in Fig. 6.41. A maximum displacement of less than 1 deg is obtained, and
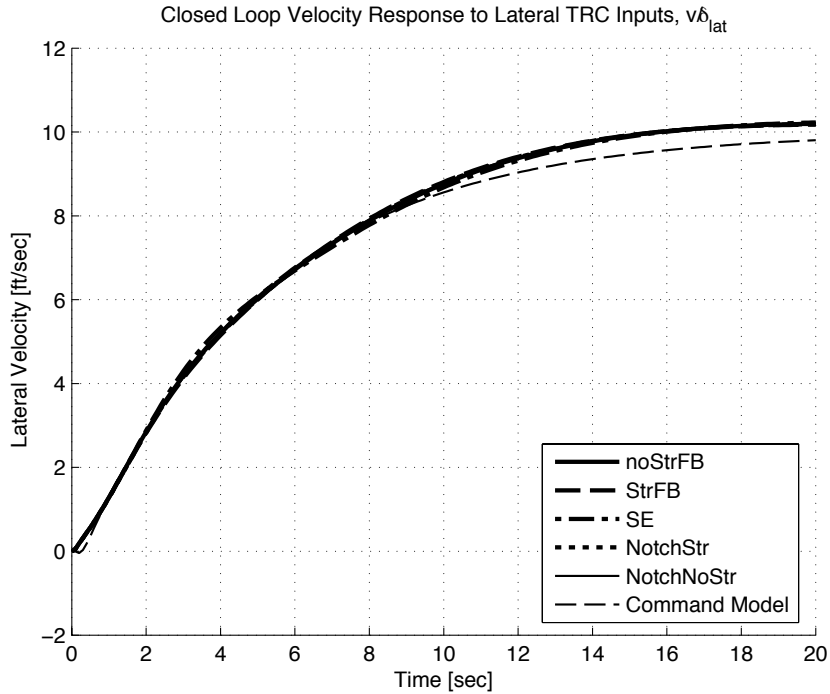
Figure 6.40: Closed loop lateral velocity TRC response to lateral stick step input

within 6 seconds the responses all have angular displacements of approximately 0.3 deg or less. The SE design has the worst performance, while the responses of the rest of the designs are very similar. To further reduce the roll displacement, the crossfeed between symmetric lateral cyclic inputs to antisymmetric collective inputs (roll) could have been improved to be more than a simple gain.

The closed loop longitudinal responses are compared in Fig. 6.42. As with the lateral axis, there is excellent low frequency model following. There is a large peak at 12 rad/sec associated with the symmetric chordwise bending structural mode. The TRC mode is very low bandwidth, so it is not anticipated that this mode will cause undesirable oscillations as pilots will not operate in TRC at 12 rad/sec. This mode also has a max peak that is 20 dB lower than the steady state response, so large oscillations should not result, even if the mode is excited.

256
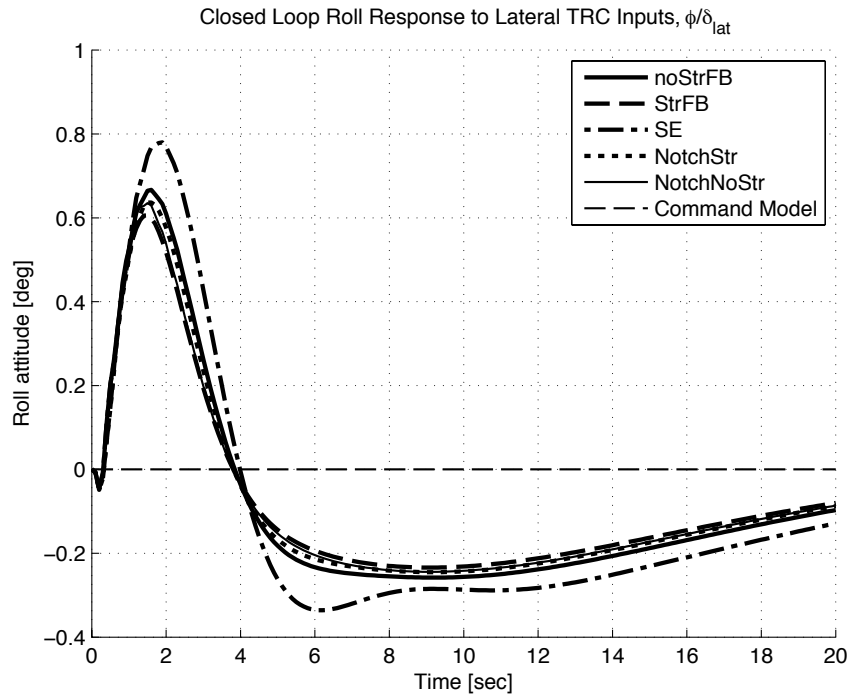
Figure 6.41: Closed loop roll rate TRC response to lateral stick step input
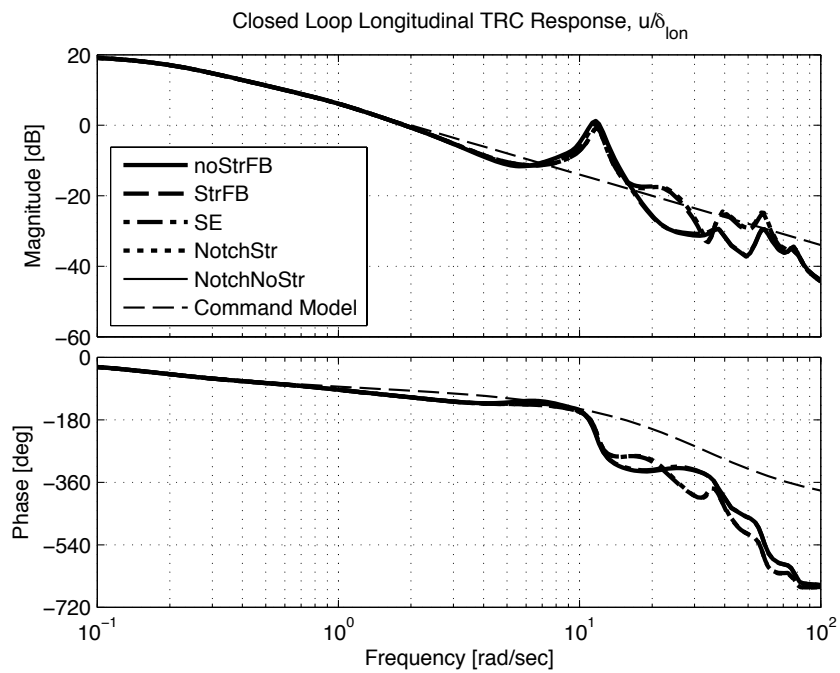
Figure 6.42: Closed loop longitudinal velocity TRC response to longitudinal stick inputs

The closed loop step response is shown in Fig. 6.43. The response shown excellent model following for all the designs over the entire simulation range. The pitch attitude response, shown in Fig. 6.44, shows near zero pitch excitation for longitudinal TRC commands. The nacelle to symmetric longitudinal cyclic crossfeed does an excellent job at eliminating the response with the maximum deviation being only ∼0.15 deg.
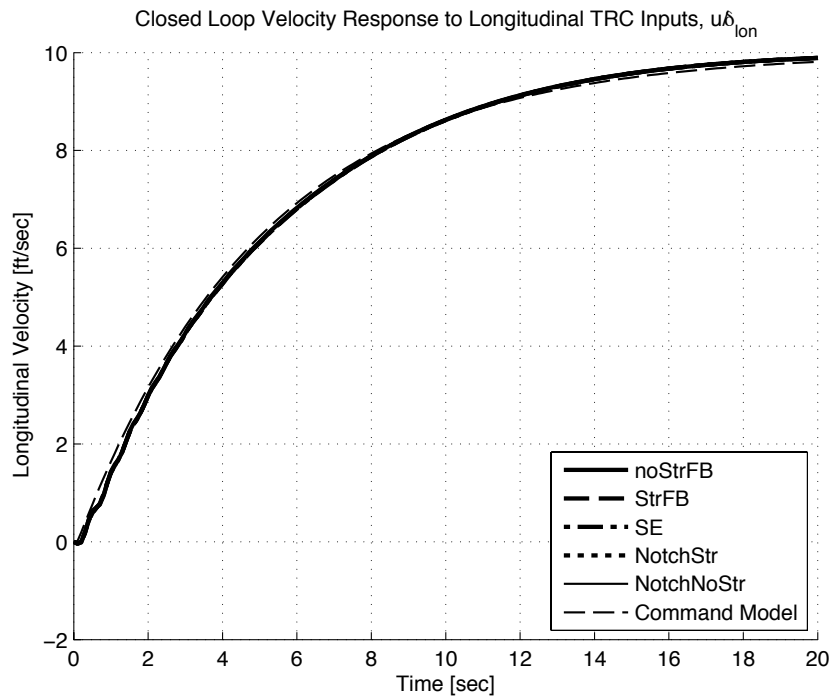
Figure 6.43: Closed loop longitudinal velocity TRC response to longitudinal stick step input

The final comparison shows the nacelle displacement for longitudinal TRC commands. The nacelle motion is driven by the velocity error and is rate and position limited. The rate and position limits come from the preferred values from the NASA piloted simulations (Ref. [31]). The nacelle quickly rotates forward to initiate a forward acceleration. The commanded acceleration is largest when the step
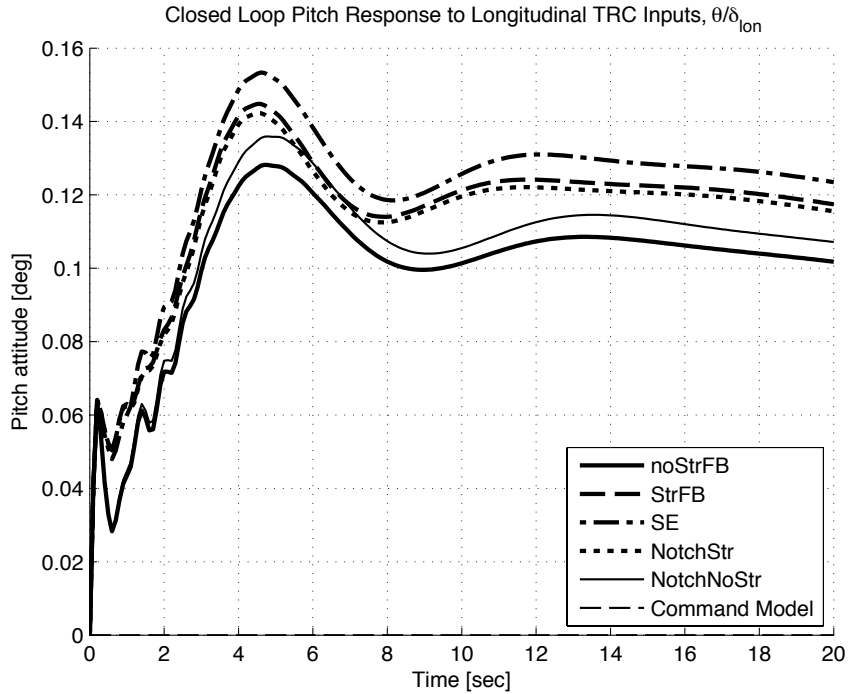
Figure 6.44: Closed loop pitch rate TRC response to longitudinal stick step input

input takes place and quickly reduces in magnitude. As the required acceleration decreases, the nacelles displacement is reduced until it reaches its trim value to maintain a steady velocity.

6.4.3 TRC Disturbance Rejection

TRC disturbance rejection requirements are reduced when compared to the ACAH requirements, and again adhere to the requirements set forth in Ref. [110]. The lateral TRC DRB responses are nearly identical. The SE design has the highest peak response, but the bandwidth is nearly identical for all the response. Note the low bandwidths as compared to the lateral ACAH DRB plot in Fig. 6.31. The aircraft cannot reject high frequency disturbances well using the TRC system.

A similar trend is shown for the longitudinal axis, but here all the plots are
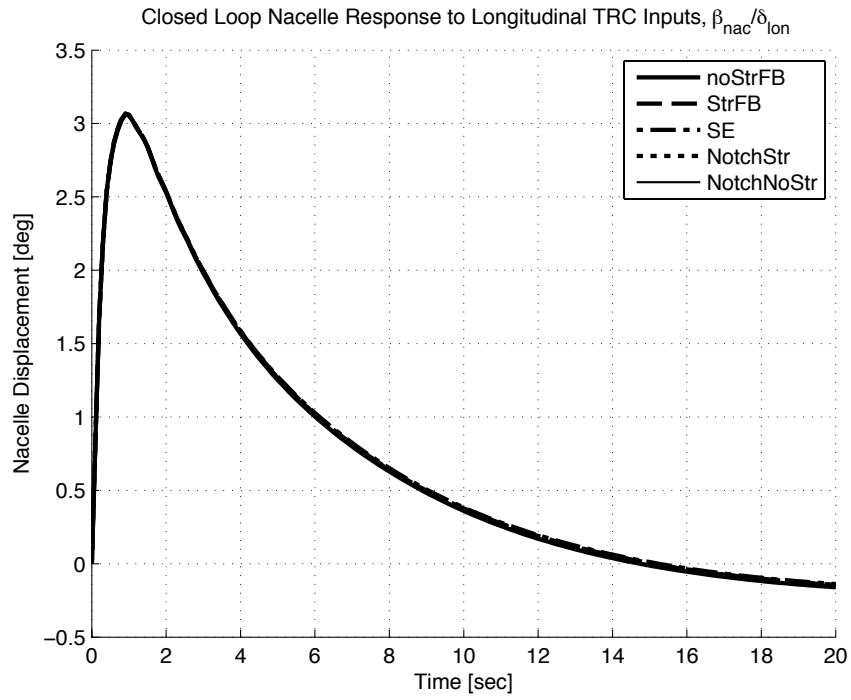
Figure 6.45: Closed loop nacelle displacement response to longitudinal stick step input
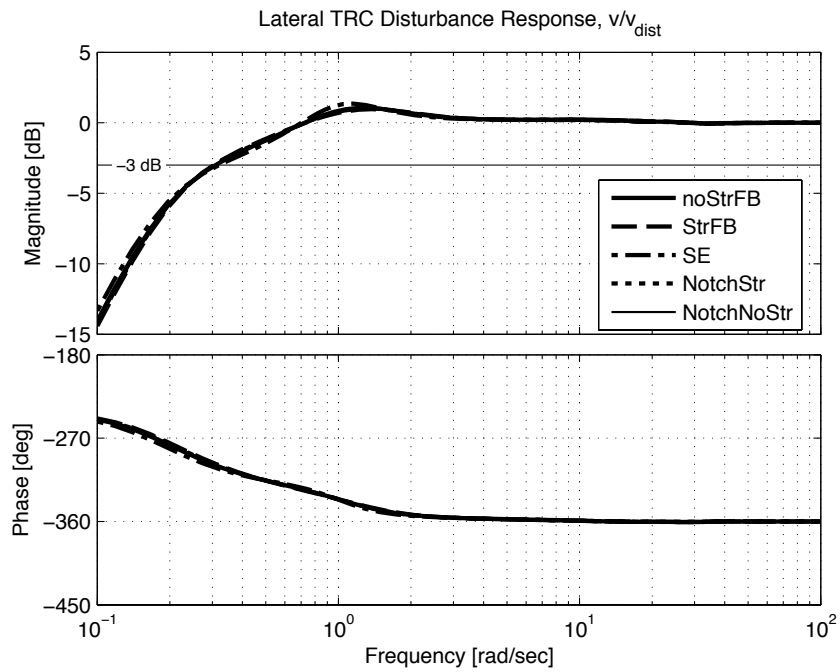
Figure 6.46: Lateral TRC disturbance rejection response

identical. Again, the bandwidth is much lower than for the longitudinal ACAH response.
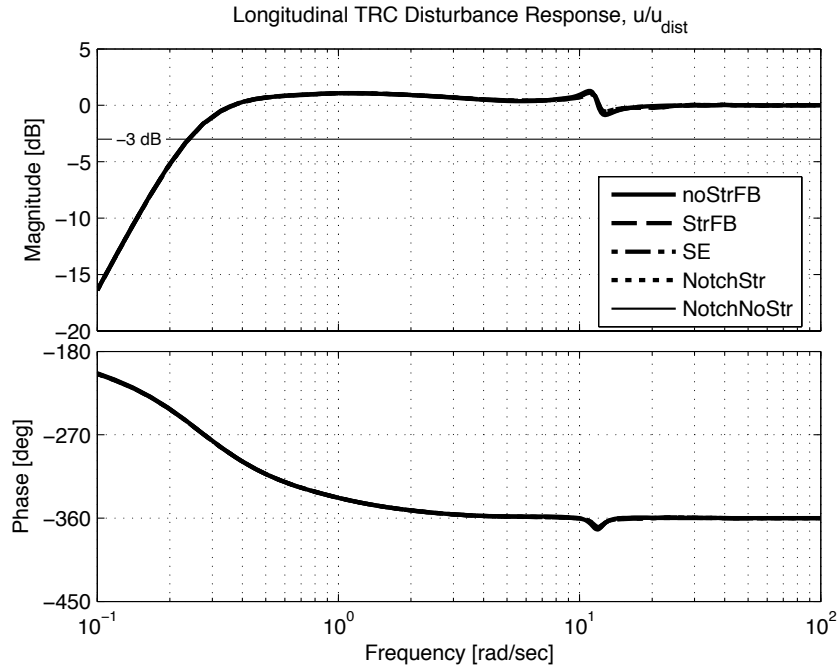
Figure 6.47: Longitudinal TRC disturbance rejection response

6.5 Structural Response

The final set of design comparisons are for the structural responses. Structural damping is compared, as are structural responses to the CETI turbulence model and pilot inputs. The turbulence model shows the effectiveness of the control system at removing realistic disturbances and thus improving ride quality. Reductions in structural motion to both turbulence and piloted inputs are also important for reducing fatigue on aircraft components. RMS values for strain are obtained from integrating the frequency response curve of the appropriate strain to turbulence inputs from 1-100 rad/sec. Turbulence inputs excite all the axes simultaneously.

261

Table 6.6: Comparisons of structural damping

	noStrFB	StrFB	SE
Antisymmetric beam damping, $[\zeta]$	0.085	0.126	0.084
Symmetric beam damping, $[\zeta]$	0.119	0.392	0.114
Antisymmetric chord damping, $[\zeta]$	0.109	0.105	0.108
Symmetric chord damping, $[\zeta]$	0.076	0.062	0.072

6.5.1   Structural Damping

The damping of the structural modes for each design are taken from the linearized closed loop response and are given in Table 6.6. Since only structural feedback changes damping, designs using the notch filters in the feedforward path are not shown. Putting the bare-airframe (which has distinct structural modes) into a control system with feedbacks and crossfeeds greatly couples the structural modes and rigid-body responses. The damping ratios given are for system modes which have the predominant structural response for the named mode. There are large damping changes for the symmetric beam mode, directly resulting in an improved structural response. Damping was also improved for the antisymmetric mode. There was no improvement in the damping for either chordwise mode. No gain was present to improve the symmetric chord mode, but gains were present for the antisymmetric chord mode. Antisymmetric chordwise acceleration was fed back to the pedals (antisymmetric longitudinal cyclic). Even though damping was not improved, the overall excitation of the mode is lower due to increase actuator usage in this axis.

Table 6.7: Comparisons of structural RMS to turbulence

	noStrFB	StrFB	SE
RMS strain beam[1]	0	-14.4	0.9
RMS strain chord[1]	0	-28.5	2.1

[1] Percent change in strain RMS from the noStrFB case (nominal)

6.5.2 Structural Response to Turbulence

The comparisons to turbulence are based on the wing root strains in the beam bending and chord bending directions and are shown in Table 6.7. The baseline RMS values are for the noStrFB case and strains are given as percentage reductions in strain from this case. Notch filter cases were not included in comparisons for excitation due to turbulence since the notch filter designs filter piloted input, which is not present in these cases.

Table 6.7 shows large improvements to the response to turbulence for the design with structural feedback. There is a nearly 30% reduction in chordwise motion and a nearly 15% reduction in beamwise motion for the design with structural feedback as compared to the noStrFB design. The SE design performs the worst, and has slightly elevated structural motion than the noStrFB design.

Time history responses are shown in Fig. 6.48 for strain responses to turbulence inputs. Beam strain is shown in Fig. 6.48a. The large improvements obtained in the StrFB case is noticeable for many of the response peaks. The improvement to the wing root strain is even more apparent in the chordwise direction, as shown in

Table 6.8: Comparisons of structural RMS to piloted inputs

	noStrFB	StrFB	SE	NotchStr	NotchNoStr
RMS strain beam/δ_{lat} [%][1]	0	-39.4	0.7	-67.0	-60.8
RMS strain beam/δ_{col} [%][1]	0	-51.0	4.4	-67.7	-60.0
RMS strain chord/δ_{ped} [%][1]	0	-22.4	3.2	-35.5	-31.1

[1] Percent change in strain RMS from the noStrFB case (nominal)

Fig. 6.48b. Here, the StrFB design has significantly lower strain values across the entire time history.

To improve modal damping and reduce structural excitation in turbulence, active structural feedback is needed in the control system.

6.5.3   Structural Response to Piloted Inputs

Table 6.8 compares changes in structural motion to pilot inputs by comparing RMS values from the closed loop response. As with the previous table, the noStrFB case serves as the baseline.

It is apparent that notch filters in the feedforward path add large reductions in the excitation of the structural modes. The StrFB design also shows large improvements, but the notch filters provide the majority of improvement. Total reductions of nearly 70% are attainable in the lateral and heave axes and reductions of 35% are attainable in the pedal axis. The SE design again has the worst performance.

Reduction due to longitudinal inputs are not included since there was no structural gain for this axis. The notch filters in themselves (NotchNoStr design) are so effective because they passively remove frequency content near the structural fre-
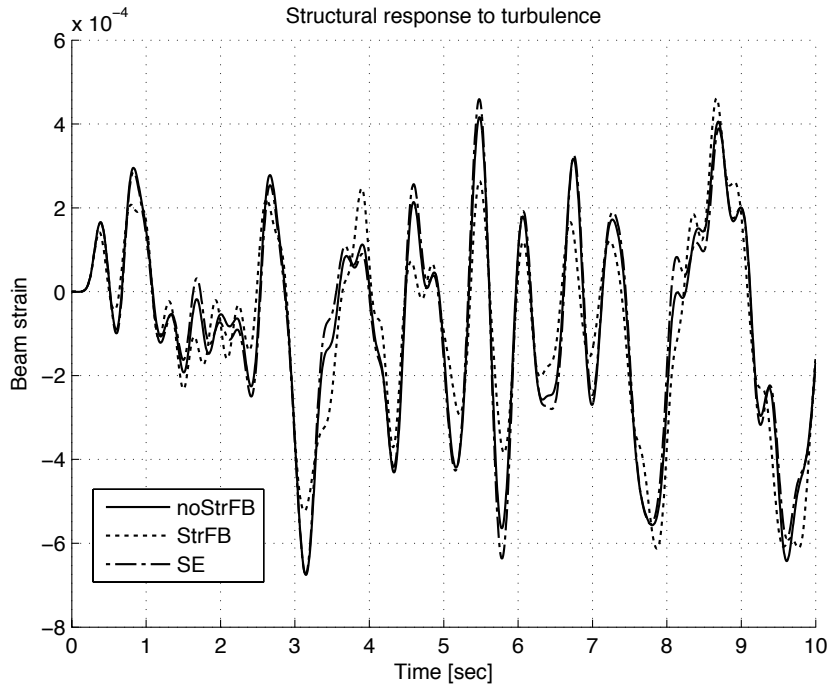
(a) Beam strain response to turbulence
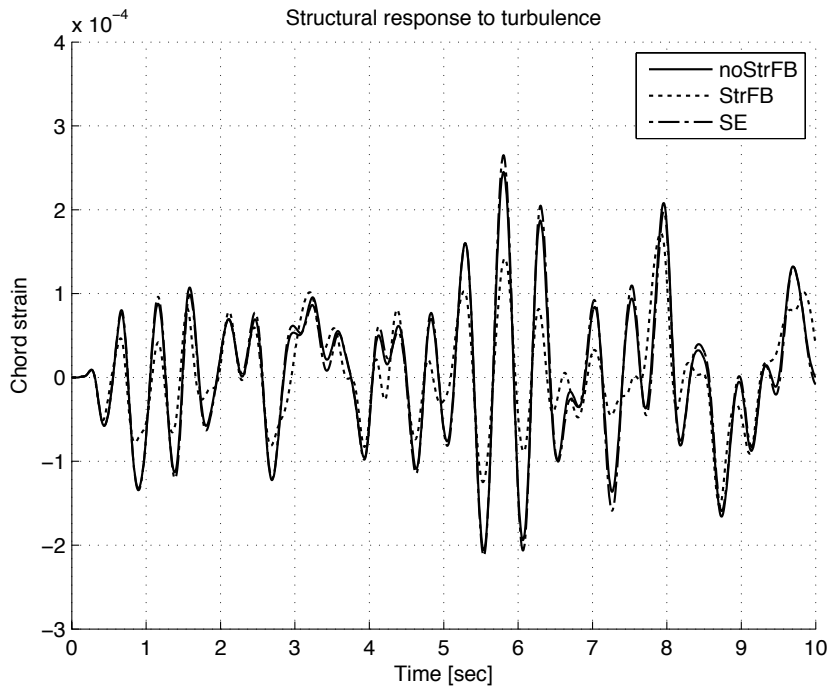
(b) Chord strain response to turbulence

Figure 6.48: Strain responses to turbulence

quencies and the pilot is not allowed to excite these modes. Without the notch filters (StrFB) the control system must actively measure and remove structural motion. Combining both approaches for the NotchStrFB design gives the best results, adding an additional 5-7% reduction over the NotchNoStr design. Figure 6.49 shows the strain time histories for a step input. These time histories validate the RMS data and show the effectiveness of the notch filters over structural feedback for reduction of structural motion to pilot inputs. Piloted time histories from simulation will be compared in Chapter 7.

Based on the analyses in this section, structural feedback improves the structural response in turbulence, and feed forward notch filters are most effective at reducing structural motion to pilot inputs.

6.6 Robustness Analysis

A robustness analysis is performed by perturbing components of the linear models associated with the structural modes and re-evaluating the specifications. Structural modes will never be known with certainty and will vary with loading and fuel use throughout the flight. Therefore, it is important that the controls systems stability and performance remains robust when there is uncertainty in the structural mode components. Stability margins are compared through Nichols plots to determine robustness. Stability is the most important metric of an aircraft control system. Deviations in closed loop bandwidth, model following, or disturbance rejection characteristics might lead to less than desirable handling qualities, but are not potentially catastrophic.
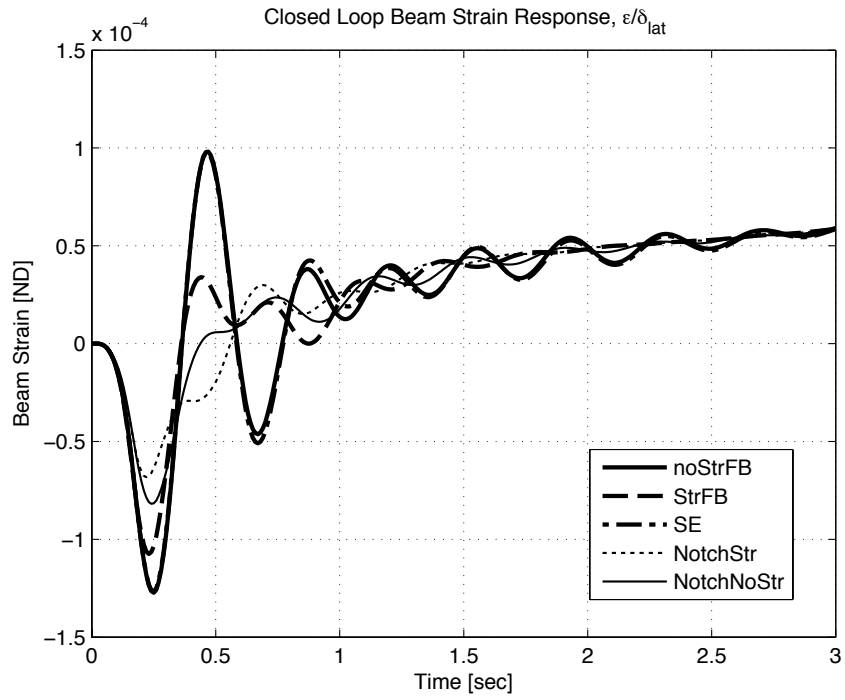
(a) Beam strain to step lateral stick input
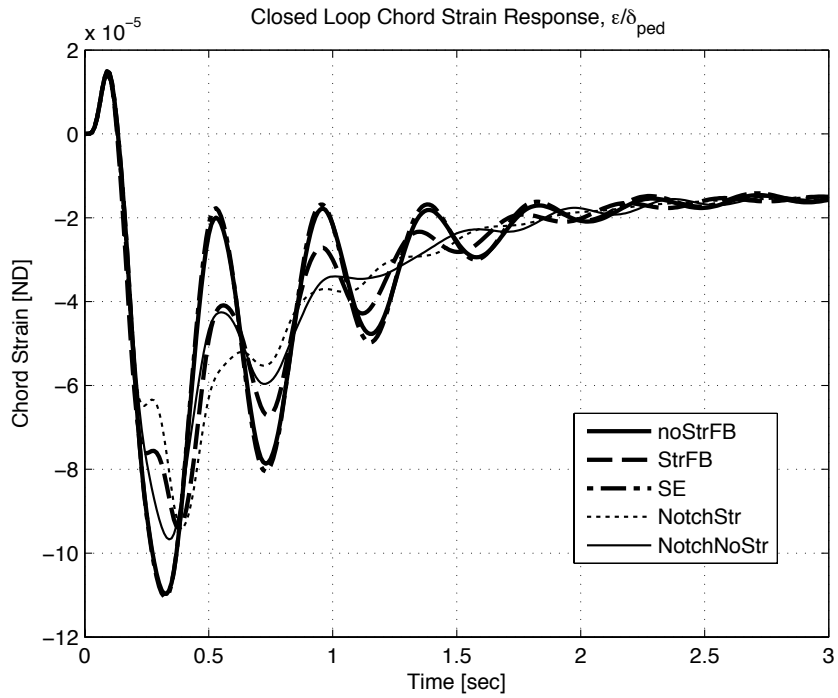
(b) Chord strain to step pedal input

Figure 6.49: Strain responses to piloted step inputs

Table 6.9: Bare airframe derivatives used in robustness analysis

Structural Mode	Modal Parameters	Rigid-Body Coupling	Aeroelastic Coupling	Control Derivative
Symmetric Beam Bending	ζ ω	η_w η_q	Z_η	$\eta_{\delta_{col}}$
Antisymmetric Beam Bending	ζ ω	η_v η_p η_r	Y_η L_η	$\eta_{\delta_{lat}}$
Antisymmetric Chord Bending	ζ ω	η_v η_p η_r	Y_η L_η N_η	$\eta_{\delta_{ped}}$

Table 6.9 shows which components of the bare airframe model were perturbed. Derivatives include the structural mode frequency, damping, and control derivative. The couplings between the rigid-body states and structural states were also perturbed. Each derivative was individually perturbed positively and negatively, then all the chosen derivatives were perturbed both positively and negatively. A perturbation of 15% was used. Smaller perturbations did not result in large instabilities in any of the designs. The analysis was done in ACAH mode, as this mode is the limiting factor for aircraft stability.

The robustness results are only shown for the limiting designs, noStrFB and NotchStr, representing the worst and best configurations designed. The rigid-body margins are not largely affected by changes in structural parameters as seen in Figs. 6.50a and 6.51a for the lateral axis. The benefit of structural feedback with notch filters comes out in the high frequency comparisons in Figs. 6.50b and 6.51b. Several designs in the noStrFB high frequency figure pass through the exclusion zone, causing potential instability. However, the NotchStr design remains stable for the same 15% change to the chosen parameters.

The other axis of interest is the directional axis. Figure 6.52 shows the high
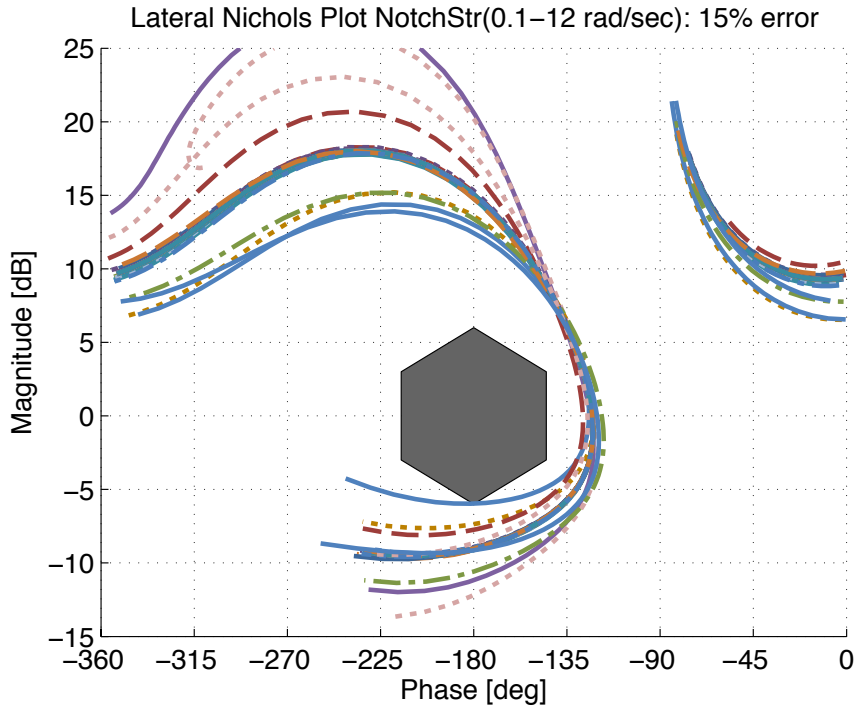
(a) Lateral axis NotchStr rigid-body frequency Nichols plot
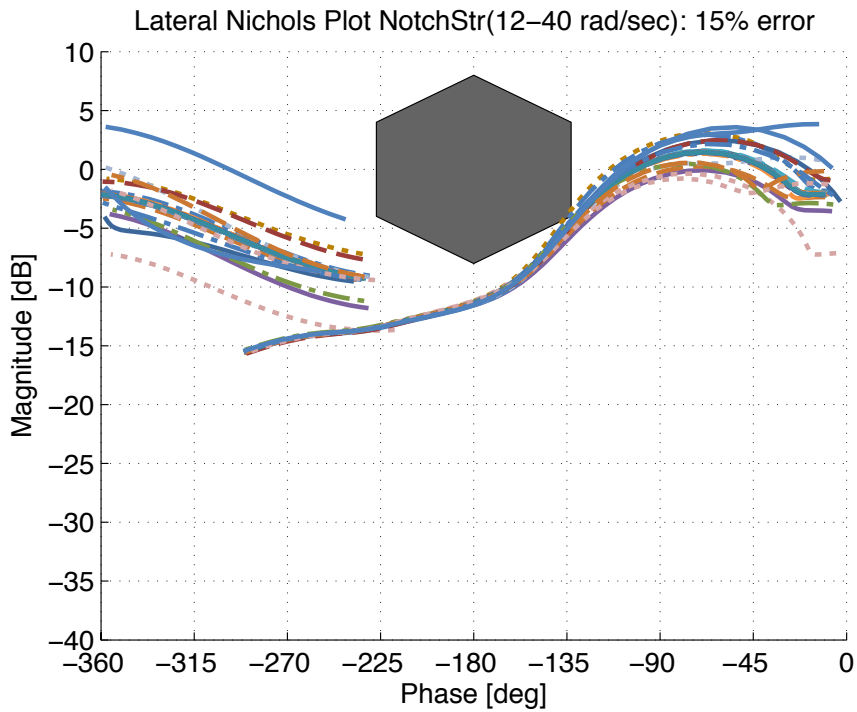
(b) Lateral axis NotchStr structural frequency Nichols plot

Figure 6.50: Lateral axis NotchStr design robustness analysis with 15% perturbation
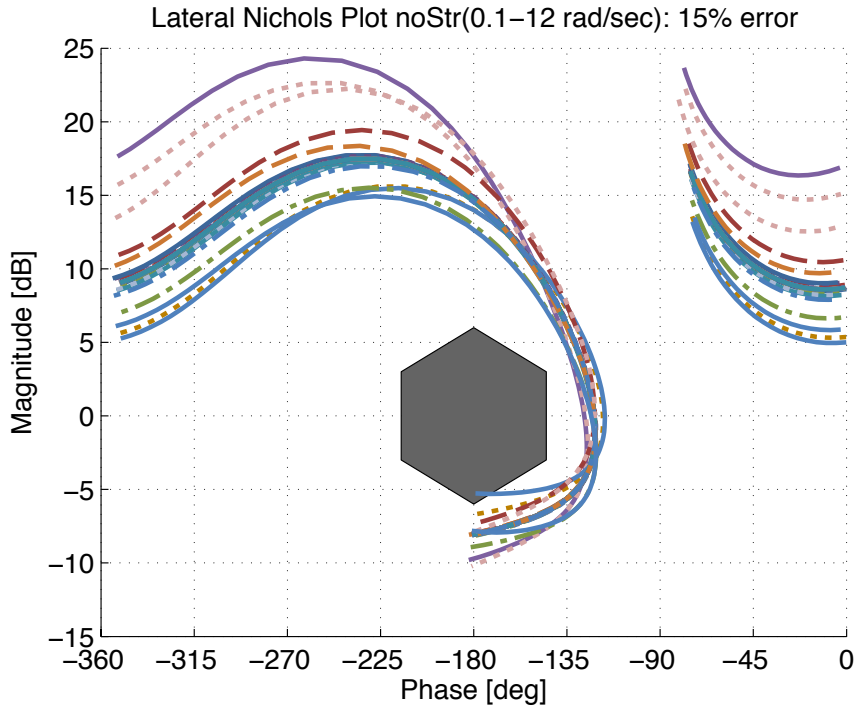
(a) Latearl axis noStrFB rigid-body frequency Nichols plot
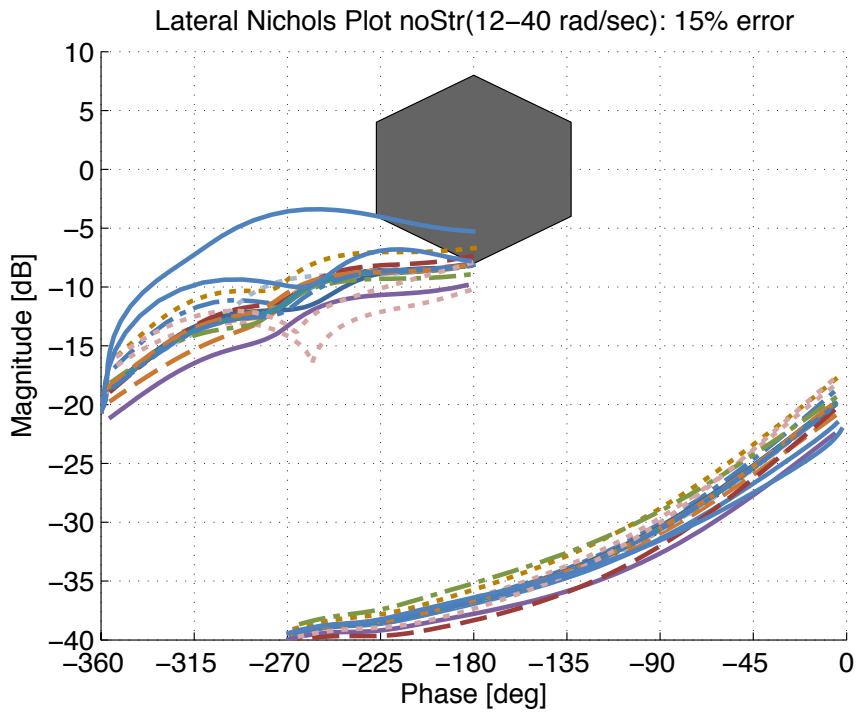
(b) Lateral axis noStrFB structural frequency Nichols plot

Figure 6.51: Lateral axis noStrFB design robustness analysis with 15% perturbation

frequency responses for the noStrFB and NotchStr designs. It is immediately apparent that the noStrFB design (Fig. 6.52a) has more crossings of the exclusion zone, with one perturbation set being nearly unstable. The NotchStr design performs much better with only minor crossings for the structural frequency range. Structural feedback with notch filters provides significant improvement over the noStrFB design in terms of robustness.

6.7   Chapter Summary

The inclusion of structural feedback in the control system for large flexible aircraft produces large improvements in the structural response of the aircraft. Notch filters are commonly used as the single means to remove structural oscillation from the control system. Notch filters provide an excellent passive method to reduce structural oscillation to piloted inputs and to ensure the control system does not excite structural modes. Active feedback provides better performance, especially in turbulence. Structural comparisons were based on the wing root strain measurements for both chordwise and beamwise beam bending.
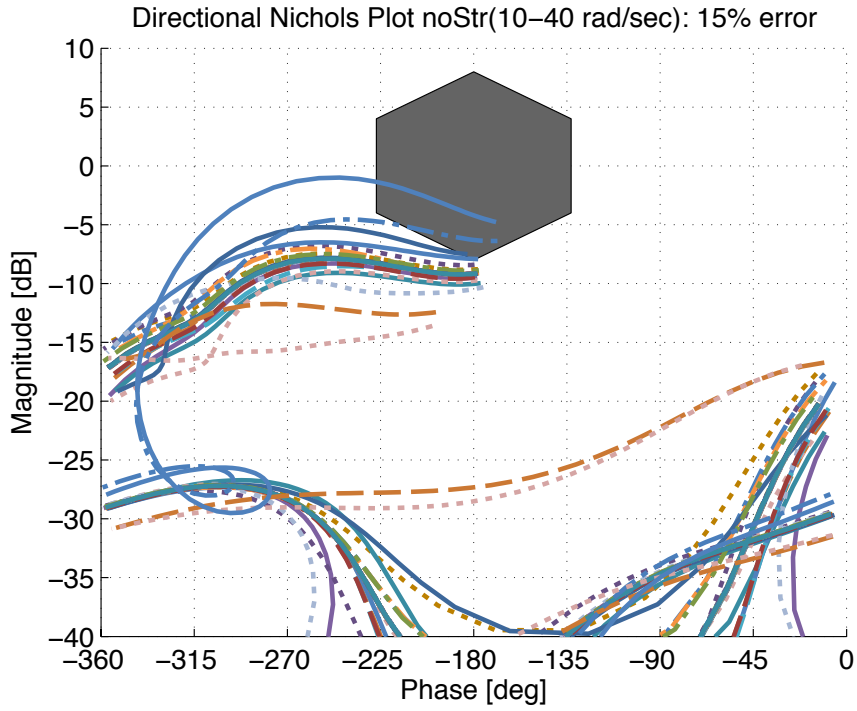
(a) Directional noStrFB structural frequency Nichols plot
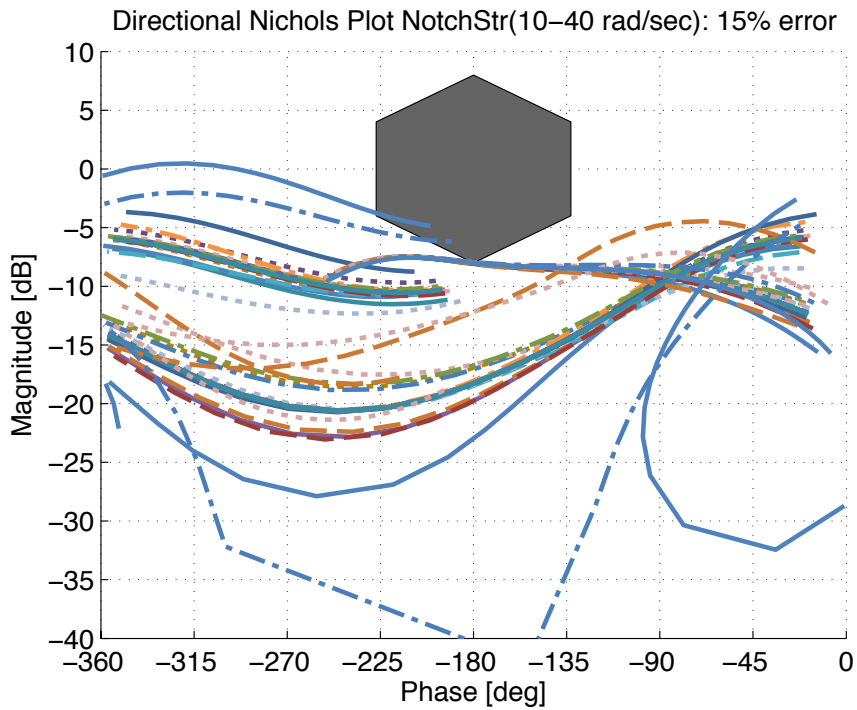
(b) Directional NotchStr structural frequency Nichols plot

Figure 6.52: Structural frequency directional robustness analysis with 15% perturbation

Chapter 7: Fixed-Base Simulation

The final chapter of this dissertation looks at the results of a piloted simulation comparing the LCTR control laws with and without structural feedback included. The aim is to provide realistic piloted inputs into the control system and compare and contrast the behavior of the two control systems.

7.1 Simulator Description

Piloted simulations were performed in a fixed based simulator located at AFDD, Moffett Field, to test the designs' performance using actual pilot inputs. The simulator consists of three large flat screen televisions mounted in front of the pilot, see Fig. 7.1. The screens were rotated horizontal and the field of view on each screen was modified to provide the pilot more than a 180 deg. total field of view. The inceptors consist of a standard collective, sidestick controllers, and rudder pedals. The pilot has the ability, through toggles to engage/disengage turbulence and switch between ACAH and TRC mode. The transition between ACAH and TRC is accomplished through a 3 second blending of the two modes, where the TRC gains are turned on and the commanded responses is transitioned from one mode to the other.

Figure 7.1: Fixed-base simulation facility

7.2   Task Description

Three pilots flew the simulator, two were Army test pilots, and one an operational HH-60 pilot. The pilots were asked to fly representative ADS-33E mission task elements (MTEs) that would highlight the control systems ability, or inability, to reduce structural oscillation. The hover, lateral reposition, and depart/abort tasks were chosen. The pilots flew two control gain sets, noStrFB and NotchStrFB, representing the worst and best structural performance. All the tasks were flown with the turbulence turned on, and pilots were not told which gain set they were currently operating.

The pilots were allowed adequate time to get acquainted with the LCTR2 model in the simulator to practice the tasks, fly with and without turbulence, and

switch between the two operating modes. The pilots were not asked to give handling quality ratings for each gain set, but rather to give comments comparing the two gain sets flown. Data collected included stick traces, ACAH/TRC mode switch position, inertial positions, as well as all state and structural information. For timing, the pilot called out the beginning and end of each maneuver and the data presented represents only data taken during each maneuver.

The data for the simulations was analyzed in the frequency domain. Input and output autospectra to time histories were identified using CIFER® [97]. The simulation was performed to determine if different piloting strategies were used, and to verify that the structural response was in fact improved under real piloted conditions. The comparisons between the noStrFB and NotchStr designs include comparing input and output autospectra, identifying the pilot cut-off frequency, and structural RMS calculations. For simplicity, the data presented in the autospectrum figures is for a single pilot, but all pilots had similar trends.

7.3 ACAH

Comparisons are first performed with the aircraft in ACAH mode.

7.3.1 Hover - ACAH

Comparisons between the input and output autospectra are shown in Fig. 7.2. The top two figures show the autospectra of the stick inputs while the bottom figures show the beam and chord strain responses. Each hover task lasted over a minute, and each task was performed three or four times, providing rich frequency content for

the identification. The lateral and longitudinal stick autospectra are nearly identical when comparing the noStrFB and NotchStr cases. The small difference around 1.2 rad/sec can be attributed to slight variations in flying the aircraft, potentially because the pilot became more familiar with the task. These plots make it apparent that the pilots flew both gain sets in the hover task nearly identically. The output autospectra look nearly identical at low frequency, but at the structural modes the NotchStr case has reduced magnitude content. It is apparent that the NotchStr design is able to reduce the structural motion at these frequencies.

To ensure the increase in magnitude around the structural frequencies was not caused by differences in piloting strategy, however small, the noStrFB pilot stick trace was used to run a time simulation with the NotchStr gain set. This creates identical input autospectra for both the noStrFB and NotchStr gain sets, matching the noStrFB lines in the first two plots in Fig. 7.2. During the replay, identical CETI inputs are also used. The output beam and chord strain responses for these "replayed" noStrFB inputs are shown in Fig. 7.3. The frequency content at the structural frequency of the replayed inputs matches that of the NotchStr case. Since within this replay, the exact same pilot and turbulence are used, any deviations in the Replay line from the noStrFB line is a result of different closed loop responses at those frequencies.

The same noStrFB input was also replayed in the other designs developed. These comparisons are shown in Fig. 7.4. The additional RB FB only design was also used and serves as a baseline with no structural compensation. Here all notch filters in the block diagram were removed and the noStrFB gain set was used. This
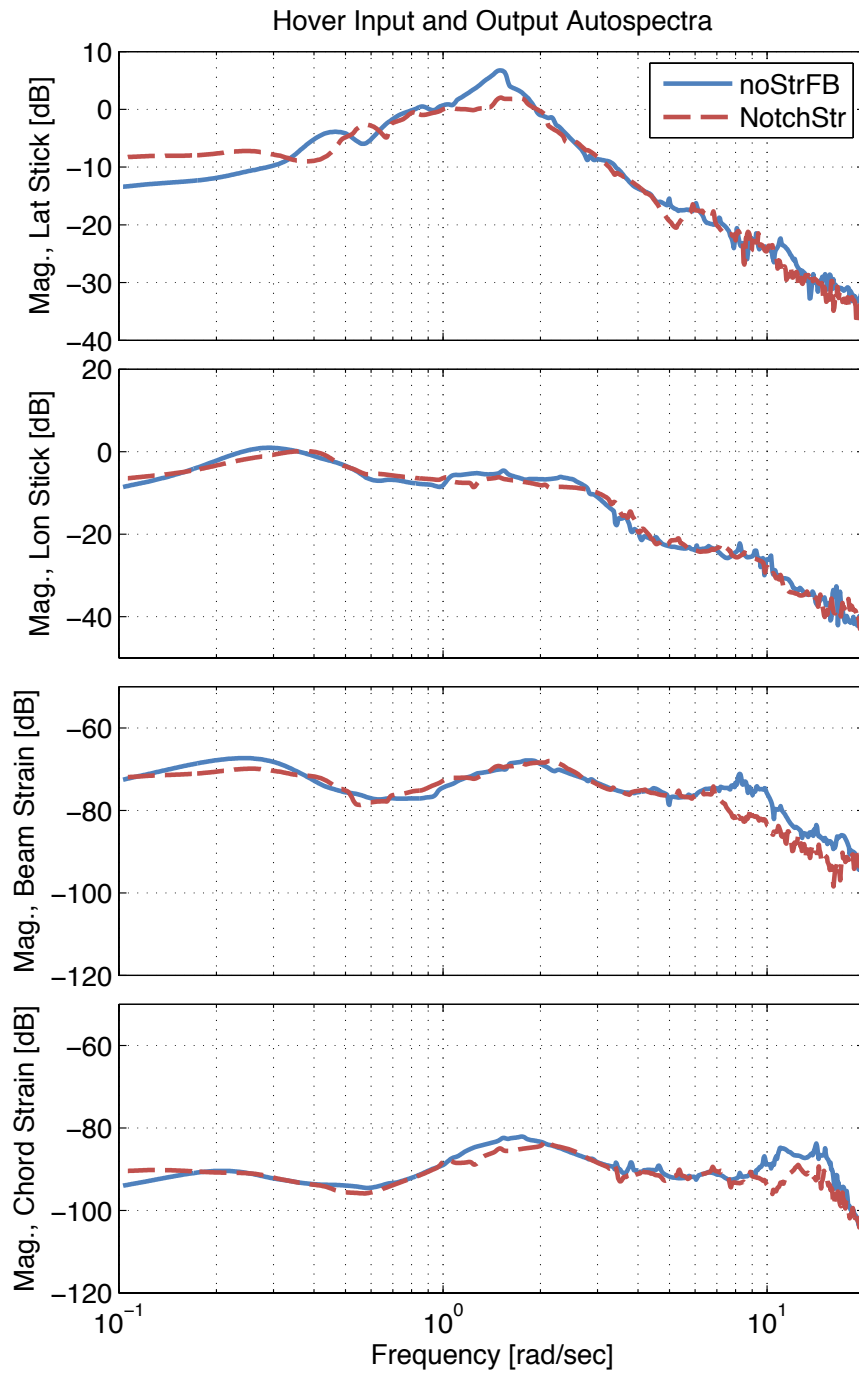
Figure 7.2: Hover input and output autospectra
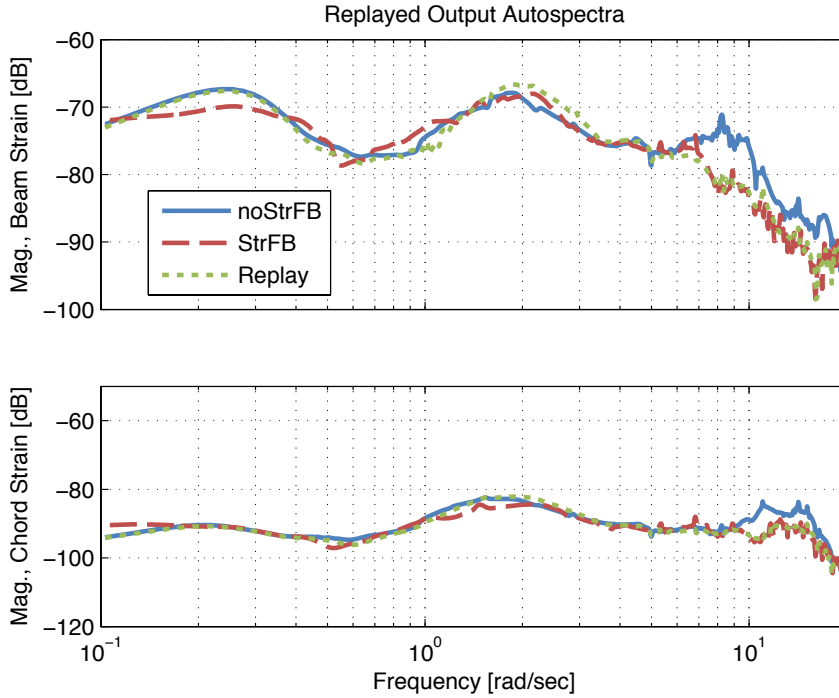
Figure 7.3: Hover replayed strain comparison to simulation data

design has the worst performance at the structural frequencies as shown by the large magnitude content in both the beamwise and chordwise directions. The other replayed designs fall into two categories. The designs without structural feedback (noStrFB and NotchNoStr) have improved performance at the structural modes over the RB FB only design, but are worse than the designs with structural feedback (StrFB and NotchStr). It has been shown that the designs with notch filters in the feedforward path perform better than the other designs to pilot inputs, regardless of structural feedback. It has also been shown that structural feedback is key to improving performance in turbulence. With this in mind, it is clear that the dominant excitation of the structural modes during the sim came from turbulence, making a strong case for using structural feedback in the flight control system.

Next, time histories are compared in Fig 7.5. Again, in order to have mean-
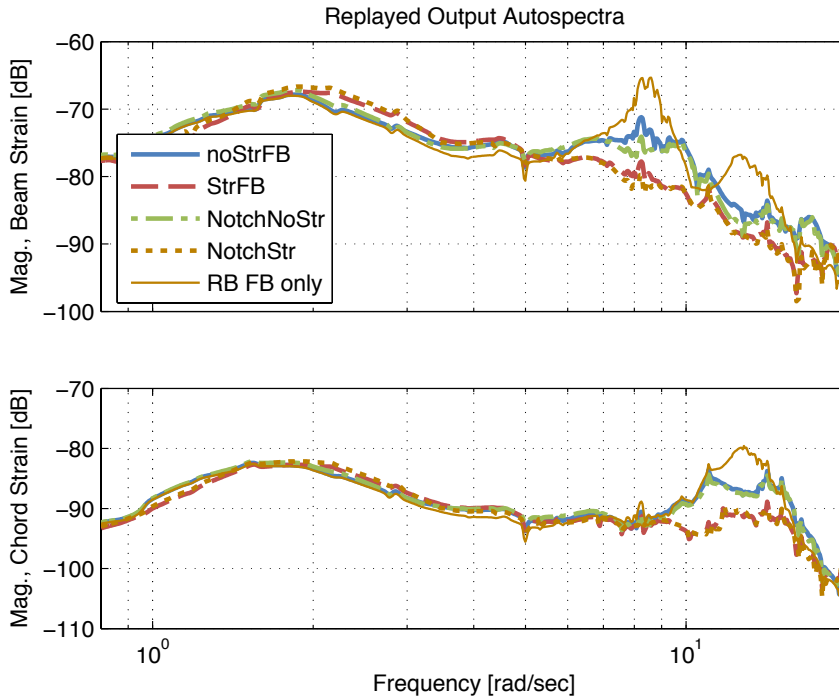
Figure 7.4: Hover replayed design comparisons

ingful comparisons the replayed designs are shown. The same conclusion can be drawn as from the frequency response. The StrFB and NotchStr designs have the least oscillation.

7.3.2 Lateral Reposition - ACAH

The lateral reposition task gave similar results to the hover task. Since this task is much shorter, 20 seconds vs 60 seconds, there is not much low frequency data to identify. However, by comparing the Lateral reposition input and output autospectrum (Fig. 7.6), we can conclude that the behavior of the noStrFB and NotchStr designs is very similar to the hover results. Even though the NotchStr had a slightly higher input power spectral density, the strain output remained lower at those frequencies. The lateral reposition task was the first to be flown, so changes in
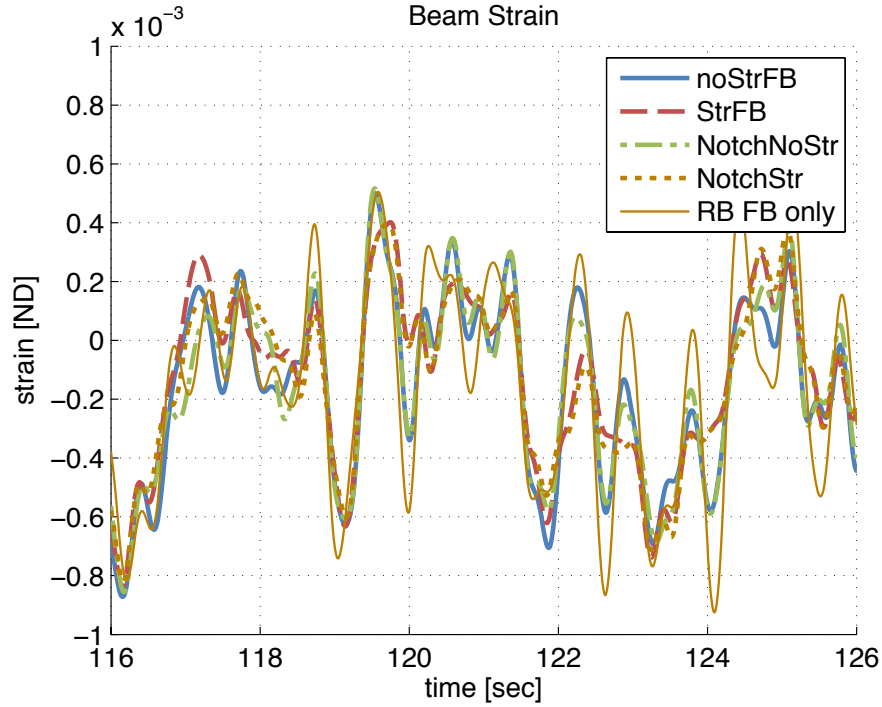
Figure 7.5: Time history of replayed designs in hover

the input autospectrum are associated pilot familiarization of the task and aircraft.

7.3.3 Depart/Abort - ACAH

The depart/abort autospectra are shown in Fig. 7.7. As with the lateral reposition, this task is much short and does not contain much low frequency data. This task confirms again the nearly identical pilot strategy and the increase in strain content at the structural frequencies for the noStrFB design.

7.4 TRC

The TRC performance will be compared only for the hover task, as the results are nearly identical for the other tasks flown. The TRC mode is much slower than the ACAH mode, so pilots must back out of the loop and not be as aggressive. This is seen as a shift in the peak of the lateral stick autospectrum (Fig. 7.8) to
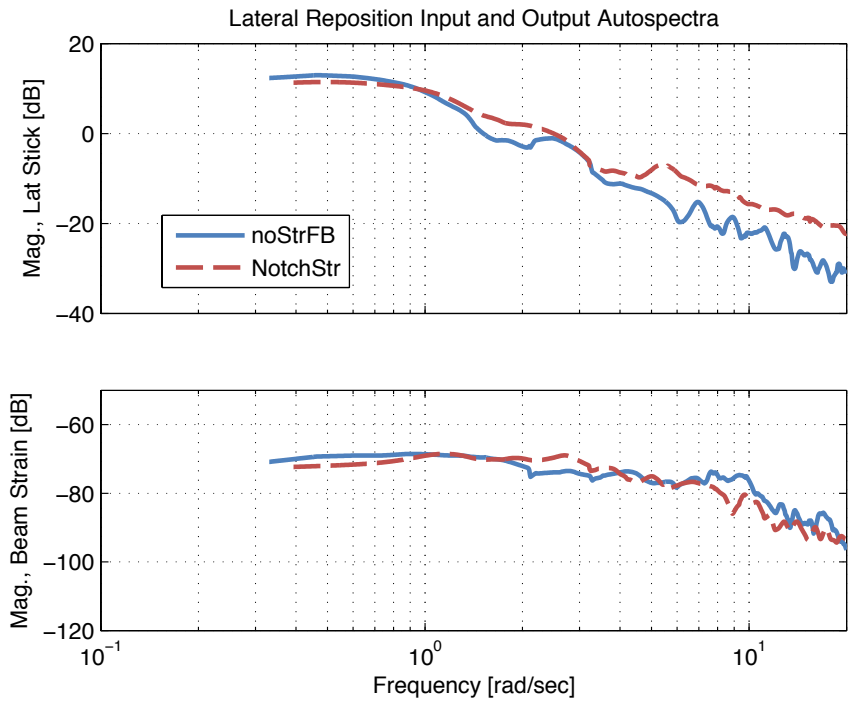
Figure 7.6: Lateral reposition input lateral stick and beam strain autospectra
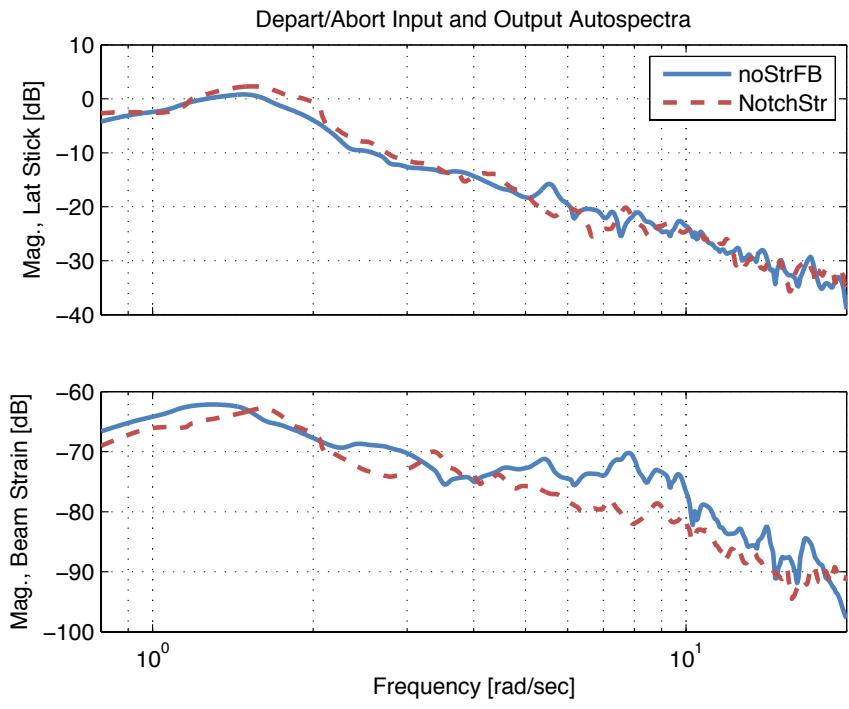
Figure 7.7: Depart/Abort input lateral stick and beam strain autospectra
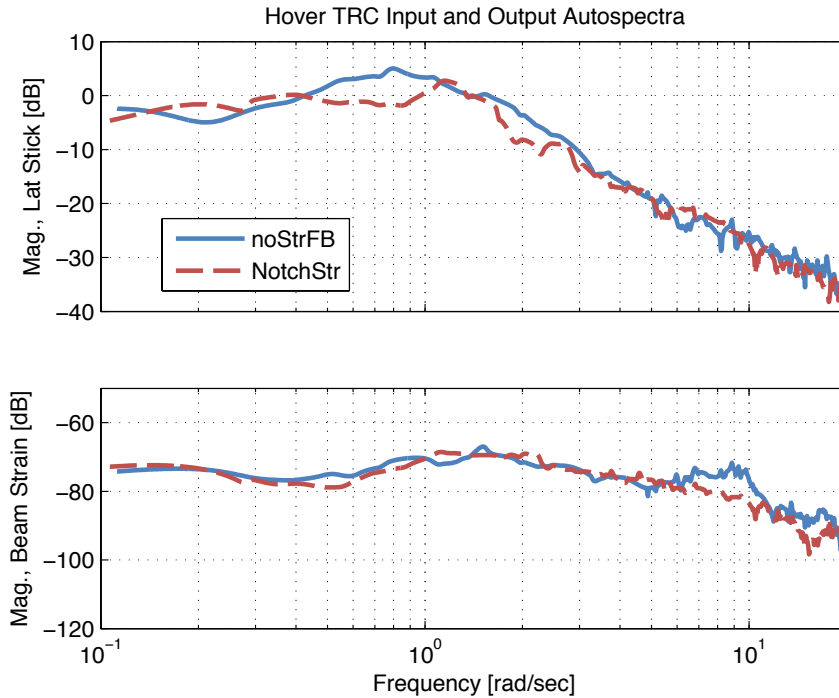
Figure 7.8: TRC Hover input lateral stick and beam strain autospectra

lower frequencies when compared to the ACAH case (Fig. 7.2). Even in TRC mode, the same trends between the noStrFB and NotchStr designs are evident. The pilot input autospectrum is very similar between the two cases, while the beam strain has a prominent increase at the structural frequency for the design without structural feedback.

7.5   Structural RMS

The total structural RMS reductions between the noStrFB and NotchStr design are given in Table 7.1. The frequency response is integrated from 4 rad/sec to 20 rad/sec to remove any effects (even if minimal) of piloting strategies. Overall, for the level of turbulence included, the pilots that flew each case, and the frequency range used in the integration, there was an average reduction in strain of 36% for the

Table 7.1: Strain reductions using the NotchStr design over the noStrFB design

Axis	Task	Pilot 1	Pilot 2	Pilot 3	Task Average	Axis Average
Beam	Lateral Reposition (ACAH)	-38 %	-33%	-27%	-33%	-36%
	Lateral Reposition (TRC)	-25 %	-	-	-25%	
	Hover (ACAH)	-31%	-47%	-49%	-42%	
	Hover (TRC)	-33%	-	-	-33%	
	Depart/Abort (ACAH)	-42%	-42%	-19%	-34%	
	Depart/Abort (TRC)	-46%	-	-	-46%	
Chord	Lateral Reposition (ACAH)	-33%	-36%	-35%	-35%	-34%
	Lateral Reposition (TRC)	-31%	-	-	-31%	
	Hover (ACAH)	-33%	-43%	-34 %	-37%	
	Hover (TRC)	-31%	-	-	-31%	
	Depart/Abort (ACAH)	-39%	-46%	-23%	-36%	
	Depart/Abort (TRC)	-22%	-	-	-22%	

beam axis and 34% in chord. The actual reductions are also given for each pilot and each task flown. These numbers match to roughly +/- 10% of the overall average, meaning the improvement is constant over different piloting strategies and tasks.

Figure 7.9 shows the reduction in beam and chord strain RMS for different designs using the replayed inputs. This figure shows that for realistic pilot inputs, the feedback notch filter and structural feedback produce the largest reductions in structural RMS. Both of these compensation strategies are important for optimal structural control. These figures also show that the feed forward notch filter has minimal impact on overall excitation for a piloted simulation.

7.6 Pilot Cut-Off

Pilot cut-off is defined as the frequency which captures 50% of the area under the stick frequency response and is considered to be a good measure of pilot crossover frequency [97]. Figure 7.10 compares the pilot cut-off frequencies for lateral and
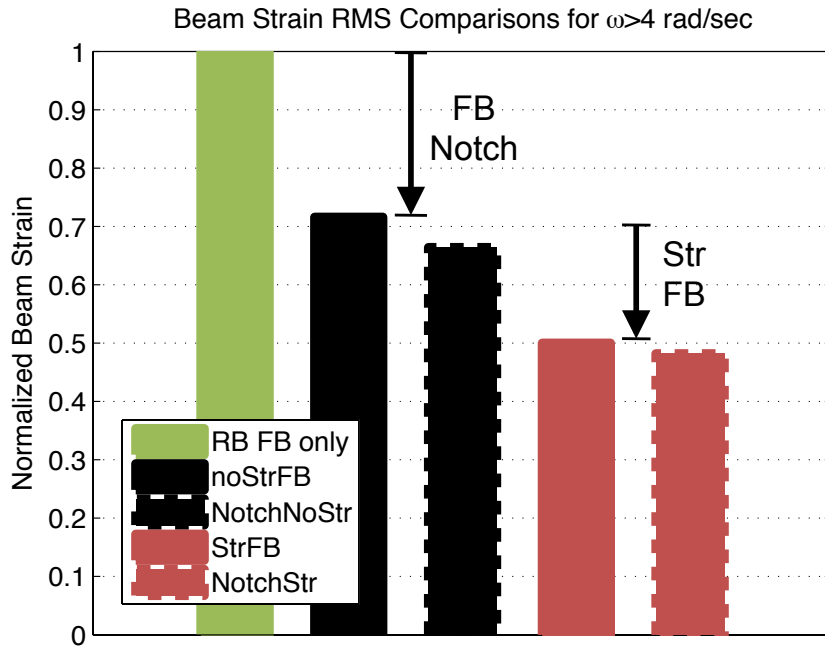
(a) Reductions in beam strain for different control strategies
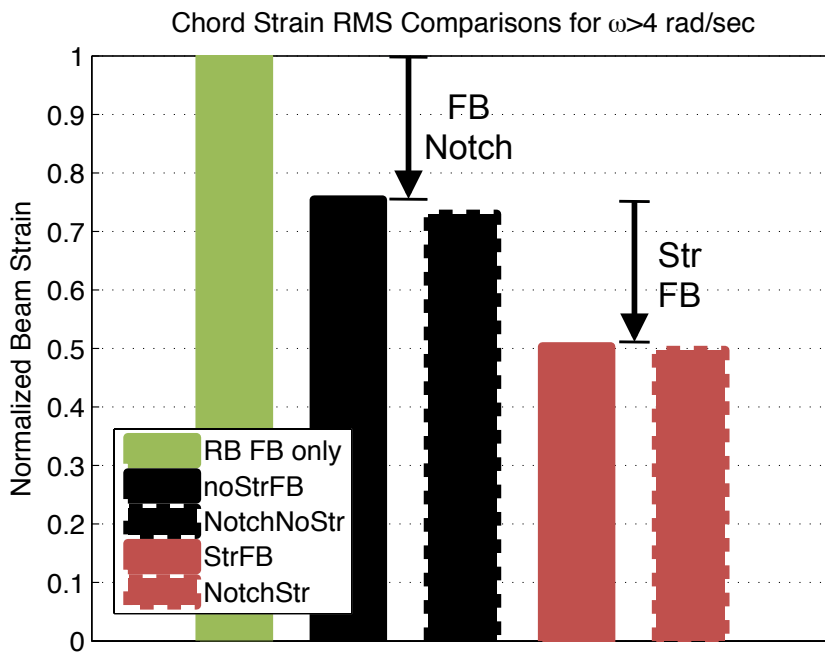
(b) Reductions in chord strain for different control strategies

Figure 7.9: Reductions in strain for different control strategies

longitudinal stick inputs for all cases flown during the sim. Since the ACAH designs were flow by all three pilots, they contain three data points, whereas only one pilot flew the TRC designs. There is considerable scatter in the data, possible from slightly different piloting strategies, but all cut off frequencies lie below 2 radians per second for ACAH mode and area near 1 rad/sec for TRC mode. This data is consistent with those of the NASA LCTR2 studies which were performed in the VMS. These studies show that for TRC mode, cut-off frequencies were generally less than 1 rad/sec [31]. The closed loop ACAH bandwidths lie just below 2 rad/sec for roll and around 2.5 rad/sec in pitch. Since the pilot is operating below the bandwidth, he is not required to add any additional lead in order to fly the aircraft [115]. If the pilot cut-off was higher than the bandwidth, the pilot would be required to add the lead necessary to bring the phase curve back to -135 deg to ensure that the pilot-aircraft broken loop system response had adequate phase margin. The bandwidth of the TRC mode is set by the TRC command model, and is also near 2 rad/sec. The pilot operated near 1 rad/sec, leaving adequate margins.

7.7   Pilot Comments

Pilots were asked to provide feedback comparing the two designs. Since this was not a handling qualities simulation, task related comments were not given. The pilots noted that the turbulence levels were quite high and potentially masked any ability to detect structural modes. They mentioned that overall, it was hard to find differences between the performance of the control systems. A pilot mentioned that the NotchStr gain set in lateral reposition "seemed less susceptible to turbu-
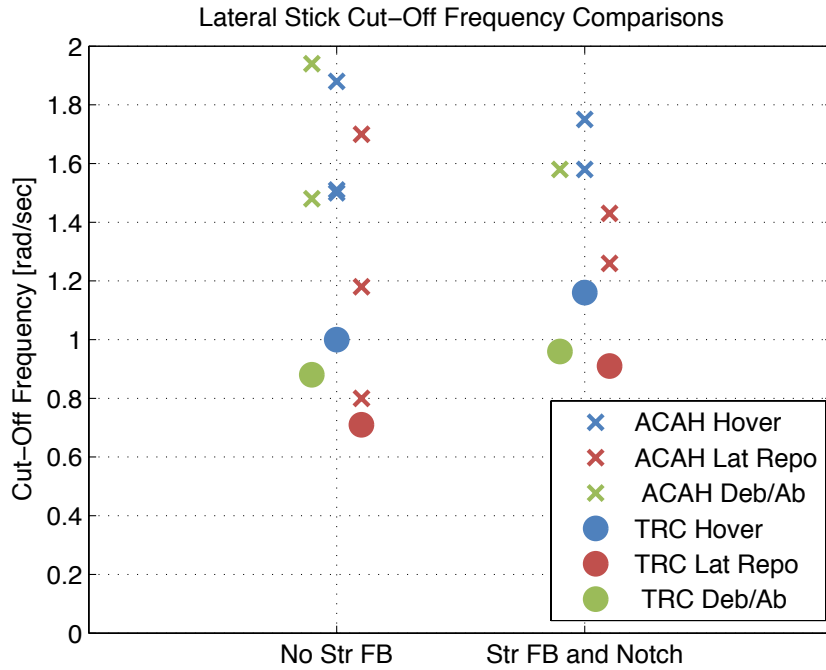
(a) Lateral stick piloted cut-off frequency]
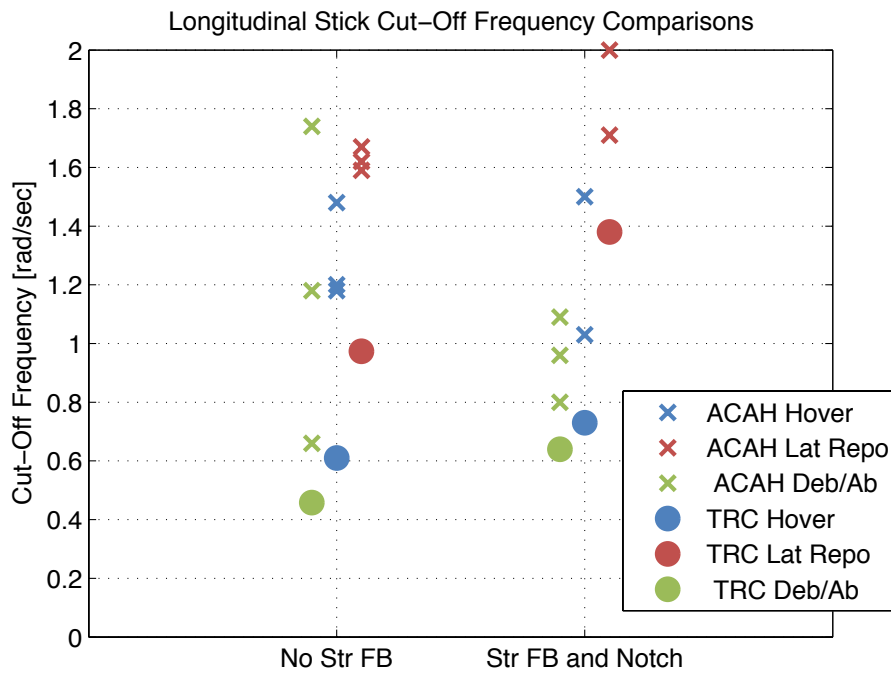
(b) Longitudinal stick piloted cut-off frequency

Figure 7.10: Pilot cut-off frequencies for all maneuvers and gain sets

lence", but "overall similar performance for tasks" was achieved even thought there was "maybe slightly reduced workload for for the [NotchStr] gain set." For the depart/abort task, this pilot mentioned that both gain sets felt "comfortable" and it was "hard to tell any real difference in workload or anything."

7.8 Chapter Summary

A model following control system was developed for the flexible LCTR aircraft. Comparisons were given based on different structural control strategies. Notch filters as well as structural feedback were shown to be important for various different excitation methods. Test pilots flew two designs in a fixed base simulator. Similar piloting strategies showed that the pilot did not feel the effects of structural control, but the loads at the wing root were reduced.

Chapter 8:   Conclusions and Future Work

The modeling and control of a large flexible tiltrotor were discussed within this dissertation. The aircraft is modeled using flexible beams for the wings, nacelle, and rotor blades. The aircraft has several structural modes near the piloted frequencies. The interaction between these modes and the rigid-body response of the aircraft was investigated. A control system was developed to reduce structural excitation so that ride quality and fatigue life of aircraft components were improved. The effect of the structural modes on aircraft closed loop and broken loop performance was evaluated.

8.1   Conclusions

Chapters 2-4 of this dissertation focused developing and validating a high-order math model of the LCTR. The following conclusions are obtained from these chapters:

1. The multi-body like formulation presented correctly predicts flexible aircraft behavior while retaining the equations of motion in simple ODE form.

2. The model correctly predicts flight dynamics behavior when compared to XV-15 flight data in hover and cruise. Differences in the hover responses are attributed to hub modeling. The XV-15 had a gimbaled hub, where the current

model has an articulated rotor with hub springs.

3. The LCTR hover configuration shows qualitatively similar dynamics to that of the XV-15. The LCTR HeliUM rigid wing model matches very well the available CAMRAD validation model, which had a rigid fuselage and wings.

4. For large aircraft, such as the LCTR, structural and rotor dynamics have large effects in the frequency ranges used for flight control designs.

Chapter 5 looked at the couplings in the linear models between the structural and rigid-body control and stability derivatives. Different models were developed which included various combinations of rigid-body to structural mode coupling. These models were evaluated in terms of their fidelity and applicability to different model development methods. The following conclusions can be made from this chapter:

1. Multi-body, mean-axis, hybrid-flexible and decoupled linear models all represent valid modeling methodologies which differ drastically in their complexity. Multi-body linear models are the most complex and are obtained from comprehensive codes, but decoupled models can still produce valid results and can be obtained much more simply.

2. It is possible to convert between the model types with the inclusion of influence coefficients. These coefficients are used in the output equations to introduce structural effects in the output equation directly.

Chapters 6 and 7 focused on the design and optimization of a control system for the LCTR2. The performance of different structural control strategies were evaluated based on a variety of closed loop and broken loop metrics. The best and worst performing control strategies were flown in a fixed base simulator and the results were used for further comparisons. Based on the results presented, the following conclusions can be made.

1. Including structural flexibility in the design process is key to correctly predicting closed-loop aircraft behavior. The LCTR has four structural modes well within the piloted frequency range that need to be accounted for during control system design.

2. A model following control system was well suited for control law development. The closed-loop aircraft performance gave Level 1 handling qualities.

3. Notch filters and proportional-integral structural feedback are both needed for optimal reduction of structural motion. Structural feedback quantities were summed and differential wing tip accelerations. Notch filters on the feedforward and feedback paths prevent the pilot and control system, respectively, from inducing structural oscillations. Structural feedback is needed to remove oscillation to turbulence. A reduction in structural motion is accompanied by a reduction in fatigue as well as an improvement in ride quality.

4. A piloted simulation showed that feedback notch filters and active structural control provided the largest reductions to structural RMS. There were small

improvements using the feed forward notch filter, but the pilots operating frequency was too low for these filters to provide large benefits.

5. There was no change in pilot strategy between the worst and best gain sets flow in the simulator. Pilots mentioned that both the noStrFB and NotchStr designs behaved similarly and had trouble distinguishing between the two. Pilot cut-off frequencies were also similar for the best and worst gain sets, another indication of the similarity between the two. This indicates that the improvements in structural vibration can be achieved without affecting the pilot's ability to control the aircraft.

6. Structural feedback and notch filters also add robustness to the control system. Robustness was analyzed by perturbing components of the bare-airframe model and evaluating the effects on the broken loop design using the Nichols plot. The design with structural feedback avoided the "exclusion zone" of the Nichols plot, while the same perturbations to the design without structural feedback caused several designs to penetrate this area.

8.2   Future Work

The comprehensive multi-body like analysis has broad range of applicability, only a small part of which has been investigated here. This dissertation focused on hover; transition and forward flight were not analyzed. Little is known about tiltrotor dynamics in the conversion corridor with the nacelles between the hover and cruise condition. More modeling work is needed here to identify any key problems

such poor flying qualities, instabilities, or actuator rate/position limiting.

The code developed is generic in nature and not limited to the tiltrotor configuration. Future military rotorcraft may include compound aircraft, tiltrotors, or other configurations. Tiltrotors have been investigated in the past, but there is currently very little insight in the behavior of other advanced configurations. One such configuration is the rigid-coaxial pusher type aircraft. It would be very useful to develop a flight dynamics model of this configuration for preliminary handling qualities testing and to determine the requirements of the control system for this type of aircraft.

Tiltrotor and other compound and advanced rotorcraft configurations benefit from having redundant controls throughout much of their flight envelope. For example, in mid and high-speed flight, titlrotors can use rotor controls in conjunction with control surfaces located on the wings and empennage. Control allocation experiments need to be performed to determine the optimal mixing of these controls for improvements in both the piloted response and ride-quality.

Finally, the structural model of the aircraft could be improved to achieve a higher fidelity structural response. Currently, flexible wings are modeled as Bernoulli beams. Actual aircraft wings are not Bernoulli beams, but more complicated structures with several connection points to the fuselage. For example, shell type wing might give higher fidelity results. Fuselage flexibility could also be included. In the work presented, the fuselage is considered rigid, with flexibility coming from only the wings. A flexible fuselage would help capture low frequency fuselage modes more accurately.

Appendix A: Kinematics of a Multi-Body System

This appendix shows the derivation of the position, velocity, and acceleration vectors of any point in a flexible multi-body system.

A.1   Positions

The position vector of a point on a body with respect to a reference point can be written as a linear combination of orthogonal unit vectors.

$$x \, \mathbf{n}_1^j + y \, \mathbf{n}_2^j + z \, \mathbf{n}_3^j = [x \; y \; z] \left\{ \begin{array}{c} \mathbf{n}_1^j \\ \mathbf{n}_2^j \\ \mathbf{n}_3^j \end{array} \right\} = \left\{ \mathbf{q}^j \right\}^T \left\{ \mathbf{n}^j \right\} \tag{A.1}$$

$\mathbf{n}_{1,2,3}^j$ are the unit vectors in reference frame j. The formulation allows for arbitrary directions of the unit vectors, but generally they are chosen to be meaningful for a given body. The fuselage unit vectors are those of the standard body axis system, with $\mathbf{n}_1$ pointing forwards, $\mathbf{n}_2$ pointing to starboard, and $\mathbf{n}_3$ pointing down. The starting point for the formulation is an inertial reference frame. This reference frame maintains its orientation in space and so is unaffected by aircraft angular motion. The reference frame always has the z-axis pointing down, with the positive direction of the x and y axes remaining unspecified (but could be prescribed, for example, to point North and East, respectively, if necessary, with no consequences on the results

of the present study).

The transformations between reference frames are carried out on the unit vectors using the standard aerospace rotation sequence, i.e., a rotation about the $\mathbf{n}_3$ axis by angle ψ, followed by a rotation by angle θ about the $\mathbf{n}_2^\psi$ axis resulting from the ψ rotation, and by a rotation by angle ϕ about the $\mathbf{n}_1^\theta$ axis resulting from the θ rotation. The transformation matrices between two reference frames j and k are as follows:

$$[\psi] = \left[S^{1j}\right] = \begin{bmatrix} \cos\psi & \sin\psi & 0 \\ -\sin\psi & \cos\psi & 0 \\ 0 & 0 & 1 \end{bmatrix}$$

$$[\theta] = \left[S^{21}\right] = \begin{bmatrix} \cos\theta & 0 & -\sin\theta \\ 0 & 1 & 0 \\ \sin\theta & 0 & \cos\theta \end{bmatrix}$$

$$[\phi] = \left[S^{k2}\right] = \begin{bmatrix} 1 & 0 & 0 \\ 0 & \cos\phi & \sin\phi \\ 0 & -\sin\phi & \cos\phi \end{bmatrix}$$

The intermediate coordinate systems are labeled $\{\mathbf{n}^1\}$ and $\{\mathbf{n}^2\}$.

$$\left\{\mathbf{n}^1\right\} = \left[S^{1j}\right]\left\{\mathbf{n}^j\right\}$$

and

$$\left\{\mathbf{n}^2\right\} = \left[S^{21}\right]\left\{\mathbf{n}^1\right\}$$

The complete transformation from body j to k is:

$$
\begin{Bmatrix} \mathbf{n}_1^k \\ \mathbf{n}_2^k \\ \mathbf{n}_3^k \end{Bmatrix} = [\phi]\,[\theta]\,[\psi] \begin{Bmatrix} \mathbf{n}_1^j \\ \mathbf{n}_2^j \\ \mathbf{n}_3^j \end{Bmatrix} \tag{A.2}
$$

$$
= \left[S^{k2}\right]\left[S^{21}\right]\left[S^{1j}\right] \begin{Bmatrix} \mathbf{n}_1^j \\ \mathbf{n}_2^j \\ \mathbf{n}_3^j \end{Bmatrix} \tag{A.3}
$$

or more compactly written as:

$$
\left\{\mathbf{n}^k\right\} = \left[S^{kj}\right]\left\{\mathbf{n}^j\right\} \tag{A.4}
$$

The components of $\left[S^{kj}\right]$ are:

$$
S^{kj} = \begin{bmatrix} S_{11} & S_{12} & S_{13} \\ S_{21} & S_{22} & S_{23} \\ S_{31} & S_{32} & S_{33} \end{bmatrix} \tag{A.5}
$$

where

$$S_{11} = \cos\theta\cos\psi$$

$$S_{12} = \cos\theta\sin\psi$$

$$S_{13} = -\sin\theta$$

$$S_{21} = \sin\phi\sin\theta\cos\psi - \cos\phi\sin\psi$$

$$S_{22} = \sin\phi\sin\theta\sin\psi + \cos\phi\cos\psi$$

$$S_{23} = \sin\phi\cos\theta$$

$$S_{31} = \cos\phi\sin\theta\cos\psi + \sin\phi\sin\psi$$

$$S_{32} = \cos\phi\sin\theta\sin\psi - \sin\phi\cos\psi$$

$$S_{33} = \cos\phi\cos\theta$$

For a wing, the unit vectors $\mathbf{n}_1, \mathbf{n}_2$, and $\mathbf{n}_3$ point, respectively, outwards along the undeformed elastic axis of the wing, forwards towards the leading edge, and upwards. The transformation from the fuselage coordinate system to that of the wing contains wing dihedral and sweep.

Once the transformation matrices from one coordinate system set to another are known, the product of the matrices allows for the formulation of a position vector in any coordinate system. The summing of the displacements in each coordinate system gives the expression for any point in the system. The reference frame is denoted with superscript $(\ldots)^0$, and is generally the inertial frame. The superscript increases with each connection. An example for a generic set of connected bodies

is given in Fig. A.1. Here, the reference frame is the inertial frame. The segment ζ is an offset from a reference point to the first body and is written in terms of the reference frame. It is set to zero for the present study, but if the bodies are free to move with respect to the reference frame, it could be used to position the bodies with respect to an arbitrary point in the reference frame: for example a location on the ground if the bodies form an aircraft. The position vectors $\mathbf{q}$ locate the connection of the next body in the current body's coordinate system. The vectors $\mathbf{r}$ locate a point within each body that is not the connection point, a center of mass for example. Thus, the position vector $\mathbf{P}$, of a point placed by vector $\mathbf{r}_3$ in the third body relative to a point in the reference frame is found in Eqn. (A.6). This position vector, and the kinematics of the bodies presented, follows the formulation found in Ref. 78. For the tiltrotor of the present study, the bodies are arranged as follows: Body 1 is the aircraft fuselage, Body 2 is the undeformed right wing, and Body 3 is the nacelle. The hub of the opposite rotor is described by a symmetric set of bodies.

$$\mathbf{P} = \{\boldsymbol{\zeta}\}^T \{\mathbf{n}^0\} + \{\mathbf{q}^1\}^T \{\mathbf{n}^1\} + \{\mathbf{q}^2\}^T \{\mathbf{n}^2\} + \qquad\qquad \text{(A.6)}$$

$$\{\mathbf{r}^3\}^T \{\mathbf{n}^3\}$$

We can write a set of unit vectors in the reference frame for the tilt rotor as follows:

$$\{\mathbf{n}^3\} = \left[S^{32}\right]\left[S^{21}\right]\left[S^{10}\right]\{\mathbf{n}^0\} = \left[S^{30}\right]\{\mathbf{n}^0\} \qquad\qquad \text{(A.7)}$$
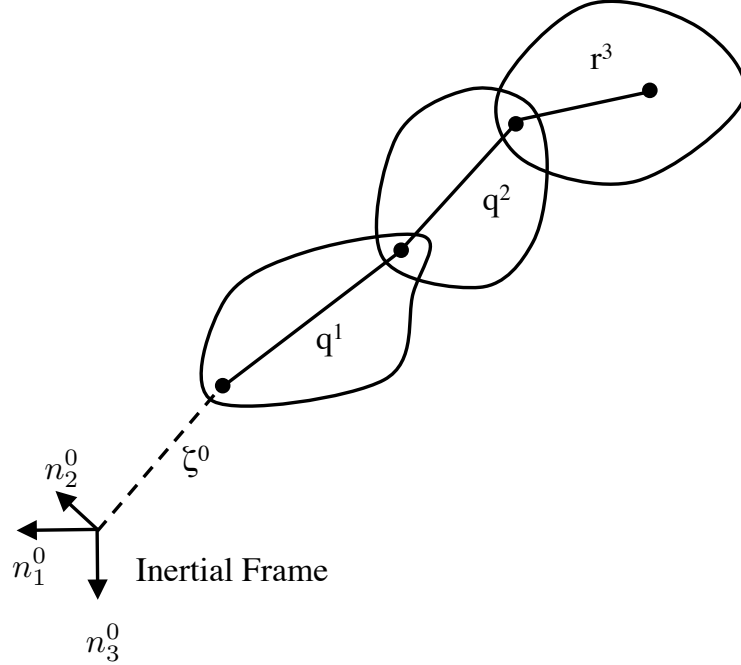
Figure A.1: Bodies connected together in a multiple body configuration

and thus:

$$\mathbf{P} = \left(\{\boldsymbol{\zeta}\}^T + \left\{\mathbf{q}^1\right\}^T \left[S^{10}\right] + \left\{\mathbf{q}^2\right\}^T \left[S^{20}\right] + \right.$$

$$\left. \left\{\mathbf{r}^3\right\}^T \left[S^{30}\right] \right) \left\{\mathbf{n}^0\right\} \tag{A.8}$$

or more generally as:

$$\mathbf{P} = \left(\{\boldsymbol{\zeta}\}^T + \sum_{i=1}^{n-1} \left\{\mathbf{q}^i\right\}^T \left[S^{i0}\right] + \left\{\mathbf{r}^n\right\}^T \left[S^{n0}\right] \right) \left\{\mathbf{n}^0\right\} \tag{A.9}$$

Flexibility effects show up by modifying the transformation matrices $\left[S^{kj}\right]$ to include the rotations due to structural flexibility, as well as adding displacements. A constant wing deflection will alter the connection point of the nacelle since the wing coordinate system is in the undeformed frame. The deflection will also introduce additional rotations in the transformation from the wing undeformed coordinate

298

system to the nacelle coordinate system. Displacements and rotations at the connection are functions of the modal temporal coordinates, $\rho(t)$ and the beam modes from the finite element beam solution, $[\mathbf{V}(x)]$. Since the beam finite element model has position and slopes at each node, flexible displacements and rotations can be written as:

$$\left\{ \begin{array}{c} \mathbf{q}_f \\ \alpha_f \end{array} \right\} = [\mathbf{V}(x)]\,\rho(t) \tag{A.10}$$

Here, $\mathbf{q}_f$ is the connection point's displacement due to flexibility, and α_f is the rotation at that point. The displacement for the connection point, including flexibility contributions for the next body is then:

$$\bar{\mathbf{q}}^j = \mathbf{q}^j + \mathbf{q}_f^j \tag{A.11}$$

The beam element formulation assumes rotations in the same order as the coordinate system transformations. Therefore, the transformation to the coordinate system of body upstream of the flexible body, when written in the same form as Eqn. (A.4), contains an additional set of rotations due to flexibility:

$$\{\mathbf{n}^k\} = \underbrace{\left[S^{kf}\right]\left[S^{fj}\right]}_{\left[S^{kj}\right]}\{\mathbf{n}^j\} \tag{A.12}$$

where,

$$\left[S^{fj}\right] = [\phi_f]\,[\theta_f]\,[\psi_f] \tag{A.13}$$

and ϕ_f, θ_f, and ψ_f are components of α_f, from Eqn. (A.10). The matrix $\left[S^{kf}\right]$ now has the same form as Eqn. (A.2), and is the transformation from the connection point

coordinate system, which is now the deformed coordinate system, to the coordinate system of the next body. In the equation above, and following the example of the flexible wing, superscript j denotes the wing undeformed coordinate system, while superscript k denotes the nacelle coordinate system. This matrix takes into account the static wing deformation.

The full position vector of any point on the aircraft, including flexibility contributions is now:

$$\mathbf{P} = \left(\{\boldsymbol{\zeta}\}^T + \sum_{i=1}^{n-1} \{\bar{\mathbf{q}}^i\}^T \left[S^{i0} \right] + \{\bar{\mathbf{r}}^n\}^T \left[S^{\mathbf{n}0} \right] \right) \{\mathbf{n}^0\} \qquad (A.14)$$

A.2 Velocities

Once the position vector of the point is known, the velocity and acceleration vectors follow. The velocity vector is simply the time derivative of the position vector.

$$\mathbf{v} = \frac{d\mathbf{P}}{dt} = \left(\{\dot{\boldsymbol{\zeta}}\}^T + \sum_{i=1}^{n-1} \left(\{\dot{\bar{\mathbf{q}}}^i\}^T \left[S^{i0} \right] + \{\bar{\mathbf{q}}^i\}^T \left[\dot{S}^{i0} \right] \right) + \qquad (A.15)$$

$$\{\dot{\bar{\mathbf{r}}}^n\}^T \left[S^{n0} \right] + \{\bar{\mathbf{r}}^n\}^T \left[\dot{S}^{n0} \right] \right) \{\mathbf{n}^0\}$$

Here, $\dot{\boldsymbol{\zeta}}$ is the velocity of the aircraft CG in the inertial reference frame. The time derivatives of the transformation matrices, $\left[\dot{S}^{i0} \right]$, as well as $\dot{\bar{\mathbf{q}}}^i$ and $\dot{\bar{\mathbf{r}}}^n$ take into account motion due to flexibility. The position and angular time derivatives again

300

come from the beam finite element:

$$\left\{ \begin{array}{c} \dot{\mathbf{q}}_f \\ \omega_f \end{array} \right\} = [\mathbf{V}(x)]\,\dot{\boldsymbol{\rho}}(t) \tag{A.16}$$

Since the bodies are not allowed to translate with respect to each other, the velocity contribution, $\dot{\mathbf{q}}$ only has terms associated with flexibility. In keeping the notation from Eqn. (A.11):

$$\dot{\mathbf{q}}^j = \mathbf{0} + \dot{\mathbf{q}}_f^j = \dot{\mathbf{q}}_f^j \tag{A.17}$$

The time derivatives of the transformation matrices require more development. The flexible contributions to angular rates, ω_f have the form:

$$\omega_f = \dot{\psi}\mathbf{n}_3^j + \dot{\theta}\mathbf{n}_2^1 + \dot{\phi}\mathbf{n}_1^2 \tag{A.18}$$

$$= \left(\dot{\phi}\cos\theta\cos\psi - \dot{\theta}\sin\psi \right) \mathbf{n}_1^j +$$

$$\left(\dot{\phi}\cos\theta\sin\psi + \dot{\theta}\cos\psi \right) \mathbf{n}_2^j + \left(\dot{\psi} - \dot{\phi}\sin\theta \right) \mathbf{n}_3^j \tag{A.19}$$

Notice the unit vectors in the final equation above are in the "downstream" coordinate system, i.e., the coordinate of system of the next body proceeding from the end of the tree toward the beginning. For the wing, or any flexible body, this is the coordinate system before elastic deformation. These angular rates act on the upstream body to the flexible body, for the tilt-rotor example, the nacelle. In general, the formulation presented assigns rotation rates in the coordinate system of the rotating body, as opposed to the upstream body. Before they are converted to the nacelle coordinate system, they must be converted through the wing deformed coordinate system as in Eq. (A.12). This allows for easier manipulation of the $\left[\dot{S} \right]$

matrices later on.

$$\{\omega_f^j\}^T \{\mathbf{n}\}^j = \underbrace{\{\omega_f^j\}^T \left[S^{jk}\right]}_{\omega_f^k} \{\mathbf{n}\}^k \tag{A.20}$$

Note the superscript order of matrix $\left[S^{jk}\right]$. For a rigid aircraft, Eq. (A.18) gives the Euler rates at the CG in the coordinate systems local to each Euler rate. For example, $\dot{\theta}$ is the Euler rate after a transformation by ψ has occured. Equation (A.19) gives the Euler rates in the inertial coordinate system, and Eq. (A.20) transforms the Euler rates into the body axis. The Euler rates in the body axis give the standard flight dynamics formulation of roll, pitch, and yaw rates.

Since the transformation matrices are pure rotations, their inverse is equal to their transpose:

$$\left[S^{kj}\right] = \left[S^{jk}\right]^T = \left[S^{jk}\right]^{-1} \tag{A.21}$$

Taking the time derivative of Eqn. A.4 directly, we obtain:

$$\left[\dot{S}^{kj}\right] = \left[\Omega^{kj}\right]\left[S^{kj}\right] \tag{A.22}$$

where $[\Omega]$ is a skew symmetric matrix. using ω_f^k from Eqn. (A.20):

$$\left[\Omega^{kj}\right] = \begin{bmatrix} 0 & \omega_{3f}^k & -\omega_{2f}^k \\ -\omega_{3f}^k & 0 & \omega_{1f}^k \\ \omega_{2f}^k & -\omega_{1f}^k & 0 \end{bmatrix} \tag{A.23}$$

The formulation for $\left[\dot{S}\right]$ thus far only accounts for a single coordinate transformation, so for two tangent bodies. For groups of transformations, as is the case with

302

almost any multi-body configuration, the treatment of $\left[\dot{S}\right]$ has additional compo-

nents.

$$\left[S^{n0}\right] = \left[S^{n,n-1}\right]\left[S^{n-1,n-2}\right]\dots\left[S^{21}\right]\left[S^{10}\right] \tag{A.24}$$

taking the time derivative:

$$\frac{d}{dt}\left[S^{n0}\right] = \frac{d}{dt}\left(\left[S^{n,n-1}\right]\left[S^{n-1,n-2}\right]\dots\left[S^{21}\right]\left[S^{10}\right]\right) \tag{A.25}$$

$$\left[\dot{S}^{n0}\right] = \left(\left[\dot{S}^{n,n-1}\right]\left[S^{n-1,n-2}\right]\dots\left[S^{21}\right]\left[S^{10}\right]\right) +$$

$$\left(\left[S^{n,n-1}\right]\left[\dot{S}^{n-1,n-2}\right]\dots\left[S^{21}\right]\left[S^{10}\right]\right) + \dots$$

$$\left(\left[\dot{S}^{n,n-1}\right]\left[S^{n-1,n-2}\right]\dots\left[\dot{S}^{21}\right]\left[S^{10}\right]\right) +$$

$$\left(\left[\dot{S}^{n,n-1}\right]\left[S^{n-1,n-2}\right]\dots\left[S^{21}\right]\left[\dot{S}^{10}\right]\right) \tag{A.26}$$

Each individual $\left[\dot{S}^{k,k-1}\right]$ is formulated in the same fashion as Eqn. (A.22). The

trigonometry of Eqn. (A.26) does not need to be carried out each time. Note the

following treatment of $\left[\dot{S}^{n0}\right]$.

$$\left[\dot{S}^{10}\right] = \left[\Omega^{10}\right]\left[S^{10}\right]$$

$$\left[\dot{S}^{20}\right] = \left[\dot{S}^{21}\right]\left[S^{10}\right] + \left[S^{21}\right]\left[\dot{S}^{10}\right]$$

$$= \left[\Omega^{21}\right]\left[S^{20}\right] + \left[S^{21}\right]\left[\Omega^{10}\right]\left[S^{10}\right]$$

$$= \left[\Omega^{21}\right]\left[S^{20}\right] + \left[S^{21}\right]\left[\dot{S}^{10}\right]$$

$$\dots$$

$$\left[\dot{S}^{n0}\right] = \left[\Omega^{n,n-1}\right]\left[S^{n0}\right] + \left[S^{n,n-1}\right]\left[\dot{S}^{n-1,0}\right]$$

$$\left[\dot{S}^{n0}\right] = \left[\Omega^{n0}\right]\left[S^{n0}\right] \tag{A.27}$$

In general, $\left[\dot{S}^{n0}\right]$ is built from outwards starting from the reference frame as each body's angular velocity has contributions from all time derivatives between bodies 0 and n, and is in the reference coordinate system. The velocity of a component of the multi-body system can now be expressed using Eqn. (A.15). Often times the angular velocities of a body in the local coordinate system need to be used. This is easily done using Eqn. (A.27). Using the formulation of Eqn. (A.22), and Eqn. (A.23):

$$\left[\Omega^{kj}\right] = \left[\dot{S}^{kj}\right]\left[S^{kj}\right]^{-1} = \left[\dot{S}^{kj}\right]\left[S^{kj}\right]^{T} \tag{A.28}$$

The skew-symmetric matrix gives the angular velocities of body k in the coordinate system of body k so individual angular rates can readily be extracted from its components. If the rates are desired in a different coordinate system they can be transformed using Eqn. (A.20).

A.3   Accelerations

The linear and angular acceleration vectors are derived in much the same way as the velocity vectors. Taking an additional time derivative of Eqn. (A.15):

$$\mathbf{a} = \frac{d\mathbf{v}}{dt} = \left(\left\{\ddot{\zeta}\right\}^{T} + \sum_{i=1}^{n-1}\left(\left\{\ddot{\bar{q}}^{i}\right\}^{T}\left[S^{i0}\right] + 2\left\{\dot{\bar{q}}^{i}\right\}^{T}\left[\dot{S}^{i0}\right] + \right.\right.$$
$$\left.\left\{\bar{q}^{i}\right\}^{T}\left[\ddot{S}^{i0}\right]\right) + \left\{\ddot{\bar{r}}^{n}\right\}^{T}\left[S^{n0}\right] + 2\left\{\dot{\bar{r}}^{n}\right\}^{T}\left[\dot{S}^{n0}\right] + \tag{A.29}$$
$$\left.\left\{\bar{r}^{n}\right\}^{T}\left[\ddot{S}^{n0}\right]\right)\left\{n^{0}\right\}$$

The first term in the derivative is the linear acceleration of the aircraft in the inertial reference frame. $\ddot{q}^T$ terms are linear accelerations of the bodies with respect to one another. The tilt-rotor model does allow for linear motion of aircraft components next to each other. Much like the velocity component in Eqn. (A.17), this terms only contains accelerations due to flexibility. The second time derivative of the transformation matrix $\left[\ddot{S}^{i0}\right]$ is the remaining component that has not been derived yet. To determine $\left[\ddot{S}^{i0}\right]$, one could take time derivatives of the transformation matrices one by one, as in Eqn. (A.26). Since $[\Omega^{i0}]$, is readily available, as in Eqn. (A.27), the following treatment is much abbreviated.

$$\frac{d}{dt}\left[\dot{S}^{i0}\right] = \frac{d}{dt}\left([\Omega^{n0}]\left[S^{n0}\right]\right) \tag{A.30}$$

$$= \left[\dot{\Omega}^{n0}\right]\left[S^{n0}\right] + [\Omega^{n0}]\left[\dot{S}^{n0}\right]$$

$$\left[\ddot{S}^{n0}\right] = \left[\dot{\Omega}^{n0}\right]\left[S^{n0}\right] + [\Omega^{n0}][\Omega^{n0}]\left[S^{n0}\right] \tag{A.31}$$

Here $\left[\dot{\Omega}^{n0}\right]$ is a skew symmetric matrix containing the summed angular accelerations of bodies 0 to n in the final body's coordinate system. It is derived in the same fashion as the skew symmetric matrix of angular velocities, Eqn. (A.23), which comes from the sequence of rotations given by Eqn. (A.18).

Appendix B: Mean-Axis Flexible Model Identification

This appendix gives details on the identification of the mean-axis flexible model structure in both hover and cruise.

B.1   Identification of Hover Mean-Axis Model

The responses used in the identification are shown in Table B.1. CIFER® was used as the system identification tool and is described in detail in Ref. 97. In this software, the state-space structure was pre-determined and many of the variables in the linear matrices were kept as constants (e.g. A_R, and B_R). The off-diagonal terms were left free in the identification. The free parameters are optimized to minimize the average coherence weighted cost function, (J_{ave}), of the responses. Once a minimum cost function is attained, parameters with high insensitivities are removed and set to zero. A parameter with high insensitivity does not have an impact on the responses used and therefore should be removed. A new model is then re-optimized. Since the previous model did not depend on the removed parameters, the average cost should not increase greatly. This is repeated until the cost increases more than one or two points. Next, parameters with high Cramer-Rao (CR) bounds are removed. Cramer-Rao bounds are a measure of correlation between parameters. If parameters

have high Cramer-Rao bounds, their influence can be picked up by other parameters are thus not important to the final solution. These parameters are frozen at their values one at a time until the cost function begins to increase again. Once this process is finished, the final model is obtained. Reference 116 provides examples of identification of three rotorcraft of varying size.

Table B.1: LCTR hover mean-axis model identification responses

Output	Input	Response Name	ω_{min}	ω_{max}	Coherence	Comment
p	Lat Stick	p/lat	0.01	100	1.0	-
r	Lat Stick	r/lat	0.01	100	1.0	-
v	Lat Stick	v/lat	0.01	100	1.0	-
ε	Lat Stick	$dstr/lat$	10	30	1.0	Wing root strain
$a_{z_{tip}}$	Lat Stick	az/lat	0.01	100	1.0	Recreated wing tip acceleration
$a_{z_{mid}}$	Lat Stick	azm/lat	0.01	100	1.0	Recreated wing mid-point acceleration
p	Lat Stick	$ps2/lat$	0.01	0.75	1.0	Low frequency rigid-body mode
p	Lat Stick	$ps3/lat$	10	30	1.0	High frequency flexible mode
p	Pedal	p/rud	0.01	100	1.0	-
r	Pedal	r/rud	0.01	100	1.0	-
v	Pedal	v/rud	0.01	100	1.0	-

The values left free in the identification are shown in Table B.2. Fictitious states are created which serve to recreate outputs with identifiable parameters, hence the M and F matrices contain many parameters which correspond to outputs. Parameters ST, and eps represent $\sin(\theta_0)$ and the constant to convert wing deformation to strain. Parameters tzo and om2 are the identified structural mode parameters $-2\zeta\omega$ and $-\omega^2$. These were left in the identification because these values would not be known when performing a system identification from flight data. The identification software easily identified these values correctly. The wing accelerometer coefficients were also left free in the identification. The parameters azp and azp2 multiply the roll acceleration and should be the distance of the accelerometer

from the cg. The exact values for these parameters are -38.7 and -19.5; both are well identified. Parameters azn and azn2 multiply the structural acceleration term and give the modal displacement at the sensor displacement. The mid-wing sensor (characterized by azp2 and azn2) is near a modal displacement node, and gives a small modal coefficient (azn2 = -1.4). The wing-tip sensor is far from a mode and is influenced by wing bending. The identified modal coefficient for this sensor, azn, has a different value than the multi-body coefficient. In the multi-body formulation, this value was defined with respect to the fuselage, but for the mean-axis model, it is defined with respect to the equivalent rigid-body motion. The control derivative $Y_{\delta_{lat}}$ (labeled Ylat) was allowed to be free in the identification because its rigid-body value was much different than the flexible value and the coupling terms were not effective enough at re-creating it. Influence coefficients (Phi_) as well as terms to reproduce the wing accelerations and strains were left free and compared to derived values. The rigid-body coupling terms are denoted as Ev, Ep and Er (η_v, η_p, and η_r). Rigid-body coupling terms Ep and Er had large insensitivities and were thus removed from the identification. The remaining rigid-body coupling terms and aeroelastic coupling terms have large Cramer-Rao bounds because they remain correlated, even with the additional accelerometer and strain responses. If any of these terms are taken out of the identification, the overall cost (Table B.3), which shows an excellent identification result, increases.

Table B.2: LCTR hover identification parameter, Cramer-Rao, and Insensitivity values

Param.	Value	CR (%)	Insens. (%)
M-matrix			
azp	-38.7	3.879	1.83
azn	9.981	11.07	5.389
azp2	-19.66	3.582	1.745
azn2	-1.4[b]	—	—
F-matrix			
Yv	-0.07988[a]	—	—
Yp	-3.206[a]	—	—
Yr	-1.279[a]	—	—
G	32.17[a]	—	—
Yn	25.48	24.37	5.951
Lv	-0.008238[a]	—	—
Lp	-1.024[a]	—	—
Lr	0.2546[a]	—	—
Ln	-0.6678	40.83	7.361
Nv	0.00102[a]	—	—
Np	0.06284[a]	—	—
Nr	-0.1941[a]	—	—
Nn	-0.2369	34.61	2.336
ST	-0.03956[a]	—	—
Ev	0.2676	31.3	1.707
Ep	0[b]	—	—
Er	0[b]	—	—
tzo	-2.158	5.864	2.771
om2	-278.5	0.7568	0.3528
p	0[b]	—	—
Phip	0.5947	1.2	0.5905
r	0[b]	—	—
Phir	-0.01624	9.737	4.765
v	0[b]	—	—
Phiv	-0.3703	11.13	4.206
eps	0.07236	3.785	1.823
G-matrix			
Ylat	-0.2282	6.194	2.336
Yped	-0.3815[a]	—	—
Llat	-0.2288[a]	—	—
Lped	-0.05041[a]	—	—
Nlat	0.02814[a]	—	—
Nped	0.03574[a]	—	—
Elat	0.4141[a]	—	—
Eped	0.2864[a]	—	—
Time delay			

[a] Fixed parameter

[b] Eliminated parameter

309

Table B.3: LCTR hover identification results

Response	Cost
p/lat	7.875
r/lat	8.293
v/lat	9.573
$dstr/lat$	5.972
az/lat	6.292
azm/lat	2.388
$ps2/lat$	4.07
$ps3/lat$	11.58
p/ped	6.837
r/ped	1.615
v/ped	44.54
J_{ave}	9.913

Figures B.1 - B.9 show the responses used in the identification. Along with the multi-body and identified mean-axis model, the rigid-body and static-elastic models are shown. The low frequency differences between the rigid-body model and the other models are due to the static-elastic effects of structural bending and come from the coupling terms.
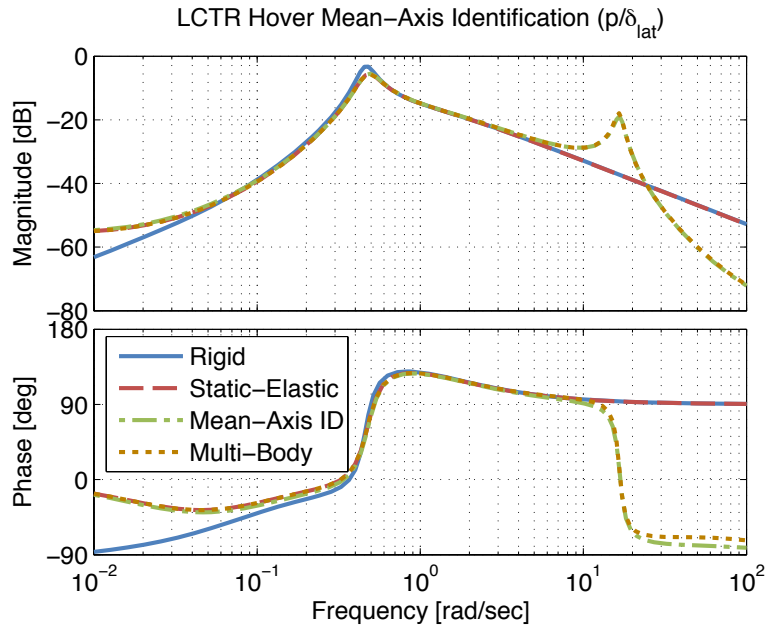
Figure B.1: $\frac{p}{\delta_{lat}}$: Models used in identification of the mean-axis model structure
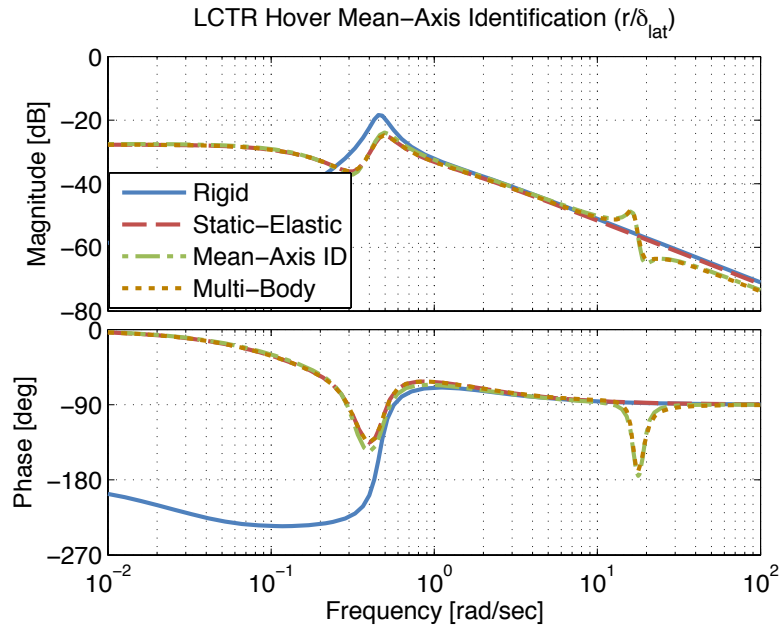

Figure B.2: $\frac{r}{\delta_{lat}}$: Models used in identification of the mean-axis model structure
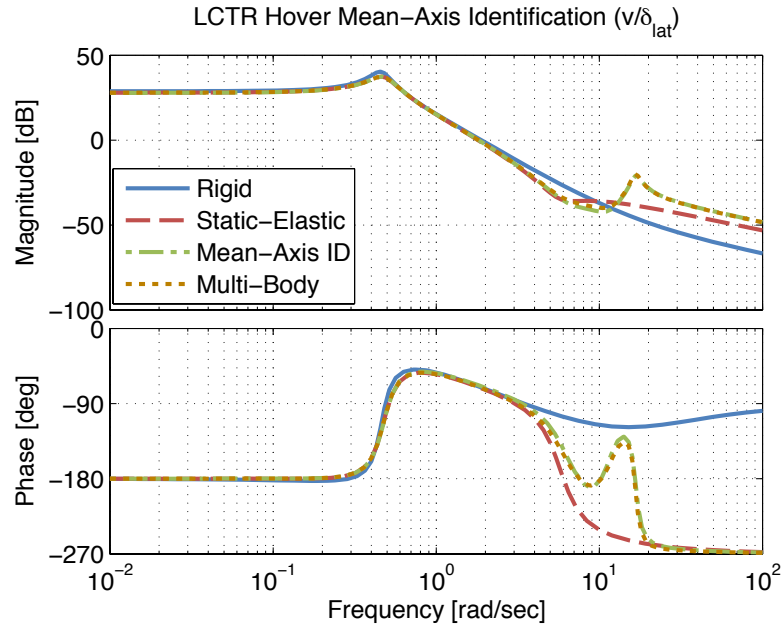
Figure B.3: $\frac{v}{\delta_{lat}}$: Models used in identification of the mean-axis model structure
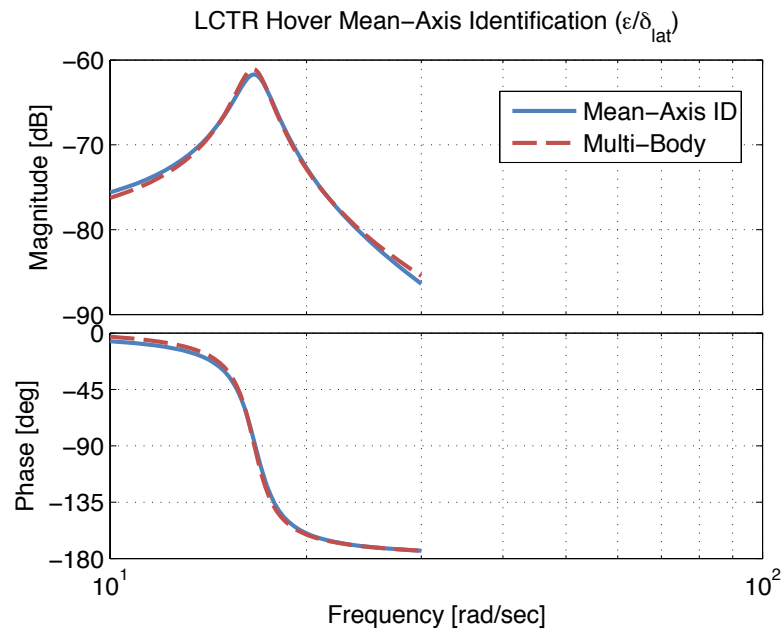

Figure B.4: $\frac{\epsilon}{\delta_{lat}}$: Wing root strain response used in identification of the mean-axis model structure
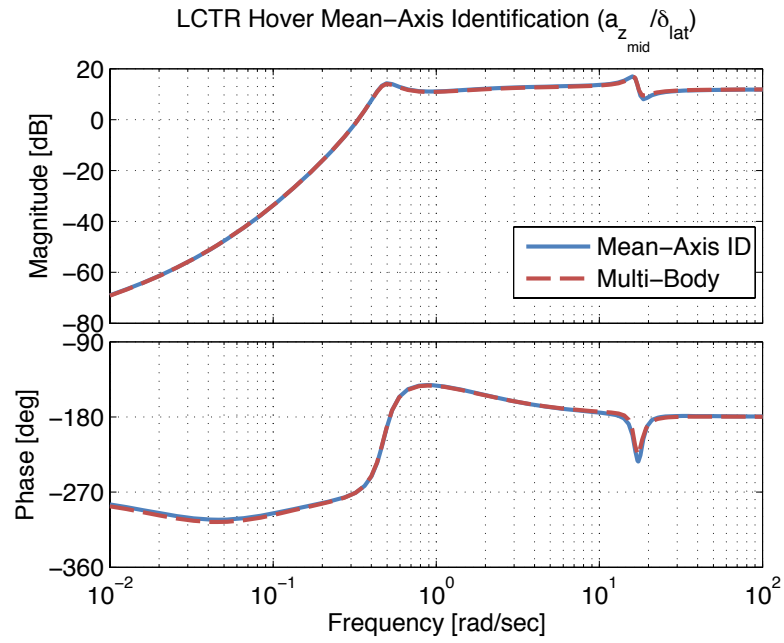
312

Figure B.5: $\frac{a_{z_{mid}}}{\delta_{lat}}$: Mid-wing accelerometer response used in identification of the mean-axis model structure
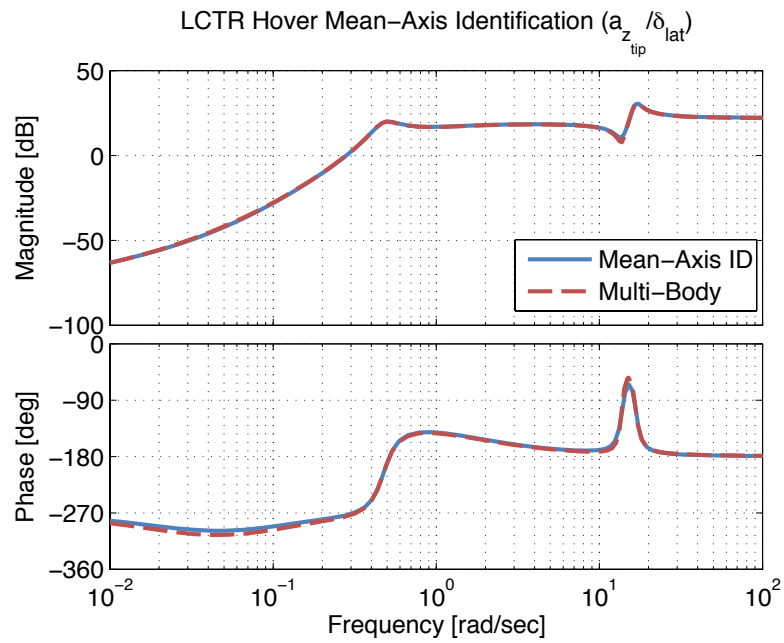

Figure B.6: $\frac{a_{z_{tip}}}{\delta_{lat}}$: Wing-tip accelerometer response used in identification of the mean-axis model structure
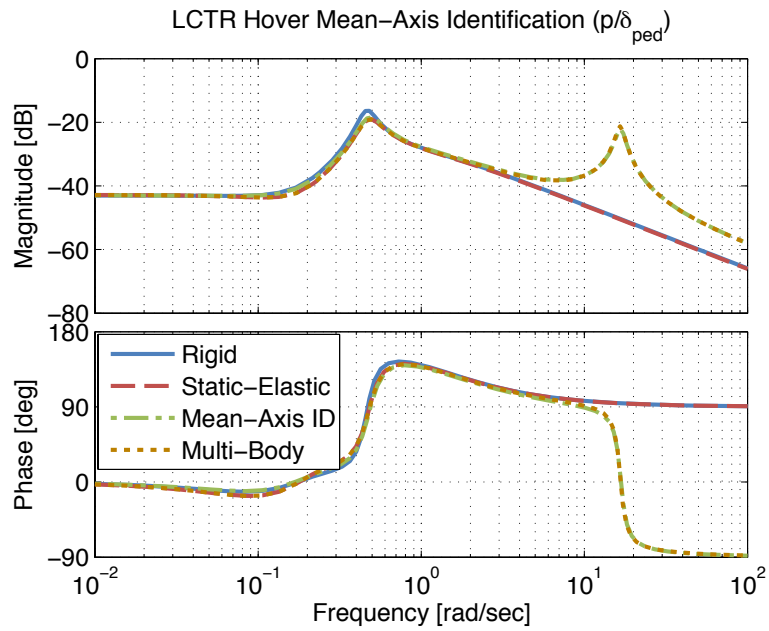
Figure B.7: $\frac{p}{\delta_{ped}}$: Models used in identification of the mean-axis model structure
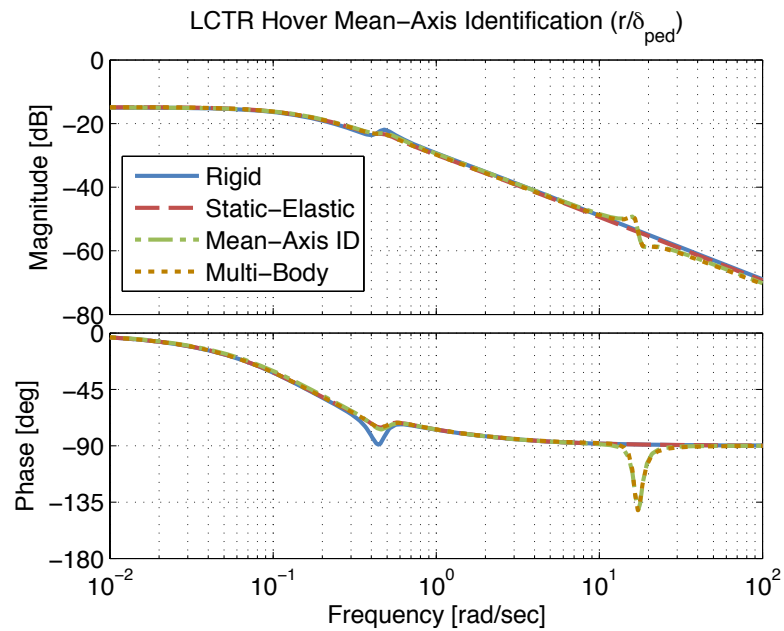

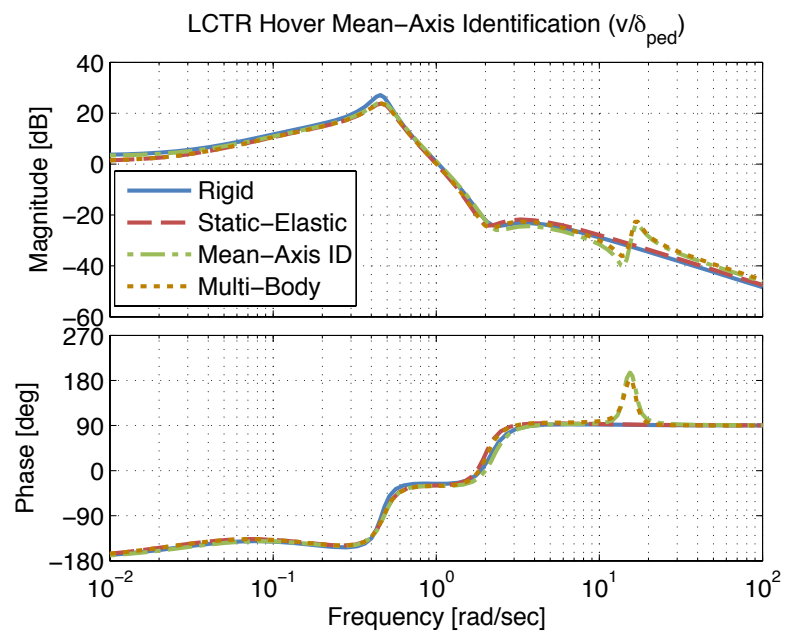Figure B.8: $\frac{r}{\delta_{ped}}$: Models used in identification of the mean-axis model structure

Figure B.9: $\frac{v}{\delta_{ped}}$: Models used in identification of the mean-axis model structure

B.2   Identification of Cruise Mean-Axis Model

In the cruise condition, some responses were truncated above 4 rad/sec because the identification software was not able to identify the coupling terms that would match both the rigid-body and structural dynamics. For these responses (predominantly off-axis responses), low frequency matching was thought to be more important. The dominant response, p/δ_{lat}, was identified to a frequency just above the structural mode. The strain response was removed from this identification. The wing accelerometer responses were retained. A lightly damped low frequency zero in the p/δ_{ped} response was not identified as the phase plot could have a 360° shift if the damping of the zero was found to be the opposite sign. This would greatly increase the cost for that response and would have a negative influence on the identification. Since the structural responses were not included in the other responses (yaw and lateral velocity), these influence coefficients were set to be zero in the identification. The responses used are shown in Table B.4.

For this model, nearly the entire control matrix was left free in the identification. The responses with the rigid-body control derivatives were not accurate enough, and the cost function was not able to be reduced to desirable values without doing so. There are significant changes in the response of the aircraft to control inputs with the wings flexed, and the coupling terms are not able to recreate those. There are a maximum of six coupling terms and two control derivatives that could be identified. These coupling terms and control derivatives affect a total of nine stability derivatives and six control derivatives, giving a over constrained problem

where there are more equations than unknowns. If the eight total unknowns are not able to reproduce the correct control and stability derivatives, additional unknowns are created by freeing the control inputs to facilitate obtaining an accurate solution.

Table B.4: LCTR cruise mean-axis model identification responses

Output	Input	Response Name	ω_{min}	ω_{max}	Coherance	Comment
p	Lat Stick	p/lat	0.01	22	1.0	-
r	Lat Stick	r/lat	0.01	4	1.0	-
v	Lat Stick	v/lat	0.01	4	1.0	-
$a_{z_{tip}}$	Lat Stick	az/lat	0.01	100	1.0	Recreated wing tip acceleration
$a_{z_{mid}}$	Lat Stick	azm/lat	0.01	100	1.0	Recreated wing mid-point acceleration
p	Lat Stick	$ps2/lat$	0.01	0.75	1.0	Low frequency rigid-body mode
p	Lat Stick	$ps3/lat$	10	22	1.0	High frequency flexible mode
p	Pedal	p/rud	0.3	100	1.0	-
r	Pedal	r/rud	0.01	4	1.0	-
v	Pedal	v/rud	0.01	4	1.0	-

The final model parameter values, along with the Cramer-Rao and insensitivity values are given in Table B.5. The cost functions for the identified models are given in Table B.6.

Table B.5: LCTR cruise identification parameter, Cramer-Rao, and Insensitivity values

Param.	Value	CR (%)	Insens. (%)
	M-matrix		
azp	-37.16	4.29	1.842
azn	15.54	12.02	4.705
azp2	-19.43	4.259	1.823
azn2	0[b]	—	—
	F-matrix		
Yv	-0.2887[a]	—	—
Yp	39.29[a]	—	—
Yr	-264.5[a]	—	—
G	32.17[a]	—	—
Yn	0[b]	—	—
Lv	0.0005355[a]	—	—
Lp	-1.136[a]	—	—
Lr	0.5671[a]	—	—
Ln	-41.32	10.2	0.7328
Nv	0.003426[a]	—	—
Np	-0.07298[a]	—	—
Nr	-0.2797[a]	—	—
Nn	-49.29	7.437	0.6843
ST	0.1551[a]	—	—
Ev	0.006217	8.386	1.079
Ep	-1.249	11.57	1.751
Er	-0.2038	41.43	12.53
tzo	-2.009	7.559	3.426
oms	-277.5	0.9698	0.3033
p	0[b]	—	—
Phip	0.4439	5.414	1.507
r	0[b]	—	—
Phir	0[b]	—	—
v	0[b]	—	—
Phiv	0[b]	—	—
	G-matrix		
Ylat	-0.2782	33	14.42
Yped	-3.007	27.65	12.33
Llat	-0.09573	3.488	0.8968
Lped	-0.0974	6.518	0.7
Nlat	0[b]	—	—
Nped	0.06407	10.29	2.093
Elat	0.1126	6.049	0.996
Eped	-0.3342[a]	—	—
	Time delay		

[a] Fixed parameter
[b] Eliminated parameter

Table B.6: LCTR cruise identification results

Response	Cost
p/lat	10.1
r/lat	9.671
v/lat	22.04
az/lat	4.855
azm/lat	22.01
$ps2/lat$	4.386
$ps3/lat$	35.18
p/ped	21.06
r/ped	12.38
v/ped	8.935
J_{ave}	15.06

Figures B.10 - B.15 show the models used in the identification. The rigid-body response is also shown to highlight the differences between the flexible and rigid-body models in cruise. These differences are much larger than the same models in hover, shown in Figures B.1 - B.9, even though the flex-factors were of similar magnitude between hover and cruise.

The identified mean-axis value of L_η is much greater in cruise, it is worth evaluating the effects of wing bending directly from the simulation model. The hover mean-axis L_η was near zero, meaning wing bending should not produce large additional roll moments in hover. Taking both the hover and cruise simulations in trim and perturbing the wings asymmetrically gives the following ratio of aerodynamic moments:

$$\frac{\Delta L_{\text{cruise}}}{\Delta L_{\text{hover}}} \approx 5 \tag{B.1}$$

The ratios of L_η is much greater than this value since the hover $L_\eta = -0.668$ and for

cruise it is $L_\eta = -41.3$. The hover L_η had a large Cramer-Rao value, meaning it is correlated with other parameters and its final value from the identification may not be exact. The hover L_η is fixed at -8 to follow the roll moment ratios in Eqn. (B.1), and a new model is identified. The cost of this hover model increases from $J_{ave} = 9.9$ to $J_{ave} = 16.9$, meaning it is less accurate than the original but still a valid solution. Even though the same ratio does not hold for L_η as did for the total ΔL, the same trend is apparent. The cruise L_η is significantly larger in cruise than in hover and wing bending produces significant aerodynamic roll moments in cruise and does not so in hover.
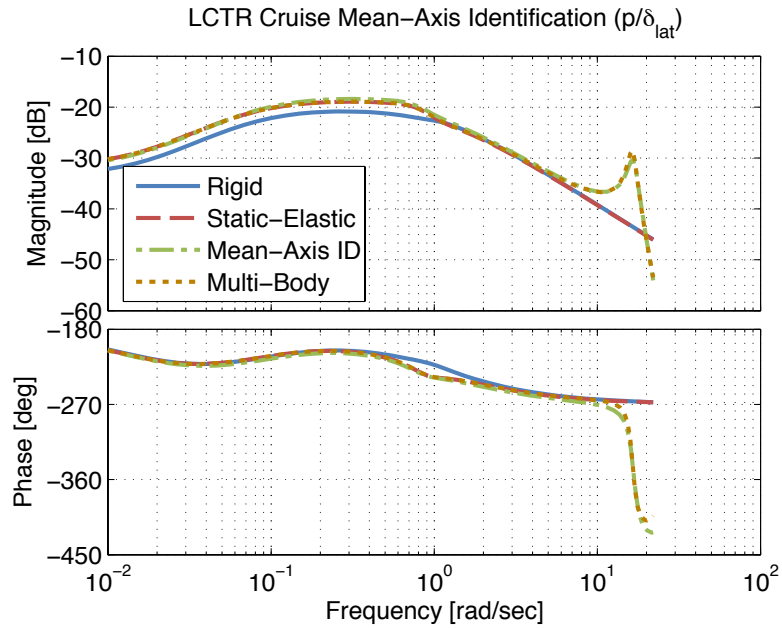

Figure B.10: $\frac{p}{\delta_{lat}}$: Models used in identification of the mean-axis model structure
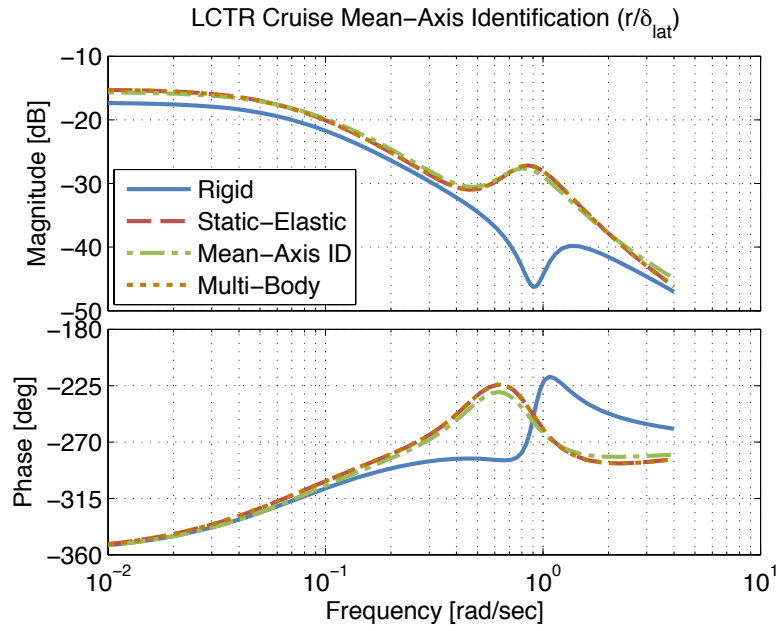
Figure B.11: $\frac{r}{\delta_{lat}}$: Models used in identification of the mean-axis model structure
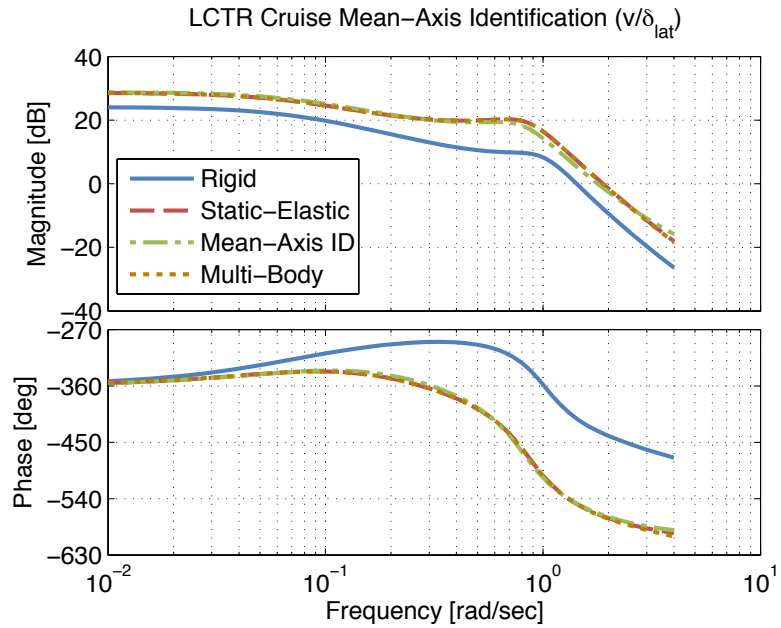

Figure B.12: $\frac{v}{\delta_{lat}}$: Models used in identification of the mean-axis model structure
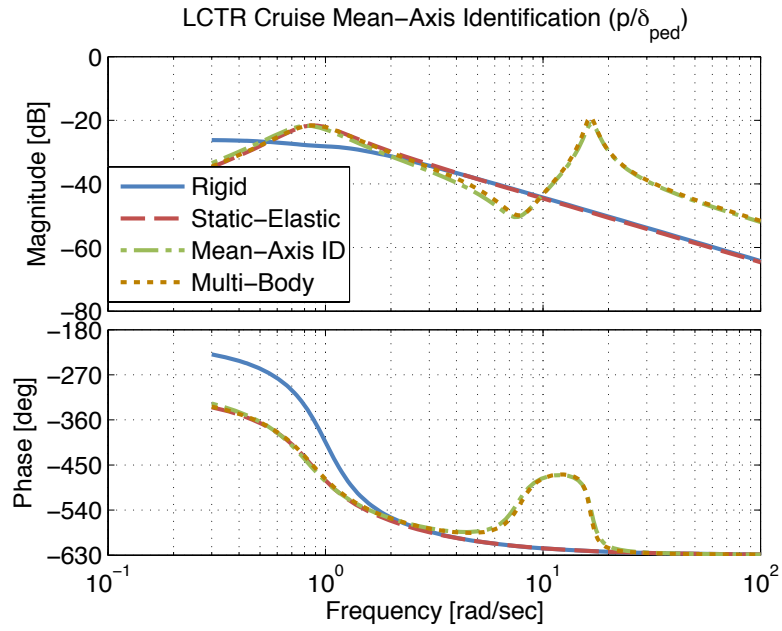
Figure B.13: $\frac{p}{\delta_{ped}}$: Models used in identification of the mean-axis model structure
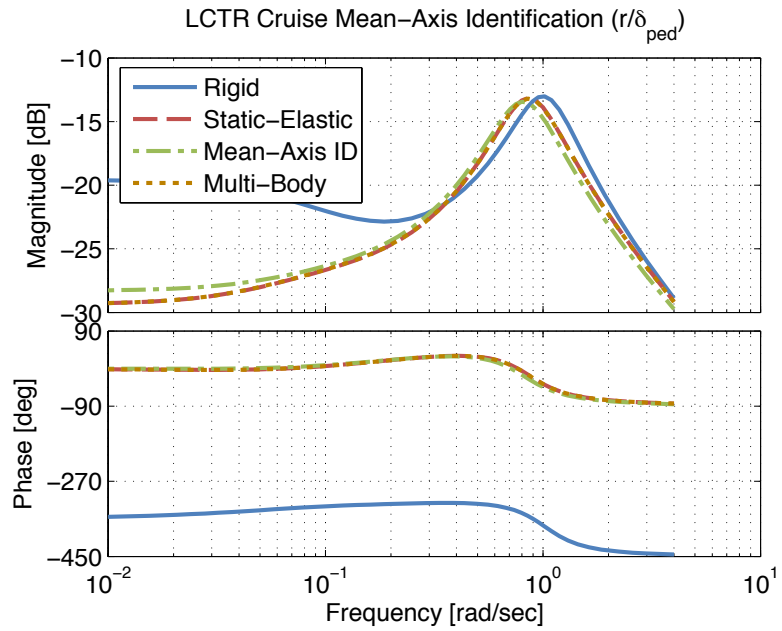

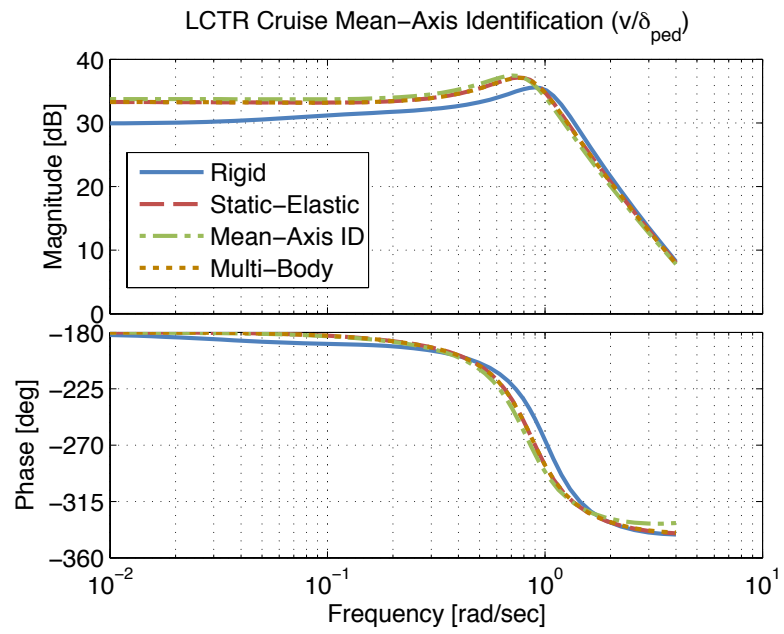Figure B.14: $\frac{r}{\delta_{ped}}$: Models used in identification of the mean-axis model structure

Figure B.15: $\frac{v}{\delta_{ped}}$: Models used in identification of the mean-axis model structure

Appendix C: Structural Feedback Concepts

C.1   Introduction

This chapter describes basic structural feedback concepts. Various types of structural feedback will be compared based on their ability to dampen a structural mode or alter the frequency of the mode. The aim is to remove structural oscillations in an effort to improve ride quality and decrease fatigue of aircraft components. The symmetric beamwise wing bending mode and feedback effects on this mode on the vertical response of the aircraft are analyzed. This mode couples with the vertical displacement of the fuselage. Available structural sensor measurements include wing root bending strain and wing tip accelerometers. The off-axis responses are constrained using coupling numerators [98]. Constrained coupling numerators assume large feedback gains for each axis, effectively decoupling each axis. A constrained coupling numerator state-space approach developed by Ivler [99], is used to isolate the vertical axis and the symmetric bending mode from the rest of the system. The constrained model (with infinite gains) is not necessarily physically realizable, but helps to isolate the feedback effects to the dominant on-axis modes of the aircraft while ignoring potentially complicating off-axis effects. A well designed control system serves to decouple the aircraft responses and would look similar to

the constrained coupling numerator result.

Structural modes are generally lightly damped, with in vacuo damping being around 6%:

$$\zeta_{\text{str}} \approx 0.06 \qquad\qquad (\text{C.1})$$

The small structural damping places the structural modes close to the Imaginary Axis. With only CG vertical velocity feedback to collective, this mode becomes unstable for small feedback gains, as shown in Figure C.1. The structural mode is located at 9 rad/sec. Positive feedback is used because vertical velocity in the body axis is measured as positive down. Positive velocity perturbations should result in positive collective increases, stabilizing the aircraft in heave. The low frequency rigid body pole around 0.1 rad/sec represents the location of the low frequency break in the response and corresponds to the effective Z_w. As gain is increased, this pole moves further negative, increasing the break frequency of the mode. CG feedback alone will not suffice to improve both the aircraft handling qualities and structural oscillation.

C.2   Structural Feedback

Structural feedback includes both cg and wing tip feedback. Since the aircraft structural dynamics are coupled into the response at the CG, the CG responses can also be used to control structural modes.
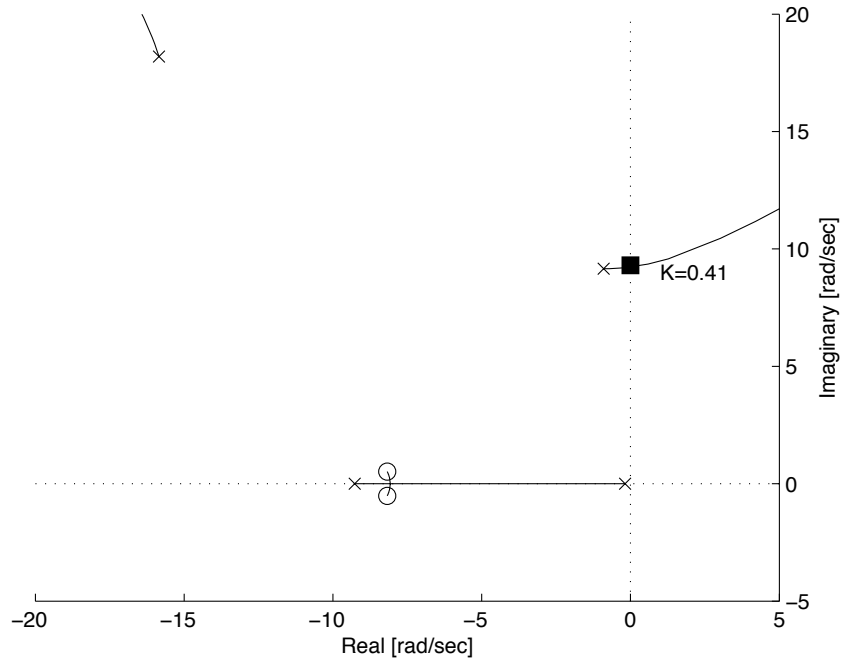
Figure C.1: Root locus plot for positive vertical CG velocity feedback to collective stick

C.2.1 Acceleration Feedback

The first set of feedback comparisons focus on acceleration feedback.

C.2.1.1 CG Acceleration Feedback

Figure C.2 shows the root locus response for feeding back CG vertical acceleration to collective. Both negative and positive feedback are shown. Negative feedback, as shown in Figure C.2a, destabilizes the structural modes and stabilizes the low frequency aircraft dynamic mode. The structural mode reduces in frequency and damping and the loci join on the real axis, creating a divergent, first order structural response. Positive feedback, shown in Figure C.2b, destabilizes the structural
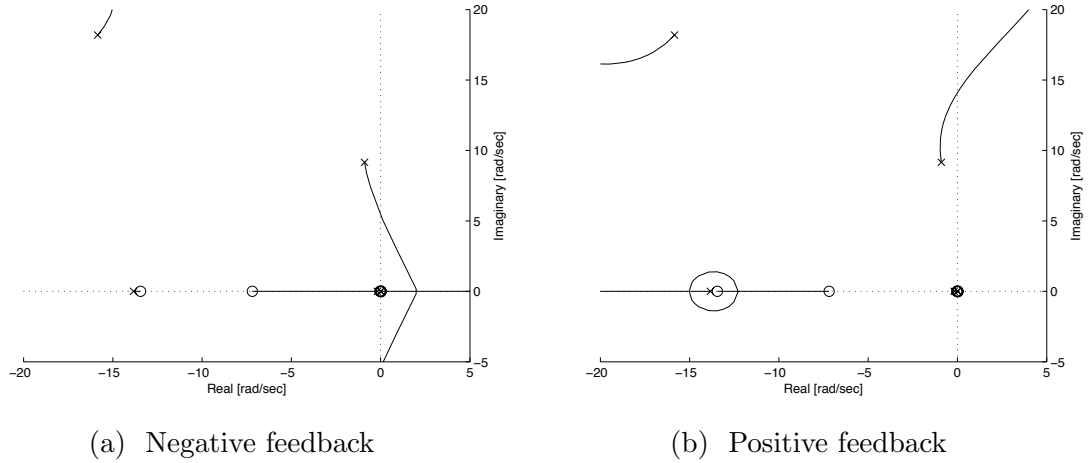
(a) Negative feedback (b) Positive feedback

Figure C.2: Root Loci for vertical CG acceleration feedback to collective

mode. The mode increases in frequency and crosses the imaginary axis around 15 rad/sec. The low frequency aircraft dynamic modes near the origin are slightly destabilized for positive feedback. These low frequency unstable modes are not present in the velocity feedback on Figure C.1. Structural damping is not improved with either feedback.

The closed loop bode plot, Figure C.3a, shows the vertical velocity response as measured at the CG. Feedback gains were chosen for positive and negative feedback that kept the system stable, but still altered the dynamics. With negative feedback, the structural mode frequency decreases as expected, but the magnitude at low frequency is higher than the other cases. The low frequency pole becomes more negative (occurs at a larger frequency) with negative feedback and becomes more positive (approaches 0 rad/sec) with positive feedback. The low frequency asymptote is identical. The heave response constrained to a single axis with a single structural mode gives three total states. Rotor states and other structural states can be reduced out of the system and the dynamics will be almost identical to that

of Figure C.3a without the high frequency rotor modes.

$$
\begin{Bmatrix} \dot{w} \\ \ddot{\eta} \\ \dot{\eta} \end{Bmatrix} = \begin{bmatrix} Z_w & Z_{\dot{\eta}} & Z_\eta \\ \eta_w & -2\zeta\omega & -\omega^2 \\ 0 & 1 & 0 \end{bmatrix} \begin{Bmatrix} w \\ \dot{\eta} \\ \eta \end{Bmatrix} + \begin{bmatrix} Z_\delta \\ \eta_\delta \\ 0 \end{bmatrix} \delta_{col} \tag{C.2}
$$

Comparing the wing tip vertical acceleration response, Figure C.3b, the magnitude of the negative feedback peak at the structural frequency is lower than the other cases. The wing tip will have smaller acceleration at the structural mode, even though the damping with negative feedback is roughly unchanged.

The bare-airframe system in *multi-body* form has the following control and stability
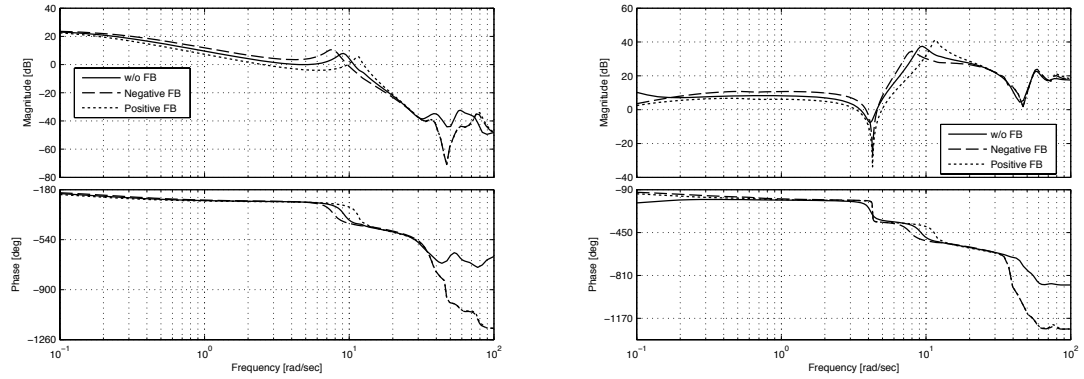
(a) CG vertical velocity response   (b) Wing tip vertical acceleration response

Figure C.3: Bode plots comparing response without feedback and with the CG vertical acceleration feedback loops closed

derivatives.

$$
\begin{array}{c|ccc}
Z_w = -0.023 & Z_{\dot{\eta}} = -6.5 & Z_\eta = -701 \\
\hline
\eta_w = 0.023 & \zeta = 0.08 & \omega = 9.73
\end{array} \tag{C.3}
$$

$$Z_\delta = 0.27$$

$$\overline{}$$

$$\eta_\delta = 0.45$$

The negative feedback case gives the following control and stability derivatives.

$$
\begin{array}{c|cc}
Z_w = -0.022 & Z_{\dot\eta} = -6.4 & Z_\eta = -686 \\
\hline
\eta_w = 0.023 & \zeta = 0.08 & \omega = 8.34
\end{array}
\tag{C.4}
$$

$$Z_\delta = 0.26$$

$$\overline{}$$

$$\eta_\delta = 0.44$$

And for positive feedback:

$$
\begin{array}{c|cc}
Z_w = -0.023 & Z_{\dot\eta} = -6.7 & Z_\eta = -720 \\
\hline
\eta_w = 0.022 & \zeta = 0.08 & \omega = 11.3
\end{array}
\tag{C.5}
$$

$$Z_\delta = 0.28$$

$$\overline{}$$

$$\eta_\delta = 0.47$$

The only significant difference between the cases with feedback and the bare-airframe is the structural frequency, which went from 9.73 rad/sec without feedback to 8.34 rad/sec with the negative feedback and 11.3 rad/sec with positive feedback.

A static-elastic reduction of the structural modes gives a simple one DOF

system with a pole at $Z_{w_{se}}$ and control derivative $Z_{\delta_{se}}$.

$$Z_{w_{se}} = Z_w + \frac{Z_\eta}{\omega^2}\eta_w \tag{C.6}$$

$$Z_{\delta_{se}} = Z_\delta + \frac{Z_\eta}{\omega^2}\eta_\delta \tag{C.7}$$

For the bare-airframe system this reduction gives $Z_{w_{se}} = -0.19$ and a control derivative of $Z_{\delta_{se}} = -3.09$. A static-elastic reduction of the structural modes gives a $Z_{w_{se}} = -0.252$ and $Z_{\delta_{se}} = -4.1$ for negative feedback and $Z_{w_{se}} = -0.145$ and $Z_{\delta_{se}} = -2.4$ for positive feedback. Since Z_η, η_w, and η_δ are nearly identical in the bare-airframe and feedback cases, the change in $Z_{w_{se}}$ and $Z_{\delta_{se}}$ comes almost purely from the change in the structural frequency of the mode. The reduction in structural mode frequency serves to increase the break frequency and control derivative of the aircraft dynamic response.

The wing tip vertical acceleration response is reduced in Figure C.3b because of changes in the output matrices due to feedback. A basic feedback system is shown in Figure C.4.
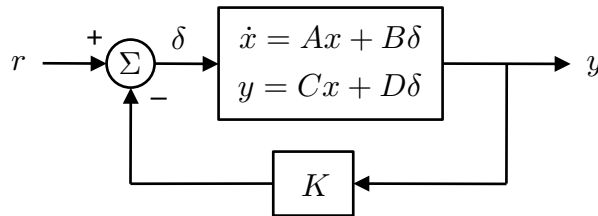

Figure C.4: Output feedback block diagram

The closed loop response has the form

$$\dot{x} = A_{FB}x + B_{FB}r \tag{C.8}$$

$$y = C_{FB}x + D_{FB}r$$

where

$$A_{FB} = A - BK\left(I + DK\right)^{-1}C \tag{C.9}$$

$$B_{FB} = B - BK\left(I + DK\right)^{-1}D \tag{C.10}$$

$$C_{FB} = \left(I + DK\right)^{-1}C \tag{C.11}$$

$$D_{FB} = \left(I + DK\right)^{-1}D \tag{C.12}$$

The alteration of the C and D matrices due to feedback causes a reduction in the output derivative associated with the wing mode. The bare-airframe system without feedback has the following components in the C and D matrices for wing tip acceleration output.

$$a_{z_{\text{wing tip}}} = \begin{bmatrix} -0.75 & 45 & 2366 \end{bmatrix} \begin{Bmatrix} w \\ \dot{\eta} \\ \eta \end{Bmatrix} + \begin{bmatrix} -14.4 \end{bmatrix} \begin{Bmatrix} \delta \end{Bmatrix} \tag{C.13}$$

With negative feedback, the output has the following form:

$$a_{z_{\text{wing tip}}} = \begin{bmatrix} -0.78 & 37 & 1575 \end{bmatrix} \begin{Bmatrix} w \\ \dot{\eta} \\ \eta \end{Bmatrix} + \begin{bmatrix} -14.1 \end{bmatrix} \begin{Bmatrix} \delta \end{Bmatrix} \tag{C.14}$$

331

And with positive feedback, the output has the following form:

$$a_{z_{\text{wing tip}}} = \begin{bmatrix} -0.72 & 54 & 3407 \end{bmatrix} \begin{Bmatrix} w \\ \dot{\eta} \\ \eta \end{Bmatrix} + \begin{bmatrix} -14.8 \end{bmatrix} \{ \delta \} \qquad (C.15)$$

The only major difference between the sensor measurements is the component which multiplies η. Negative structural feedback serves to reduce the effect of the structural displacement state in the measured output. Positive feedback increases this value, increasing the response in Figure C.3b.

Time histories of the CG velocity and wing tip acceleration are shown in Figure C.5 and further highlight the effects mentioned above. An increase in low frequency content in the negative feedback CG response leads to a faster response in the time history, as shown in Figure C.5a. A decrease in the peak magnitude of the wing tip response with positive feedback leads to smaller peak deflections of the wing in the time history, Figure C.5b.
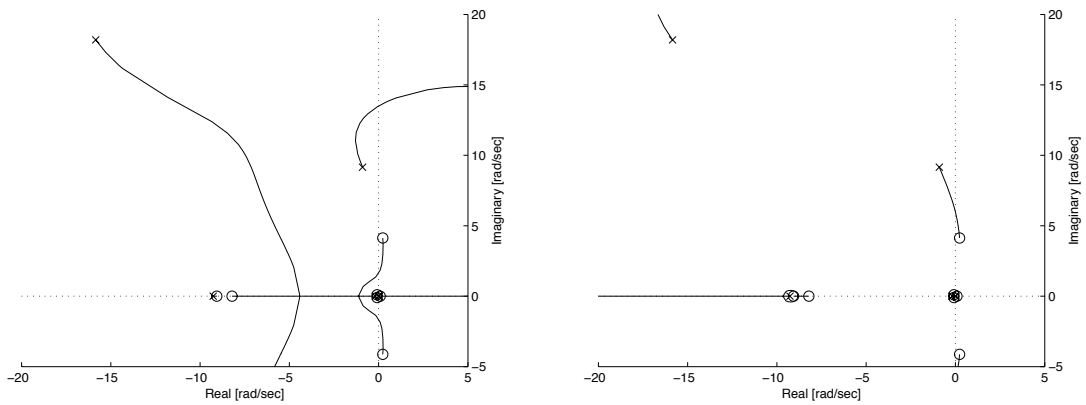
C.2.1.2 Wing Tip Acceleration Feedback

Figure C.6 shows the root locus response for feeding back wing tip vertical acceleration to collective. Both negative and positive feedback are shown. For negative feedback, shown in Figure C.6a, the unstable zeros at 4 rad/sec serve to attract, and eventually destabilize, a low frequency aircraft dynamic pole and a rotor flapping pole. The structural mode increases in frequency and is destabilized. For positive
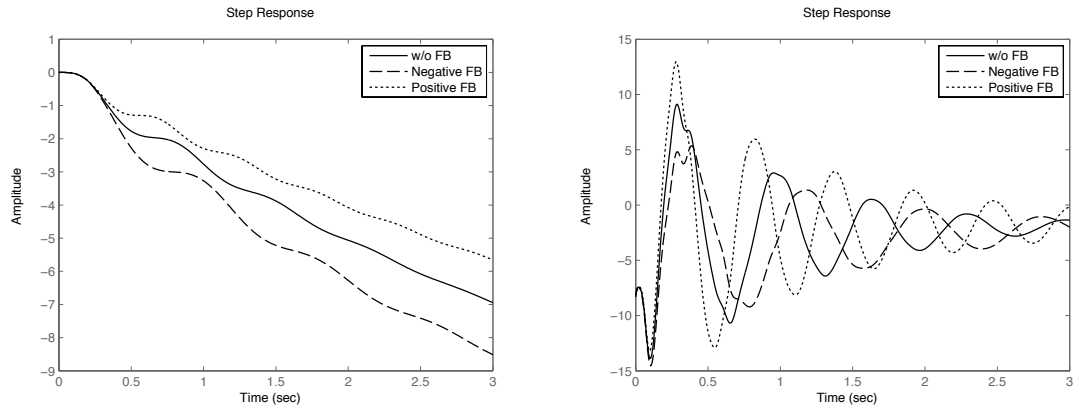
(a) CG vertical velocity response

(b) Wing tip vertical acceleration response

Figure C.5: Collective step input response without feedback and with the CG vertical acceleration feedback loops closed

(a) Negative feedback

(b) Positive feedback

Figure C.6: Root Loci for wing tip vertical acceleration feedback to collective

feedback, shown in Figure C.6b, the structural mode is reduced in frequency and damping. The loci are attracted to the zeros at 4 rad/sec. The low frequency aircraft dynamic mode moves towards the right half plane for positive feedback. A low frequency pole is stabilized by negative feedback, but a pole at the origin is drawn into the right half plane, destabilizing the system.

It is interesting to note that the effect on the structural mode of CG and wing

accelerometer feedback have opposite effects. The negative feedback of wing tip acceleration, shown in Figure C.6a, has similar effects to the structural mode as positive feedback of CG acceleration, shown in Figure C.2b. Negative feedback of CG acceleration has a similar effect to the positive feedback of wing tip acceleration. However, positive and negative feedbacks have the same effect on the low frequency aircraft dynamics modes in both acceleration feedbacks. This is clarified by the Bode diagram in Figure C.7. At low frequency, the phasing of the CG and wing tip accelerometer responses is identical. Feeding back low frequency content to collective stick will have similar results. The unstable zero at 4 rad/sec in the wing tip response drops the phase curve 180 degrees from the CG response. This offset continues to the structural modes, meaning that feeding back accelerometer information will have opposite effects.

A comparison of Bode response plots between bare-airframe, positive, and negative feedback is shown in Figure C.8. The low frequency response is nearly identical in both plots for all the cases shown. This is in contrast to the CG acceleration feedback case, (Figure C.3) where the low frequency response was altered. Feeding back wing tip acceleration seems only alter the frequency of the structural mode based on the response at the CG, Figure C.8a. However, the peak structural response as shown by the wing tip vertical acceleration in Figure C.8b is able to be reduced for the positive feedback case, which corresponds to a reduction in the structural mode frequency. An increase in structural mode frequency with negative feedback is accompanied by an increase in the peak structural response.
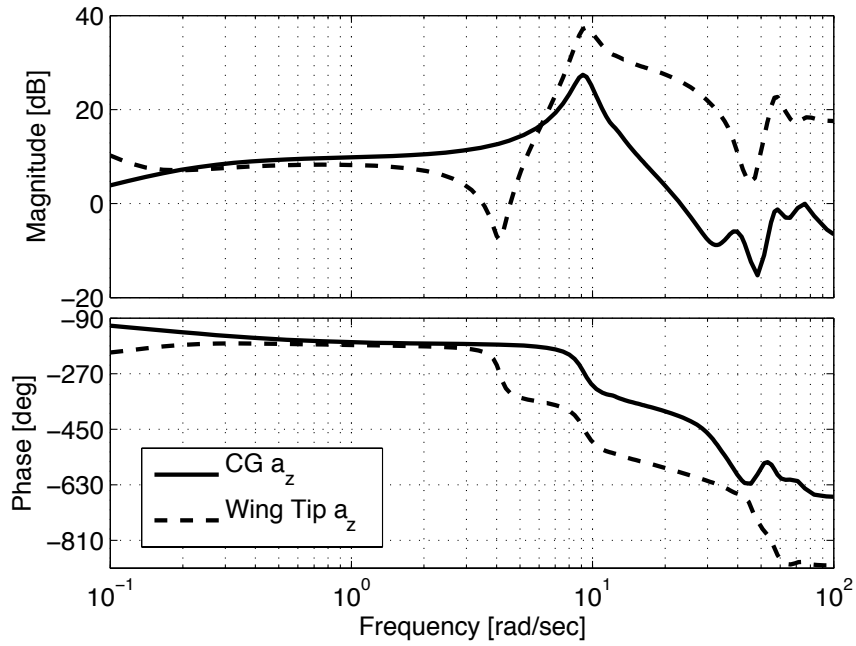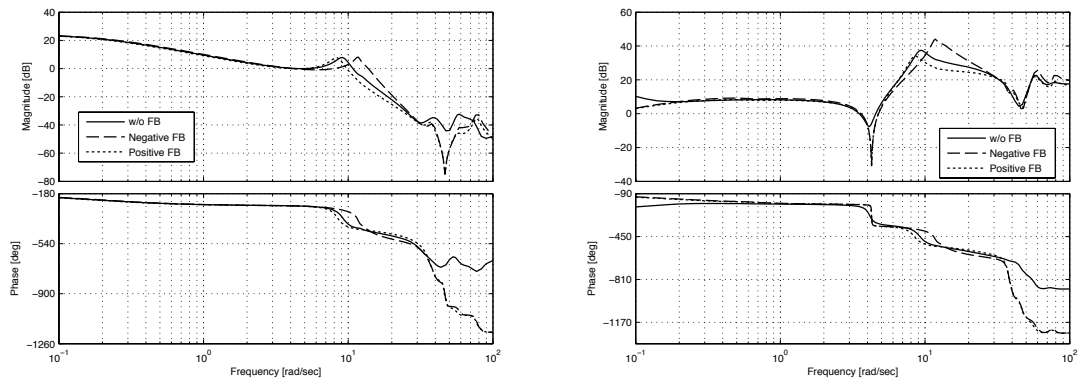
Figure C.7: Bode plot comparing wing tip and CG acceleration response to collective inputs

(a) CG vertical velocity response

(b) Wing tip vertical acceleration response

Figure C.8: Bode plots comparing response without feedback and with the CG vertical acceleration feedback loops closed

The stability and control derivatives for negative feedback are (bare-airframe

derivatives are given in Eqn. (C.3)):

$$\begin{array}{c|cc} Z_w = -0.017 & Z_{\dot{\eta}} = -6.9 & Z_\eta = -720 \\ \hline \eta_w = 0.033 & \zeta = 0.097 & \omega = 11.26 \end{array} \tag{C.16}$$

$$\begin{array}{c} Z_\delta = 0.39 \\ \hline \eta_\delta = 0.65 \end{array}$$

And for positive feedback:

$$\begin{array}{c|cc} Z_w = -0.026 & Z_{\dot{\eta}} = -6.35 & Z_\eta = -691 \\ \hline \eta_w = 0.017 & \zeta = 0.07 & \omega = 8.82 \end{array} \tag{C.17}$$

$$\begin{array}{c} Z_\delta = 0.21 \\ \hline \eta_\delta = 0.35 \end{array}$$

These derivatives show large changes in structural frequency, rigid-body coupling (η_w), and Z_w. Both control derivatives are also considerably different. The aeroelastic coupling term, Z_η, remains relatively unchanged. Taking the quasi-static reduction of the structural modes as in Eqn (C.6) gives $Z_{w_{se}} = -0.20$ and $Z_{\delta_{se}} = -3.31$ for negative feedback and $Z_{w_{se}} = -0.18$ and $Z_{\delta_{se}} = -2.91$ for positive feedback. These values are very similar to the bare-airframe values of $Z_{w_{se}}$ and $Z_{\delta_{se}}$ given above. This similarity indicates that as ω is changed by structural feedback, η_w and η_δ are also altered by the same amount. Feeding back wing tip acceleration alters the rigid-body coupling and structural control derivative, leaving the low frequency

aircraft dynamic response intact. With negative feedback, the wing tip acceleration output has the following form:

$$a_{z_{\text{wing tip}}} = \begin{bmatrix} -1.08 & 63.8 & 3396 \end{bmatrix} \begin{Bmatrix} w \\ \dot{\eta} \\ \eta \end{Bmatrix} + \begin{bmatrix} -20.7 \end{bmatrix} \begin{Bmatrix} \delta \end{Bmatrix} \qquad (C.18)$$

And with positive feedback, the output has the following form:

$$a_{z_{\text{wing tip}}} = \begin{bmatrix} -0.88 & 34.5 & 1836 \end{bmatrix} \begin{Bmatrix} w \\ \dot{\eta} \\ \eta \end{Bmatrix} + \begin{bmatrix} -11.2 \end{bmatrix} \begin{Bmatrix} \delta \end{Bmatrix} \qquad (C.19)$$

The structural displacement component and control component in the output have smaller values with positive feedback than the bare-airframe and negative feedback cases. This reduction of the structural mode with positive feedback is also seen in the time histories shown in Figure C.9. The wing tip acceleration is much reduced with positive feedback, but the overall aircraft response remains unchanged.
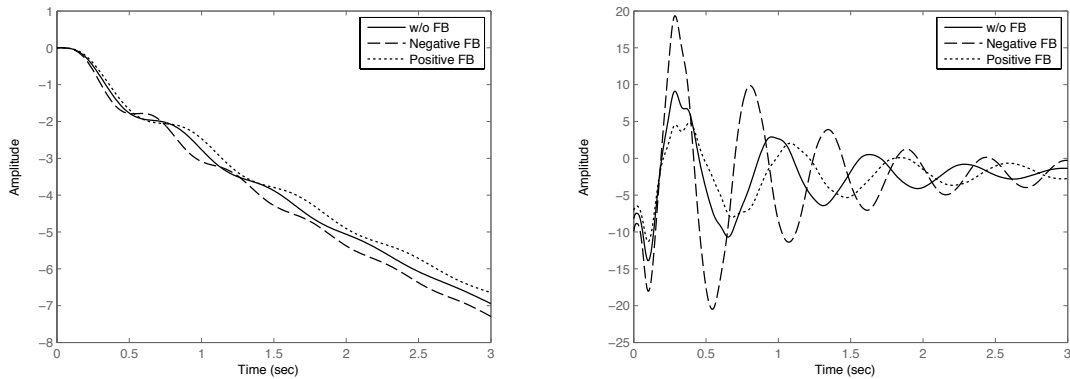
(a) CG vertical velocity response   (b) Wing tip vertical acceleration response

Figure C.9: Collective step input response without feedback and with the wing tip vertical acceleration feedback loop closed

C.2.1.3 Differential Acceleration Feedback

In an effort to focus on structural feedback alone, the wing tip acceleration may be subtracted from the CG acceleration. The resulting response (Figure C.10) has a much smaller magnitude at low frequency, and a large peak at the structural mode. Low frequency differences in vertical acceleration between the CG and wing tip accelerometer cause the magnitude of the response to rise below 0.1 rad/sec. The responses match, and thus cancel, well between 0.2 and 2 rad/sec.
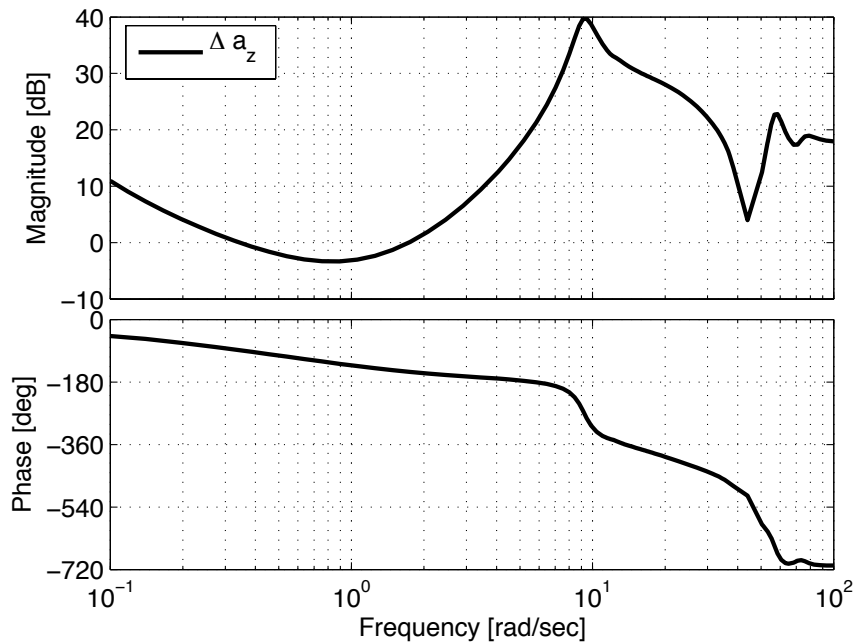
Figure C.10: Bode plot showing the differential vertical acceleration $(a_{z_{CG}} - a_{z_{wing\ tip}})$ response to collective inputs

The corresponding root locus plots for feeding back the differential vertical acceleration are shown in Figure C.11.

The root loci for differential acceleration feedback look much like the CG ver-
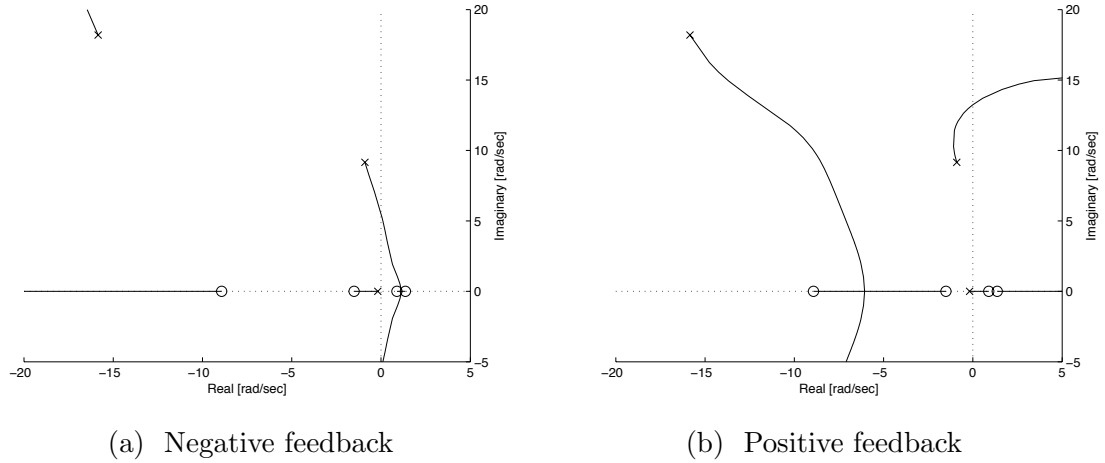
(a) Negative feedback　　　(b) Positive feedback

Figure C.11: Root Loci for differential vertical acceleration ($a_{z_{\text{CG}}} - a_{z_{\text{wing tip}}}$) feedback to collective

tical acceleration responses. A negative feedback serves to lower the frequency of the mode and destabilize it. Positive feedback tends to increase the frequency of the wing mode and destabilize it. Structural damping remains unchanged or worsens with any form of acceleration feedback. The closed loop responses and linear model structure look nearly identical to the wing tip acceleration feedback cases.

C.2.2　Velocity Feedback

Velocity feedback at the CG and wing tips are compared next.

C.2.2.1　CG Velocity Feedback

Integrating acceleration would provide structural velocity information and a means to alter damping. The acceleration of a second order system is tied to its mass properties, and thus natural frequency. It is therefore not surprising that

339

acceleration feedback mostly affects structural frequencies, as has been shown in the previous figures. Velocity is tied directly to damping. Integrating the CG acceleration would result in the heave velocity, the feedback of which is shown in Figure C.1. This feedback type must be preserved in order to stabilize the low frequency aircraft dynamics. For completeness, positive and negative feedback will be shown here to determine the effects of these feedbacks on closed loop dynamics and the linear model structure. Figure C.12 shows velocity feedback mostly altering the damping of structural modes. It can also either stabilize or destabilize the low frequency flight dynamics modes.

(a) Negative feedback
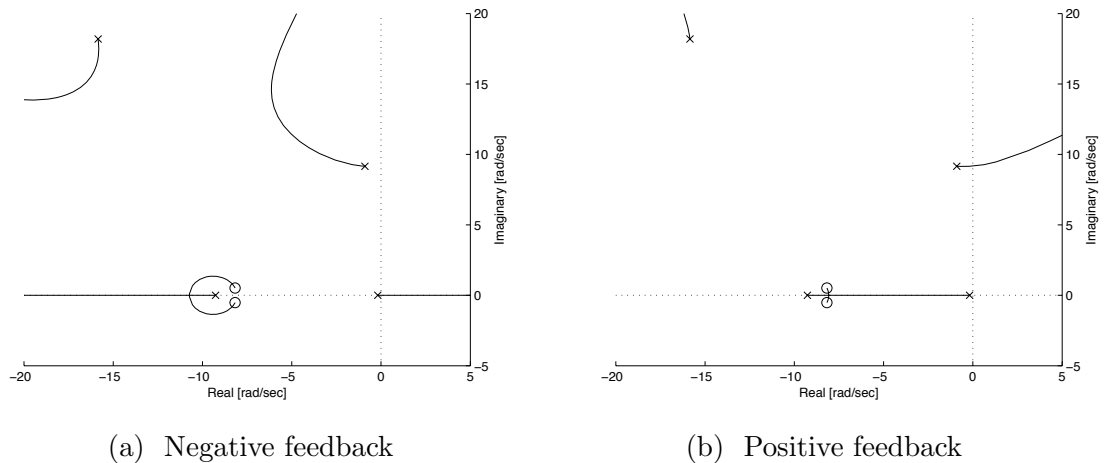
(b) Positive feedback

Figure C.12: Root Loci for CG velocity feedback to collective

The closed loop responses shown in Figure C.13 show the CG feedback effects not only structural damping, but also the response at low frequencies. Positive feedback drops the CG response magnitude significantly (Figure C.13a). For the gains chosen, negative feedback slightly destabilizes the low frequency flight dynamics mode, as is seen by the low frequency phase difference in the CG response. As expected, this feedback type does not alter the frequency of the structural mode.

340
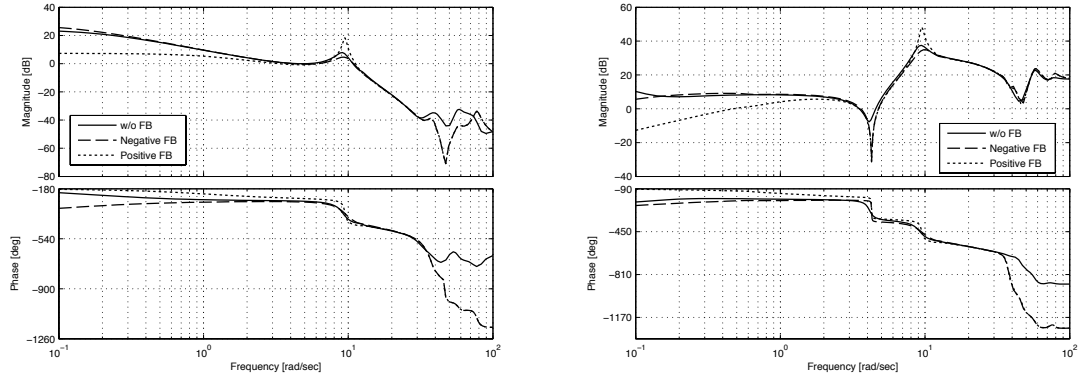
(a) CG vertical velocity response   (b) Wing tip vertical acceleration response

Figure C.13: Bode plots with comparing response without feedback and with the CG vertical velocity feedback loops closed

The closed loop model has the following control and stability derivatives. For negative feedback:

$$
\begin{array}{c|cc}
Z_w = -0.050 & Z_{\dot\eta} = -6.54 & Z_\eta = -701 \\
\hline
\eta_w = -0.024 & \zeta = 0.081 & \omega = 9.73
\end{array}
\tag{C.20}
$$

$$
\begin{array}{c}
Z_\delta = 0.27 \\
\hline
\eta_\delta = 0.45
\end{array}
$$

And for positive feedback:

$$
\begin{array}{c|cc}
Z_w = 0.077 & Z_{\dot\eta} = -6.54 & Z_\eta = -701 \\
\hline
\eta_w = 0.19 & \zeta = 0.081 & \omega = 9.73
\end{array}
\tag{C.21}
$$

$$
\begin{array}{c}
Z_\delta = 0.27 \\
\hline
\eta_\delta = 0.45
\end{array}
$$

341

The only differences in the A and B matrices for the system with feedback are in the first column of A. The change in structural damping comes from the rigid-body coupling term, η_w. Z_w and η_w even change signs based on the feedback. A quasi static reduction gives the $Z_{w_{se}} = 0.126$ for negative feedback and $Z_{w_{se}} = -1.33$ for positive feedback. The quasi-static control derivative does not change since Z_η and ω remain the same. The time histories of CG velocity and wing tip acceleration are shown in Figure C.14. The positive feedback CG (Figure C.14a) response slowly diverges due to the positive low frequency pole. Large changes in wing tip damping are obvious in the wing tip acceleration response, Figure C.14b, but the initial peak structural response is not altered significantly.
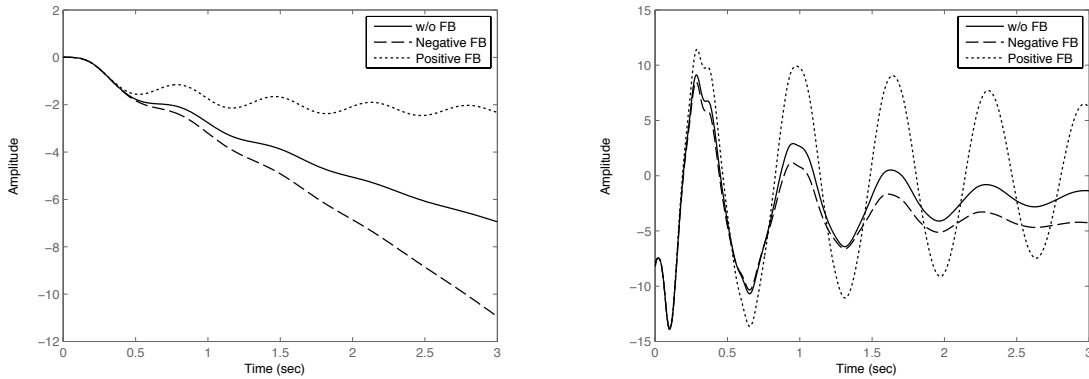
(a) CG vertical velocity response (b) Wing tip vertical acceleration response

Figure C.14: Collective step input response without feedback and with the CG vertical velocity feedback loop closed

C.2.2.2   Wing Tip Velocity Feedback

Wing tip integral acceleration (velocity) feedback root loci are shown in Figure C.15.

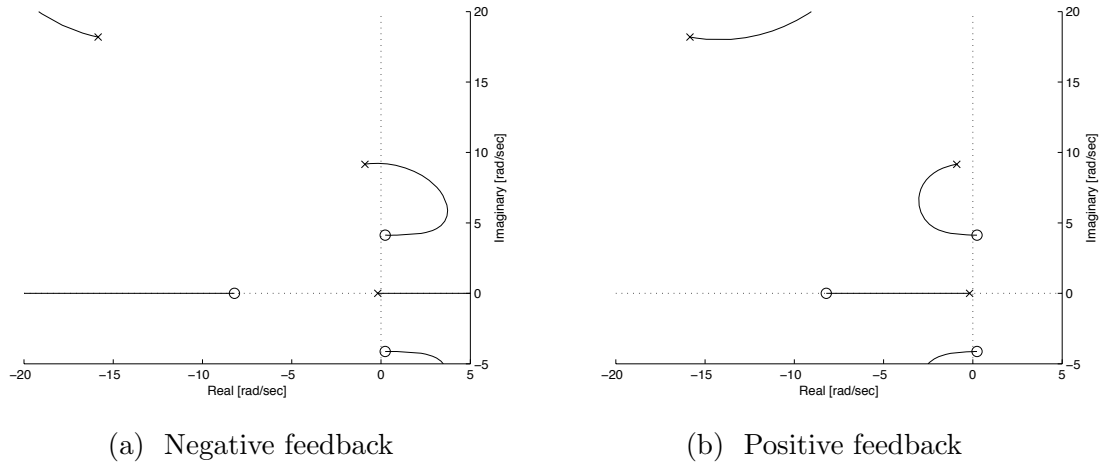(a) Negative feedback   (b) Positive feedback

Figure C.15: Root Loci for wing tip velocity feedback to collective

The negative feedback root locus plot, Figure C.15a shows the structural mode destabilizing quickly. The low frequency aircraft dynamic poles are also destabilized. The positive feedback case shows improvements in damping of the structural mode for moderate gains. The structural mode is attracted to the zero at 4 rad/sec, and will destabilize for large enough gains for either feedback case. Low frequency aircraft dynamics are further stabilized by this feedback type.

Gains are chosen to alter the dynamics for both positive and negative feedback. For positive feedback, a gain is chosen to maximize the structural mode damping. The closed loop frequency responses are plotted in Figure C.16. Feeding back positive wing tip velocity significantly improves the damping of the structural mode. Positive feedback also reduces the wing tip acceleration response (Figure C.16b) over low and mid frequency ranges. Negative feedback is destabilizing to both the structural mode and low frequency dynamics.

The velocity feedback adds another state to the dynamics. In order to compare the linear model structure, system identification was performed to remove the
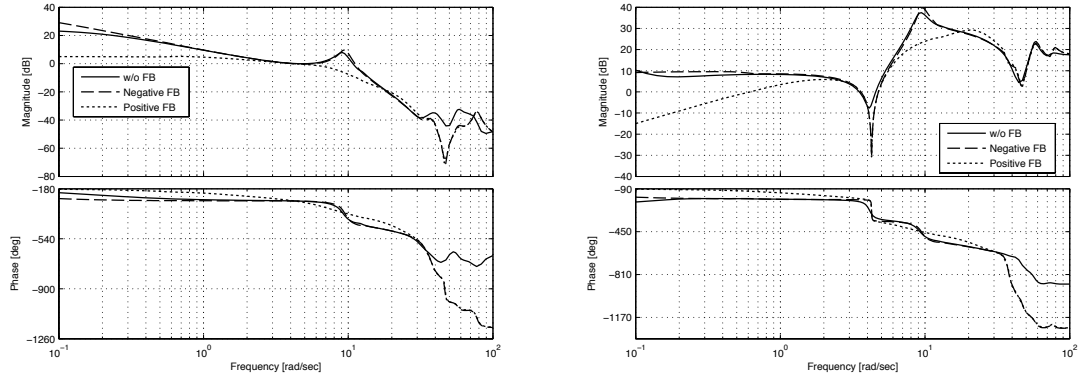
(a) CG vertical velocity response   (b) Wing tip vertical acceleration response

Figure C.16: Bode plots comparing response without feedback and with the CG vertical velocity feedback loops closed

additional state. The costs for fitting positive and negative feedback cases to the CG velocity and wing tip acceleration responses was very low ($J_{ave} < 5$), meaning a highly accurate models were obtained.

For negative feedback:

$$
\begin{array}{c|cc}
Z_w = 0.133 & Z_{\dot{\eta}} = -6.54 & Z_\eta = -708 \\
\hline
\eta_w = 0.023 & \zeta = 0.078 & \omega = 9.73
\end{array}
\tag{C.22}
$$

$$
\frac{Z_\delta = 0.27}{\eta_\delta = 0.45}
$$

And for positive feedback:

$$
\begin{array}{c|cc}
Z_w = -1.68 & Z_{\dot{\eta}} = -6.54 & Z_\eta = -628 \\
\hline
\eta_w = 0.023 & \zeta = 0.381 & \omega = 9.73
\end{array}
\tag{C.23}
$$

$$Z_\delta = 0.26$$

$$\eta_\delta = 0.54$$

This structural feedback effects stability derivatives Z_w, Z_n and structural damping, and the control derivative η_δ. Time histories are shown in FIgure C.17. These figures verify that negative feedback is destabilizing for both the low frequency mode and the structural mode. Positive feedback reduces the steady state response magnitude and improves damping significantly.
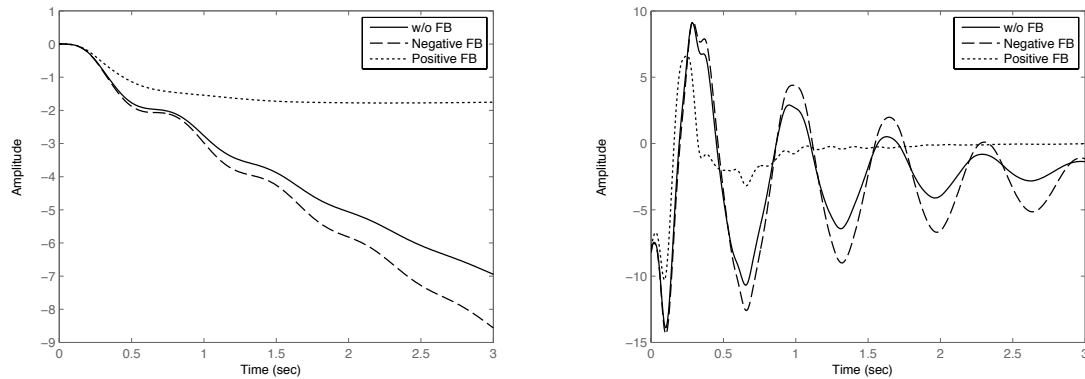
(a) CG vertical velocity response   (b) Wing tip vertical acceleration response

Figure C.17: Collective step input response without feedback and with the integral wing tip vertical acceleration feedback loop closed

C.2.2.3   Differential Velocity Feedback

The final velocity feedback curve, shown in Figure C.18, looks at differential velocity feedback, subtracting the wing tip vertical velocity from the CG velocity.

The negative feedback (Figure C.18a) case shows large improvements to wing structural damping, with the structural modes even becoming first order for high enough gains. There are small changes to the low frequency dynamics and for
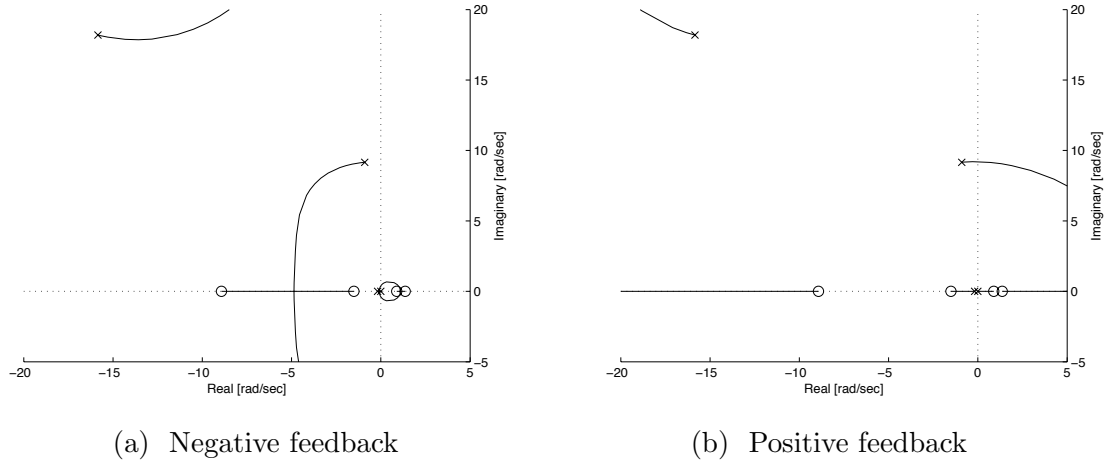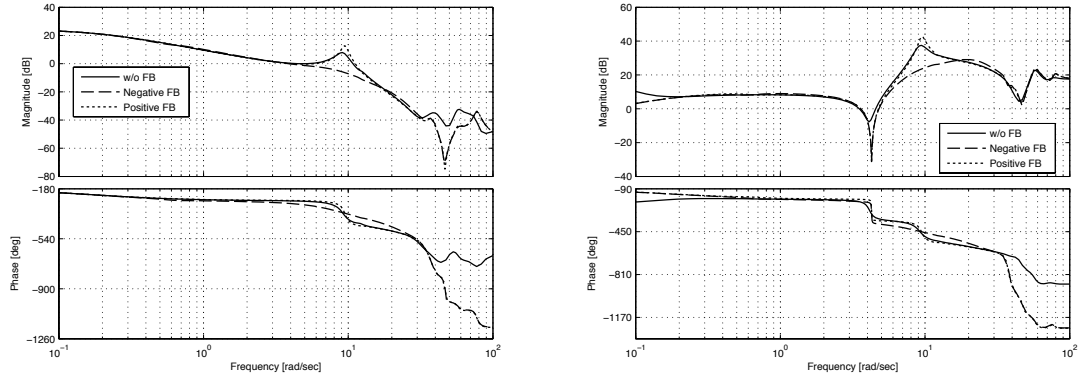
(a) Negative feedback   (b) Positive feedback

Figure C.18: Root Loci for differential vertical velocity ($w_{\text{CG}} - w_{\text{wing tip}}$) feedback to collective

large gains low frequency modes are brought into the right half plane. For positive feedback, Figure C.18b, the structural mode is again quickly destabilized. As before, different sets of gains are used to highlight the differences between the positive and negative feedback systems and the bare-airfame. The closed loop responses are shown in Figure C.19. Based on these figures, the negative feedback of differential acceleration does an excellent job of adding damping to the structural mode without affecting low frequency dynamics. The positive feedback, as expected based on the root locus plot, is destabilizing to the structural mode.

The linear model again had to be identified to convert it to a 3 state form. The identification costs were less than one ($J_{ave} < 1$) for both feedback cases. For negative feedback:

$$
\begin{array}{c|cc}
Z_w = -0.023 & Z_{\dot{\eta}} = -6.54 & Z_\eta = -701 \\
\hline
\eta_w = 0.023 & \zeta = 0.362 & \omega = 9.73
\end{array}
\tag{C.24}
$$

(a) CG vertical velocity response   (b) Wing tip vertical acceleration response

Figure C.19: Bode plots comparing response without feedback and with the CG vertical velocity feedback loops closed

$$Z_\delta = 0.27$$
$$\overline{}$$
$$\eta_\delta = 0.45$$

And for positive feedback:

$$
\begin{array}{c|cc}
Z_w = -0.023 & Z_{\dot\eta} = -6.54 & Z_\eta = -701 \\
\hline
\eta_w = 0.023 & \zeta = 0.035 & \omega = 9.73
\end{array}
\tag{C.25}
$$

$$Z_\delta = 0.27$$
$$\overline{}$$
$$\eta_\delta = 0.45$$

Integral differential acceleration does an excellent job of directly impacting the damping of the structural mode. No other control or stability derivatives are altered. The time responses, which confirm that the aircraft dynamics remain intact while the structural mode damping is altered, are shown in Figure C.20.
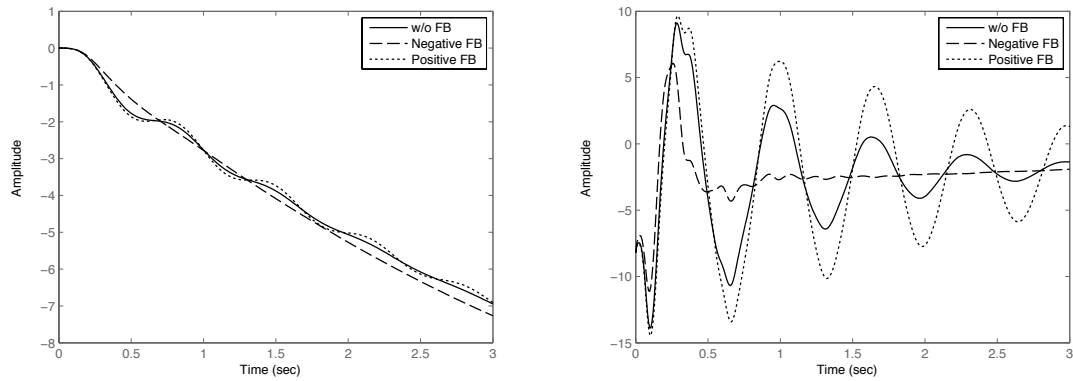
(a) CG vertical velocity response   (b) Wing tip vertical acceleration response

Figure C.20: Collective step input response without feedback and with the integral differential acceleration feedback loop closed

C.2.3   Position Feedback

The final feedback type that may be used is wing deflection. Wing root strain measurements correlate directly to wing tip deflection and their feedback is shown in Figure C.21.

(a) Negative feedback   (b) Positive feedback

Figure C.21: Root Loci for wing root strain feedback to collective

The strain feedback root loci are similar in nature to the acceleration feedbacks. The structural poles increase or decrease in frequency and become unstable for either

feedback. Since strain is a measure of displacement, strain feedback is equivalent to altering the stiffness of a second order system. Similarly to acceleration, this alters the natural frequency, but not the damping, of the system. Close loop responses are shown in Figure C.22.
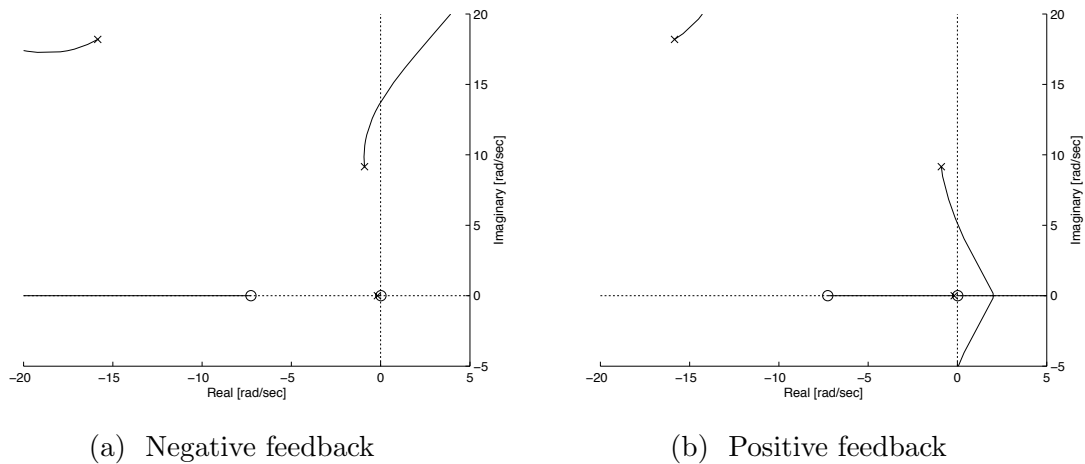

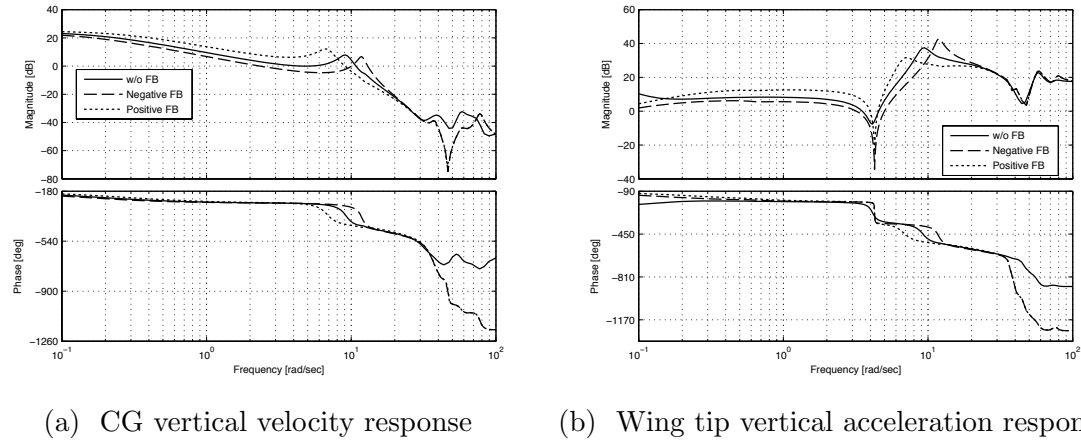(a) CG vertical velocity response   (b) Wing tip vertical acceleration response

Figure C.22: Bode plots comparing response without feedback and with the wing root strain feedback loops closed

$$
\begin{array}{c|cc}
Z_w = -0.023 & Z_{\dot{\eta}} = -6.54 & Z_\eta = -723 \\
\hline
\eta_w = 0.023 & \zeta = 0.0685 & \omega = 11.47
\end{array}
\tag{C.26}
$$

$$
\frac{Z_\delta = 0.27}{\eta_\delta = 0.45}
$$

And for positive feedback:

$$\begin{array}{c|cc} Z_w = -0.023 & Z_{\dot{\eta}} = -6.54 & Z_\eta = -678 \\ \hline \eta_w = 0.023 & \zeta = 0.104 & \omega = 7.56 \end{array} \tag{C.27}$$

$$\frac{Z_\delta = 0.27}{\eta_\delta = 0.45}$$

Both Z_η and ω change altering the low frequency pole location. Time histories are shown in Figures C.23. The time histories confirm that this feedback has the same effect as the acceleration feedback.
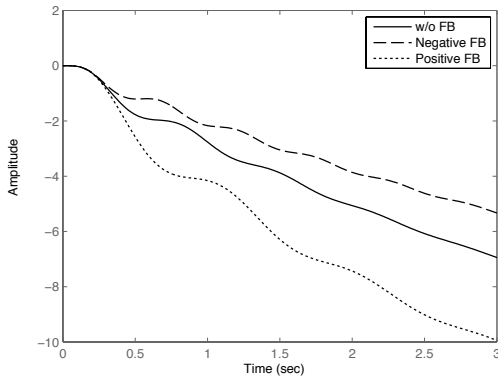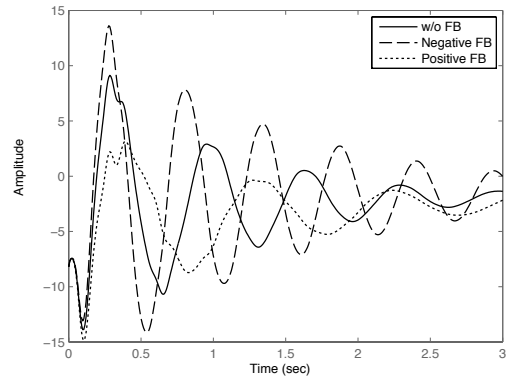
(a) CG vertical velocity response   (b) Wing tip vertical acceleration response

Figure C.23:   Collective step input response without feedback and with the wing root strain feedback loop closed

C.3   Proportional-Integral Feedback

It has been shown the the preferred feedback for structural control is differential velocity feedback, to improve damping, and differential acceleration feedback,

to reduced the peak structural response. This leads to a proportional-integral (PI type) feedback system:

$$K = \left(P + \frac{I}{s} \right) \tag{C.28}$$

$$= \frac{P \left(s + \frac{I}{P} \right)}{s} \tag{C.29}$$

The differential feedback also serves to isolate the structural dynamics from the low frequency dynamics. An isolated structural mode has the follow dynamics:

$$\frac{\ddot{\eta}}{\delta} = \frac{\eta_\delta s^2}{s^2 + 2\zeta\omega s + \omega^2} \tag{C.30}$$

Closing the loop around this system, the broken loop response is (broken at the actuator):

$$\frac{\delta_{in}}{\delta_{out}} = P \frac{\eta_\delta s \left(s + \frac{I}{P} \right)}{s^2 + 2\zeta\omega s + \omega^2} \tag{C.31}$$

The broken loop response removes a s from the numerator and adds a zero instead. The location of this zero is the gain ratio. It is best to place this gain ratio above the structural frequency so that the broken loop response does not excited high frequency dynamics too much and is mostly constrained to the structural mode. The closed loop response, to a system of the form of Figure C.4, is:

$$\frac{\ddot{\eta}}{\delta} = \frac{\eta_\delta s^2}{s^2 + \underbrace{\left(\frac{2\zeta\omega + P\eta_\delta + \frac{I}{P}}{1 + P\eta_\delta} \right)}_{2\zeta_{cl}\omega_{cl}} s + \underbrace{\frac{\omega^2}{1 + P\eta_\delta}}_{w_{cl}^2}} \tag{C.32}$$

351

The feedback is shown to modify the closed loop structural damping and frequency, ζ_{cl} and ω_{cl}.

$$\omega_{cl} = \frac{\omega}{\sqrt{1 + P\eta_\delta}} \tag{C.33}$$

$$\zeta_{cl} = \frac{\zeta}{\sqrt{1 + P\eta_\delta}} + \frac{P\eta_\delta + \frac{I}{P}}{2\omega\sqrt{1 + P\eta_\delta}} \tag{C.34}$$

The value of $\frac{I}{P}$ is the ratio of integral to structural feedback and can be determined a priori. It has already been stated that the ratio should be larger than the structural frequency in order to obtain a good broken loop response. Figure C.24 shows an example set of ratios, ranging from pure integral feedback to pure proportional feedback. Based on this figure, a PI ratio between 10 and 40 give good damping while still reducing structural frequency and minimizing peak response for the mode presented, which occurs around 9 rad/sec. This leaves only the proportional gain to be chosen for the feedback loop, simplifying the design process.

C.4 Notch Filters

Notch filters are commonly used to remove frequency content at a structural mode to prevent the control system from destabilizing the mode. Notch filters are second order, with the damping of the zero placed near that of the structural mode.

$$N(s) = \frac{s^2 + 2\zeta_{\text{num}}\omega s + \omega^2}{s^2 + 2\zeta_{\text{den}}\omega s + \omega^2} \tag{C.35}$$

This notch zero then attracts the pole, increasing stability margins. The notch pole is well damped. A notch filter may be placed on the velocity feedback, shown
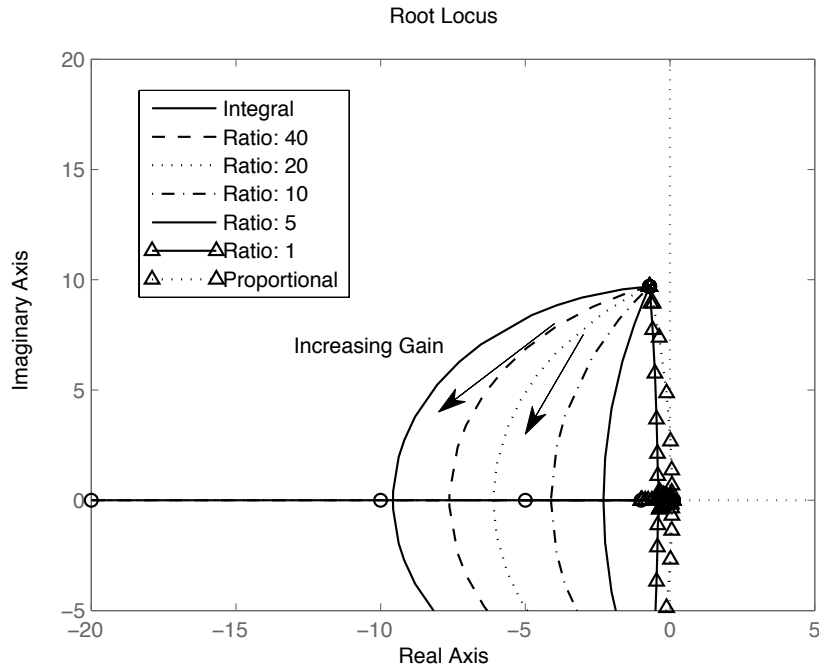
Figure C.24:   Root locus plot showing a variety of proportional to integral gain ratios

in Figure C.1. The notch will improve stability margins, allowing for larger rigid-body feedback gains before instability occurs. Figure C.25 shows the same velocity feedback to collective with the notch filter included.

The gain needed to destabilize the structural mode using notch filters is 2.23. Without notch filters (Figure C.1), the gain to destabilize the structural mode is 0.41. Using notch filters greatly increases the gain margin, thus increasing the range of feedbacks allowed to stabilize and control flight dynamics of the aircraft. The total increase in gain margin is:

$$GM = 20 \log_{10} \left(\frac{2.23}{0.41} \right) = 14.7 \text{ dB} \tag{C.36}$$
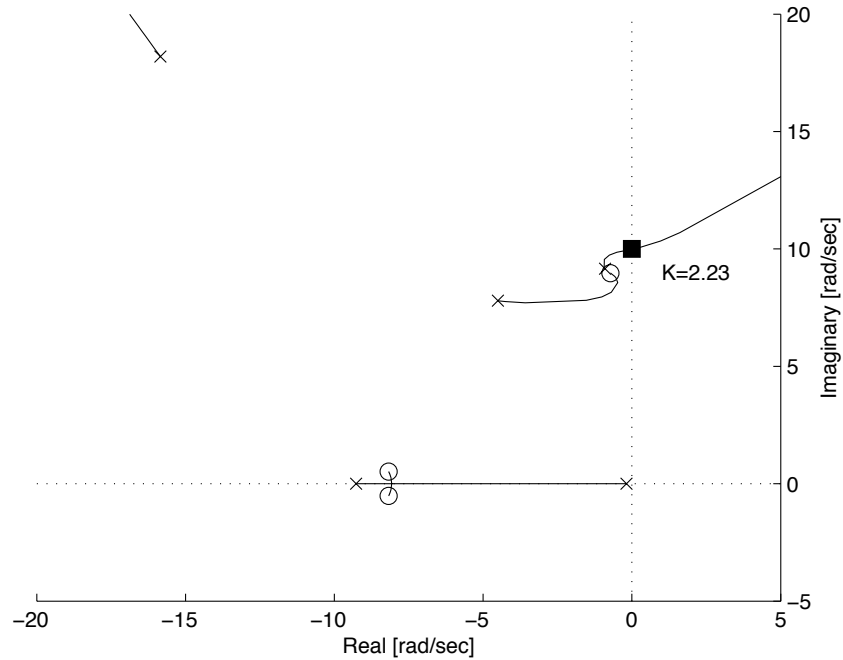
Figure C.25: Root locus plot of CG velocity feedback to collective with a notch filter placed at the structural mode frequency

This same information could be obtained from the bode plots shown in Figure C.26. These bode plots show the responses of the feedback system to collective inputs with and without notch filters. In this example response, the gain margin at the structural mode has been increased by ~15 dB through the use of notch filters.

Notch filters do not fix all problems associated with control of flexible aircraft, they simply remove the structural mode from the feedback and do not allow the control system to destabilize it. The mode still exists in the physical aircraft. The pilot and external disturbances can still excite it. Active control of the structural modes is necessary to control the structural modes themselves.
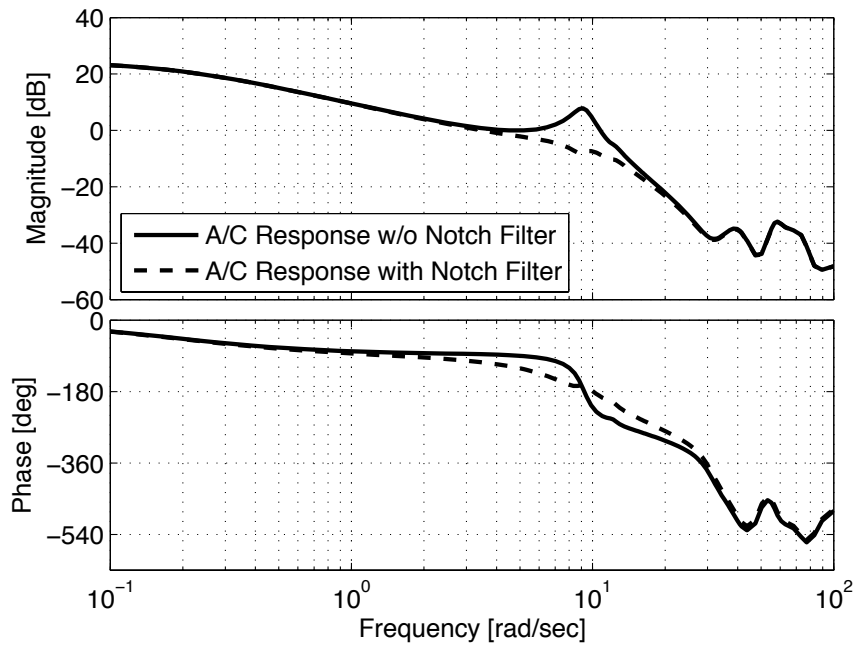
Figure C.26: Bode plot comparisons of vertical velocity feedback response with and without notch filters

C.5 Flexible Aircraft Control

The control of flexible aircraft can be divided into control of low frequency aircraft dynamic modes (such as phugoid, short period, dutch roll, etc.), and control of aircraft structural modes. It is best to divide the control so that gains can be tuned independently to meet both aircraft dynamic and structural specifications. For example, the low frequency aircraft dynamic response must meet bandwidth, model following, and disturbance rejection specifications. Structural modes specifications can include requirements on damping, structural RMS position, or strain. There are also tighter stability margin requirements in the frequency range of structural modes. It would be difficult to achieve optimal performance using only one set of

feedback gains for both groups of responses.

When multiple loops are being closed, the higher frequency loops are closed first. Structural feedback is used to dampen the structural mode and decreases its overall impact on the frequency response. Even though the feedback of acceleration and root strain does not increase damping, these feedbacks might be useful to decrease the peak structural response. Once the structural mode dynamics have been improved, low frequency aircraft dynamics can be augmented. Control of low frequency aircraft dynamic modes is accomplished through feedback using sensors placed at the CG. In the heave case, vertical velocity, w, is typically fed back to collective. This feedback will destabilize the structural mode, much as in Figure C.1, but with the increased damping given by the structural feedback, there will be larger margins at the structural mode.

As an example, PI feedback on differential acceleration will be used to improve the damping of the structural mode by 50%. A high enough gain on the low frequency vertical velocity feedback must be used so that the broken loop crossover frequency will be around 1 rad/sec. This will help ensure adequate piloted handling qualities. The block diagram of the preceding control system is shown in Figure C.27. In this block diagram, P_{Str} is the proportional structural feedback, and R_{Str} is the desired structural feedback ratio, which has been chosen to be 40 for heave axis. P_{RB} is the low frequency, or rigid-body proportional feedback. R_{RB} is the ratio of low frequency integral gain over proportional gain. This ratio is generally chosen to be 1/5 of the broken loop crossover frequency. The gain, K sets the desired vertical velocity per unit stick displacement. The entire structure contains

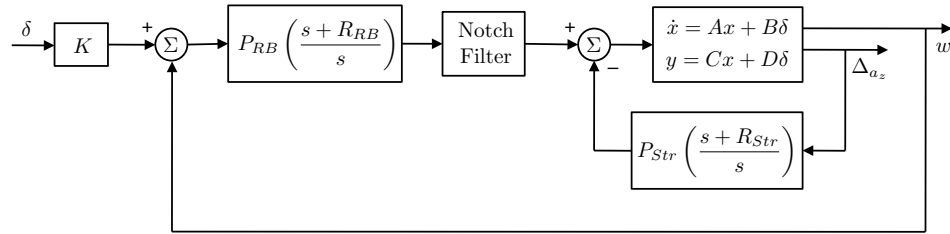only two free variables, the proportional gains on the structural feedback and the rigid-body feedback.

Figure C.27: Block diagram showing sequential loop closure of structural mode followed by low frequency dynamics mode

Various different compensation strategies will now be considered. The most basic case considers only low frequency rigid-body feedback and does not include notch filters of the structural feedback loop, this is referred to as *RB Compensated.* The next case, *Str. Compensated,* closes the loop around the structural modes as well. The *Notch Filters* system does not include structural feedback, but places notch filters at the structural mode. The notch zero is placed on the structural pole and the pole of the notch is well damped. The final design, *Notch and Str.* uses both notch filters and structural feedback. The notch zero in this system is placed on the pole with the structural loop closed. The pole is again chosen to be well damped. This feedback architecture combines benefits from both the notch filter and structural feedback cases. The cases are summarized in Table C.1.

The broken loop responses are shown in Figure C.28. For the structural feedback case, there is large frequency content at the structural mode giving several 0 dB crossings of the magnitude plot. This is due to the large compensation necessary to remove the structural response from the system. The first crossings are at

Table C.1: Design summary

	rigid-body feedback	structural feedback	notch filters
RB Compensated	✓	-	-
Str Compensated	✓	✓	-
Notch Filters	✓	-	✓
Notch and Str	✓	✓	✓

1 rad/sec, as set by the design requirements. The notch filter completely removes frequency content at the structural frequency at the cost of reducing phase at lower frequencies. The notch filters are added in the feedforward path. Here, the notch filters prevent the control system or pilot from exciting the structural modes. There is loss of phase at low frequencies due to the notch filter, so if there are tight phase margins, a smaller notch filter will need to be used. The Rigid-Body (RB) compensation comes from disregarding structural modes. The system is nearly unstable at the structural frequency.

The closed loop responses are shown in Figure C.29. A steady state gain of 10 feet/second per unit stick sets the low frequency asymptote of the compensated responses. There is good tracking up to 1 rad/sec. The RB compensation has the largest structural response. The structural and notch filters both remove the large structural peak. The notch filter almost completely removes the structural pole, while a slight oscillation remains in the structural compensation case.

The time history shown in FIgure C.30 shows that all the compensation strategies obtain 10 feet per second climb rates for a unit stick input. The RB feedback case excites the structural mode, which is very lightly damped. The notch filters do an excellent job at suppressing the structural mode due to pilot inputs. The struc-
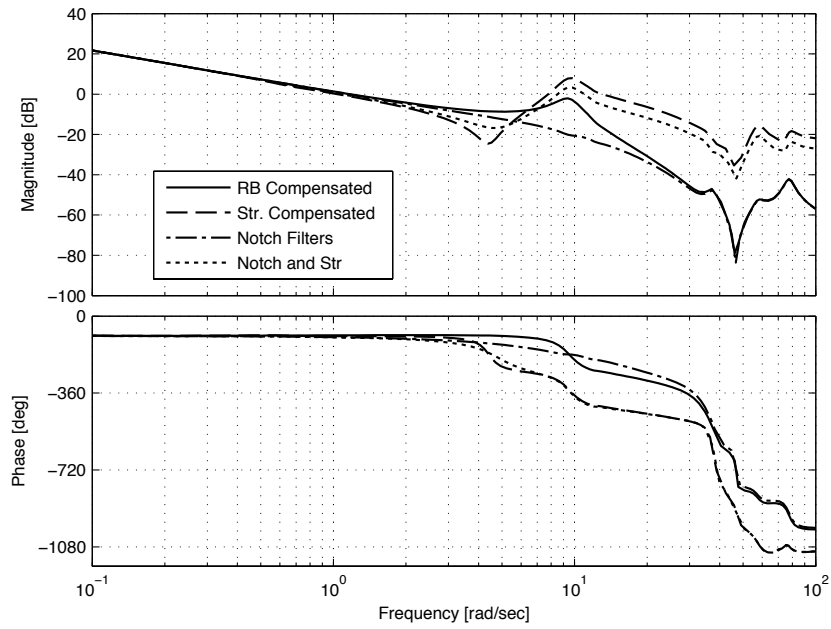
Figure C.28: Comparison of broken loop responses
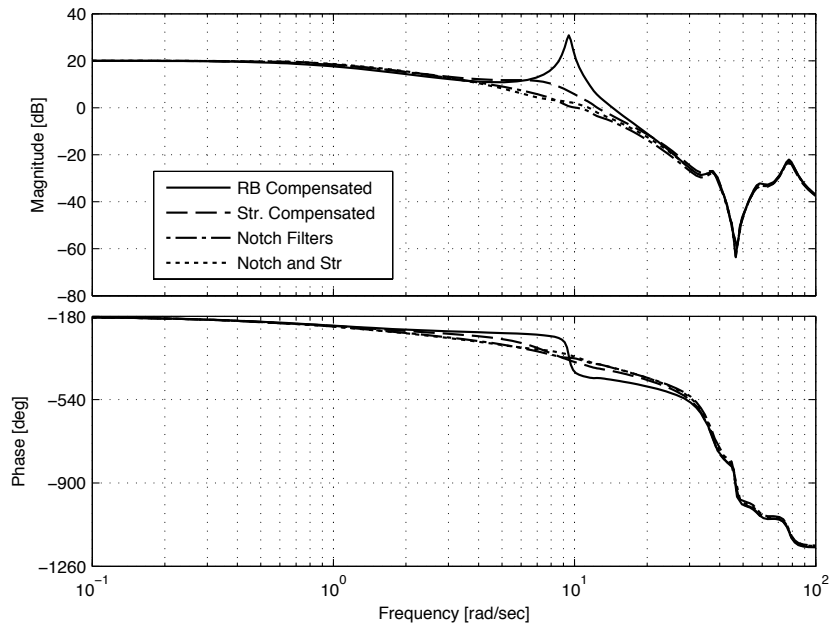
Figure C.29: Heave closed loop response comparing structural compensation schemes

tural compensation cases damp out the structural motion after a few oscillations.
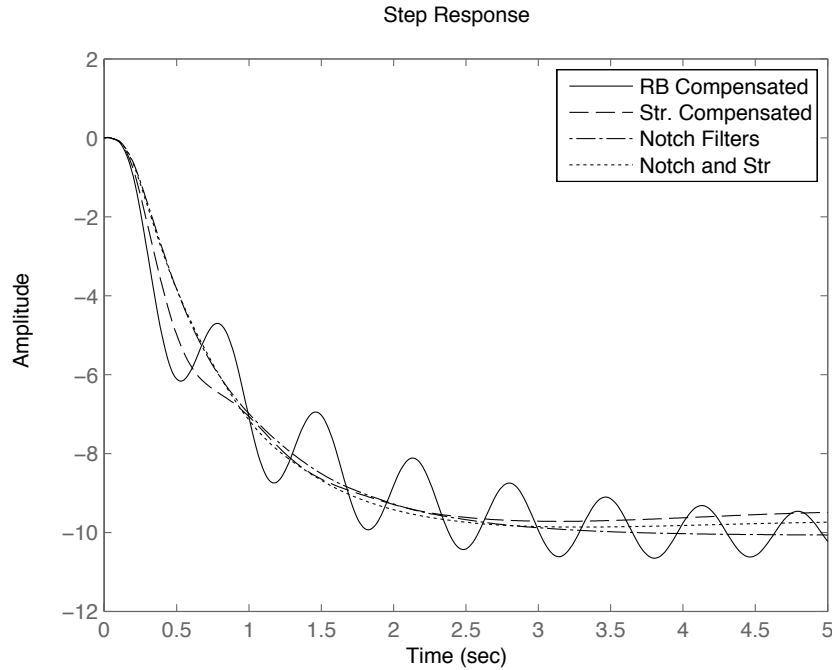
Figure C.30: Heave closed loop step response comparing structural compensation schemes

Finally, Figure C.31 shows disturbance rejection characteristics to disturbances coming at the actuators. The notch filters act on the compensator to remove all frequency content at the structural mode. Therefore, if disturbances come in at the structural frequency, they are not compensated for. The structural compensation is able to remove disturbances at the structural frequency. Figure C.32 shows the step disturbance response. The notch filter case retains some structural oscillation, while both systems with structural feedback remove the oscillation.
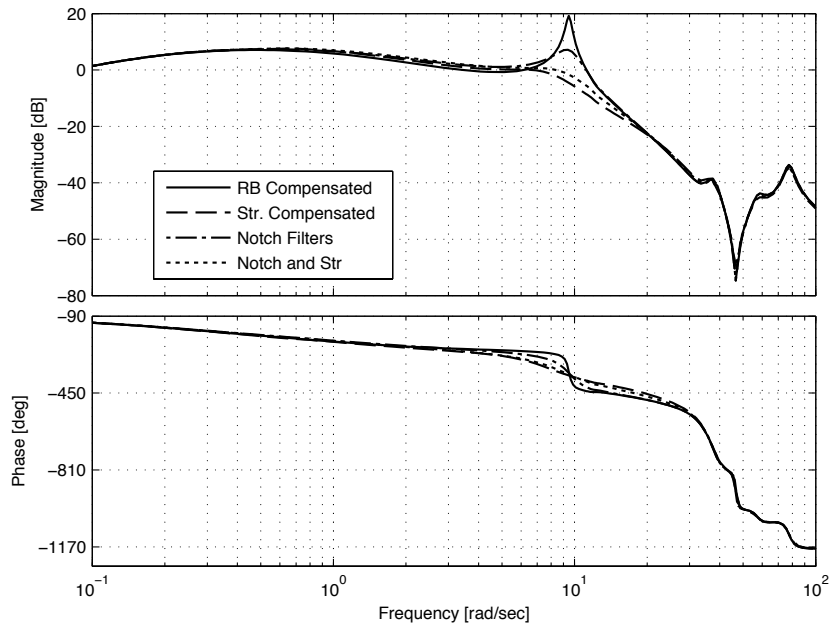
Figure C.31: Heave response to disturbance inputs comparing structural compensation schemes

C.6 Summary

Varying feedbacks were analyzed to determine their effect on structural and low frequency response. Differential responses were deemed the best to isolate feedback control to the structural mode. Velocity feedback effects structural damping, while acceleration or strain responses alter the structural frequency.

Various feedback systems were compared to establish needs for structural compensation and notch filters. Notch filters were excellent at suppressing the closed loop structural response due to pilot inputs and removing the structural component in the broken loop response. However, notch filters reduce phase margins and cannot control the structural mode in disturbances. Structural feedback can damp
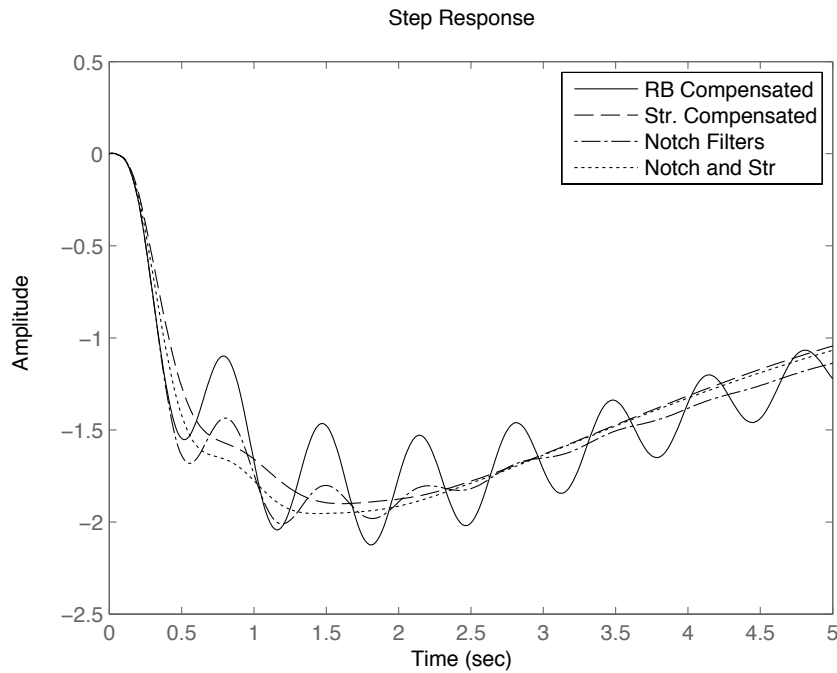
Figure C.32: Heave step response to disturbance inputs comparing structural compensation schemes

the structural mode in the closed loop system and also provides better disturbance rejection characteristics when compared to the notch filter. Structural feedback comes at a cost of increase frequency content in the broken loop response. Combined notch filters and structural feedback give the best closed loop and disturbance rejection characteristics. This system retains the benefits of both notch filters and structural feedback. The costs of improved performance are present in the broken loop response in terms of reduced phase margins, as with the notch filter case, and increased frequency content at the structural mode, as with the structural feedback case.

Bibliography

[1] Johnson, W., Yamauchi, G., and Watts, M. E., "NASA Heavy Lift Rotorcraft Systems Investigation," NASA/TP 213467, December 2005.

[2] Acree, C. W. and Johnson, W., "Aeroelastic Stability of the LCTR2 Civil Tiltrotor," American Helicopter Society Technical Specialist's Meeting, Dallas, TX, October 2008.

[3] Reeder, J. P., "Handling Qualities Experience with Several VTOL Research Aircraft," NASA/TN D-735, March 1961.

[4] Deckert, W. E. and Ferry, R. G., "Preliminary Report: AFFTC Flight Evaluation of the XV-3," Technical Report ADA951617, July 1959.

[5] Quigley, H. C. and Koenig, D. G., "A Flight Study of the Dynamic Stability of a Tilting-Rotor," NASA/TN D-778, April 1961.

[6] Maisel, M., "NASA/Army XV-15 Tilt Rotor Research Aircraft Familiarization Document," NASA/TM X-62,407, January 1976.

[7] Harendra, P. B., Joglekar, M. J., Gaffey, T. M., and Marr, R. L., "V/STOL Tilt Rotor Study—Volume V, A Mathematical Model for the Real Time Flight Simulation of the Bell Model 301 Tilt Rotor Research Aircraft," NASA/CR 114614, April 1971.

[8] Marr, R. L., Sambell, K. W., and Neal, G. T., "V/STOL Tilt Rotor Study—Volume VI, Hover, Low Speed and Conversion Tests of a Tilt Rotor Aeroelastic Model," NASA/CR 114615, May 1973.

[9] Marr, R. L. and Roderick, W. E. B., "Handling Qualities Evaluation of the XV-15 Tilt Rotor Aircraft," *Journal of the American Helicopter Society*, Vol. 20, (2), April 1975.

[10] Anonymous, "Military Specification: Flying Qualities of Piloted V/STOL Aircraft," MIL-F-83300, December 1970.

[11] Ferguson, S. W., "A Mathematical Model for Real Time Flight Simulation of a Generic Tilt-Rotor Aircraft," NASA/CR 166536, September 1988.

[12] Schillings, J. J., J, R. B., Wood, T. L., and Wernicke, K. G., "Maneuver Performance Comparison Between the XV-15 and an Advanced Tiltrotor Design," *Journal of the American Helicopter Society*, Vol. 35, (2), May 1990.

[13] Johnson, W., "Analytical Model for Tilting Proprotor Aircraft Dynamics, Including Blade Torsion and Coupled Bending Modes, and Conversion Mode Operation," NASA/TM X-62,369, August 1974.

[14] Johnson, W., "Analytical Modeling Requirements for Tilting Proprotor Aircraft Dynamics," NASA/TN D-8013, July 1975.

[15] Johnson, W., "Predicted Dynamic Characteristics of the XV-15 Tilting Proprotor Aircraft in Flight and in the 40-by 80-Ft Wind Tunnel," NASA/TM X-73,158, June 1976.

[16] Churchill, G. B. and Dugan, D. C., "Simulation of the XV-15 Tiltrotor Research Aircraft," NASA/TM 84222, March 1982.

[17] Marr, R. L., Willis, J. M., and Churchill, G. B., "Flight Control System Development for the XV-15 Tilt Rotor Aircraft," American Helicopter Society's 32th Annual Forum, Washington, DC, May 1976.

[18] Tischler, M. B., "Frequency-Response Identification of XV-15 Tilt-Rotor Aircraft Dynamics," NASA/TM 89428, May 1987.

[19] Tischler, M. B., Leung, J. G. M., and Dugan, D. C., "Identification and Verification of Frequency-Domain Models for XV-15 Tilt-Rotor Aircraft Dynamics," NASA/TM 83009, August 1984.

[20] Acree, C. W. and Tischler, M. B., "Determining XV-15 Aeroelastic Modes from Flight Data with Frequency-Domain Methods," NASA/TP 3330, May 1993.

[21] Creech, J., "Joint Services Vertical Lift Development (JVX) Program: Looking to the Future," *Vertiflite*, Vol. 30, (7), Nov/Dec 1984, pp. 21–34.

[22] King, D. W., Dabundo, C., Kisor, R. L., and Agnihotri, A., "V-22 Load Limiting Control Law Development," American Helicopter Society's 49th Annual Forum, St. Louis, MO, May 1993.

[23] Dabundo, C., J, W., and Joglekar, M., "Flying Qualities Evaluation for the V-22 Tiltrotor," American Helicopter Society's 47th Annual Forum, Phoenix, AZ, May 1991.

[24] Miller, D. G., Black, T. M., and Joglekar, M., "Tiltrotor Control Law Design for Rotor Loads Alleviation Using Modern Control Techniques," American Control Conference, Boston, MA, June 1991.

[25] Landis, K. H., Davis, J. M., Dabundo, C., and Keller, J. F., "Advanced flight control research and development at Boeing Helicopters," *Advances in Aircraft Flight Control*, edited by M. B. Tischler, Taylor and Francis, Philadelphia, PA, 1996.

[26] Brunken, J. E., Popelka, D. A., and Bryson, R. J., "A Review of the V-22 Dynamics Validation Program," American Helicopter Society's 45th Annual Forum, Boston, MA, May 1989.

[27] Blanken, C. L., Lusardi, J. A., Ivler, C. M., Tischler, M. B., Decker, W. A., Malpica, C., Berger, T., Tucker, G. E., and Hofinger, M. T., "An Investigation of Rotorcraft Stability - Phase Margin Requirements in Hover," American Helicopter Society 65th Annual Forum, Grapevine, TX, May 2009.

[28] Malpica, C., Decker, W. A., Theodore, C. R., Blanken, C. L., and Berger, T., "An Investigation of Large Tilt-Rotor Short-term Attitude Response Handling Qualities Requirements in Hover," American Helicopter Society 66th Annual Forum, Phoenix, AZ, May 2010.

[29] Malpica, C., Theodore, C. R., Decker, W. A., Lawrence, B., and Blanken, C. L., "An Investigation of Large Tilt-Rotor Hover and Low Speed Handling Qualities," American Helicopter Society 67th Annual Forum, Virginia Beach, VA, May 2011.

[30] Lawrence, B., Malpica, C., Theodore, C. R., Decker, W. A., and Lindsey, J. E., "Flight Dynamics Aspects of a Large Civil Tiltrotor Simulation using Translational Rate Command," American Helicopter Society 67th Annual Forum, Virginia Beach, VA, May 2011.

[31] Malpica, C., Theodore, C. R., Lawrence, B., Blanken, C. L., and Lindsey, J., "Handling Qualities of the Large Civil Tiltrotor in Hover using Translational Rate Command," American Helicopter Society 68th Annual Forum, Fort Worth, TX, May 2012.

[32] Anonymous, "Aeronautical Design Standard-33E-PRF, Performance Specification, Handling Qualities Requirements for Military Rotorcraft," US Army AMCOM, March 2000.

[33] Anonymous, "Flying Qualities of Piloted Aircraft," MIL-STD-1797B, Department of Defense, April 2008.

[34] Meyer, M. A. and Padfield, G. D., "First Steps in the Development of Handling Qualities Criteria for a Civil Tiltrotor," American Helicopter Society's 58th Annual Forum, Montreal, CA, June 2002.

[35] Yomchinda, T., Horn, J. F., and Cameron, N., "Integrated Flight Control Design and Handling Qualities Analysis for a Tilt Rotor Aircraft," AIAA Atmospheric Flight Mechanics Conference, Chicago, IL, August 2009.

[36] Manimala, B., Padfield, G. D., Walker, D., Naddei, M., Verde, L., U, C., Rollet, P., and Sandri, F., "Load Alleviation in Tilt Rotor Aircraft Through Active Control; Modeling and Control Concepts," American Helicopter Society's 59th Annual Forum, Phoenix, AZ, May 2003.

[37] Fortenbaugh, R. L., King, D. W., and Paryea, M. A., "Flight Control Features of the Bell-Agusta (BA) 609 Tiltrotor: A Handling Qualities Perspective," 25th European Rotorcraft Forum, Rome, IT, September 1999.

[38] Johnson, W., "A Comprehensive Analytical Model of Rotorcraft Aeromechanics and Dynamics. Part 1: Analysis and Development," NASA/TM 81182, June 1980.

[39] Johnson, W., "CAMRAD II Comprehensive Analytical Model of Rotorcraft Aeromechanics and Dynamics - Theory Manual," Johnson Aeronautics Palo Alto, CA, June 1993.

[40] Johnson, W., "Technology Drivers in the Development of CAMRAD II," American Helicopter Society Aeromechanics Specialists Conference, San Francisco, CA, January 1994.

[41] Acree, C. W., Peyran, R. J., and Johnson, W., "Rotor Design for Whirl Flutter: An Examination of Options for Improving Tiltrotor Aeroelastic Stability Margins," American Helicopter Society 55th Annual Forum, Montreal, Quebec, CA, May 1999.

[42] Acree, C. W., Peyran, R. J., and Johnson, W., "Rotor Design Options for Improving Tiltrotor Whirl-Flutter Stability Margins," *Journal of the American Helicopter Society*, Vol. 46, (2), April 2001, pp. 87–95.

[43] Acree, C. W., Peyran, R. J., and Johnson, W., "Rotor Design Options for Improving XV-15 Whirl-Flutter Stability Margins," NASA/TP 212262, March 2004.

[44] Masarati, P., Ghiringhelli, G. L., Lanz, M., and Mantegazza, P., "Experiences of Multibody Multidisciplinary Rotorcraft Analysis," XVI Congresso Nazionale AIDAA, Palermo, IT, September 2001.

[45] Mattaboni, M., Masarati, P., and Mantegazza, P., "Multibody simulation of a generalized predictive controller fro tiltrotor active aeroelastic control," *Proceedings of the Institution of Mechanical Engineers*, Vol. 226, Part G: Journal of Aerospace Engineering, March 2011.

[46] Mattaboni, M., Masarati, P., Quaranta, G., and Mantegazza, P., "Multibody simulation of Integrated Tiltrotor Flight Mechanics, Aeroelasticity, and Control," *Journal of Guidance, Control, and Dynamics*, Vol. 35, (5), September-October 2012.

[47] Du Val, R. W., "A Real-Time Multi-Body Dynamics Architecture for Rotorcraft Simulations," RAeS and AHS International Conference on The Challenge of Realistic Rotorcraft Simulation, London, UK, November 2001.

[48] Lawrence, B., Malpica, C., Theodore, C. R., Decker, W. A., and Lindsey, J. E., "The Development of a Large Civil Tiltrotor Simulation for Hover and Low-Speed Handling Qualities Investigations," 36th European Rotorcraft Forum, Paris, France, September 2010.

[49] Hill, G., Du Val, R. W., Green, J. A., and C, H. L., "Comparisons of Elastic and Rigid Blade-Element Rotor Models Using Parallel Processing Technology for Piloted Simulations," NASA/TM 102859, June 1991.

[50] Srinivas, V. and Chopra, I., "Validation of a Comprehensive Aeroelastic Analysis for Tiltrotor Aircraft," *Journal of the American Helicopter Society*, Vol. 43, (4), October 1998, pp. 333–341.

[51] Srinivas, V., Chopra, I., and Nixon, M. W., "Aeroelastic Analysis of Advanced Geometry Tiltrotor Aircraft," *Journal of the American Helicopter Society*, Vol. 43, (3), July 1998, pp. 212–220.

[52] Singh, B. and Chopra, I., "Whirl Flutter Stability of Two-Bladed Proprotor/Pylon Systems in High Speed Flight," *Journal of the American Helicopter Society*, Vol. 48, (2), April 2003, pp. 99–107.

[53] Singh, B. and Chopra, I., "Elastic-Blade Whirl Flutter Stability Analysis of Two-Bladed Proprotor/Pylon Systems," *Journal of Aircraft*, Vol. 42, (2), March-April 2005, pp. 519–527.

[54] Nixon, M. W., *Aeroelastic Response and Stability of Tiltrotors with Elastically-Coupled Composite Rotor Blades*, Ph.D. thesis, Department of Aerospace Engineering, University of Maryland, College Park, MD, 1993.

[55] Johnson, W., "A History of Rotorcraft Comprehensive Analyses," NASA/TP 216012, April 2012.

[56] Kim, F. D., Celi, R., and Tischler, M. B., "High-Order State Space Simulation Models of Helicopter Flight Mechanics," *Journal of the American Helicopter Society*, Vol. 38, (4), 1993.

[57] Howlett, J. J., "UH-60A Black Hawk Engineering Simulation Program - Volume II - Mathematical Model," NASA/CR 166309, December 1981.

[58] Turnour, S. R. and Celi, R., "Modeling of Flexible Rotor Blades for Helicopter Flight Dynamics Applications," *Journal of the American Helicopter Society*, Vol. 41, (1), Correction in Vol. 41, (3), July 1996, pp. 191–194, January 1996, pp. 52–66.

[59] Theodore, C. and Celi, R., "Helicopter Flight Dynamic Simulation with Refined Aerodynamics and Flexible Blade Modeling," *Journal of the American Helicopter Society*, Vol. 39, (4), July-August 2002, pp. 577–586.

[60] Thompson, G. O. and Arnold, J. I., "B-52 Controls Configured Vehicle System Design," AIAA Guidance and Control Conference, Stanford, Ca, August 1972.

[61] Hodges, C. E., "Active Flutter Suppression - B-52 Controls Configured Vehicle," AIAA Dynamics Specialists Conference, Williamsburg, VA, March 1973.

[62] Edinger, L. D., Schenk, F. L., and Curtis, A. R., "Study of Load Alleviation and Mode Suppression System (LAMS) on the YF-12 Airplane," NASA/CR 2158, December 1972.

[63] Powers, B. G., "Structural Dynamic Model Obtained From Flight for Use With Piloted Simulation and Handling Qualities Analysis," NASA/TM 4747, June 1996.

[64] Thornton, S. V., "Reduction of Structural Loads Using Maneuver Load Control on the Advanced Fighter Technology Integration (ATFI)/F-111 Mission Adaptive Wing," NASA/TM 4526, September 1993.

[65] Clarke, R., Allen, M. J., Dibley, R. P., Gera, J., and Hodgkinson, J., "Flight Test of the F/A-18 Active Aeroelastic Wing Airplane," NASA/TM 213664, August 2005.

[66] Dibley, R. P., Allen, M. J., Clarke, R., Gera, J., and Hodgkinson, J., "Development and Testing of Control Laws for the Active Aeroelastic Wing Program," NASA/TM 213666, December 2005.

[67] Allen, M. J., Lizotte, A. M., Dibley, R. P., and Clarke, R., "Loads Model Development and Analysis for the F/A-18 Active Aeroelastic Wing Airplane," NASA/TM 213663, November 2005.

[68] Chin, A., Brenner, M. J., and Pickett, M. D., "Integration of Aeroservoelastic Properties into the NASA Dryden F/A-18 Simulator Using Flight Data from the Active Aeroelastic Wing Program," AIAA Atmospheric Flight Mechanics Conference, Portland, OR, August 2011.

[69] Sahasrabudhe, V., Faynberg, A., Pozdin, M., Cheng, R., Tischler, M. B., Stumm, A., and Lavin, M., "Balancing CH-53K Handling Qualities and Stability Margin requirements in the Presence of Heavy External Loads," American Helicopter Society 63rd Annual Forum, Virginia Beach, VA, May 2007.

[70] Wykes, J. H., Borland, C. J., Klelp, M. J., and MacMiller, C. J., "Design and Development of a Structural Mode Control System," NASA/CR 143846, December 1977.

[71] Wykes, J. H., Klepl, M. J., and J, B. M., "Flight Test and Analyses of the B-1 Structural Mode Control System at Supersonic Flight Conditions," NASA/CR 170405, December 1983.

[72] Kubica, F., "New Flight Control Laws for Large Capacity Aircraft Experimentation on Airbus A340," 21st ICAS Conference, Melbourne, Australia, September 1998.

[73] LeGarrec, C. and Humbert, M. L., "Identification of the Aeroelastic Model of a Large Transport Civil Aircraft for Control Law Design and Validation," 22nd ICAS Conference, Harrogate, UK, August-September 2000.

[74] LeGarrec, C. and Kubica, F., "In-Flight Structural Modes Identification for Comfort Improvement by Flight Control Laws," *Journal of Aircraft*, Vol. 42, (1), Engineering Notes, January-February 2005.

[75] Najmabadi, K., Fritchman, B., and Tran, C., "A Process for Model Identification and Validation of Dynamical Equations for a Flexible Transport Aircraft," RTO SCI Symposium on 'System Identification for Integrated Aircraft Development and Flight Testing', Madrid, Spain, May 1998.

[76] Wagner, M. and Norris, G., *Boeing 787 Dreamliner*, MBI Publishing Group, Minneapolis, MN, 2009.

[77] Schmidt, D. K., *Modern Flight Dynamics*, McGraw Hill, New York, NY, 2012.

[78] Amirouche, F. M. L., *Fundamentals of Multibody Dynamics*, Birkhauser, 2006.

[79] Nguyen, N., Tuzcu, I., Yucelen, T., and Calise, A., "Longitudinal Dynamics and Adaptive Control Application for an Aeroelastic Generic Transport Model," AIAA Atmospheric Flight Mechanics Conference, Portland, OR, August 2011.

[80] Meirovitch, L. and Tuzcu, I., "Integrated Approach to the Dynamics and Control of Maneuvering Flexible Aircraft," NASA/CR 211748, 2003.

[81] Waszak, M. R. and Schmidt, D. K., "Flight Dynamics of Aeroelastic Vehicles," *Journal of Aircraft*, Vol. 25, (6), June 1988.

[82] Avanzini, G., Capello, E., and Pianceza, I. A., "Mixed Newtonian-Lagrangian Approach for the Analysis of Flexible Aircraft Dynamics," AIAA Atmospheric Flight Mechanics Conference, Portland, OR, August 2011.

[83] Rosen, A. and Friedmann, P. P., "Nonlinear Equations of Equilibrium for Elastic Helicopter of Wind Turbine Blades Undergoing Moderate Deflections," NASA/CR 159478, December 1978.

[84] Theodore, C. R., *Helicopter Flight Dynamics Simulation with Refined Aerodynamic Modeling*, Ph.D. thesis, Department of Aerospace Engineering, University of Maryland, College Park, MD, 2000.

[85] Leishman, J., *Principles of Helicopter Aerodynamics*, Cambridge University Press, New York, NY, second edition, Chapter 8, 2006.

[86] Johnson, W., *Helicopter Theory*, Dover Publications, Inc., New York, NY, Chapter 10, 1994.

[87] McCormick, B. W., *Aerodynamics, Aeronautics, and Flight Mechanics*, John Wiley and Sons, Inc., second edition, Chapter 3, 1995.

[88] Pitt, D. M. and Peters, D. A., "Theoretical Prediction of Dynamic Inflow Derivatives," *Vertica*, Vol. 5, (1), 1981, pp. 21–34.

[89] Peters, D. A. and HaQuang, N., "Dynamic Inflow for Practical Applications," *Journal of the American Helicopter Society*, Vol. 33, (4), October 1988, pp. 64–68.

[90] Celi, R., "Solution of Rotary-Wing Aeromechanical Problems Using Differential-Algebraic Equation Solvers," *Journal of the American Helicopter Society*, Vol. 45, (4), October 2000, pp. 253–262.

[91] Celi, R., "Helicopter Rotor Blade Aeroelasticity in Forward Flight with an Implicit Structural Operator," *AIAA Journal*, Vol. 30, (9), 1992.

[92] Kim, F. D., Celi, R., and Tischler, M. B., "Forward Flight Trim and Frequency Response Validation of a Helicopter Simulation Model," *Journal of the American Helicopter Society*, Vol. 30, (6), Nov-Dec 1993, pp. 854–863.

[93] Chen, R. T. N. and Jeske, J. A., "Kinematic Properties of the Helicopter in Coordinate Turns," NASA/TP 1773, April 1981.

[94] Moré, J. J., Garbow, B. S., and Hillstrom, K. E., "User Guide for MINPACK-1," Technical Report ANL-80-74, pub-ANL, pub-ANL:adr, aug 1980.

[95] Petzold, L., "Description of DASSL: A Differential/Algebraic System Solver," Technical Report SAND82-8637, Sandia National Laboratories, Sep 1982.

[96] Tischler, M. B. and Remple, R. K., *Aircraft and Rotorcraft System Identification: Engineering Methods with Flight Test Examples*, AIAA, Reston, VA, 2006.

[97] Tischler, M. B. and Remple, R. K., *Aircraft and Rotorcraft System Identification: Engineering Methods with Flight Test Examples*, AIAA, second edition, Reston, VA, 2012.

[98] McRuer, D. T., Ashkenas, I. L., and Graham, D., *Aircraft Dynamics and Automatic Control*, Princeton University Press, Princeton, NJ, 1973.

[99] Ivler, C. M., *Design and Flight Test of a Cable Angle Feedback Control System for Improved Helicopter Slung Load Operations at Low Speed*, Ph.D. thesis, Stanford University, Stanford, CA, December 2012.

[100] Juhasz, O., Celi, R., Ivler, C. M., Tischler, M. B., and Berger, T., "Flight Dynamic Simulation Modeling of Large Flexible Tiltrotor Aircraft," American Helicopter Society 68th Annual Forum, Fort Worth, TX, May 2012.

[101] Waszak, M. R., Davidson, J. B., and Schmidt, D. K., "A Simulation Study of the Flight Dynamics of Elastic Aircraft," NASA/CR 4102, 1987.

[102] Waszak, M. R., Buttrill, C. S., and Schmidt, D. K., "Modeling and Model Simplification of Aeroelastic Vehicles: An Overview," NASA/TM 107691, September 1992.

[103] de Oliveira Silva, B. G., "Data Gathering and Preliminary Results of the System Identification of a Flexible Aircraft Model," AIAA Atmospheric Flight Mechanics Conference, Portland, OR, August 2011.

[104] de Oliveira Silva, B. G. and Mönnich, W., "System Identification of Flexible Aircraft in Time Domain," AIAA Atmospheric Flight Mechanics Conference, Minneapolis, MN, August 2012.

[105] Theodore, C. R., Ivler, C. M., Tischler, M. B., Field, E. J., Neville, R. L., and Ross, H. P., "System Identification of Large Flexible Transport Aircraft," AIAA Atmospheric Flight Mechanics Conference and Exhibit, Honolulu, HI, August 2008.

[106] Lusardi, J. A., Blanken, C. L., and Tischler, M. B., "Piloted Evaluation of a UH-60 Mixer Equivalent Turbulence Simulation Model," American Helicopter Society 59th Annual Forum, Phoenix, AZ, May 2003.

[107] Berger, T., Tischler, M. B., Hagerott, S. G., Gangsaas, D., and Saeed, N., "Longitudinal Control Law Design and Handling Qualities Optimization for a Business Jet Flight Control System," AIAA Atmospheric Flight Mechanics Conference, Boston, MA, August 2012.

[108] Berger, T., Tischler, M. B., Hagerott, S. G., Gangsaas, D., and Saeed, N., "Lateral/Directional Control Law Design and Handling Qualities Optimization for a Business Jet Flight Control System," AIAA Atmospheric Flight Mechanics Conference, Boston, MA, August 2013.

[109] Catapang, D. R., Tischler, M. B., and Biezad, D. J., "Robust Crossfeed Design for Hovering Rotorcraft," *International Journal of Robust and Nonlinear Control*, Vol. 4, May-June 1994, pp. 161–180.

[110] Mansur, M. H. and Tischler, M. B., "Flight Test Comparison of Alternate Strategies for Multi-Loop Control Law Optimization," American Helicopter Society 69th Annual Forum, Phoenix, AZ, May 2013.

[111] Tischler, M. B., Ivler, C. M., Mansur, M. H., Cheung, K. K., Berger, T., and Berrios, M., "Handling-Qualities Optimization and Trade-offs in Rotorcraft

Flight Control Design," Rotorcraft Handling Qualities Conference, University of Liverpool, UK, November 2008.

[112] Duda, H., "Prediction of Pilot-in-the-Loop Oscillations due to Rate Saturation," *Journal of Guidance, Navigation, and Control*, Vol. 20, (3), May-June 1997.

[113] Anonymous, "Flight Control Systems - Design, Installation, and Test of Piloted Aircraft, General Specifications for," MIL-DTL-9490E, Department of Defense Interface Standard, February 2006.

[114] Stein, G., "Respect the Unstable," *IEEE Control Systems Magazine*, August 2003, pp. 12–25.

[115] Fujizawa, B. T., Lusardi, J. A., Tischler, M. B., Braddom, S. R., and Jeram, G. J., "Response Type Tradeoffs in Helicopter Handling Qualities for the GVE," American Helicopter Society 67th Annual Forum, Virginia Beach, VA, May 2011.

[116] Ivler, C. M. and Tischler, M. B., "System Identification Modeling for Flight Control Design," RAeS Rotorcraft Handling-Qualities Conference, University of Liverpool, UK, November 2008.